University of Naples Federico II

Department of Structures for Engineering and Architecture

31st cycle Ph.D program in Structural and Geotechnical Engineering and Seismic Risk

SEISMIC FRAGILITY ASSESSMENT OF CODE-CONFORMING BUILDINGS IN ITALY

A thesis submitted to the Department of Structures for Engineering and Architecture,

University of Naples Federico II,

in partial fulfillment of the requirements for the degree of Doctor of Philosophy in Engineering

by

Akiko Suzuki

under the supervision of

Professor Iunio Iervolino

June 2019

Abstract

The current European building codes, espousing performance-based seismic design principles, require safety verifications of structures under different levels of earthquakes. Although design seismic actions are prescribed on a probabilistically uniform basis referring to specific earthquake return periods, an explicit control of structural reliability of new constructions has not been implemented into the current practice.

To assess implicit seismic risk of new constructions in Italy, a large national research project, named *Rischio Implicito Norme Tecniche per le Costruzioni* (RINTC), was developed for the years 2015-2017. One of the main contributions of this thesis is to gather insights into seismic risk of Italian code-conforming structures from a large building data set of the project. From a seismic design point of view, seismic performance of the prototype buildings is discussed through SDoF approximation of the detailed structural models, maintaining a wide variety of structural types, configurations, and seismic hazard levels at the building site. The study presented herein describes that heterogeneity of seismic risk among different structural types and different sites is mainly ascribed to actual strength reduction factors and local seismicity above the design seismic action.

Since seismic fragility curves of the examined prototype buildings were neither needed nor obtained in the RINTC project, the thesis also provides lognormal fragility parameters estimated through state-of-the-art approaches in performance-based earthquake engineering. For all examined buildings, fragility curves are estimated in terms of spectral acceleration at the fundamental vibration period of the structure, that is structure-specific. For the sake of comparison of structural fragility across multiple buildings, PGA-fragility curves are also examined for some selected building cases. To this aim, a probabilistic framework for hazard-consistent intensity measure conversion is established.

Furthermore, the effects of seismic sequences, which are not considered in the current seismic design philosophy nor in the RINTC project, are also addressed in the context of long-term seismic risk assessment of code-conforming buildings.

Research framework

Parts of the study presented in this thesis have been developed within the research activities of the following projects: *Rete dei Laboratori Universitari di Ingegneria Sismica* (ReLUIS) activities funded by *Presidenza del Consiglio dei Ministri – Dipartimento della Protezione Civile* (2014-2018 program) and *Rischio Implicito Norme Tecniche per le Costruzioni* (RINTC) project developed by the joint working group between ReLUIS and *Centro Europeo di Ricerca e Formazione in Ingegneria Sismica* (EUCENTRE), with the funding of *Dipartimento della Protezione Civile.* The funding, data, and technical supports from the projects are gratefully acknowledged.

Acknowledgements

Pursuing a Ph.D. abroad was the bravest decision I have ever made in the past twenty-seven years of my life. For the last three years, I have been feeling, without exaggeration, as if walking a tightrope high above the ground without the net afforded by my country and sometimes reflected on how overly optimistic and easy-going I was three years ago! Approaching to the end of this journey, however, I realize there are many people that have supported me and guided me to get here. Taking this opportunity I would like to express my deepest gratitude to all of them.

First of all, I would like to sincerely appreciate my adviser, Prof. Iunio Iervolino, for his continued support and patience throughout my Ph.D study, as well as for giving me the opportunity to relish this journey. I owe him all I have learned and experienced in the three years, which is I strongly believe going to be ones of the most valuable assets in my future life. Among all, what I am the most grateful for him is to have taught me his never-compromising attitude in quality of work, which has roots in his passion and respect for research. His rigorous and to-the-point supervision strengthened me as a researcher and always led me to the right direction.

I would like to say a big thank you to Dr. Georgios Baltzopoulos and Dr. Eugenio Chioccarelli for their technical supports and collaborations. I still remember when I visited this university for the first time to find you Ph.D. researchers in Naples excellent! Through my three years, I hope I became some steps closer to you than my younger self at that time. Also, many thanks go to Pasquale, Roberto, Adriana, Francesco, and Marbel for sharing their knowledge and techniques with me.

I greatly acknowledge *Rete dei Laboratori Universitari di Ingegneria Sismica* (ReLUIS) and the College Woman Association of Japan not only for providing me with the scholarship fundings but also for giving me confidence in steering my life in this direction.

I cannot imagine my Ph.D life without Sofia Dias and Mariana Zimbru, my new best friends and comrades at the university. Even though we were basically at different offices or

campuses, I was lucky to have a place where I was able to be who I am. I really appreciate you sharing beautiful memories with me in Naples (many of pizzas I had with you were even tastier!), and I do hope our friendship will continue from here on. My thanks also go to Bikash, Gilbert, Greta, and Giorgios, my friends from the international doctoral student network in Naples.

I owe a deep sense of gratitude and respect to Prof. Masayoshi Nakashima and Prof. Masahiro Kurata for sending me to Italy as well as for taking care of me studying abroad like a family. Without them, I would not have met most of the people acknowledged in these pages.

I would like to extend my sincere thanks to my housemates, Francesca De Marinis, Umberto Di Lorenzo and Giusy de Martino, as well as people around them, who made my life in Naples even more colorful. The home was the most comfortable place for me, and at the same time, I was always inspired by the ways they lead their lives.

I am also very grateful to my friends from my university days in Kyoto: Sei Yoshikawa, Manami Inoue, Miho Sato, Hiroyuki Inamasu, and Francesca Barbagallo. Reunions with you in Italy were so special to me that every time I regained energy for living abroad. Also, special thanks are extended to my old friends, Ai, Aya, Maya, Chihiro-chan, who kept me updated by airmails in this digital world.

I would like to also extend many “Grazie” to those who I have met in this chaotic but charming city, Naples. The larger share is intended for mere acquaintances in my neighborhood, but I truly feel they are the ones who made my every single day of the three years. I would definitely miss my friendly neighbors with the charms of the city.

Finally, I mustn’t close this page without thanking my family: my father and mother for their continuous supports, love, and encouragement; my sister for being always my wonderful role model in blazing a new path. I have been blessed with a very loving and supportive family and appreciate them for making me who I am today.

Akiko Suzuki

Naples, June 2019

Contents

List of Tables

List of Figures

List of Acronyms

AN: as-new

ASCE: American Society of Civil Engineers

APSHA: aftershock probabilistic seismic hazard analysis

AQ: L'Aquila

B2BIDA: back-to-back IDA

BI: base-isolation

BF: bare-frame

CBF: concentrically braced frame

CDF: cumulative distribution function

CEN: European Committee for Standardization

CMS: conditional mean spectrum

CNR: *Consiglio Nazionale delle Ricerche*

CoV: coefficient of variation

CP: collapse prevention

CS: conditional spectra

D/C: demand-to-capacity ratio

DM: *Decreto Ministeriale*

DPC*: Dipartimento della Protezione Civile*

DS: damage state

DSHA: deterministic seismic hazard analysis

DV: Decision variable

EC8: Eurocode 8

EDP: engineering demand parameter

ESDoF: equivalent single-degree-of-freedom

EUCENTRE: European Centre for Training and Research in Earthquake Engineering

FEMA: Federal Emergency Management Agency

GC: global collapse

GM: ground motion

GMPE: ground motion prediction equation

HPP: homogeneous Poisson process

HAZUS: Hazard in the United States

IDA: Incremental dynamic analysis

IDR: inter-story drift ratio

IF: infilled frame

IM: intensity measure

IML: intensity measure level

LS: life-safety

LSA: linear static analysis

MAF: mean annual frequency

MI: Milan

MRF: moment resisting frame

MRS: modal response spectra

MSA: multiple stripe analysis

NA: Naples

NDP: Nationally Determined Parameters

NLDA: nonlinear dynamic analysis

NLSA: nonlienar static analysis

NTC: *le Norme Tecniche per le Costruzioni*

PBEE: performance-based earthquake engineering

PBSD: Performance-based seismic design

PDF: probability density function

PEER: Pacific Earthquake Engineering Research

PF: pilotis frame

PGA: peak ground acceleration

PL: performance level RC: reinforced concrete

RD: *Regio Decreto*

RDL: *Regio Decreto Legge*

RDR: roof drift ratio

RINTC: *Rischio Implicito Norme Tecniche per le Costruzioni*

RV: random variable

UPD: usability-preventing damage

URM: un-reinforced masonry

S: steel

Sa: spectral acceleration

SB: simple building (rules)

SEAOC: Structural Engineers Association of California

SLC: *collapse prevention limit state*

SLD: *damage limit state*

SLO: *operational limit state*

SLS: *serviceability limit state*

SLV: *life-safety limit state*

SPO: static pushover

SPSHA: sequence-based probabilistic seismic hazard analysis

UHS: uniform hazard spectra

ULS: *ultimate limit state*

3D: three-dimensional

Chapter 1

Introduction

1.1 Background and Motivation

1.1.1 The RINTC project 2015-2017

In the current Italian building code, *le Norme Tecniche per le Costruzioni* (NTC; [CS.LL.PP., 2008; 2018]), structural performance with respect to the violation of given limit states (*failure*) has to be verified for levels of ground motions (GMs) associated with specific exceedance return periods at the building site, similarly to Eurocode 8 (EC8) [CEN, 2004]. In case of ordinary structures, for example, safety verifications for *damage limitation* and *life-safety* limit states are required against GM levels corresponding to exceedance return periods (T_R) of 50 and 475 years (probabilities of exceedance of 63% and 10% in 50 years), respectively. In such design practice, it is generally expected that the probability of failure given the occurrence of an design level earthquake will be smaller than that of exceedance of the considered GM intensity thanks to code requirements, however, the safety margins at the structure level are not explicitly controlled in seismic design.

To quantitatively address the seismic risk that the code-conforming design implicitly exposes structures to, a large national research project was carried out in Italy during 2015-2017. This project, named *Rischio Implicito Norme Tecniche per le Costruzioni* (RINTC), was developed by the joint working group between *Rete dei Laboratori Universitari di Ingegneria Sismica* (ReLUIS) and *Centro Europeo di Ricerca e Formazione in Ingegneria Sismica* (EUCENTRE), with the funding of *Dipartimento della Protezione Civile* (DPC). In this project, structures belonging to a variety of structural types (i.e., un-reinforced masonry (URM), reinforced concrete (RC), precast reinforced concrete (PRC), steel (S), and base-isolated reinforced concrete (BI) buildings) and configurations, were designed according to the current

Italian code provisions for a number of sites with different hazard levels (Milan, Caltanissetta, Rome, Naples, and L'Aquila; Figure 1-1) and local site conditions (A and C according to EC8 classification). The seismic risk of the designed structures was assessed in terms of mean annual failure rates with respect to *global collapse* and *usability-preventing damage* via a state-of-the-art approach within the performance-based earthquake engineering (PBEE) framework. The failure criteria were defined in a uniform manner among structures belonging to the same typology. For each building, the failure probability was computed at discrete GM intensity measure (IM) levels through nonlinear dynamic analysis using the three-dimensional (3D) structural models and then was integrated with the seismic hazard at the building site. As a summary of the results of RINTC, Figure 1-2 reports the annual collapse rates (see the following chapters for computation details) for the prototype buildings designed at the selected five sites, arranged in ascending order of design hazard at the site with respect to peak ground acceleration (PGA); see [RINTC-Workgroup, 2018] and Chapter 2 for more detailed descriptions. As illustrated in the figure, the project concluded with the following main findings that: (i) the heterogeneity of seismic safety among structural types designed for the same hazard and (ii) a general trend of increasing risk with the increasing design hazard of the building site [Iervolino et al., 2017; 2018]. Some may argue that (i) is well expected due to the different design procedures which pertain to different structural types (e.g., RC and URM buildings); on the other hand, (ii) should be limited to some extent, that is to say, to a tolerable reliability threshold toward the revision of the current building code in the coming years.

In fact, gradual implementation of explicit probabilistic approaches for structural analysis and reliability criteria into the codes have been discussed in the European research community in recent years. The Annex to the revised EC8 Part 1 [CEN 2017], which has been drafted by [Dolšek et al., 2017], is being expected to contain some tolerable reliability criteria, as well as explicit probabilistic approaches, yet simplified for the preliminary stage of implementation [Fajfar, 2018]. From this point of view, it is essential to deeper the understanding on the relationship between the structural seismic performance of current code-conforming buildings and the degree of reliability.

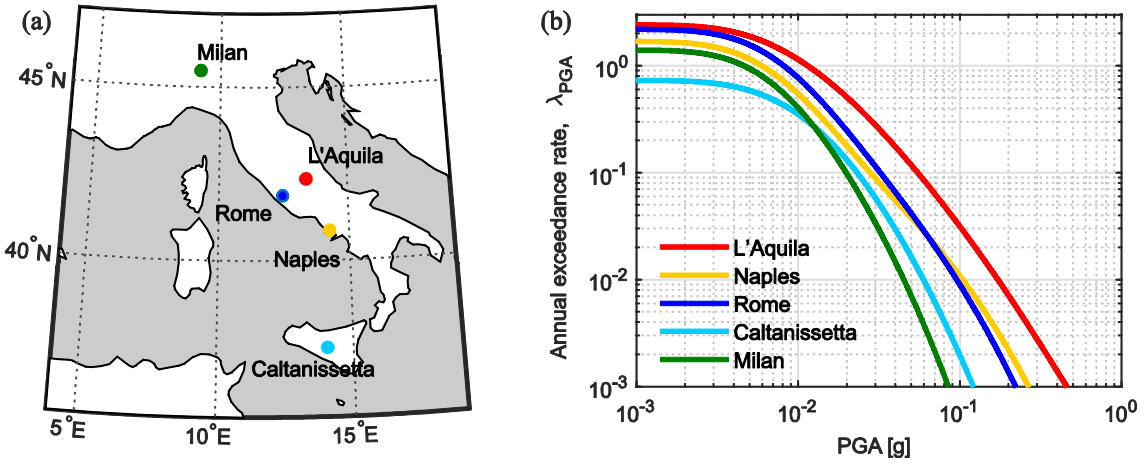

Figure 1-1 Selected five Italian cities in the RINTC project; (a) locations; (b) annual exceedance rates of PGA on soil condition C according to EC 8 classification.

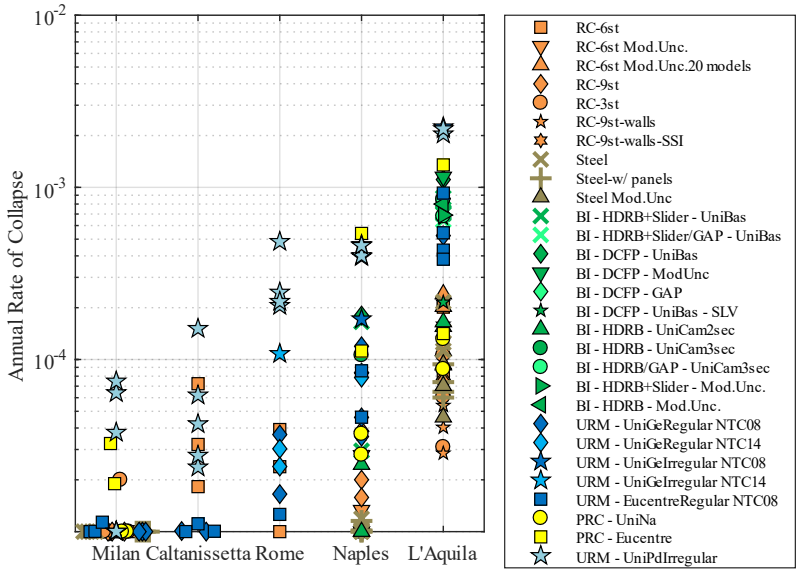

Figure 1-2 Annual collapse rates for the examined structural typologies and sites (on soil C) in the RINTC project; adopted from [RINTC-Workgroup, 2018].

1.1.2 Objectives of the thesis

In order to deepen the aforementioned issues regarding the heterogeneity of seismic risk, the present thesis aims to examine the structural seismic performance of current code-conforming Italian buildings and their relationships with the degree of the resulting structural reliability in the PBEE framework. To this end, some representative buildings designed, modeled and

analyzed within the RINTC project are selected as to maintain its variety of structural types and configurations and site hazard levels as much as possible. Their structural design features and resulting fragility are extensively discussed in this thesis using the simplified models equivalent to the original 3D structural models. Each of the structural numerical models analyzed in the RINTC project is converted into the equivalent single-degree-of-freedom (ESDoF) system based on the static pushover (SPO) curve. Particularly, the thesis is devoted to achieve the following objectives:

- ***Objective 1:*** *Evaluation of structural performance factors of code-conforming structures through SDoF approximation*.

  It is considered that the heterogeneity of seismic risk of code-conforming buildings may arise from the diversity in design assumptions pertaining to different structural types and configurations and site hazard levels. One of the objectives in this thesis is to examine the observed trend of the seismic risk of the code-conforming prototype buildings with respect to seismic structural features that originate from design. In particular, the inelastic capacities of the designed structures, such as resistance and ductility capacities, as well as the other fundamental structural properties, are translated into the SDoF quantities, which facilitate to discuss their relationships with the resulting seismic risk.

- ***Objective 2*****:** *Evaluation of seismic fragility and safety margins of code-conforming buildings with respect to damage-onset and global collapse limit states.*

  Since the fragility curves were neither needed nor obtained in the RINTC project, this thesis aims to develop hazard-consistent seismic fragility curves for the code-conforming building structures in the Italian context. More specifically, the study primarily provides parametric (lognormal) collapse fragility functions estimated using the ESDoF systems of the selected prototype buildings. Moreover, the collapse safety margins are expressed in terms of the ratio of GM IM level causing structural collapse to that of the design seismic action. Usability-preventing damage onset fragility is also

addressed in a similar manner but referring to the structural response from the 3D structural models in this thesis.

- ***Objective 3*****:** *Hazard-consistent intensity measure conversion for fragility curves and applications to the RINTC prototype buildings.*

  When the seismic risk of structures featuring various structural characteristics and seismic hazard levels at the construction site is concerned, the comparison of seismic fragility between multiple buildings/sites is not a trivial task because the choice of the IM used for the seismic risk assessment is structure-specific. This thesis aims to develop a probabilistic framework for converting IMs of fragility curves, which ensures hazard consistency for the building site. Through the applications of the proposed framework to the prototype buildings under consideration, this thesis also presents a direct comparison of the structural fragilities between some RINTC prototype buildings in terms of a common IM (i.e., PGA) converted from the structural response given the original structural-specific IMs.

- ***Objective 4*****:** *Quantifications of effects of earthquake sequences to code-conforming buildings.*

  In the current formulation of the PBEE framework, seismic loss assessment of structures typically neglects the progressive attainment of a certain loss level due to damage accumulation in multiple earthquakes. However, this issue can be relevant in cases of the occurrence of a mainshock-aftershock sequence during which repair cannot be promptly enforced, as the 2016 Central Italy earthquake sequence reminded. To address such issues, a Markov-chain-based reliability model of damage accumulation in structures due to mainshock-aftershock sequences is developed. The structural reliability of code-conforming building structures against seismic sequences is discussed through the application study using the ESDoF systems of selected prototype code-conforming buildings. The effects of seismic sequences, which have not been mentioned in the RINTC project, are discussed for the sites with different hazard levels through a comparison with the reliability model which neglects aftershock events.

1.1.3 Organization of the thesis

The present thesis is structured such that:

In the remainder of **Chapter 1**, the development of the European/Italian building codes and some general concepts regarding the design and seismic risk assessment in the PBEE framework are first briefly overviewed. In particular, the technical conventions and the state-of-the-arts in PBEE are recalled with a particular focus on probabilistic hazard and fragility analyses.

In **Chapter 2**, the case-study buildings of this study are first specified from the prototype buildings of the RINTC project, followed by the calibration of their simplified equivalent models (i.e., ESDoF systems) based on the SPO curves of the original 3D structural models. The equivalent models are validated through the comparisons with the original models, in terms of the structural dynamic response (i.e., demand-to-capacity ratio of an *engineering demand parameter*, of interest, EDP). Using these models, the inelastic capacities of the case study buildings are evaluated in terms of fundamental seismic performance factors, such as strength reduction factors and ductility capacity up to structural failure. Across different structural types, configurations, and sites with different hazard levels, the trends of such performance factors are summarized in relation to the resulting structural reliability.

In **Chapter 3**, lognormal collapse fragility functions are estimated for the case study buildings through nonlinear dynamic analysis using the calibrated ESDoF systems. The chapter primarily provides hazard-consistent collapse fragility curves, in terms of spectral acceleration at a period close to the fundamental vibration periods of the structure, for the buildings designed at high-hazard sites. Subsequently, those for low-to-moderate seismicity sites are presented with some discussions on relevant scientific issues regarding GM record selection. The derived fragility models are validated through the comparisons of the annual collapse rates with non-parametric fragility functions computed from the original 3D structural models. The fragility functions with respect to usability-preventing damage are also provided using structural response of the original 3D models.

In **Chapter 4**, possible strategies for converting GM IMs of fragility curves are discussed following a rigorous probabilistic framework. Particularly, the present study

examines three conversion strategies for spectral-acceleration-based measures under different assumptions on the sufficiency of IMs involved in calculations. The chapter first explores all possible strategies referring to the examined prototype RC buildings at a high hazard site under a variety of conversion conditions, such as the combinations of IMs and the performance levels. Subsequently, the IM conversions are performed for the other building typologies located at the same site through the optimal strategy for the case at hand. The seismic fragility of the prototype buildings featuring a variety of structural types/configuration is compared in terms of a common IM, that is, PGA in the study presented in this chapter.

In **Chapter 5**, a homogeneous Markov-chain model for damage accumulation in structures due to mainshock-aftershock seismic sequences is formulated, being extended from an existing model considering only mainshocks. In particular, a discrete-time and discrete-state Markovian process is characterized by a stationary transition matrix consisting of the probabilities the structure changes its state during a seismic sequence. It allows to predict the time-variant seismic risk of structures considering homogeneous Poisson mainshock-aftershock sequences which are characterized through sequence-based probabilistic seismic hazard analysis. The proposed reliability model is illustrated through applications to the calibrated ESDoF systems of selected code-conforming RC buildings, then the resulting seismic risk is compared with the existing model that neglects the effects of aftershocks.

In **Chapter 6**, the important contributions and findings of the study are summarized.

1.2 Performance-based earthquake engineering - Seismic design and risk assessment of structures -

1.2.1 Development of performance-based seismic design framework

The design philosophy of Performance-Based Seismic Design (PBSD) first appeared in the 1967 edition of the SEAOC model code (Blue Book) [Diebold et al., 2008] which built the conceptual basis of the modern building regulations in seismic regions: (1) to withstand minor (low-intensity) earthquakes without any damage in the structural and non-structural elements; (2) to withstand moderate (medium-intensity) earthquakes limiting damage in nonstructural components; (3) to withstand major (high-intensity) earthquakes without the overall or partial collapse of buildings but with some structural and/or nonstructural damage. This concept was later followed by ATC 3-06 [ATC, 1978], which was the first modern building code released in the US, in 1978. The code was established primarily aiming at the protection of human life through the prevention of the global and partial collapse, hence it contained the regulations to satisfy only the *life-safety* performance objective under GMs with the 475 year- return period of exceedance. However, the aftermath of the strong earthquakes in the mid-nineties (e.g., 1994 Northridge earthquake in California and 1995 Kobe earthquake in Japan) revealed that the economic loss due to downtime and repair costs of the damaged structures were intolerably high even if the structures comprised with the regulations based on traditional design philosophy [Lee and Mosalam, 2006]. These lessons motivated to establish the PBEE framework that attempts to address the maintenance and safety control of structures primarily, in terms of collapse risk, fatalities, repair costs, and post-earthquake downtime loss. The first generation of PBEE principally aimed to frame the PBSD criteria, and the well-known pioneering works are Vision 2000 report [SEAOC, 1995] and [FEMA, 1997] which aimed to ensure the desired structural performances at various intensity levels of seismic hazard. In particular, the structural performance levels are classified into four as *fully operational*, *operational*, *life-safety*, and *near collapse* whereas seismic hazard levels are categorized based on return periods (corresponding to a certain exceedance probability within the life span of the structure) as frequent, occasional, rare, and very rare seismic events. Depending on the

objectives and the functions of a structure of interest, the design criteria that simultaneously meet the expected combinations of structural performance and hazard levels (i.e., diagonal multi-tiers shown in Figure 1-3) are determined. The proposed design earthquake levels by Vision 2000 report, for example, correspond to the return periods of 43, 72, 475, and 970 years, corresponding to exceedance probabilities of 69, 50, 10, and 5% during the expected building lifespan of 50 years.

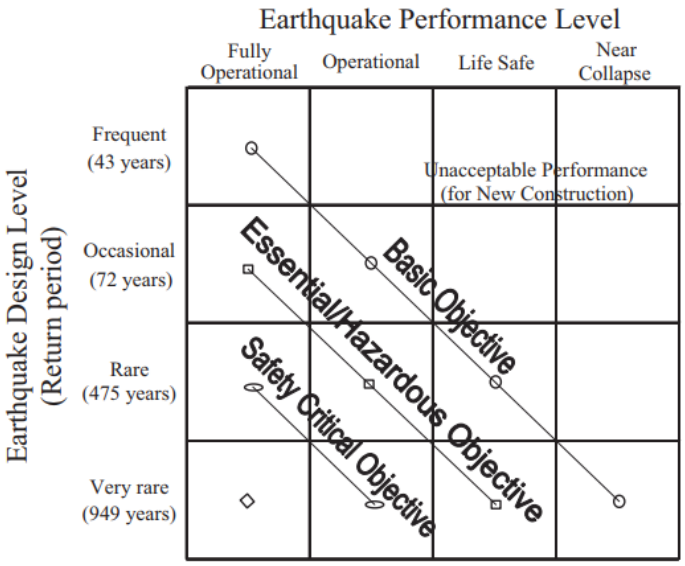

Figure 1-3 Seismic performance objectives for building proposed by the Vision 2000 report after [SEAOC, 1995].

In Europe, the PBSD concept first appeared in the 1960s, e.g., [CEB, 1970] and the definitions of the appropriate limit states for intended structural performances had been discussed since then. The first standards for seismic design of new buildings, European Design Standard EN1998-1 - EC8 Part 1: Design of structures for earthquake resistance (hereafter denoted as EC8) – was published by the European Committee for Standardization in 2004 [CEN, 2004]. The current version of EC8 embodies the PBSD concept to a limited extent, asking for safety verifications at two performance levels; no collapse requirement at an *ultimate limit state* (ULS) and damage limitation requirement at a *serviceability limit state* (SLS) each of which corresponds to a certain return period. Following the aforementioned PBSD principles, the former requirement aims at the protection of human life under a rare event, through the

prevention of the global or local collapse of the structure and the retention of structural integrity and load-resisting capacity while the latter targets at the reduction of economic losses preventing any significant damage in structural and non-structural components under frequent earthquakes. It should be noted that, in order to account for diversity in engineering traditions and geographic and climatic natures among the member countries of the European Community, the values of return periods, as well as other "Nationally Determined Parameters (NDPs)", are prescribed not by EC8 but by National Annexes for each of them. For ordinary structures, the recommended return periods are 475 years for ULS and 95 years SLS corresponding to 10% exceedance probability in 50 years and in 10 years, respectively.

It is worth recalling that the return periods are derived assuming a Poisson model for the occurrence of earthquakes exceeding a certain threshold. Given a target probability of exceedance (P_{V_R}) within a reference time period (in most countries, equal to the expected lifespan of the structure, V_R), the corresponding return period of exceedance T_R is given by:

$$T_R = \frac{1}{\lambda_{im}} = -\frac{V_R}{\ln\left(1-P_{V_R}\right)} \tag{1-1}$$

where the reciprocal of T_R, i.e., λ_{im}, is the mean annual rate of seismic events exceeding the corresponding IM level.

Unlike explicit PBSD approaches, the enhanced safety of structures essential for civil protection or with large occupancy is achieved through the use of "importance factors" (γ_{I}) by which the design seismic action under the 475 year- GMs is increased to satisfy life-safety criteria in a more conservative manner. According to EC8, buildings are categorized into four classes (Class I – IV) depending on the consequences of collapse for human life, their importance for public safety and civil protection in the immediate post-earthquake period, and the social and economic consequences of collapse. The recommended values for this factor are $\gamma_{\mathrm{I}} = 1.0$ for ordinary structures (i.e., classified into Importance Class II in EC8) , $\gamma_{\mathrm{I}} = 1.2$ for buildings whose seismic resistance is essential with respect to the consequences of the structural collapse (e.g. schools, assembly halls, cultural institutions etc.); $\gamma_{\mathrm{I}} = 1.4$ for buildings essential for civil protection (e.g. hospitals, fire stations, power plants, etc.); $\gamma_{\mathrm{I}} = 0.8$ for

buildings of minor importance for public safety (e.g., those for agricultural use). The main analysis procedure is linear modal response spectrum analysis and EC8 standard prescribes the design lateral strength accounting for the hysteretic energy dissipation of the structure by means of behavior factors, q, as with other modern building codes that espouse PBSD principles. A behavior factor q is used to reduce the elastic strength demand, with the tradeoff of acquiescing to plastic deformation under the design actions, thus it is given depending on structural typology, configuration and ductility class. The equivalent static lateral force procedure can be used under some restrictions. Nonlinear analysis is permitted either by pushover analysis or by nonlinear dynamic analysis (NLDA).

1.2.2 An overview of seismic regulations in Italy

1.2.2.1 Early years (1909-1973): Equivalent static lateral force method

After the 1908 Messina earthquake (moment magnitude M_w 7.1), a quantitative procedure for seismic design of structures was established by a committee of Italian experts. The proposed procedure, which was formulated mainly based on the results of the studies on three timber-framed buildings which had survived the Messina earthquake with little or no damage, became mandatory in 1909 through the enforcement of the first Italian seismic building code issued by the Royal Decree (*Regio Decreto*; RD) [RD 193/09, 1909; Sorrentino, 2007]. Assuming only specified regions classified as seismic zones (category I), it introduced some limitations on building height and on the use of materials for different structural types. According to Freeman [1932], the code required to design structures so that they would resist a lateral force equivalent to 1/12 and 1/8 of the story weight (so-called "*seismic coefficients*" or "*seismic ratios*" equal to 0.08 and 0.13) in the first story and in the second/third story, respectively. This regulation was later adjusted in the *Regio Decreto Legge* (RDL) [RDL 573/15, 1915] as to provide the seismic coefficients of 1/8 and 1/6, after the 1915 Avezzano earthquake. Since then, the concept of the equivalent static procedure for seismic analysis had great impact on subsequent early earthquake engineering in Italy, and the Italian building code had been continuously evolved involving some modifications with respect to the seismic coefficients and seismic zones: in 1924, RDL 2089/24 [1924] mentioned a decoupling assumption of horizontal and vertical loads

acting on the structure; in 1927, more detailed seismic classification was introduced, then the seismic actions and less demanding structural provisions were prescribed for the sites with moderate seismicity belonging to *category II* [RDL 431/27, 1927]; the law enacted in 1935 [RDL 640/35, 1935] imposed the development of the local building regulations on each municipality and also reduced the vertical seismic actions (to 40% and 25% of live and dead loads, respectively) and the seismic coefficients (to 10% and 7% of the story weight for *category I* and *II*, respectively); furthermore, some modifications particularly regarding the seismic coefficients were made in the following three decades for the specific sites belonging to seismic zones, i.e., [RDL 2105/37, 1937] and [L 1684/62, 1962].

1.2.2.2 Modern years (1974 – 2002): Considerations on dynamic behaviors of structures

The seismic regulations enforced in the mid-seventies brought a turning point to the Italian building code. In 1974, the law [L 64/74, 1974], which established the administrative framework of seismic regulations in Italy allowing technical provisions to be constantly modified or updated by the Italian government, was enacted. The Ministerial Decree (*Decreto Ministeriale*; DM) issued in the following year [DM 40/75, 1975] introduced, for the first time in the Italian history, the response spectrum and design options with dynamic or static analyses [De Marco et al., 2000]. In case of static analysis, the lateral seismic forces applied to the building were prescribed by the following equation:

$$F_h = C \cdot R \cdot \varepsilon \cdot \beta \cdot W \tag{1-2}$$

where W is the total weight of the structure; R is the response coefficient derived from a function of the fundamental vibration period of the structure; C is the seismic action defined by means of a seismic intensity parameter; coefficients ε and β account for soil compressibility ($\varepsilon = 1.00$ for stiff soil and $\varepsilon = 1.30$ for soft soil) and the presence of structural walls ($\beta = 1.20$ with the presence of infilled walls, otherwise $\beta = 1.0$), respectively. As indicated by the equation, the product of C and R can be considered as a design acceleration demand accounting for the dynamic properties and the inelastic capacity of the structure.

Although the code highlighted the dynamic nature of the structure by introducing the response spectrum, the reference seismic action and the derivation of the design spectrum had not been prescribed, and the base shear coefficient for structures whose fundamental vibration period was shorter than 0.8s was fixed to 0.07 for both of the seismic categories, which was equal to that already adopted in 1935.

DM 515/81 [1981] issued in the following year of the 1980 Irpinia- Basilicata earthquake (M_w 6.9) defined a third seismic category for which a coefficient C was set to 0.04. In 1984, DM 208/84 [1984] introduced different levels of safety margins for particular categories of buildings by increasing the design seismic lateral forces by the "importance factors" equal to 1.2 for buildings whose seismic resistance is essential with respect to the consequences of the structural collapse, and 1.4 for those essential for civil protection.

DM 16/01/1996 [1996] followed the similar framework as the previous regulations but contained some new features. The most noteworthy is that the code allowed one to use the limit state design approach for ULS assessment, increasing the horizontal design seismic action by 1.5 as an alternative to the admissible stress approach which had been adopted in the previous code. The introduction of the new verification method was in accordance with the DM of 09/01/1996 [DM 09/01/1996, 1996] which allowed one to design RC and steel constructions following Eurocodes 2 and 3, respectively. Also, the code started to regulate buildings not with respect to the number of floors but with respect to the height.

In the following year, 1997, the first indications for the capacity-based design targets, such as the attainment of local and global ductility capacity, were provided with an explanatory document attached to *Circolare Ministero* LL.PP. no.65 of 04/10/1997 [M.LL.PP. 65, 1997], which is recognized as an important step toward the PBSD approach.

1.2.2.3 Pre-NTC (2003-2007): Transition to the EC8 compliance criteria

The 2003 seismic code [O.P.C.M. 3274, 2003], followed by the modifications [O.P.C.M. 3431, 2005], brought the most relevant change in the Italian building seismic provisions over thirty years toward the EC8 compliance. In particular, it introduced the forth category for seismic classification and an innovative definition on seismic input by means of an elastic spectrum

whose shape is determined, based on local soil and topographic conditions, as to be anchored to a PGA value corresponds to a 10% exceedance probability in 50 years for the seismic category of the site. In accordance with EC8, the code introduced the concept of behavior factors by which an elastic acceleration spectrum is reduced to obtain a design acceleration spectrum. Thus, design horizontal seismic load, F_h, was given by the following equation:

$$F_h = \frac{Sa(T_s) \cdot W \cdot \lambda}{q \cdot g} \tag{1-3}$$

where $Sa(T_s)$ is the elastic spectral acceleration at the fundamental vibration period of structure T_s (approximately calculated based on the structural typology and structural height), λ is a coefficient equal to 0.85 for static analysis, g is the gravitational acceleration.

It is also worth noting that the 2003 seismic code explicitly introduced the concept of capacity design presenting the strength hierarchy and structural regularity principles.

1.2.2.4 Current building code (2008 – present):

The current version of the Italian seismic building code, which was issued in 2008 (NTC08), finally incorporated the PBSD principles toward the compliance with EC8 after March 2010 [Fardis, 2009].[1] In particular, design seismic hazard was defined no longer on a municipality basis (i.e., seismic zones) but completely on a probabilistic basis as a function of geographic coordinates of the building site (i.e., Probabilistic Seismic Hazard Analysis; PSHA). As mentioned above, the limit states and the corresponding design earthquake levels are prescribed in the National Annex, and NTC08 defines the following four combinations of the performance limit states and hazard levels:

For the SLSs,

- *Operational limit state* (SLO; 43 year- return period; 81% exceedance probability in 50 years): the structure must withstand a frequent event without the disruption of the use preventing any significant damage in structural and non-structural elements and in the systems critical to its serviceability.

[1] National design standards had been used in parallel with EC8 until March 2010. After that, some regulations conflicting with any EN-Eurocode had to be withdrawn.

- *Damage limit state* (SLD; 72 year- return period; 63% exceedance probability in 50 years): the structure must withstand an occasional event without any significant damage that can thread the human life and reduce the load-bearing capacity in horizontal and vertical directions. The systems may have minor damage that can be easily or economically repaired after the event, thus resulting in the immediate occupancy of the structure.

For the ULSs,

- *Life-safety limit state* (SLV; 475 year- return period; 10% exceedance probability in 50 years): After a rare event, the structure may suffer partial and global collapse of non-structural components and significant damage in structural components associated with a substantial loss of lateral stiffness, however, the structure retains its vertical load-resisting capacity and sufficient residual seismic performance against lateral loads to guarantee human life safety.
- *Collapse prevention limit state* (SLC; 975 year- return period; 5% exceedance probability in 50 years): After a very rare event, the structure is heavily damaged both in non-structural and structural components. It retains little residual lateral load-bearing capacity at the verge of collapse, but its vertical elements can still carry the gravity loads.

It should be noted that NTC08 adopts several particular terms in prescribing seismic hazard and seismic actions on structures, extending the EC8 recommendations.

First, NTC08 prescribes a reference period V_R in Eq. (1-1) as the product of the nominal life of a structure V_N and its coefficient of use C_U, instead of increasing the hazard level through the use of importance factors. V_N is the expected lifespan of the structure under the regular maintenance, which is defined 10 years for temporary structures, 50 years for ordinary structures, and 100 years for large or strategic structures. C_U is given depending on the class of use of the structure, whose definition is similar as importance factors. The prescribed values for this factor are $C_U = 1.0$ for ordinary structures (i.e., with a normal number of people, without hazardous contents for the environment or essential public and social functions.); $C_U = 1.5$ for buildings (with a large number of people or for industrial use involving hazardous activities to the environment); $C_U = 2.0$ for buildings with publicly and strategically important functions and those essential for civil protection; $C_U = 0.7$ for

buildings with only occasional presence of people and agricultural buildings.

For more detailed descriptions on the evolution of the Italian building code up to NTC08, see also [De Marco et al., 2000], [Ricci et al., 2011], and [Petruzzelli and Iervolino, 2013].

1.2.3 Seismic risk assessments in the PBEE framework

The goals of PBEE is to improve decision-making procedures through the developments of new design and assessment methods which allow to quantify and control the seismic risk of structures considering inherent uncertainties. As discussed above, the first generation of PBEE made efforts to frame the PBSD concept to ensure the desired structural performances at different intensity levels of seismic hazard. However, the methodology had lack of probabilistic evaluations of the element performance and of the relationship between the performance of the global system and that at element scale. In order to evaluate the seismic risk of structures in a more explicit manner, the Pacific Earthquake Engineering Research (PEER) Center further developed the PBEE methodology during 1997-2010, which became the current technical basis of probabilistic seismic risk assessment procedures. One of the key features of the second generation PBEE methodology is the explicit probabilistic characterizations of uncertainty variables, such as earthquake intensity, GM characteristics, structural response, physical damage, and economic and human losses, thus it allows to express the seismic risk as the exceeding rate of a Decision Variable (DV) that represents the direct interest of various stakeholders, such monetary losses, downtime, and casualties.

Figure 1-4 illustrates the flow of the seismic loss assessment procedure in the PEER methodology [Porter, 2003; Krawinkler, 2005]. It consists of the following four steps: hazard analysis, structural analysis, damage analysis, and loss/downtime analysis. According to the assessment flow in the figure, the procedure and outcome of each analysis is briefly overviewed in the following.

***Hazard analysis*:** seismic hazard at a particular site is evaluated accounting for the uncertainties in the location and the size of structure-damaging earthquakes via PSHA. The shaking level of GMs is expressed with a GM IM, which is typically PGA or elastic spectral acceleration at the fundamental vibration period of the structure. The corresponding hazard

curve, which represents the mean annual frequency of earthquakes exceeding a certain (im) value of an IM, i.e., λ_{im}; the expected number of the earthquake occurrences in a year, is provided as the outcome of this analysis. It should be noted that the choice of an appropriate IM is determined not only based on its "*hazard computability*" [Giovenale et al., 2004] as well as considering "*sufficiency*" and "*efficiency*" criteria [Luco and Cornell, 2001] to properly evaluate structural response and its circumstances in the following analyses (see also discussions in Chapter 4).

***Structural analysis*:** structural response under earthquake excitation is probabilistically estimated considering uncertainties related to GM characteristics, i.e., *record-to-record variability*. A series of NLDA is performed using a numerical structural model of the facility (denoted in the figure as SFS in the figure) and a (statistically sufficient) number of GM records. For each GM record conditioned at a particular IM level, structural responses are measured in terms of engineering demand parameters, *EDP* s, relevant to damage and losses. A vector of *EDP* s can include internal member forces or local and global deformations. This procedure yields the probability distribution of *EDP* conditional to the IM, i.e., $P[EDP = edp \mid IM = im]$ as the product of this analysis phase.

***Damage analysis*:** At the stage of damage analysis, the selected EDPs are associated to particular levels of physical damage for each of structural and non-structural components which are relevant to losses. In particular, a fragility function, i.e., the probability of observing or exceeding a specific level of physical damage for a certain (edp) value of *EDP*, is modelled as a function of damage measure, *DM*. Thus, the probability term, $P[DM = dm \mid EDP = edp]$ is provided as the outcome of this analysis. Damage measures qualitatively describe the damage and its consequences to the global system or to a local component of the system. They also may include descriptions of necessary repairs to structural or nonstructural components and can be defined correspondingly to several discrete damage levels (e.g., DM_1= initial cracking, DM_2 =shear failure, DM_3 = axial failure, etc., in case of concrete structural components).

***Loss analysis*:** Once the fragility curves with respect to the damage states of all relevant components of the system are established, the DVs of interest (such as monetary losses,

downtime, and casualties) can be related to DM by means of loss functions expressed in the form of $P[DV = dv \mid DM = dm]$. The mean annual rate of exceeding a certain DV value, λ_{dv}, that is the final outcome of the PEER PBEE methodology, can be computed with the following equation by integrating the four probabilistic functions, i.e., hazard, structural response, damage, and loss functions, which are modelled up to this stage.

$$\lambda_{dv} = \int_{DM}\int_{EDP}\int_{IM} G(dv \mid dm)\left|dG(dm \mid edp)\right|\left|dG(edp \mid im)\right|\left|d\lambda_{im}\right| \qquad (1\text{-}4)$$

where $G(\bullet)$ denotes a complementary cumulative distribution function, hence $G(x \mid y)$ represents the exceedance probability of x conditional to a given y value, i.e., $P[X \geq x \mid Y = y]$; $dG(x \mid y)$ and $d\lambda_{im}$ are the differentials of the functions of the corresponding variables. This equation frames the PEER PBEE methodology mathematically, in accordance with the assessment flowchart in Figure 1-4.

Since the next chapters of this thesis particularly are developed involving seismic hazard analysis and structural analysis, the basics and the state-of-arts of probabilistic seismic hazard and fragility assessments will be recalled in the following subsections.

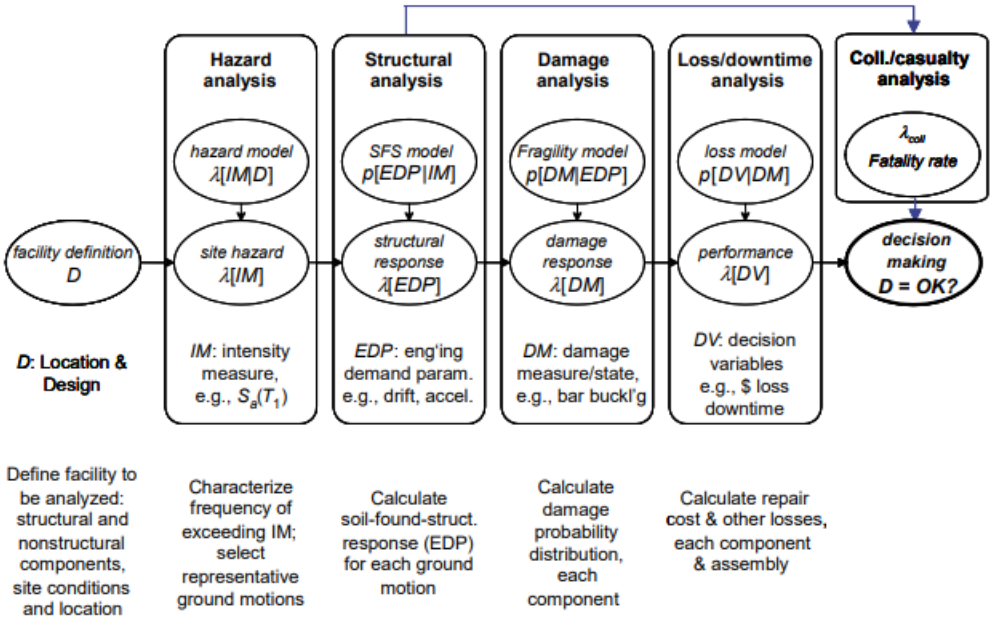

Figure 1-4 Seismic loss assessment flowchart of PEER methodology; adopted from [Krawinkler, 2005]

1.2.3.1 Probabilistic seismic hazard analysis

Occurrence rate of earthquakes

In line with the PBEE framework, the assessment methods of seismic hazard have been developed in order to prescribe GM intensity levels to be considered in designing structures for a particular site. There are two different approaches in assessing seismic hazard, *deterministic seismic hazard analysis* (DSHA) and PSHA; the former approach defines seismic hazard deterministically assuming a particular seismic scenario with seismic magnitude and source-to-site distance, which is typically a worst-case scenario (i.e., earthquakes with the largest magnitude and the shortest source-to-site distance for a seismogenic zone of interest); the latter approach characterizes the hazard at the site by aggregating the contributions from all possible earthquake scenarios on a probabilistic basis. In the early years of structural and geotechnical earthquake engineering, DSHA had been commonly used in practice, however, it was later replaced by PSHA as implemented in the current performance-based seismic building codes. For this reason, this thesis does not deal with DSHA; see for details see [Reiter, 1990] and [Kramer, 1996].

The classical formulation of PSHA was formulated in the milestone work by [Cornell, 1968]. The goal of PSHA is to estimate the probability of exceeding a certain IM level at a particular site, considering uncertainties related to seismogenic zones and their GM features, such as earthquake size, location, and occurrence. In case of considering a single seismogenic zone, a *hazard curve*, representing the mean annual frequency (MAF) of earthquakes exceeding a particular IM value, im, can be calculated as:

$$\lambda_{im} = \nu_E \cdot P\left[IM > im\right] = \nu_E \cdot \int_R \int_M P\left[IM > im \,|\, M = m, R = r\right] \cdot f_M\left(m\right) \cdot f_R\left(r\right) dm \cdot dr \qquad (1\text{-}5)$$

where ν_E is the mean annual occurrence rate of earthquakes with magnitude exceeding its lower threshold, $P\left[IM > im \,|\, M = m,\ R = r\right]$ is obtained from a ground motion prediction equation (GMPE) providing the probability distribution of IM for a given magnitude and source-to-site distance, M and R, respectively, $f_M\left(m\right)$ and $f_R\left(r\right)$ are the probability density functions (PDFs) for the magnitude and the site-to-site distance, which are derived from the (bounded) *Gutenberg-Richter law* and from a source model, respectively. It should be noted

that, in the above equation, *M* and *R* are assumed to be independent random variables.

If multiple (N_S) earthquake sources, whose MAF of threshold magnitude exceedance is denoted as v_i where $i=\{1,2,\ldots,N_S\}$, can contribute to the seismic hazard at the site, the mean annual exceedance rate considering all sources potentially affecting the site is given by:

$$\lambda_{im}=\sum_{n_s=1}^{Ns} v_{E,n_s}\cdot\int_R\int_M P[IM>im\,|\,M=m,R=r]\cdot f_{M,n_s}(m)\cdot f_{R,n_s}(r)\,dm\cdot dr \qquad (1\text{-}6)$$

As discussed in Section 1.2.1, the occurrence of earthquakes is typically represented by a homogeneous Poisson model, which is applied to describe the occurrence of events that follows a homogeneous Poisson process (HPP; i.e., a *memoryless* random process). When an event E denotes the occurrence of earthquakes exceeding a certain IM level, the probability of at least one exceedance (i.e., the number of earthquakes $k\geq 1$) within a time interval $(t,t+\Delta t)$ can be expressed with the following equation:

$$P[E,(t,t+\Delta t)]=P[k\geq 1]=1-e^{-\lambda_{im}\Delta t}=1-e^{-\frac{\Delta t}{T_R}} \qquad (1\text{-}7)$$

It is worth noting that, in the modern performance-based building seismic codes, the return period (T_R) is computed by substituting a target probability of exceedance (P_{V_R}) and a reference time period (V_R) into the equation above, i.e., $P_{V_R}=P[E,(0,V_R)]$ given $t=0$ corresponds to the time of the construction of the structure.

Other random process models also have been developed to consider the dependency of the earthquake occurrence on the seismic history in the past, which is not considered in a memoryless HPP model; e.g., nonhomogeneous Poisson models with a time-variant annual rate of exceedance and renewal models with gamma or Weibull distributions. For more details of other types of seismic occurrence models, see, for example, [Shinozuka and Deodatis, 1988].

Hazard disaggregation

As introduced above, PSHA computes the MAF of the occurrence (or exceedance) of a certain IM level through the hazard integral considering all possible earthquake scenarios. When the

most likely earthquake scenario for a certain IM is rather of interest, *hazard disaggregation* (*or deaggregation*), that is, the procedure to evaluate the hazard contribution from each earthquake scenario to the occurrence (or exceedance) rate, can be performed [Bazzurro and Cornell, 1999]. In addition to magnitude and source-to-site distance, it often includes the GM residual (ε), which is defined as the number of standard deviations that is away from the median predicted by the GMPE adopted in PSHA [Baker and Cornell, 2006]. Based on Bayes' theorem, the joint probability distribution of a certain values of $\{M,R,\varepsilon\}$ given IM, $f_{M,R,\varepsilon|IM}(m,r,e)$, is computed with the following equation.

$$f_{M,R,\varepsilon|IM}(m,r,e)=\frac{\sum_{n_s=1}^{N_s} v_{E,n_s}\cdot I\left[IM>im\,|\,m,r,e\right]_{n_s}\cdot f_{M,R,\varepsilon,n_s}(m,r,e)}{\lambda_{im}} \tag{1-8}$$

where $I\left[IM>im\,|\,m,r,e\right]$ is an indicator functions that is equal to one if IM exceeds a given value im conditional to $\{M,R,\varepsilon\}$, while $f_{M,R,\varepsilon,n_s}(m,r,e)$ is the distributions of the variables characterized for each source in PSHA. For more details, see [Bazzurro and Cornell, 1999].

1.2.3.2 Probabilistic structural damage assessment

This section introduces state-of-the-art analytical methods for predicting structural response in line with the PBEE methodology. Following the format of Eq. (1-4), the MAF of exceeding a certain EDP threshold, i.e., λ_{edp}, can be obtained through integrating a fragility curve over the corresponding *IM* hazard curve,

$$\lambda_{edp}=\int_{im} P\left[EDP>edp\,|\,IM=im\right]\left|d\lambda_{im}\right| \tag{1-9}$$

When *structural failure* (F) is defined as the exceedance of a particular EDP threshold $\left(EDP_f\right)$, i.e., $F\equiv EDP>EDP_f$, it is also common to express the seismic risk of a structure in terms of annual failure rate, λ_f, instead of the expression of Eq. (1-9).

$$\lambda_f=\int_{im} P\left[F\,|\,IM=im\right]\left|d\lambda_{im}\right| \tag{1-10}$$

In the equation, $P\left[F\,|\,IM=im\right]$ is seismic fragility of the structure, providing the failure probability of the structure as a function of IM. In the state-of-the art approach, it is obtained

through NLDA using a numerical model of the structure and a set of GM records. In the following, common NLDA methods in earthquake engineering research, i.e., *cloud analysis* [Cornell et al., 2002], *incremental dynamic analysis* (IDA; Vamvatsikos and Cornell [2002]), *multiple stripe analysis* (MSA; Jalayer and Cornell [2003]), will be briefly recalled, as well as the fragility assessment procedure depending on the choice of response sampling approaches.

Cloud analysis

In cloud analysis, NLDA is performed using a set of unscaled GM records (or scaled by a constant factor) selected so as to cover a wide range of a target IM. As the name suggests, the scatter plot of the measured EDP values against the IM values forms a "cloud" or a rough ellipse, which allows one to estimate overall structural response via regression analysis using relatively small number of structural response data (Figure 1-5).

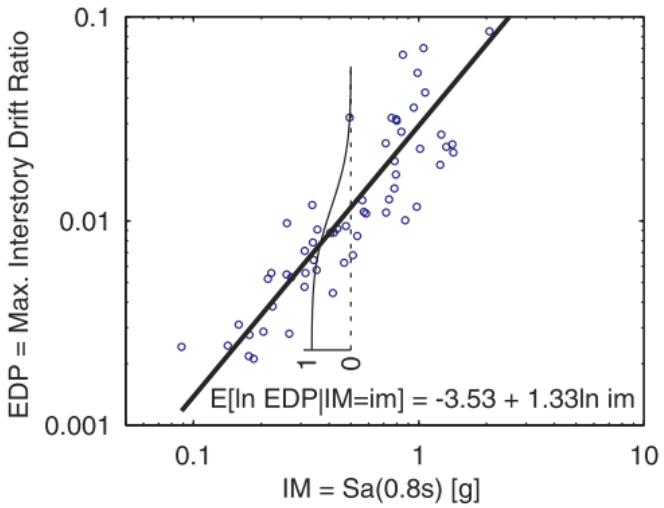

Figure 1-5 Example of fragility fitting via cloud analysis; plots of EDP values fitted through a linear regression; adopted from [Baker, 2007].

For the obtained response data, a log-linear regression form is typically applied to model the relationship between the response (dependent) variable of EDP and candidate explanatory (independent) variables [Baker, 2007]. In case of considering a scalar IM, the logarithm of EDP is given by:

$$\ln EDP = \ln \overline{EDP} + \eta_{\ln EDP} \cdot \sigma_{\eta} = \beta_0 + \beta_1 \cdot \ln im + \eta_{\ln EDP} \cdot \sigma_{\eta} \tag{1-11}$$

where $\ln\overline{EDP}$ is the conditional mean given IM $E\left[\ln\overline{EDP}\,|\,IM=im\right]$, $\left\{\beta_0,\beta_1,\sigma_\eta\right\}$ are regression parameters, and $\eta_{\ln EDP}$ (i.e., the regression residual) is the standard normal variable.

As indicated in the equation, a linear regression model assumes a constant variance over the IM domain (*homoscedasticity*), then the standard deviation, σ_η, can be estimated as the residual standard error of the regression model.

$$\sigma_\eta=\sqrt{\frac{\sum_{i=1}^{N_{tot}}\left(\ln edp_i-\ln\overline{EDP_i}\right)}{N_{tot}-2}} \tag{1-12}$$

where N_{tot} is the total number of analysis (i.e., the number of records) while the residual $e_i=\ln edp_i-\ln\overline{EDP_i}$ is the difference between the observed and predicted values associated with *i*-th record. Assuming EDP has a lognormal distribution, the exceedance probability of EDP_f is given by:

$$P\left[EDP\geq EDP_f\,|IM=im\right]=\left(1-\Phi\left(\frac{\ln EDP_f-\ln\overline{EDP}}{\sigma_\eta}\right)\right) \tag{1-13}$$

where $\Phi(\bullet)$ is a standard normal cumulative distribution function (CDF). As an example, the obtained fragility curve as a function of $EDP_f\,(edp)$ given $IM=Sa(0.8s)=0.5g$ is illustrated in Figure 1-5.

Incremental dynamic analysis and multiple stripe analysis

Compared to cloud analysis, IDA and MSA methods are suitable options when structural response at specific IM levels are of interest. In these analysis methods, a suite of GM records is scaled to target IM levels, then the distribution of EDP is obtained from the measured structural response stripe-wisely. In IDA, a series of NLDAs is performed for each GM record, which is incrementally scaled up to the maximum IM of interest or to the attainment of structural collapse. A plot of the measured EDP values and the corresponding IM levels of a single GM is called an *IDA curve*, which is collected for all GM records (grey lines in Figure 1-6). MSA is also a collection of NLDA performed at multiple IM levels (*stripes*), however, it can employ multiple sets of GM records selected based on hazard disaggregation results per stripe. Thus, it

is considered technically superior or more elaborate to IDA with respect to hazard-consistency.

The following presents some of possible approaches for estimating fragility functions using structural response data obtained through either IDA or MSA. In particular, *IM-based* approach, *EDP-based* approach, and *non-parametric fragility* are introduced herein following the definitions by [Iervolino, 2017]. For other fitting approaches which are not introduced in this thesis, the reader can refer to [Baker, 2007] and [Iervolino, 2017].

IM-based approach

When dynamic analysis, in particular, IDA is performed using a set of N_{tot} GM records, one can obtain a vector of IM values, $im=\{im_1, im_2, \ldots, im_n\}$ at which each IDA curve reaches a certain EDP threshold, EDP_f (denoted with the x-crosses on the left side of Figure 1-6). Assuming such values are generated from a lognormal distribution of the selected IM causing failure, i.e., IM_f, the probability of failure can be approximately given by Eq. (1-14) characterized with the estimated logarithmic median and logarithmic standard deviation of IM_f, $\hat{\theta}$ and $\hat{\beta}$, respectively:

$$P\left[F \middle| IM=im\right]=P\left[IM_f \le im\right]=\Phi\left(\frac{\ln im-\ln\hat{\theta}}{\hat{\beta}}\right) \tag{1-14}$$

$$\text{where } \ln\hat{\theta}=\frac{1}{N_{tot}}\sum_{i=1}^{N_{tot}}\ln\left(im_i\right), \quad \hat{\beta}=\sqrt{\frac{1}{N_{tot}-1}\sum_{i=1}^{N_{tot}}\left[\ln\left(im_i\right)-\ln\hat{\theta}\right]^2}$$

The left side of Figure 1-6 illustrates an example of this approach applied to IDA curves in terms of 5%-damped spectral acceleration at the fundamental vibration period of a structure in the cited study. When IM_f values are sampled given the EDP threshold set to 3% inter-story drift ratio (IDR), the fragility function denoted with the red curve is obtained from Eq. (1-14), and the failure probability for a given IM, e.g., $Sa\left(T=1.82s\right)=0.5g$, corresponds to the shaded area in the figure.

EDP-based approach

EDP-based approach can be an option when IDA or MSA is performed using $N_{tot,i}$ records at multiple (m) IM levels. A set of two fragility function parameters $\left\{\hat{\theta},\hat{\beta}\right\}$ can be estimated based on the maximum likelihood estimation method, using $1\times N_{tot,i}$ EDP vectors measured at each IM level, $edp_i=\left\{edp_1,edp_2,\ldots,edp_{N_{tot,i}}\right\}$ where $i=\{1,2,\ldots,m\}$. For each vector, they are subsequently partitioned into two classes: $N_{f,i}$ *failure* and $\left(N_{tot,i}-N_{f,i}\right)$ *non-failure* cases, then the lognormal fragility parameters are given by Eq. (1-15) that serves to maximize the likelihood of the entire data set being observed [Baker, 2007].

$$P\left[F\left|IM=im\right.\right]=\Phi\left(\frac{\ln im-\ln\hat{\theta}}{\hat{\beta}}\right) \tag{1-15}$$

where $\left\{\hat{\theta},\hat{\beta}\right\}$

$$=\arg\max_{\theta,\beta}\left[\sum_{i=1}^{m}\ln\binom{N_{tot,i}}{N_{f,i}}+N_{f,i}\ln\left\{\Phi\left[\frac{\ln\left(im_i/\theta\right)}{\beta}\right]\right\}+\left(N_{tot,i}-N_{f,i}\right)\cdot\ln\left\{1-\Phi\left[\frac{\ln\left(im_i/\theta\right)}{\beta}\right]\right\}\right]$$

For the same set of the IDA curves used in the example of the IM-based approach, the middle panel of Figure 1-6 represents the measured EDP values which are partitioned by EDP_f, highlighting the selected two IM levels, i.e., $Sa(T)=0.2g$ and $Sa(T)=0.4g$.

It should be mentioned that, in NLDA, some GM records provide no meaningful EDP values (significantly large or not-a-number) when the structure experiences the nonlinear excursion to a great extent. These cases are categorized as *numerical instability* or *collapse cases* according to the definition in [Shome and Cornell, 2000], for which failure can be represented by the fractions of collapse cases (at the right panel of Figure 1-6), i.e., the ratio of the number of collapse cases to the total number of records, $N_{col,i}/N_{tot,i}$. The total number of failure cases is then given as the sum of the collapse cases and the exceedance cases with $edp\geq EDP_f$.

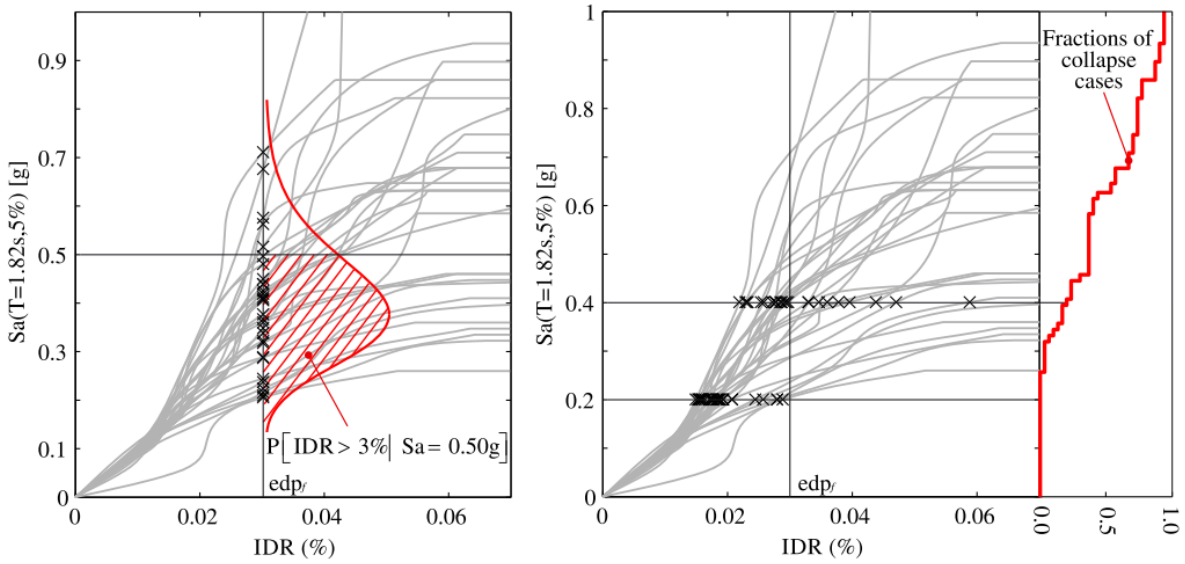

Figure 1-6 Examples of IDA and fragility fitting approaches; adopted from [Iervolino, 2017].

Non-parametric fragility

Another alternative for the response data obtained via IDA or MSA is to empirically derive a non-parametric fragility function without involving any probabilistic models. For each IM stripe of response data, the failure probability is computed as the number of failure cases over the total number of records:

$$P\left[F \mid IM = im_i\right] = \frac{N_{f,i}}{N_{tot,i}} \tag{1-16}$$

Hybrid approach

It is also possible to define the failure probability given IM as a stepwise function which accounts for the contributions from collapse cases and non-collapse cases (NC; with meaningful EDP values). Assuming a lognormal distribution of the measured EDP values $edp_i = \left\{edp_1, edp_2, \ldots, edp_{N_{tot,i}}\right\}$ and empirical collapse fragility for collapse data $P[C] = N_{col,i} / N_{tot,i}$, the failure probability conditional to a certain IM level is characterized by the following three parameters, i.e., the probability of non-collapse, $P[NC]$, and the logarithmic mean and the standard deviation of EDP $\left\{\hat{\mu}_{\ln EDP,i}, \hat{\sigma}_{\eta,i}\right\}$ estimated from no-collapse data [Shome and Cornell, 2000].

$$P\left[F \mid IM = im_i\right] = P\left[EDP > EDP_f \mid NC\right] \cdot P\left[NC\right] + P\left[C\right]$$
$$= \left[1 - \Phi\left(\frac{\ln\left(EDP_f\right) - \hat{\mu}_{\ln EDP,i}}{\hat{\sigma}_{\eta,i}}\right)\right] \cdot \left(1 - \frac{N_{col,i}}{N_{tot,i}}\right) + \frac{N_{col,i}}{N_{tot,i}} \quad (1\text{-}17)$$

where $P\left[NC\right] = 1 - P\left[C\right]$

$$\hat{\mu}_{\ln EDP,i} = \frac{1}{N_{tot,i} - N_{col,i}} \sum_{k=1}^{N_{tot,i} - N_{col,i}} \ln edp_k, \quad \hat{\sigma}_{\eta,i} = \sqrt{\frac{1}{N_{tot,i} - N_{col,i} - 1} \sum_{k=1}^{N_{tot,i} - N_{col,i}} \left[\ln edp_k - \hat{\mu}_{\ln EDP,i}\right]^2}$$

References

ATC [1978] Tentative provisions for the development of seismic regulations for buildings, ATC 3-06. National Bureau of Standards, Washington, DC, USA.

Baker, J. W. [2007] "Probabilistic structural response assessment using vector-valued intensity measures," *Earthq. Eng. Struct. Dyn.*, 36(13), 1861–1883. DOI:10.1002/eqe.700.

Baker, J. W., Cornell, A. C. [2006] "Spectral shape, epsilon and record selection," *Earthq. Eng. Struct. Dyn*, 35, 1077–1095. DOI:10.1002/eqe.571.

Bazzurro, P., and Cornell, A. C. [1999] "Disaggregation of seismic hazard," *Bull. Seismol. Soc. Am.*, 89(2), 501–520. DOI:10.1785/0120060093.

CEB [1970] CEB-FIP International Recommendations for the design and construction of concrete structures: 1 Principles and Recommendations, Bulletin No. 72. Comité Euro-international du Beton, Paris, France.

CEN [2004] Eurocode 8: Design Provisions for Earthquake Resistance of Structures, Part 1.1: General rules, seismic actions and rules for buildings, EN1998-1.

CEN [2017] "Draft Annex F (Informative): simplified reliability-based verification format, Annex to European standard EN 1998–1. Eurocode 8: Design of structures for earthquake resistance. Part 1: General rules, seismic action and rules for buildings," European Committee for Standardization, Brussels (Prepared by Dolšek M, Žižmond J, Kosič M, Lazar Sinković N).

Cornell, A. C. [1968] "Engineering seismic risk analysis," *Bull. Seismol. Soc. Am.*, 58(5), 1583–1606.

Cornell, A. C., Jalayer, F., Hamburger, R. O., Foutch, D. A. [2002] "Probabilistic basis for 2000 SAC federal emergency management agency steel moment frame guidelines," *J. Struct. Eng.*, 128(4), 526–533. DOI:10.1061/ASCE0733-94452002128:4526.

CS.LL.PP., Decreto Ministeriale 14 gennaio [2008] Norme tecniche per le costruzioni (in Italian), Gazzetta Ufficiale della Repubblica Italiana, 29, Italy.

CS.LL.PP. [2018] Aggiornamento delle norme tecniche per le costruzioni, Gazzetta Ufficiale della Repubblica Italiana 42. (in Italian.)

De Marco, R., Martini, M. G., Di Pasquale, G., Fralleone, A., Pizza, A. G., Viola, V. [2000] La classificazione e la normativa sismica italiana dal 1909 al 1984, Italian National Seismic

Survey Report, Italy.

Diebold, J. Moore K, Hale T, Mochizuki G. [2008] "SEAOC Blue Book: Seismic Design Recommendations 1959 to 2008," In Proc. of *14th World Conf. Earthq*. *Eng.*, Beijing, China.

DM 40/75 [1975] Decreto Ministeriale n. 40 del 03/03/1975, Approvazione delle norme tecniche per le costruzioni in zone sismiche. G.U. della Repubblica Italiana n. 93 dell'08/04/1975. (in Italian).

DM 515/81 [1981] Decreto Ministeriale n. 515 del 03/06/1981, Classificazione a bassa sismicità S = 6 del territorio dei Comuni delle Regioni Basilicata, Campania e Puglia. G.U. della Repubblica Italiana n. 162 del 15/06/1981. (in Italian).

DM 208/84 [1984] Decreto Ministeriale del 19/06/1984, Norme tecniche per le costruzioni in zone sismiche," G.U. della Repubblica Italiana n.208 del 30/07/1984. (in Italian).

DM 16/01/1996 [1996] Decreto Ministeriale del 16/01/1996, Norme tecniche per le costruzioni in zone sismiche. G.U. della Repubblica Italiana n. 29 del 05/02/1996. (in Italian).

DM 09/01/1996 [1996] Decreto Ministeriale del 09/01/1996, Norme tecniche per il calcolo, l'esecuzione ed il collaudo delle strutture in cemento armato, normale e precompresso e per le strutture metalliche.

Dolšek M, Žižmond J, Kosič M, Lazar Sinković N [2017] Simplified reliability-based verification format, working material for Annex F to revised EN 1998-1. University of Ljubljana, Ljubljana.

Fajfar, P. [2018] Analysis in seismic provisions for buildings: past, present and future. In European Conference on Earthquake Engineering Thessaloniki, Greece (pp. 1-49). Springer, Cham.

Fardis, M. N. [2009] Seismic Design, Assessment and Retrofitting of Concrete Buildings: Based on EN-Eurocode 8, Springer Science & Business Media.

FEMA [1997] FEMA 273, NEHRP Guidelines for the Seismic Rehabilitation of Buildings, Washington, DC, USA.

Freeman, J. R. [1932] "Earthquake Damage and Earthquake Insurance: Studies of a Rational Basis for Earthquake Insurance, Also Studies of Engineering Data for Earthquake-resisting Construction,". McGraw-Hill.

Giovenale, P., Cornell, A. C., and Esteva, L. [2004] Comparing the adequacy of alternative ground motion intensity measures for the estimation of structural responses, Earthq. Eng. Struct. Dyn., 33(8), 951–979. DOI:10.1002/eqe.386.

Iervolino, I. [2017] "Assessing uncertainty in estimation of seismic response for PBEE," *Earthq. Eng. Struct. Dyn.*, 46(10), 1711–1723. DOI:10.1002/eqe.2883.

Iervolino, I., Spillatura, A., Bazzurro, P. [2017] "RINTC project: Assessing the (implicit) seismic risk of code-conforming structures in Italy," In *Proc. of VI ECCOMAS Thematic Conference on Computational Methods in Structural Dynamics and Earthquake Engineering*, Rhodes, Greece, 15– 17 June.

Iervolino, I., Bazzurro, P., Spillatura, A., [2018] "Seismic reliability of code-conforming Italian buildings," *J. Earthq. Eng.*, 22(sup2), 5–27. DOI:10.1080/13632469.2018.1540372.

Jalayer, F., Cornell, A.C. [2003] "Direct probabilistic seismic analysis: implementing non-linear dynamic assessments," Ph.D. Thesis, Stanford University, California, USA.

Kramer [1996] Geotechnical Earthquake Engineering, Pearson.

Krawinkler, H. [2005] Van Nuys Hotel Building Testbed Report: Exercising Seismic Performance Assessment, PEER Rep. 2005/11, PEER Center, University of California, Berkeley, CA, USA.

L 1684/62 [1962] Legge n.1684 del 25/12/1962, Provvedimenti per l'edilizia, con particolari prescrizioni per le zone sismiche. Supplemento Ordinario n.1 alla G.U. della Repubblica Italiana n. 326 del 22/12/1962. (in Italian).

L 64/74 [1974] Legge n.64 del 02/02/1974, Provvedimenti per le costruzioni con particolari prescrizioni per le zone sismiche. G.U. della Repubblica Italiana n. 76 del 21/3/1974. (in Italian).

Lee, T. H., Mosalam, K. M. [2006] Probabilistic seismic evaluation of reinforced concrete structural components and systems, PEER Report 4, PEER Center, University of California, Berkeley, CA, USA.

Luco, N., Cornell, A. C. [2002] "Probabilistic seismic demand analysis, SMRF connection fractures, and near-source effects," Ph.D Thesis, Stanford University, California, USA.

M.LL.PP. [1997] Circolare del Ministero dei Lavori Pubblici n. 65 del 10/04/1997 Istruzioni per l'applicazione delle Norme tecniche per le costruzioni in zone sismiche di cui al Decreto Ministeriale 16 gennaio 1996. G.U. della Repubblica Italiana n. 97 del 28/04/1997. (in Italian).

O.P.C.M. 3274 [2003] Ordinanza del Presidente del Consiglio dei Ministri n. 3274 del 20/03/2003, Primi elementi in materia di criteri generali per la classificazione sismica del territorio nazionale e di normative tecniche per le costruzioni in zona sismica. G.U. della Repubblica Italiana n. 105 dell'8/5/2003. (in Italian).

O.P.C.M. 3431 [2005] Ordinanza del Presidente del Consiglio dei Ministri n. 3431 del 03/5/2005, Ulteriori modifiche ed integrazioni all'ordinanza del Presidente del Consiglio dei Ministri n. 3274 del 20 marzo 2003. G.U. della Repubblica Italiana n.107 del 10/5/2005. (in Italian).

Petruzzelli, F., Iervolino, I. [2013] "Scale-Dependent Procedures for Seismic Risk Assessment and Management of Industrial Building Portfolios," Ph.D. thesis, University of Naples Federico II, Naples, Italy.

Porter K. A. [2003] "An Overview of PEER's Performance-Based Earthquake Engineering Methodology," In: Proc. of *9th International Conference on Applications of Statistics and Probability in Civil Engineering*.

Reiter, L. [1991] Earthquake Hazard Analysis: Issues and Insights, Columbia University Press.

RD 193/09 [1909] Regio Decreto n.193 del 18/04/1909, Norme tecniche ed igieniche obbligatorie per le riparazioni ricostruzioni e nuove costruzioni degli edifici pubblici e privati nei luoghi colpiti dal terremoto del 28 dicembre 1908 e da altri precedenti elencati nel R.D. 15 aprile 1909. G.U del Regno d'Italia n.95 del 22/04/1909. (in Italian).

RDL 573/15 [1915] Regio Decreto Legge n. 573 del 29/04/1915 che riguarda le norme tecniche ed igieniche da osservarsi per i lavori edilizi nelle località colpite dal terremoto del 13 gennaio 1915. G.U. del Regno d'Italia n. 117 del 11/05/1915. (in Italian).

RDL 2089/24 [1924] Regio Decreto Legge n. 2089 del 23/10/1924, Norme tecniche ed igieniche di edilizia per le località colpite dal terremoto. G.U. del Regno d'Italia n. 303 del 30/12/1924. (in Italian).

RDL 431/27 [1927] Regio Decreto Legge n. 431 del 13/03/1927, Norme tecniche ed igieniche di edilizia per le località colpite dai terremoti. G.U. del Regno d'Italia n. 82 del 8/04/1927. (in Italian).

RDL 640/35 [1935] Regio Decreto Legge n. 640 del 25/03/1935, Nuovo testo delle norme tecniche di edilizia con speciali prescrizioni per le località colpite dai terremoti. G.U. del Regno d'Italia n. 120 del 22/05/1935. (in Italian).

RDL 2105/37 [1937] Regio Decreto Legge n. 2105 del 22/11/1937, Norme tecniche di edilizia con speciali prescrizioni per le località colpite dai terremoti. G.U. del Regno d'Italia n. 298 del 27/12/1937. (in Italian).

Ricci, P., De Luca, F., Verderame, G. M. [2011] "6th April 2009 L'Aquila earthquake, Italy: reinforced concrete building performance," *Bull. of Earthq. Eng.*, 9(1), 285-305.

RINTC-Workgroup [2018] Results of the 2015-2017 implicit seismic risk of code-conforming

structures in Italy (RINTC) Project. ReLUIS Report, Rete Dei Laboratori Universitari Di Ingegneria Sismica (ReLUIS), Naples, Italy.

SEAOC Vision 2000 Committee [1995] Performance-Based Seismic Engineering, Report prepared by Structural Engineers Association of California, Sacramento, California, USA.

SEAOC Seismology Committee [1967]. Recommended Lateral Force Requirements and Commentary, Seismology Committee, Structural Engineers Association of California.

Shinozuka, M., Deodatis, G. [1988] "Stochastic process models for earthquake ground motion,". *Probabilistic engineering mechanics*," 3(3), 114-123.

Shome, N., Cornell, A. C. [2000] "Structural seismic demand analysis: Consideration of "Collapse"," In Proc. of *PMC2000 - 8th ASCE Specialty Conference on Probabilistic Mechanics and Structural Reliability*. University of Notre Dame, South Bend, Indiana, USA, 24-26 July 2000.

Sorrentino, L. [2007] "The early entrance of dynamics in earthquake engineering: Arturo Danusso's contribution," Indian Soc Earthquake Technol J, 44(1), 1-24.

Vamvatsikos, D., Cornell, A. C. [2002] "Incremental dynamic analysis," *Earthquake Engineering & Structural Dynamics*, 31(3), 491-514.

Chapter 2

Seismic performance evaluation of Italian code-conforming buildings based on SDoF approximation

Abstract

This chapter presents the seismic performance of a series of structures designed, modeled and analyzed within the RINTC (*Rischio Implicito di strutture progettate secondo le Norme Tecniche per le Costruzioni*) project. The RINTC project, funded by the *Italian Department for Civil Protection* is a multiple-year effort during 2015-2017 as a joint collaboration between ReLUIS (*Rete dei Laboratori Universitari di Ingegneria Sismica*) and EUCENTRE (*Centro Europeo di Formazione e Ricerca in Ingegneria Sismica*). In the project, the structures, with a variety of structural types and configurations and locations with different seismic hazard levels, were designed in compliance with the current Italian code provisions. The seismic risk of the structures was computed, in terms of annual failure rates, following the framework of performance-based earthquake engineering. The results of RINTC show a generally increasing trend of the annual collapse rates, as well as usability-preventing damage onset rates, with the increasing seismic hazard at the building site. Aiming at investigating the primary results of the RINTC project, this chapter examines structural features to gather insights on the heterogeneity of the collapse risk among the prototype buildings. In particular, some regular buildings selected from the prototype buildings are examined using single-degree-of freedom systems equivalent to the detailed structural models, in order to capture the overall tendencies of the structural features that originate from seismic design. It appears that the increasing trend of the failure rates with site hazard is reflected in the actual strength reduction factors of the equivalent systems, even among the same structural typology for which the uniform value of the behavior factor was set to define the reference design strength of the buildings.

Keywords: *Performance-based earthquake engineering; strength reduction factors; NTC.*

2.1 Introduction

In the current Italian building code, *le Norme Tecniche per le Costruzioni*, shortly NTC [CS.LL.PP, 2008, 2018], structural safety with respect to the desired structural performance levels has to be verified for the design ground motion (GM) levels associated with specific exceedance return periods, T_R, at the building site, as with Eurocode 8 (EC8) [CEN, 2004]. In case of ordinary structures, for example, safety verifications for *damage limitation* and *life-safety* limit states are required against GM levels corresponding to T_R of 50 and 475 years, respectively.

While the design seismic actions are prescribed on a uniform hazard basis referring to the same exceedance return periods, the modern seismic design regulations also allow to reduce the design seismic actions, in cases of linear modal response spectrum analysis, by means of so-called *response modification factor* (shortly R factors), accounting for the energy dissipation capacity in ductile structures and the inherent member overstrength. The R factor was first introduced for a standard linear analysis by the ATC-3-06 report published in the late 1970s [ATC, 1978], and its equivalent term called behavior factor q has been adopted in the current European standard EC8 as well as in NTC. As the factor serves to reduce the elastic strength demand with the tradeoff of acquiescing to plastic deformation, the code-prescribed value depends on structural typology, configuration and ductility class. It is a practical and convenient design tool to simply approximate the complicated structural dynamic behavior in the nonlinear range.

However, the current prescribed q factors are largely based on expert judgements and qualitative comparisons with the known response capabilities of some generic structural systems. Therefore, the seismic performance and structural features that actually result from such design practice still involve uncertainty and may differ from the expected behavior for structures featuring particular structural types, configurations and design detailing. Furthermore, different design approaches other than linear analysis can pertain depending on structural types, construction techniques, and hazard levels at the building site, thus the actual seismic performance can vary also among those design approaches and/or conditions. Thanks to code

requirements, it is generally expected that the probability of failure will be smaller than that of exceedance of the design GM intensity, however, the safety margins at the structure level are not explicitly controlled during design.

The benchmark study that preliminarily addressed seismic performance of modern code-conforming buildings in light with structural seismic reliability is the FEMA P-695 Methodology [FEMA, 2009], which was developed for reliably quantifying building system performance and response parameters for use in seismic design. The proposed methodology provides a technical basis for evaluating the seismic performance factors critical to the collapse risk of the current code-conforming structures in the US [FEMA, 2004] [ASCE, 2006], such as response modification (strength reduction) factor and overstrength factor. As of today, however, few studies have systematically addressed the issues on the seismic performance and implicit seismic risk of code-conforming buildings in the European or in the Italian context.

During 2015-2017, a large research project was carried out in Italy by the joint working group between *Rete dei Laboratori Universitari di Ingegneria Sismica* (ReLUIS; http://www.reluis.it/) and *Centro Europeo di Ricerca e Formazione in Ingegneria Sismica* (EUCENTRE), with the funding of *Dipartimento della Protezione Civile* (DPC). The goal of this project, named *Rischio Implicito Norme Tecniche per le Costruzioni* (RINTC) was to quantitatively address the seismic risk to which the building design codes implicitly expose structures to. In this project, structures belonging to a variety of structural types and configurations were designed according to the current Italian code provisions in a number of sites at different hazard levels. More specifically, the structural types considered are: un-reinforced masonry (URM), reinforced concrete (RC), precast reinforced concrete (PRC), steel (S), and base isolated reinforced concrete (BI) buildings, while the sites considered are: Milan, Caltanissetta, Rome, Naples, and L'Aquila under two different local site conditions, A and C (according to EC8 classification; CEN, 2004). The seismic risk of the designed structures, with respect to global collapse and usability-preventing-damage-onset, was evaluated in a state-of-the-art approach referring to PBEE. It included nonlinear dynamic analysis (NLDA) of the 3D structural models and integration of probabilistic hazard with probabilistic vulnerability. The failure criteria were defined in a uniform manner among the structures belonging to the same

typology. The main findings of the project were that: (i) the heterogeneity of seismic safety among structural types designed for the same hazard and (ii) a general trend of increasing risk with the increasing design hazard of the building site [Iervolino et al., 2017; Iervolino et al., 2018]. Some may argue that (i) is well expected due to the different design procedures which pertain to different structural types (e.g., RC and URM buildings); on the other hand, (ii) should be limited to some extent, to a permissible reliability threshold, which is being expected to be incorporated in the revised version of the current codes in the near future [Dolšek et al., 2017].

On the presume that the heterogeneity of seismic risk that has been observed in the RINTC project may arise from such diversity of design assumptions pertaining to different structural types, configurations, and site hazard levels, this study aims to quantify the actual seismic performance of structures that originate from the code-conforming design. For the purpose of this investigation, some regular buildings are selected as case study examples from all structural types but the BI buildings (i.e., URM, RC, S, PRC) as to retain the variety in the project. For the selected buildings, the original full-dimensional structural models used in the RINTC project are converted into the equivalent single-degree-of-freedom (ESDoF) systems based on their SPO curves. The approximation introduced is verified through a comparison of the structural responses between the original and simplified models following the same analytical procedure adopted in the project. The trends of basic seismic performance factors, such as strength reduction factors and failure ductility capacities will be compared across different structural types and building sites referring to the ESDoF quantities. In particular, the former considers the strength reduction factors those with respect to the 475-year design elastic spectra and the expected peak-over-threshold level given the exceedance of the design acceleration to investigate the seismic demands implicitly controlled and not controlled, respectively.

The remainder of the chapter is structured such that the next section describes the prototype buildings covered in this study, followed by their ESDoF approximation. Subsequently, the structural response obtained from the ESDoF systems are compared with those from the original models. Then, some design structural features of those structures are presented to address the observed trend of seismic risk. Final remarks close the chapter.

2.2 Prototype buildings of the RINTC project

Among the buildings designed in the RINTC project, this study exclusively examines some regular buildings belonging to four different structural types (i.e., URM, RC, S, and PRC buildings) and located at three sites (i.e., Milan, Naples, and L'Aquila, hereafter denoted as MI, NA, AQ, respectively) representing low-, mid- and high-hazard in Italy. In the project, the 3D numerical models for structural analysis were constructed in OpenSees [McKenna et al., 2000] except for URM buildings that were analyzed using TREMURI [Lagomarsino et al., 2013]. In the following, the main features of the considered buildings are first reviewed, followed by the methodology and derivation of the ESDoF models.

2.2.1 Design and damage limitation seismic action

NTC mentions that structural systems must withstand the design seismic action with the return period of exceedance corresponding to the limit state of interest at the building site. For ordinary structures, which were examined in the RINTC project, design seismic actions are prescribed by means of elastic response spectra for the *damage limitation* (SLD) and *life-safety* (SLV) limit states, $Sa_{SLD}(T)$ and $Sa_{SLV}(T)$, which are close approximations of the 50- and 475-year return period uniform hazard spectra (UHS) at the building site, respectively. Figure 2-1 shows the official Italian seismic hazard map in terms of peak ground acceleration (PGA) with 475-year return period of exceedance on rock and the code-prescribed horizontal elastic response spectra for the considered three sites under two soil conditions A and C according to EC8 classification; [CEN, 2004].

In case that linear analysis is carried out for design, the code allows to introduce a behavior factor, q, to reduce the elastic strength demand indirectly accounting for plastic excursion beyond the elastic limit (i.e., ductility and energy dissipation capacities). Thus, design seismic action is obtained from the elastic response spectra divided by the q factor prescribed depending on structural typology, configuration, regularity, and ductility class.

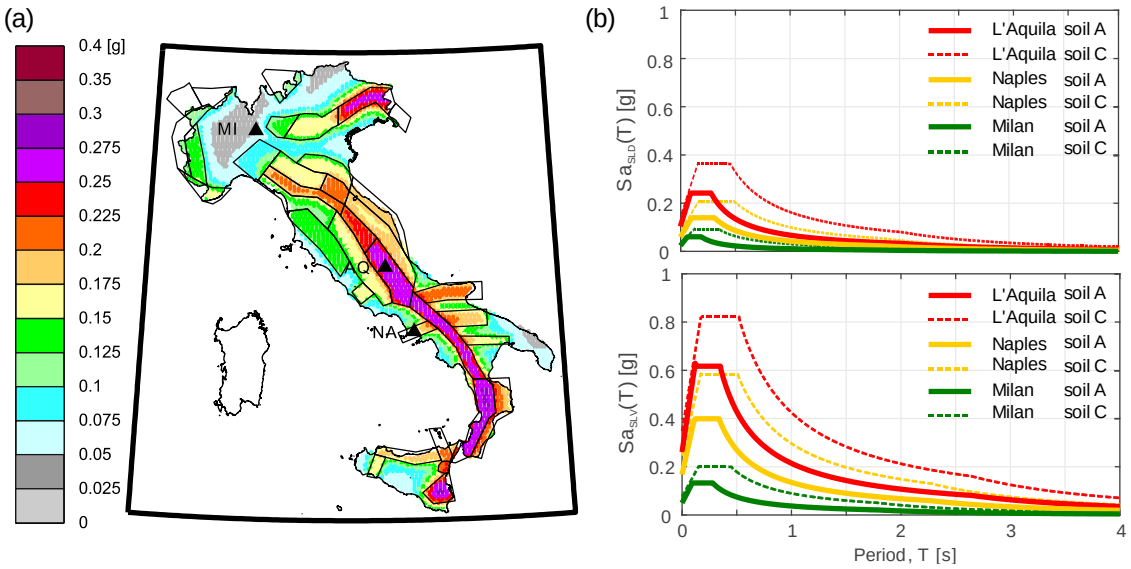

Figure 2-1 Seismic hazard at the three sites under consideration; (a) official Italian seismic source zones and hazard map in terms of PGA with 475-year return period of exceedance on rock; (b) design elastic spectra corresponding to 50-year (top) and 475-year return periods (bottom).

2.2.2 Residential unreinforced masonry buildings

A series of two- or three- story (2st, 3st) URM buildings made of perforated clay units with mortar joints was designed with a variety of different architectural configurations for the three sites on both the soil conditions A and C. Specifically, eight different (in plan) architectural configurations, either regular or irregular according to the definition provided by NTC, were considered as to represent typical Italian residential buildings: regular C (C1-C7 to be defined later), E2, E8, E9 and irregular I, E5, F, and G types [Manzini et al., 2018; Cattari et al., 2018]. For the purpose of investigation, the buildings with the different configuration types were first designed given some structural features in common (e.g., materials and typologies of horizontal diaphragms), then the optimal building-site combinations that had yielded a code-conforming yet not over-dimensioned building design were selected based on a *global safety factor*, which was defined as the ratio of PGA level causing the attainment of the ultimate structural capacity to the 475-year return period design level; see Manzini et al., [2018]. The applied design methods are: *simple building* (SB) rules, *linear static analysis* (with equivalent frame, LSA-F,

or with cantilever modelling, LSA-C), and *nonlinear static analysis* (NLSA).[2] In case of LSA, design seismic action was determined by the elastic response spectra divided by a behavior factor q of 3.6. Among the configurations designed in the project, this study exclusively examined those with regularity both in plan and in elevation (i.e., C and E2, E8, E9), which amount to thirty-one building-site combinations in total. For further details on the structural design of the examined regular buildings, as well as the other irregular building cases, see Manzini et al., [2018] and Cattari et al., [2018].

***C-type configuration*:** Figure 2-2 shows the 3D model and the plan of a C-type configuration building, which is regular in both plan and elevation. For this type of configuration, two- and three-story 5×2 bays masonry buildings with a variety of wall thickness (i.e., percentage of resistant area, A_{res}) were designed. The floor area of each building is 22.5×12.3 m^2 and each story height is 3.1m. For each number of stories, seven configurations with different thickness of the load-bearing walls, denoted as C1-C7, were designed as to cover the possible minimum A_{res} prescribed by the design code: C1 with the smallest A_{res} of the floor, 4.4%; C7 with the largest, $\geq$ 7%; C2-C6 with the intermediate values). Among the considered buildings with the C-type configurations, the sixteen building-site combinations in total (as it will be clarified later) were considered to have met the design criteria for the three sites.

***E-type configurations (E2, E8, E9)*:** the panels c-f of Figure 2-2 show the 3D model of the E2 building and the plans of the three different configurations, E2, E8, and E9, respectively, all of which are regular in both plan and elevation. The floor area ranges between approximately 150 m^2 – 290 m^2 and each plan is characterized by a layout of masonry walls different from one another. As for the C-type configuration, two- and three-story buildings with the story height of 3.1 m were designed for each configuration, then the design solutions for each site were identified based on the global safety factors. As a result, the fifteen building-site combinations in total were examined in this study.

[2] In general, the choice of analysis methods for structural design of masonry buildings is made depending on the regularity of the structure and the hazard level at the site.

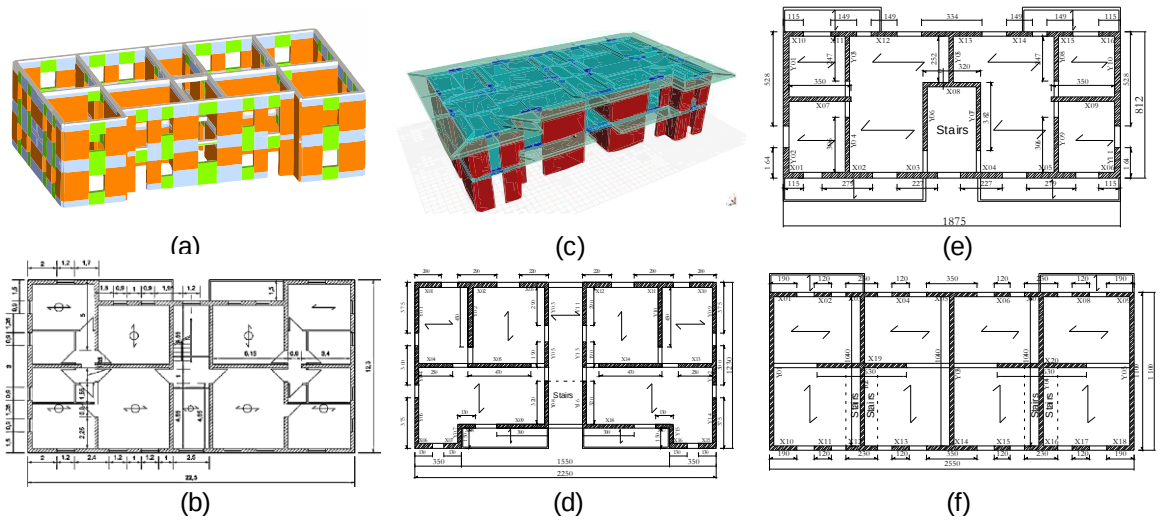

Figure 2-2 Examined URM buildings; (a) 3D view of the two-story C-type building (with equivalent frame model); (b) C-type plan; (c) 3D view of E-type building (with equivalent frame model); (d) E2 type plan; (e) E8 type plan; (f) E9 type plan.

2.2.3 Residential reinforced concrete buildings

In the RINTC project, a series of three-, six-, and nine-story (3st-, 6st-, 9st) RC moment-resisting frame (MRF) buildings and nine-story RC shear wall buildings were designed for each of the three sites with different levels of seismicity (soil C for all sites and soil A only for AQ), including considerations on soil-structure interaction and modelling uncertainty for some selected cases [RINTC-Workgroup, 2018; Franchin et al., 2018]. In cases of the MRFs, three different structural configurations (i.e., bare-, infilled-, and *pilotis*-frames, hereafter denoted as BF, IF, and PF, respectively; Figure 2-3a) were considered, and this study exclusively examined all of those without modelling uncertainty and soil-structure interaction. The buildings were intended for residential use and are all 5×3 bays MRFs characterized by regularity in plan (Figure 2-3b) and elevation. The floor area of the buildings is approximately $21.4\times11.7\text{m}^2$, which is common for all cases. The ground floor height and all other story heights are 3.4m and 3.05m, respectively. The RC frames include knee-joint beams designed to bear the staircases. From a design point of view, the structural members of BF and IF are identical in dimensions and reinforcement detailing (i.e., the difference lies in the presence of infills) while the vertical

structural members at the ground floor of PF were strengthened to account for the infill reduction, as per code requirements.

For each site, seismic design was performed by means of modal response spectrum (MRS) analysis. The reference design strength was assigned by the design response spectrum obtained from the horizontal elastic response spectrum for soil C (Figure 2-1b) divided by a behavior factor q = 3.9 (for multi-story RC frames in low ductility class; note that masonry infills are not explicitly accounted for in the NTC code-conforming design, hence the reference to BF alone covering all frames). For more details on the structural design and subsequent numerical modelling, see Ricci et al., [2018].

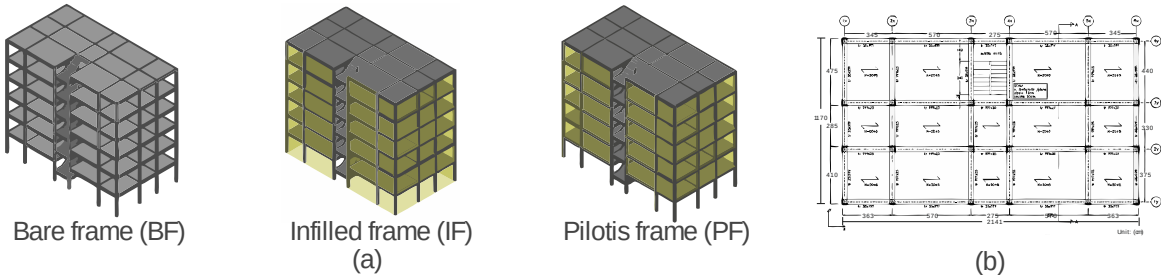

Figure 2-3 Prototype RC buildings; (a) BF, IF; PF buildings; (b) plan view.

2.2.4 Industrial steel buildings

A series of industrial steel buildings was designed for the three sites on both the soil conditions A and C. As shown in Figure 2-4, each building, equipped with an overhead travelling crane, consists of five transverse single-span duo-pitch portal frames connected to one another through longitudinal beams at the apex, eaves and bracket levels. While lateral loads are sustained by the MRF system in the transverse direction, the resistance in the longitudinal direction is mainly provided by the diagonal concentric brace members symmetrically placed in the outer spans of the frame (i.e., concentrically braced frame, CBF; cross and single braces at the ground level and at the crane-bracket level, respectively). As secondary structural elements, purlins, supporting the roof cladding and transferring loads from the roof cladding to the rafters, were also placed on the rafters with a constant interval. Roof cross braces were arranged in the outer bays to transfer lateral loads to the vertical braces. The connection details of the frames are as

follows: the full-strength bolted end-plate connections were adopted at the apex and eaves, including haunches to improve the structural performance as well as to facilitate the construction; hinged and pinned connections were adopted for the column-based connections and the purlin-rafter connections, respectively; the brace members were installed through gusset plate connections.

For each site, four different configurations were considered varying four geometry parameters of the portal frames, i.e., transverse and longitudinal bay widths and story- and crane-bracket heights; denoted as L_X, L_Y, H, and H_c, as provided in Table 2-1. MRS analysis was performed for seismic design. The design seismic actions in horizontal and vertical directions were obtained from the elastic spectra divided by a q factor equal to 4.0 (for both MRF and CBF systems in low ductility class). In fact, the cross-section designs of structural members for all the combinations of four geometry types (denoted as Geo1-4), three sites, and two soil conditions, resulted in nine different configurations after all, showing that soil condition does not differentiate structural member design. The 3D numerical models were constructed by modelling structural components, including the crane runway beam, by nonlinear beam-column finite elements with fiber sections. For more details of structural design and modelling, see Scozzese et al., [2018].

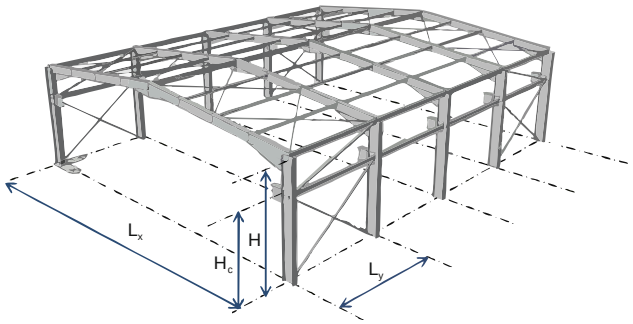

Figure 2-4 Prototype steel frame building.

Table 2-1 Geometry parameters for the prototype steel buildings.

Geometry	Lx [m]	Ly [m]	H [m]	Hc [m]
1	20	6	6	4.5
2	20	8	6	4.5
3	30	6	9	7.5
4	30	8	9	7.5

2.2.5 Industrial precast concrete buildings

Single-story industrial PRC buildings were designed at the three sites with different hazard levels (on soil A and C). Each building features five one-bay transverse duo-pitched portal frames (i.e., 4×1 bays) consisting of columns and prestressed principal beams, longitudinal beams, prestressed roof elements, and vertical/horizontal cladding panels. Figure 2-5a,b show the plan and elevation views of the prototype buildings, respectively. The columns were assumed to be fixed at the isolate socket foundation at the base and to be connected at the top to both the transverse and longitudinal beams through dowel connections [CNR 10025/98, 2000]. The roof system consists of precast π-shaped elements, which are pinned to the beams by means of dowel connections and connected to each other by steel elements in conjunction with a cast-in-situ concrete slab (slab thickness of 50mm) ensuring the rigid diaphragm assumption. The vertical cladding panels are connected to the beams and columns by means of an interlocking system made of steel elements. Each building, typically intended for industrial use, has an overhead travelling crane (not modelled, but accounted for in design), thus there are precast brackets supporting steel runway beams at the middle height of the vertical columns. The beams have variable cross-sections varying width and height along the longitudinal and transversal directions, respectively, while columns have rectangle cross-sections with reinforcing steel bars in two horizontal directions. As with the steel buildings, for each site, four different configurations were considered to represent the typical industrial constructions in Europe, varying four geometry parameters of the frames. Those parameters are summarized in Table 2-2.

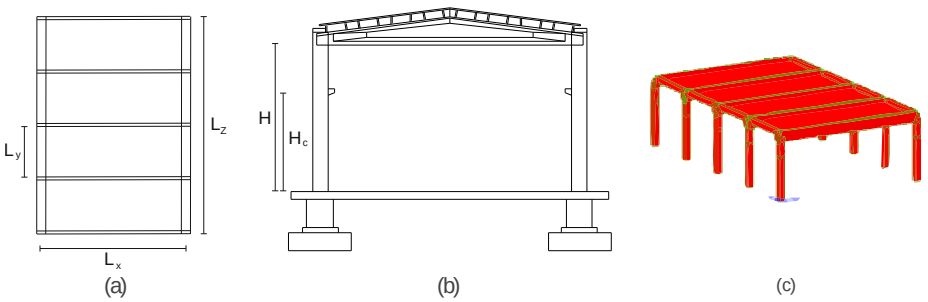

Figure 2-5 Prototype PRC buildings; (a) numerical model (b) plan; (c) elevation.

Table 2-2 Geometry parameters for prototype PRC buildings.

Geometry	L_x [m]	L_y [m]	H [m]	H_c [m]
1	15	6	6	4.5
2	20	8	6	4.5
3	15	6	9	7.5
4	20	8	9	7.5

The seismic design of the buildings was performed by means of MRS analysis for two horizontal and vertical directions at each site. The design response spectrum was obtained from the horizontal elastic response spectra (Figure 2-1b) divided by a behavior factor $q = 2.5$, which was prescribed by NTC for low ductility class precast buildings with isostatic columns. See Magliulo et al., [2018] for more details of structural design and modelling.

2.2.6 Collapse criteria examined using 3D structural models

The RINTC project assessed structural reliability with respect to the exceedance of two performance levels, global collapse and usability-preventing damage. As the next sections develop the equivalent simplified models aiming to predict structural response up to the former condition, this section briefly reviews the collapse criteria adopted in the project. For the latter conditions, see Section 3.2.2 for the details.

The collapse criteria were in general defined based on the deformation capacity corresponding to a certain level of strength deterioration; i.e., 50% of the maximum base-shear on the static pushover (SPO) curves of the structures for each horizontal direction. This is the case of the URM, RC and PRC buildings, however, there are some exceptions or adjustments required for some structural typologies, which are explained below.

For the URM buildings, the collapse criteria were defined based on the maximum inter-story-drift ratio (IDR) of single-wall elements corresponding to a 50% drop of the maximum base-shear from pushover analysis. For each structure, SPO analysis was carried out under several load patterns (uniform or inverted triangular) in both horizontal directions, whose minimum value was defined as the collapse limit threshold. Some adjustment was made in case the deformation capacity observed in dynamic analysis was found to be lower than the SPO-

based threshold value (possibly because of torsional effects and cyclic degradation): the threshold was adjusted to the maximum IDR corresponding to a 35% drop of the maximum base-shear on the static capacity curve [RINTC-Workgroup, 2018].

Particularly to PRC buildings, a local collapse condition corresponding to the attainment of the maximum shear strength of the beam-column connections, which is critical for this structural type, was also considered.

Since the prototype steel buildings have different load-resisting systems in two horizontal directions, the collapse criteria were defined individually for each of them: 10% IDR was selected for the direction with the MRF system following indications by FEMA 350 [FEMA, 2013], whereas the collapse in the CBF system corresponds to the attainment of the maximum strain range, defined as the difference between minimum and maximum strain responses measured at the cross sections of brace members under earthquake excitation, equal to 4.9%. For the latter, the strain range threshold was set according to the past studies on local collapse in brace members due to low-cyclic fatigue; e.g., [Hsiao et al., 2013].

It should be mentioned that the coupled responses were considered through the simultaneous input of pairs of horizontal accelerograms to the 3D models and that there were some cases of *numerical instability*, according to [Shome and Cornell, 2000]), observed in dynamic analysis. Thus, structural failure with respect to global collapse was considered to have been reached in cases of numerical instability or the attainment of the collapse criteria in either of the two horizontal directions.

2.3 Simplified models of case study buildings

2.3.1 Equivalent-single-degree-of-freedom characterization

The conversion to an ESDoF model involves the definitions of the SDoF oscillator's characteristics (e.g., the equivalent mass m^* and vibration period T^*) and SPO backbone parameters, and the characterization of the hysteretic behavior. The dynamic and static capacities are first defined based on the SPO curves and the modal contribution of the dominant vibration mode of the original multi (n)-story structural models, then the choice of hysteretic

models follows. Figure 2-6 illustrates the detailed conversion process of the 3D structural models of the prototype buildings to the ESDoF systems. First of all, SPO analysis was carried out per principal direction of each 3D structural model under the modal load distribution, in which the load profile F_i, the product of the floor mass m_i and the dimensionless displacement profile ϕ_i, was applied to each floor level, $i=\{1,2,...,n\}$ (Figure 2-6a). The obtained SPO curve was then multi-linearized to characterize the force-displacement relationship of the original structure, opting for bi-linear, tri-linear, and quad-linear fitting depending on the structural type and/or configuration at hand, according to the criteria set forth by [De Luca et al., 2013]. Approximating the original frame model with a lumped mass multiple-degree-of-freedom (MDoF) system (Figure 2-6b), the MDoF quantities were subsequently transformed to those of the ESDoF system [Fajfar, 2000] as follows: the equivalent mass was given by $m^*=\sum_{i=1}^{n} m_i\phi_i$, while the equivalent vibration period T^* was determined as $T^*=2\pi\sqrt{m^*\delta_y^*/F_y^*}$, where F_y^* and δ_y^* were the yield strength and the yield displacement of the multi-linearized SPO curve (F_y and δ_y, respectively) divided by the modal participation factor, $\Gamma=m^*/\sum_{i=1}^{n} m_i\phi_i^2$; the yielding spectral acceleration at the equivalent period was then obtained by $Sa_y\left(T^*\right)=F_y^*/m^*$; since mass- and initial stiffness proportional Rayleigh damping models were adopted for all 3D models, this study assigned, to each ESDoF, the viscous damping ratio corresponding to the two significant vibration modes of the original 3D models at which the Rayleigh damping model was determined (ξ^* was set to 3% for the URM buildings and 5% for the other three structural types). Meanwhile, the SPO backbone curve of the ESDoF system was derived from the multi-linear-fitted SPO curve scaled down by Γ, maintaining the same dimensionless parameters to characterize the multi-linear backbone, such as the capping-point ductility μ_c and failure (global collapse) ductility μ_{GC} (Figure 2-6c). For the given SPO parameters, a hysteresis law that can approximately represent the overall structural response was applied depending on the structural type at hand.

It should be noted that, in this study, the structural responses in the two horizontal directions were examined independently by defining two uncoupled ESDoF systems for each structure and simulating each of them excited by one of two horizontal components of a GM record. For the URM and RC buildings, longitudinal and transversal directions are denoted as

X and Y, respectively, while the opposite (X-transversal, Y-longitudinal) is applied for the rest. As regards the collapse criteria, the ESDoF models retain those adopted for the 3D structural models as long as the corresponding engineering demand parameter (EDP) was a global response measure which can be directly converted to an equivalent quantity. For the structures whose local collapse condition concerns, an alternative or equivalent EDP is introduced (see the following for the details).

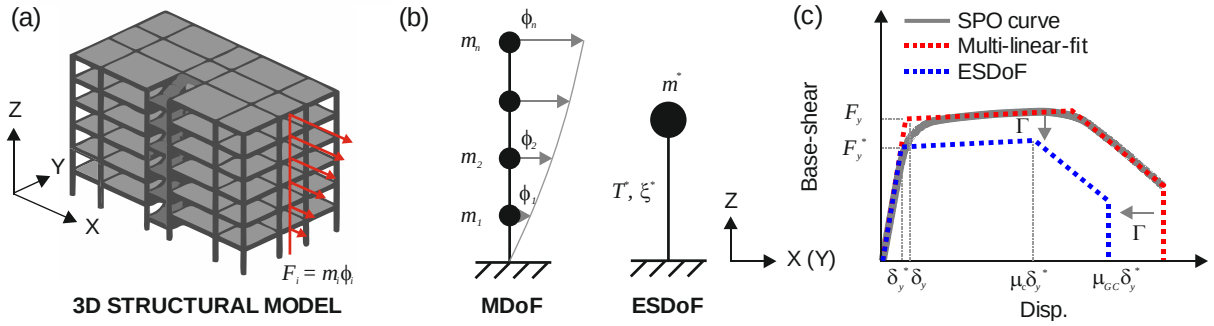

Figure 2-6 ESDoF conversion; (a) SPO analysis with a 3D model; (b) conversion through lumped mass MDoF approximation; (c) characterization of the SPO backbone of the ESDoF system.

2.3.1.1 Residential unreinforced masonry buildings

The ESDoF systems of the selected URM buildings entailed the following assumptions because the rigid floor slab assumption is not applicable: (i) during the modal analysis with the original models, the average response of all the nodes at each floor was considered to represent the displacement profile of the lumped-mass MDoF system (Figure 2-6b) and (ii) the floor mass was computed assuming the total floor weights lumped at each floor, in consideration of masonry walls' contribution. Figure 2-7 shows the SPO backbones (base-shear, F, vs displacement, δ) of the obtained ESDoF systems for the two horizontal directions. In each panel of the figure, the piece-wise linear fitted SPO backbones are shown, compared with the SPO curves of the original 3D structural models scaled down by the corresponding modal participation factor, Γ. The end of each backbone indicates the collapse condition defined above.

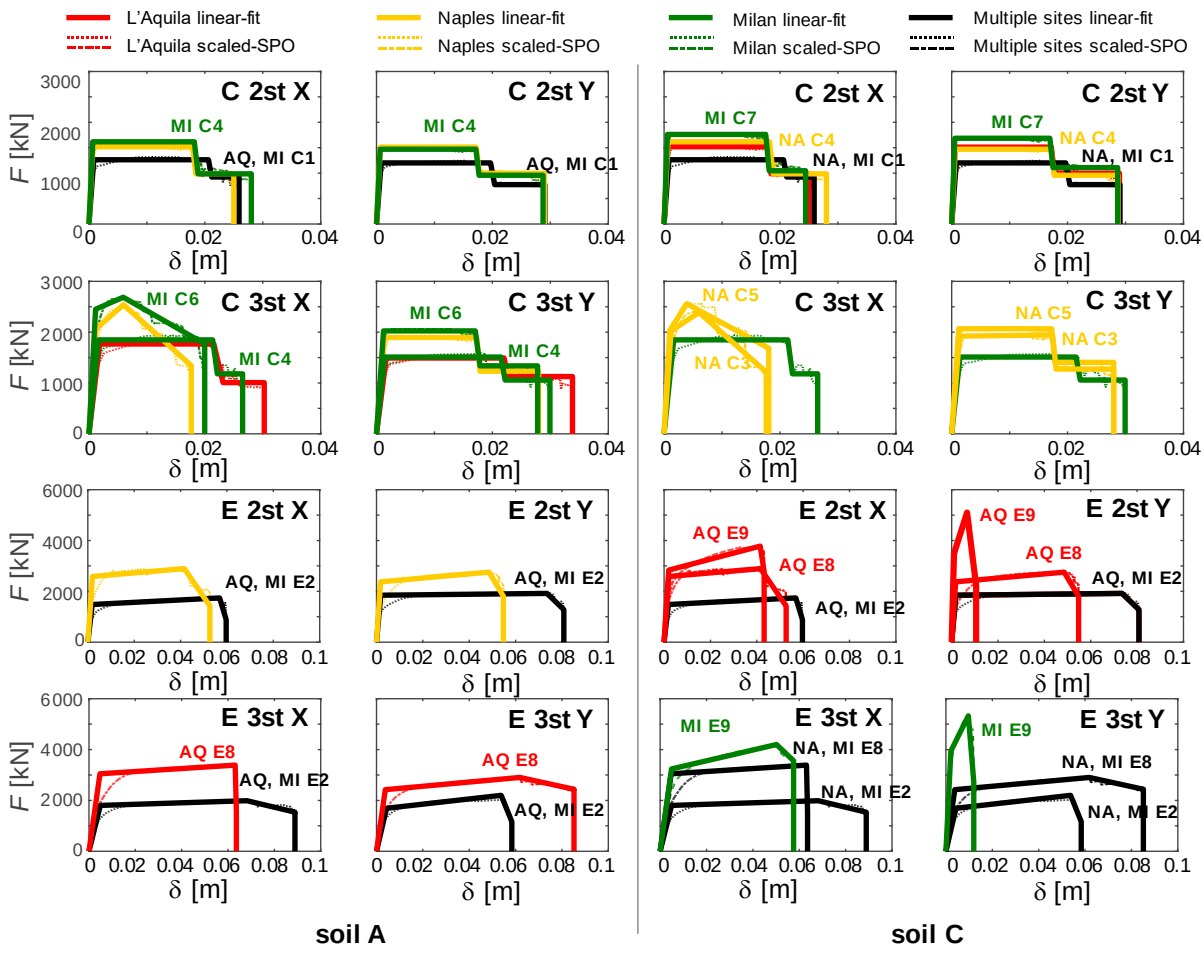

Figure 2-7 ESDoF-SPO backbones of the C and E-type URM prototype buildings.

The SPO curves were obtained assuming inverted-triangular load distribution. The SPO curves received either tri-linear or quadri-linear fit; the curve up to the maximum base-shear (elastic and hardening branches) were first bi-linearly fitted according to the criteria set forth by [De Luca et al., 2013] and then softening and residual strength branches were determined as to capture the exact SPO curve.

Table 2-3 and Table 2-4 report the structural parameters of the ESDoF systems calibrated based on the SPO curves in Figure 2-7, for each case study labeled with acronyms indicating the building site, soil condition, configuration type, and adopted analysis method (e.g., MI A/C1 2st/SB). In the table, the 475 year-return period elastic design spectrum at the equivalent period (at the bottom of Figure 2-1b), $Sa_{SLV}\left(T^*\right)$, are provided for a reference to the yield spectral acceleration at the equivalent period, $Sa_y\left(T^*\right)$. The summary of design structural parameters shows that the equivalent period of vibration T^* ranges between

approximately 0.1-0.2s, generally consistent to that of the corresponding original numerical model. It should be also noted that the first vibration period in the direction of interest, T_1, was derived from the eigenvalue analysis of the corresponding original 3D model and is not necessarily identical to the equivalent period, T^*, which was derived through defining the elastic blanch up to the point where the scant stiffness reduced by less than 30% of the initial stiffness.

Table 2-3 Structural parameters of the URM buildings (Soil A).

Site/config./ analysis type	Dir.	F_y [kN]	T_1 [s]	T^* [s]	m^* [ton]	F_y^* [kN]	$Sa_y(T^*)$ [g]	$Sa_{SLV}(T^*)$ [g]
MI A/C1 2st	**X**	1542	0.10	0.09	301	1263	0.43	0.12
/SB	**Y**	1513	0.10	0.09	306	1202	0.40	0.12
MI A/C4/2st	**X**	1955	0.09	0.07	316	1615	0.52	0.11
/LSA-F,-C	**Y**	1852	0.09	0.08	326	1472	0.46	0.12
NA A/C3 2st	**X**	1855	0.09	0.07	317	1523	0.49	0.31
/SB	**Y**	1888	0.09	0.07	323	1505	0.48	0.31
AQ A/C1 2st	**X**	1542	0.10	0.09	301	1263	0.43	0.51
/NLSA	**Y**	1513	0.10	0.09	306	1202	0.40	0.51
MI A/C2 3st	**X**	2328	0.15	0.14	419	1844	0.45	0.13
/SB	**Y**	2009	0.15	0.13	428	1516	0.36	0.13
MI A/C6 3st	**X**	3013	0.13	0.09	485	2453	0.52	0.13
/LSA-C	**Y**	2672	0.13	0.11	502	2022	0.41	0.13
NA A/C4 3st	**X**	2533	0.14	0.10	456	2057	0.46	0.37
/SB	**Y**	2501	0.14	0.11	472	1894	0.41	0.39
AQ A/C1/3st	**X**	2209	0.15	0.13	398	1770	0.45	0.62
/NLSA	**Y**	1954	0.15	0.13	406	1490	0.37	0.62
MI A/E2 2st	**X**	1811	0.12	0.13	322	1481	0.47	0.13
/LSA-C	**Y**	2244	0.10	0.11	322	1846	0.58	0.13
NA A/E8 2st	**X**	3112	0.12	0.12	476	2584	0.55	0.40
/SB	**Y**	2851	0.10	0.12	475	2373	0.51	0.40
AQ A/E2 2st	**X**	1811	0.12	0.13	322	1481	0.47	0.62
/SB	**Y**	2244	0.10	0.11	322	1846	0.58	0.60
MI A/E2 3st	**X**	2344	0.18	0.22	433	1801	0.42	0.13
/LSA-C	**Y**	2205	0.16	0.21	425	1693	0.41	0.13
AQ A/E2 3st	**X**	2344	0.18	0.22	433	1801	0.42	0.62
/NLSA	**Y**	2205	0.16	0.21	425	1693	0.41	0.62
AQ A/E8 3st	**X**	3927	0.19	0.20	626	3049	0.50	0.62
/NLSA	**Y**	3125	0.16	0.20	616	2422	0.40	0.62

Table 2-4 Structural parameters of the URM buildings (Soil C).

Site/config./ analysis type	Dir.	F_y [kN]	T_1 [s]	T^* [s]	m^* [ton]	F_y^* [kN]	$Sa_y(T^*)$ [g]	$Sa_{SLV}(T^*)$ [g]
MI C/C1 2st	**X**	1542	0.10	0.09	301	1263	0.43	0.14
/SB	**Y**	1513	0.10	0.09	306	1202	0.40	0.14
MI C/C7 2st	**X**	2148	0.08	0.07	357	1764	0.50	0.13
/LSA-F	**Y**	2125	0.08	0.07	365	1689	0.47	0.13
NA C/C1 2st	**X**	1542	0.10	0.09	301	1263	0.43	0.41
/NLSA	**Y**	1513	0.10	0.09	306	1202	0.40	0.41
NA C/C4 2st	**X**	1955	0.09	0.07	316	1615	0.52	0.39
/SB	**Y**	1852	0.09	0.08	326	1472	0.46	0.41
AQ C/C3 2st	**X**	1855	0.09	0.07	317	1523	0.49	0.54
/NLSA	**Y**	1888	0.09	0.07	323	1505	0.48	0.54
MI C/C2 3st	**X**	2328	0.15	0.14	419	1844	0.45	0.19
/SB	**Y**	2009	0.15	0.13	428	1516	0.36	0.18
NA C/C3 3st	**X**	2510	0.14	0.10	460	2017	0.45	0.45
/NLSA	**Y**	2536	0.14	0.11	466	1920	0.42	0.47
MI C/E2 2st	**X**	1811	0.12	0.13	322	1481	0.47	0.18
/LSA-F	**Y**	2244	0.10	0.11	322	1846	0.58	0.17
AQ C/E2 2st	**X**	1811	0.12	0.13	322	1481	0.47	0.71
/NLSA	**Y**	2244	0.10	0.11	322	1846	0.58	0.65
AQ C/E8 2st	**X**	3112	0.12	0.12	476	2584	0.55	0.68
/NLSA	**Y**	2851	0.10	0.12	475	2373	0.51	0.68
AQ C/E9 2st	**X**	3386	0.12	0.12	535	2832	0.54	0.68
/NLSA	**Y**	4112	0.07	0.08	557	3483	0.64	0.57
MI C/E2 3st	**X**	2344	0.18	0.22	433	1801	0.42	0.20
/LSA-F	**Y**	2205	0.16	0.21	425	1693	0.41	0.20
MI C/E8 3st	**X**	3927	0.19	0.20	626	3049	0.50	0.20
/LSA-C	**Y**	3125	0.16	0.20	616	2422	0.40	0.20
MI C/E9 3st	**X**	4165	0.18	0.20	703	3240	0.47	0.20
/SB, LSA-F,C	**Y**	4929	0.11	0.12	752	3942	0.53	0.18
NA C/E2 3st	**X**	2344	0.18	0.22	433	1801	0.42	0.58
/SB, NLSA	**Y**	2205	0.16	0.21	425	1693	0.41	0.58
NA C/E8 3st	**X**	3927	0.19	0.20	626	3049	0.50	0.58
/NLSA	**Y**	3125	0.16	0.20	616	2422	0.40	0.58

It is worth to mention that the ESDoF systems corresponding to the URM structures were analyzed using OpenSees. Two different hysteresis rules were selected from those available in the OpenSees material library to capture the main collapse mechanisms of the structures under consideration: (1) *flag-shaped* [Christopoulos et al., 2008; Tremblay et al., 2008] with moderate energy dissipation and (2) *peak-oriented* [Altoontash and Deierlein, 2004] without cyclic strength/stiffness deterioration. The hysteresis rule (1) was opted, even though it was originally intended for self-centering energy dissipative bracing systems, based on the hysteresis response of the original models under cyclic loading that showed a flexure-dominated structural behavior [Camilletti et al., 2017], while (2) was found to capture well the

shear-dominated dynamic hysteresis responses of some original models. It should be noted that one of flexure-, shear-, or mixed type hysteresis models was assigned to each masonry panel of the 3D structural models, depending on the collapse mechanism associated with the geometry of the panel. The computed ESDoF systems will be further verified in terms of dynamic structural response in the following section.

2.3.1.2 Residential reinforced concrete buildings

The ESDoF systems of the RC buildings were constructed on the basis of rigid floor diaphragm and lumped floor mass assumptions. Figure 2-8 shows the SPO backbones of the obtained ESDoF systems for the two horizontal directions. In each panel, the piecewise-linear-fitted backbones of the ESDoF systems are compared with the 3D structural models' SPO backbones scaled down by the corresponding modal participation factor. For the structures with the same number of stories, their static load capacity increases with the increasing site hazard, and IF and PF have higher strength and stiffness than BF due to the additional lateral strength provided by the infill walls. The structural parameters of the ESDoF systems were determined through the tri-linear or quadri-linear idealization of each SPO backbone via Monte-Carlo-based optimization approach [Baltzopoulos et al., 2017]. These parameters are summarized in Table 2-5 for each configuration. T^* varied between 0.2-2.1s (the shortest: 3st IF; the longest: 9st BF). For the given SPO parameters, a moderately pinching, peak-oriented hysteretic behavior without any cyclic stiffness/strength deterioration, e.g., [Vamvatsikos and Cornell, 2006] was applied.

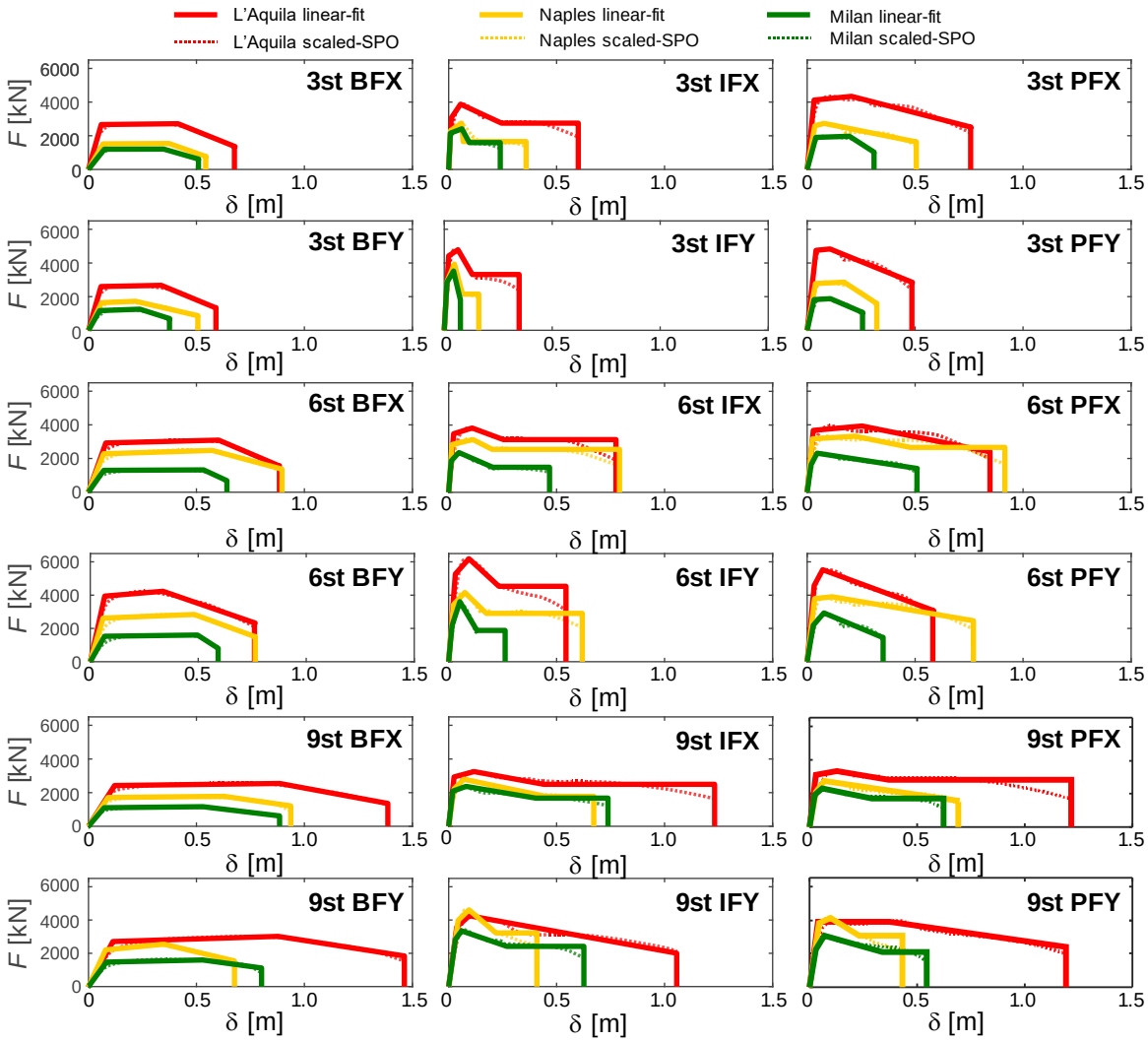

Figure 2-8 ESDoF-SPO backbones of the prototype RC buildings.

Table 2-5 Structural parameters of the RC buildings (Soil C).

Site/config./	Dir.	F_y [kN]	T_1 [s]	T^* [s]	m^* [ton]	F_y^* [kN]	$Sa_y(T^*)$ [g]	$Sa_{SLV}(T^*)$ [g]
MI C/BF 3st	**X**	1542	1.04	1.10	497	1201	0.25	0.08
	Y	1492	0.90	0.95	508	1171	0.23	0.09
NA C/BF 3st	**X**	1959	0.89	0.93	496	1520	0.31	0.32
	Y	2100	0.83	0.86	510	1643	0.33	0.34
AQ C/BF 3st	**X**	3455	0.66	0.68	534	2668	0.51	0.62
	Y	3344	0.67	0.69	543	2600	0.49	0.61
MI C/IF 3st	**X**	2718	0.21	0.27	517	2154	0.43	0.20
	Y	3584	0.24	0.30	524	2851	0.56	0.20
NA C/IF 3st	**X**	2898	0.22	0.28	531	2302	0.44	0.58
	Y	3642	0.24	0.31	538	2907	0.55	0.58
AQ C/IF 3st	**X**	3839	0.23	0.30	580	3059	0.54	0.82
	Y	5514	0.25	0.33	590	4422	0.76	0.82
MI C/PF 3st	**X**	1956	0.74	0.76	701	1905	0.28	0.12
	Y	1891	0.67	0.69	693	1821	0.27	0.13
NA C/PF 3st	**X**	2709	0.60	0.62	703	2594	0.38	0.48
	Y	2912	0.60	0.62	700	2776	0.40	0.48
AQ C/PF 3st	**X**	4506	0.43	0.47	730	4119	0.58	0.82
	Y	5198	0.50	0.50	731	4754	0.66	0.82

Table 2-5 (continued) Structural parameters of the RC buildings (Soil C).

Site/config./	Dir.	F_y [kN]	T_1 [s]	T^* [s]	m^* [ton]	F_y^* [kN]	$Sa_y(T^*)$ [g]	$Sa_{SLV}(T^*)$ [g]
MI C/BF 6st	**X**	1658	1.70	1.70	1245	1299	0.11	0.05
	Y	1924	1.48	1.48	1283	1529	0.12	0.06
NA C/BF 6st	**X**	2935	1.25	1.25	1306	2283	0.18	0.24
	Y	3300	1.11	1.11	1376	2618	0.19	0.27
AQ C/BF 6st	**X**	3829	1.13	1.13	1177	2923	0.25	0.38
	Y	5246	0.88	0.87	1147	3941	0.35	0.49
MI C/IF 6st	**X**	2458	0.53	0.53	1161	1865	0.16	0.17
	Y	2874	0.58	0.58	1165	2164	0.19	0.15
NA C/IF 6st	**X**	3714	0.52	0.53	1265	2842	0.23	0.56
	Y	4493	0.57	0.57	1262	3419	0.28	0.52
AQ C/IF 6st	**X**	4544	0.51	0.57	1230	3485	0.29	0.74
	Y	6827	0.50	0.54	1247	5269	0.43	0.78
MI C/PF 6st	**X**	1874	0.92	0.92	1616	1636	0.10	0.10
	Y	2597	0.88	0.88	1533	2184	0.15	0.10
NA C/PF 6st	**X**	3874	0.69	0.69	1560	3170	0.21	0.43
	Y	4672	0.73	0.73	1530	3787	0.25	0.40
AQ C/PF 6st	**X**	4616	0.60	0.65	1401	3671	0.27	0.65
	Y	6080	0.54	0.57	1251	4581	0.37	0.74
MI C/BF 9st	**X**	1451	2.12	2.09	1684	1105	0.07	0.04
	Y	1944	1.93	1.93	1677	1472	0.09	0.04
NA C/BF 9st	**X**	2262	1.88	1.92	1763	1711	0.10	0.15
	Y	2972	1.55	1.56	1721	2208	0.13	0.19
AQ C/BF 9st	**X**	3181	1.86	1.86	1774	2423	0.14	0.23
	Y	3639	1.67	1.68	1725	2707	0.16	0.25
MI C/IF 9st	**X**	2811	0.77	0.77	1639	2094	0.13	0.12
	Y	3892	0.84	0.84	1591	2846	0.18	0.11
NA C/IF 9st	**X**	2941	0.89	0.90	1829	2228	0.12	0.33
	Y	5329	0.88	0.89	1792	3983	0.23	0.33
AQ C/IF 9st	**X**	3844	0.76	0.78	1728	2936	0.17	0.54
	Y	4874	0.84	0.84	1695	3589	0.22	0.50
MI C/PF 9st	**X**	2423	0.97	0.97	2011	1898	0.10	0.09
	Y	2945	1.00	1.00	1886	2232	0.12	0.09
NA C/PF 9st	**X**	2723	0.99	1.00	2012	2106	0.11	0.30
	Y	5082	0.94	0.95	1917	3847	0.21	0.31
AQ C/PF 9st	**X**	4077	0.89	0.87	2012	3140	0.16	0.49
	Y	5148	0.89	0.89	1853	3859	0.21	0.48

2.3.1.3 Industrial steel buildings

The industrial steel buildings are all single-story frames, hence the ESDoF systems were constructed based on the unscaled static capacity curves. Since each portal frame behaves individually, due to the absence of a rigid roof diaphragm, the SPO curves were obtained from the roof-top and column-top displacement responses of the intermediate frame in X and Y directions, respectively. Figure 2-9a and Table 2-6 show the SPO backbones and the structural parameters of the obtained ESDoF systems (each was designed for both the soil conditions A

and C). Each SPO curve received bi-linear fitting (similar to URM) up to the maximum strength, then the softening phase was added in case the curve indicates strength deterioration. Reflecting the different load-resisting systems in the two horizontal directions, each structure exhibits the higher resistance capacity in the X direction and the shorter vibration period in the Y direction. Moreover, it can be observed that the capacities of the structures with the same configuration are nearly identical, in spite of the different hazard levels at the three sites. Given the characteristics of each load-bearing system, a bilinear hysteresis model [Ibarra et al., 2005] and moderately pinching peak-oriented hysteresis model (the same for RC buildings), both without any cyclic stiffness/strength deterioration, were applied in the X and Y directions, respectively. As alternatives to the local collapse criterion for brace members explained above, this study investigated three global quantities which can be possibly treated as an equivalent response measure for the failure in the bracings. Assuming that the static strain capacity under monotonic loading can somewhat indicate the dynamic strain capacity of the brace members, the first two are displacement capacities on the pushover curve corresponding to the attainment of a certain brace strain (ε), that is, (1) 4.9% (the equivalent strain range under monotonic loading; $\delta_{f,\varepsilon=4.9\%}$) and (2) 2.45% (the equivalent strain range under ideally symmetric loading; $\delta_{f,\varepsilon=2.45\%}$). As illustrated in Figure 2-9b, the brace strain responses were monitored simultaneously in pushover analysis, then those strain thresholds were translated into the corresponding displacements (only when available). The third is a displacement corresponding to (3) 2.0% transient IDR suggested by FEMA 356 [ASCE, 2000] for collapse prevention performance level of braced steel frames, $\delta_{f,FEMA}$. The three of them are also indicated together with the capacity curves in Figure 2-9a,b, as well as the displacement limit values, $\delta_{f,IDR10\%}$ in the X direction.

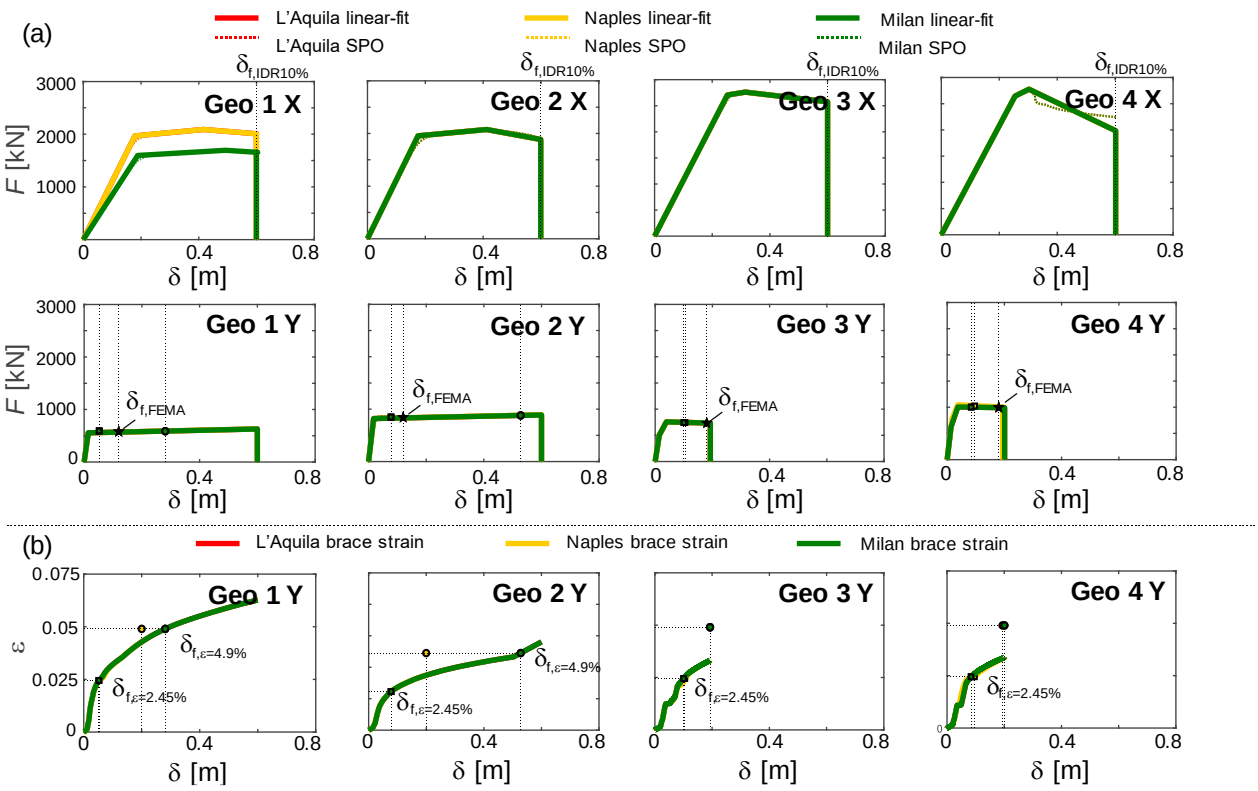

Figure 2-9 ESDoF-SPO backbones of steel buildings.

Table 2-6 Structural parameters of the steel buildings (Soil A and C).

Site/ config.	Dir.	T_1 [s]	T^* [s]	m^* [ton]	F_y^* [kN]	$Sa_y(T^*)$ [g]	Soil A $Sa_{SLV}(T^*)$ [g]	Soil C $Sa_{SLV}(T^*)$ [g]
MI	**X**	0.67	0.59	73	1597	2.22	0.06	0.15
/Geo 1	**Y**	0.32	0.27	73	557	0.77	0.12	0.20
NA	**X**	0.60	0.51	73	1967	2.73	0.26	0.58
/Geo 1	**Y**	0.30	0.27	73	557	0.77	0.40	0.58
AQ	**X**	0.60	0.51	73	1967	2.73	0.42	0.82
/Geo 1	**Y**	0.32	0.27	73	557	0.77	0.62	0.82
MI	**X**	0.66	0.58	95	1956	2.10	0.06	0.15
/Geo 2	**Y**	0.35	0.35	95	820	0.88	0.11	0.20
NA	**X**	0.66	0.58	95	1956	2.10	0.23	0.51
/Geo 2	**Y**	0.34	0.28	95	820	0.88	0.40	0.58
AQ	**X**	0.66	0.58	95	1956	2.10	0.37	0.73
/Geo 2	**Y**	0.35	0.35	95	820	0.88	0.61	0.82
MI	**X**	0.79	0.63	108	2707	2.56	0.06	0.14
/Geo 3	**Y**	0.37	0.35	108	503	0.48	0.11	0.20
NA	**X**	0.79	0.63	108	2707	2.56	0.21	0.47
/Geo 3	**Y**	0.38	0.35	108	503	0.48	0.39	0.58
AQ	**X**	0.79	0.63	108	2707	2.56	0.34	0.67
/Geo 3	**Y**	0.37	0.35	108	503	0.48	0.61	0.82
MI	**X**	0.85	0.70	130	2645	2.07	0.05	0.13
/Geo 4	**Y**	0.38	0.33	130	628	0.49	0.11	0.20
NA	**X**	0.85	0.70	130	2645	2.07	0.20	0.43
/Geo 4	**Y**	0.37	0.33	130	781	0.61	0.40	0.58
AQ	**X**	0.85	0.70	130	2645	2.07	0.31	0.61
/Geo 4	**Y**	0.38	0.33	130	628	0.49	0.62	0.82

2.3.1.4 Industrial precast reinforced concrete buildings

As with the steel buildings, the ESDoF systems of the PRC buildings were constructed directly based on the unscaled static capacity curves assuming a lumped mass and rigid diaphragm at the roof level. Figure 2-10 shows the SPO backbones of the obtained ESDoF systems for the two horizontal directions. In fact, the SPO curves of the original structural models exhibited the multi-linear backbones owing to its modelling approaches, thus the ESDoF systems retain the exact SPO curves without any fitting. The SPO curve of each system consists of three segments (elastic-hardening-softening), whose endpoint corresponds to the displacement-based collapse criterion defined above. As it regards the local collapse criterion for the beam-column connection, the ratio of the maximum base-shear recorded in dynamic analysis and connection shear capacity reported in [Magliulo et al., 2018] was considered as an alternative response measure. As seen in the figure, structural resistance varies across the different configurations and hazard levels at the sites, while the deformation capacity does not change significantly among the four configurations. The computed structural parameters for all considered cases are summarized in Table 2-7; T^* ranges between 1.2-2.4s and the computed $Sa_y\left(T^*\right)$ values resulted to be larger than the corresponding $Sa_{SLV}\left(T^*\right)$ for all cases. The peak-oriented hysteretic behavior model embedded into the column hinges of the original models [Ibarra et al., 2005] was considered in this study, however no cyclic stiffness/strength deterioration was assumed unlike the original models.

To close this section, Figure 2-11 shows the hysteresis loops under cyclic loading for some representative cases of each structural type.

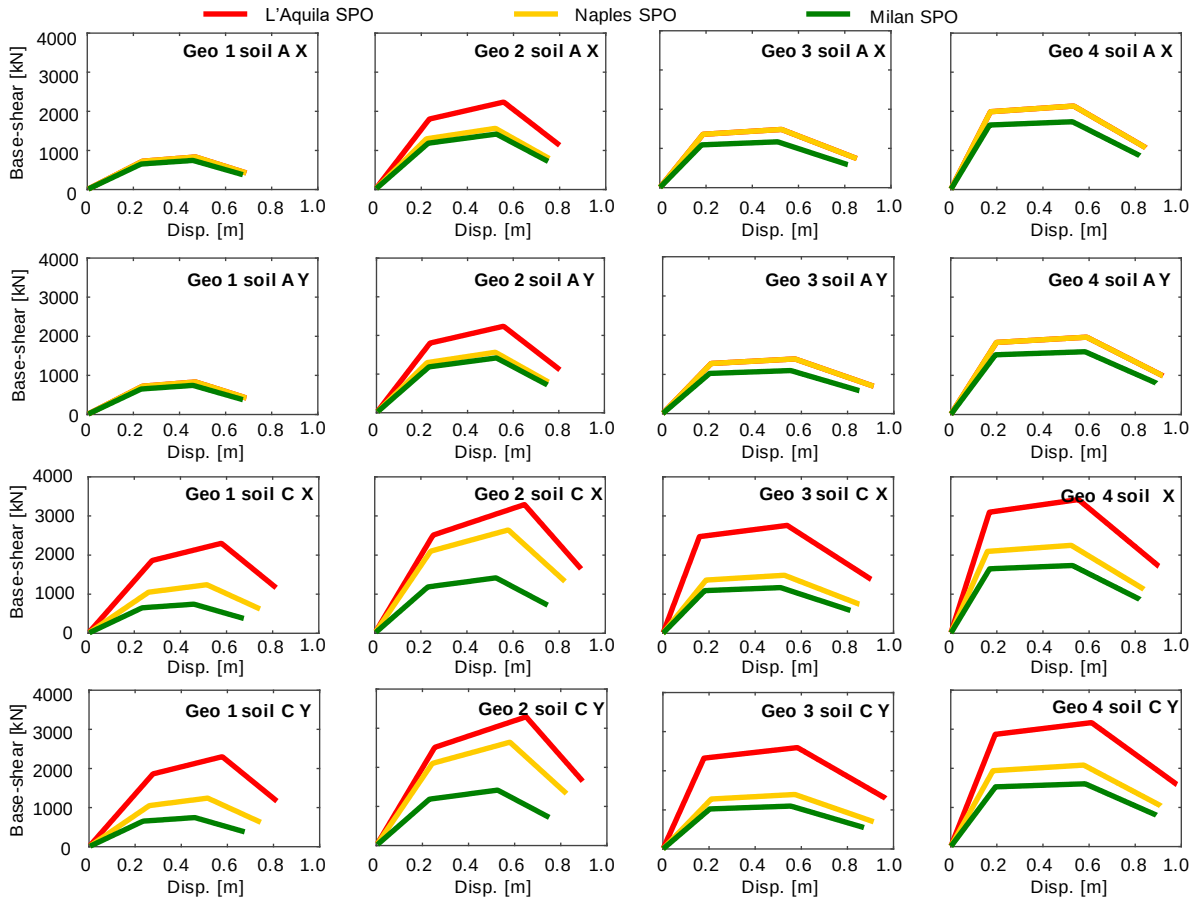

Figure 2-10 ESDoF-SPO backbones of the prototype PRC buildings.

Table 2-7 Structural parameters of the PRC buildings (Soil A and C).

Site/config.	Dir.	T_1 [s]	T^* [s]	m^* [ton]	F_y^* [kN]	$Sa_y(T^*)$ [g]	$Sa_{SLV}(T^*)$ [g]
MI A/Geo 1	**X**	2.28	2.37	398	654	0.17	0.01
	Y	2.28	2.37	398	654	0.17	0.01
NA A/Geo 1	**X**	2.20	2.28	398	725	0.19	0.06
	Y	2.20	2.28	398	725	0.19	0.06
AQ A/Geo 1	**X**	2.20	2.28	398	724	0.19	0.09
	Y	2.20	2.28	398	741	0.19	0.09
MI A/Geo 2	**X**	2.02	2.08	566	1186	0.21	0.02
	Y	2.02	2.08	566	1186	0.21	0.02
NA A/Geo 2	**X**	1.91	1.96	566	1299	0.23	0.07
	Y	1.91	1.96	566	1298	0.23	0.07
AQ A/Geo 2	**X**	1.68	1.71	566	1804	0.33	0.13
	Y	1.68	1.71	566	1804	0.33	0.13
MI A/Geo 3	**X**	1.78	1.84	515	1091	0.22	0.02
	Y	1.94	2.01	515	1024	0.20	0.02
NA A/Geo 3	**X**	1.63	1.67	515	1361	0.27	0.08
	Y	1.78	1.83	515	1278	0.25	0.07
AQ A/Geo 3	**X**	1.63	1.67	515	1361	0.27	0.13
	Y	1.78	1.83	515	1278	0.25	0.12

Table 2-7 (continued) Structural parameters of the PRC buildings (Soil A and C).

Site/config.	Dir.	T_1 [s]	T^* [s]	m^* [ton]	F_y^* [kN]	$Sa_y(T^*)$ [g]	$Sa_{SLV}(T^*)$ [g]
MI A/Geo 4	**X**	1.74	1.80	802	1650	0.21	0.02
	Y	1.94	2.01	802	1528	0.19	0.02
NA A/Geo 4	**X**	1.61	1.66	802	1991	0.25	0.08
	Y	1.79	1.85	802	1844	0.23	0.07
AQ A/Geo 4	**X**	1.29	1.66	802	1990	0.25	0.13
	Y	1.44	1.85	802	1843	0.23	0.11
MI C/Geo 1	**X**	2.28	2.37	398	654	0.17	0.03
	Y	2.28	2.37	398	654	0.17	0.03
NA C/Geo 1	**X**	1.91	1.98	398	1052	0.27	0.15
	Y	1.91	1.98	398	1052	0.27	0.15
AQ C/Geo 1	**X**	1.51	1.53	398	1865	0.48	0.28
	Y	1.51	1.53	398	1865	0.48	0.28
MI C/Geo 2	**X**	2.02	2.08	566	1186	0.21	0.04
	Y	2.02	2.08	566	1186	0.21	0.04
NA C/Geo 2	**X**	1.58	1.61	566	2103	0.38	0.18
	Y	1.58	1.61	566	2103	0.38	0.18
AQ C/Geo 2	**X**	1.48	1.50	566	2513	0.45	0.28
	Y	1.48	1.50	566	2513	0.45	0.28
MI C/Geo 3	**X**	1.78	1.84	515	1091	0.22	0.05
	Y	1.94	2.05	515	1024	0.20	0.04
NA C/Geo 3	**X**	1.63	1.67	515	1361	0.27	0.17
	Y	1.78	1.86	515	1278	0.25	0.16
AQ C/Geo 3	**X**	1.16	1.17	543	2473	0.46	0.35
	Y	1.26	1.31	543	2324	0.44	0.32
MI C/Geo 4	**X**	1.74	1.80	802	1656	0.21	0.05
	Y	1.94	2.01	802	1527	0.19	0.04
NA C/Geo 4	**X**	1.52	1.56	812	2094	0.26	0.19
	Y	1.70	1.74	812	1940	0.24	0.17
AQ C/Geo 4	**X**	1.61	1.31	802	3097	0.39	0.32
	Y	1.79	1.46	802	2870	0.36	0.28

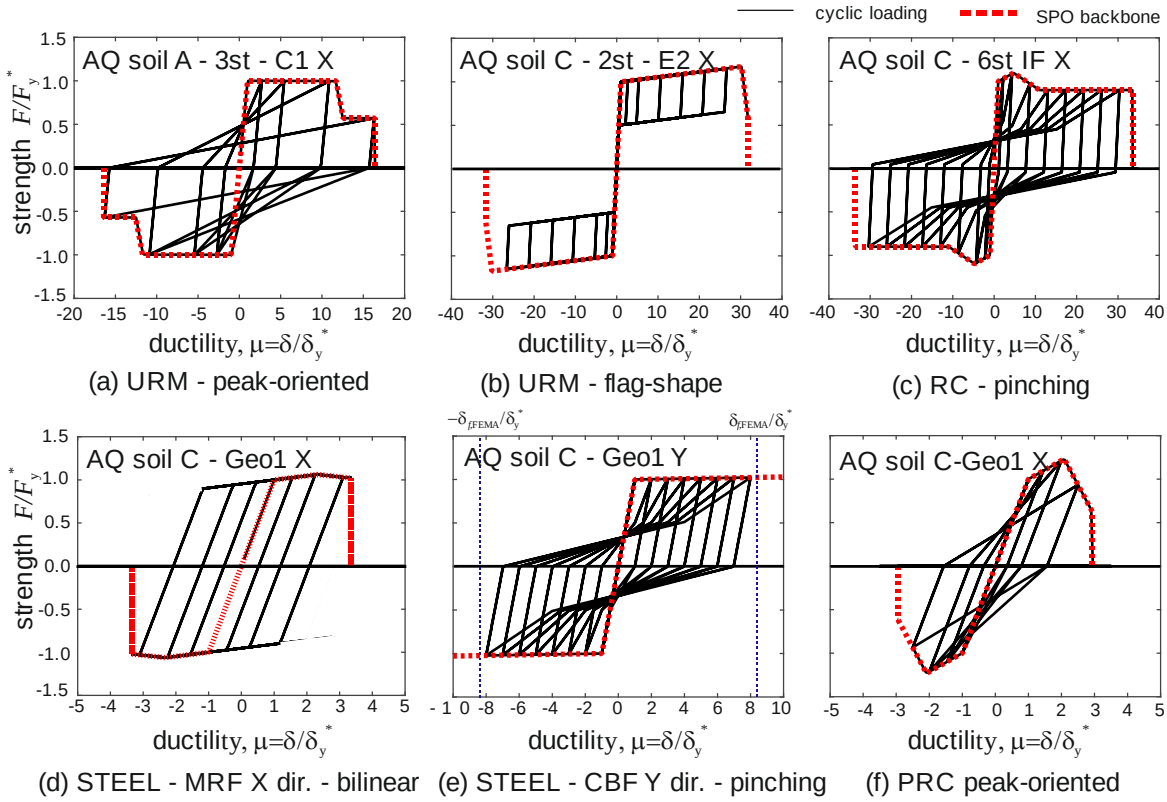

Figure 2-11 Hysteresis laws for each structural type and configuration.

2.3.2 Model verification: ESDoF vs 3D model responses

This section verifies the approximation of the computed ESDoF models, which will be used to develop fragility functions in the next section. For some representative cases, the structural responses in terms of demand-to-capacity (D/C) ratio of the corresponding EDP, which is computed in the same manner as the RINTC project, are compared with those obtained from the original 3D structural models [RINTC-Workgroup, 2018]. The following first briefly recalls the RINTC risk assessment scheme, followed by the comparisons of the D/C ratios.

In the RINTC project, the seismic risk of the examined code-conforming structures were quantified as the expected number in one year of earthquakes capable to causing structural failure, that is, in terms of annual failure rate, λ_f, via Eq. (1-10). The fragility term $P\left[F\left|IM=im\right.\right]$ in the equation was computed via Eq. (1-17) through multiple stripe analysis (MSA) using the 3D nonlinear structural models. For each structure, MSA was performed at ten IM levels (IMLs), $IM_i = im_i$ where $i=\{1,2,...,10\}$ corresponding to exceedance return periods of $T_{R,i}=\{10,50,100,250,500,1000,2500,5000,10000,100000\}$ years, up to which

PSHA was carried out for each site (the risk integral with the truncated hazard will be discussed in Chapter 3, Section 3.3.1.5). In the RINTC project, hazard curves were computed for the pseudo-acceleration spectral ordinates at the periods $T=\{0.15\text{s},0.5\text{s},1.0\text{s},1.5\text{s},2.0\text{s}\}$, which cover the range of the first mode vibration periods of the 3D models (approximately between 0.10s-2.3s; see Table 2-4-Table 2-7). Then, the spectral acceleration at the period closest to the first-mode period, $Sa(T)$, was selected as the IM to condition the GM records for response assessment. (The conditioning period closest to the structural fundamental period in the X direction was chosen for the steel buildings whose fundamental periods of vibration have a range between the two horizontal directions.) For each site, record selection was *hazard-consistent* by means of the conditional spectrum (CS) approach [Lin et al., 2013; Kohrangi et al., 2017] collecting twenty GM records for each IML of the selected IMs; see Iervolino et al. [2018]. As an example. Figure 2-12 shows the GM spectra of the selected record sets for the ten IMLs of the three sites on the soil condition C, which were all conditioned at $T=0.5\text{s}$. For the rest of the record sets with other conditioning periods and/or for the soil condition A, see Appendix.

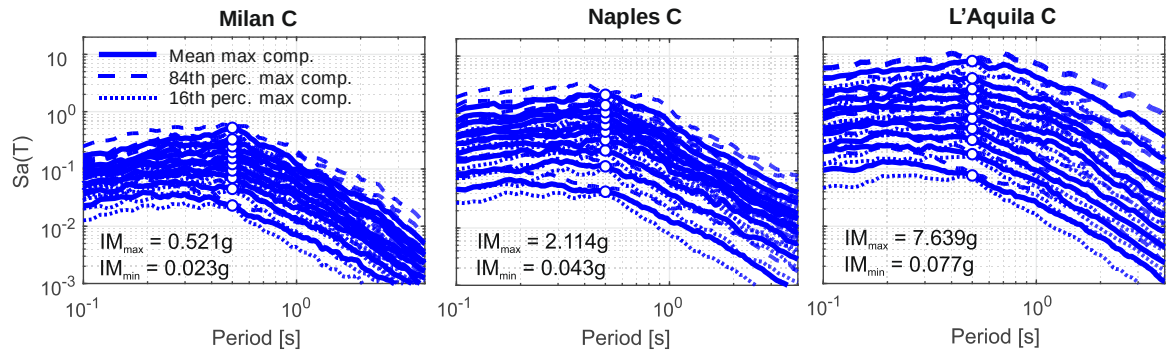

Figure 2-12 Examples of the selected GM records conditioned with respect to a vibration period of 0.5s for the three sites on soil C (a) Milan; (b) Naples, (c) L'Aquila.

MSA was performed using the calibrated ESDoF systems following the structural analysis strategy adopted in the RINTC project. The D/C ratios were computed by taking the ratio of the measured EDP in MSA analysis to the capacity defined based on the pushover curve of the structure (or based on the FEMA 356 recommendations for steel buildings). Figure 2-13

shows the measured D/C ratios at the ten IMLs, as well as the numbers of failure cases ($N_{f,i}$, with the lowercase letters representing the corresponding system) out of the total number of records, $N_{tot,i} = 20$, for some representative cases of each structural type and/or configuration. The buildings designed at the most severe hazard site of the three sites, AQ, are chosen for the sake of illustration.

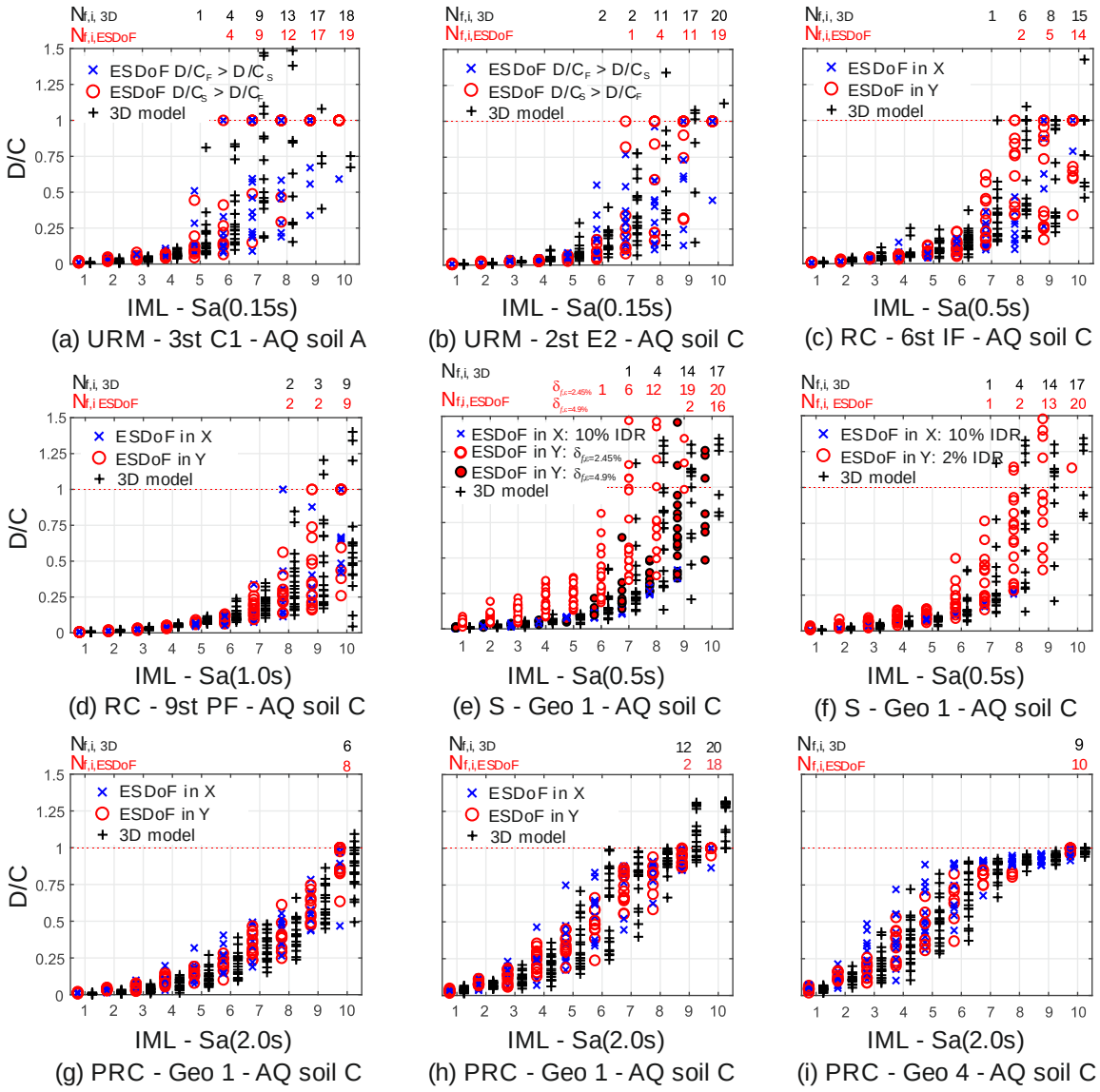

Figure 2-13 Comparisons of the computed D/C ratios.

Figure 2-13a,b show the results for two cases of URM buildings, the three-story C-type (C1, soil A) and the two-story E-type building (E2, soil C), respectively. The ESDoF models assume either flexure- or shear-dominated hysteresis response unlike the original 3D

models (denoted as cross markers in the figure) where the response is mixed considering the contributions from multiple masonry panels. For this reason, the figures show the larger value of the D/C ratios between the flexure- (F) and shear-(S) dominated hysteresis models for each (j) GM record $j=\{1,2,\ldots,N_{tot,i}\}$ at each (i) IML, i.e., $D/C=\max\left(D/C_{F,i,j}, D/C_{S,i,j}\right)$. It is observed that the ESDoF responses succeeded to capture the trends of the original 3D models (black cross markers) and the number of failure cases over the IMLs, especially for the C-type buildings, however, resulted in some underestimation, especially at the intermediate IMLs for the E-type buildings. This is mainly because: (1) the considered EDP for the original models, that is the maximum IDR of the single wall elements, is larger than the corresponding roof drift considered for the ESDoFs when a soft story collapse mechanism occurs; (2) the actual tangent stiffness of the exact pushover curve of each E-type building, corresponding to the elastic branch of the multi-fitted SPO, reduces from the equivalent stiffness (see Figure 2-7 and Section 2.3.1.1).

Figure 2-13c,d show the results for two cases of the RC buildings, six-story IF and nine-story PF buildings, respectively. The D/C ratios are shown in the figures with colored markers to distinguish the principal direction which led to the larger value of the D/C ratio and are compared to those from the original 3D models. As seen in the presented cases, the computed D/C ratios and the number of failure cases have a good agreement between the two structural systems, in most cases, over the multiple IMLs. Figure 2-13e,f represent the results for the steel building with Geo 1 (AQ on soil C). As reported in the study with the original 3D models, the D/C ratios at the larger IMLs mostly come from the longitudinal (Y) direction associated with the failure in brace members. Consistently, the D/C ratios computed from ESDoF systems significantly varied depending on the considered candidate global response measures. Among those, the displacement limit values associated with the local strain thresholds, $\delta_{f,\varepsilon=4.9\%}$ and $\delta_{f,\varepsilon=2.45\%}$ did not agree with the observed responses of the frame models under earthquake excitation (Figure 2-13e). On the other hand, 2.0% IDR suggested by FEMA 356, $\delta_{f,FEMA}$, (Figure 2-13f) resulted in the best estimates of the D/C ratios in most of the cases, although some may argue it is not comparable with the strain-based EDP for the original frame models.

Figure 2-13g,h,i show the computed D/C ratios for the PRC buildings of Geo 1 and 4 (AQ soil C) with respect to the displacement-based global collapse criteria and the force-based ones associated with the connection failure. Both the approaches (i.e., displacement-based and force-based) somewhat agree with the original models for all considered cases (e.g., Figure 2-13g,i), except the force-based approach for Geo 1 and 2 (e.g., Figure 2-13h). This is because, in fact, the original structural models of these configurations assumed the mass distributed at the connection- and crane-bracket levels as well as at the roof top, whereas the roof-top lumped mass was assumed for the other configurations. For this reason, larger shear forces were applied during the dynamic analyses for such cases (see [Magliulo et al., 2018] for detailed descriptions).

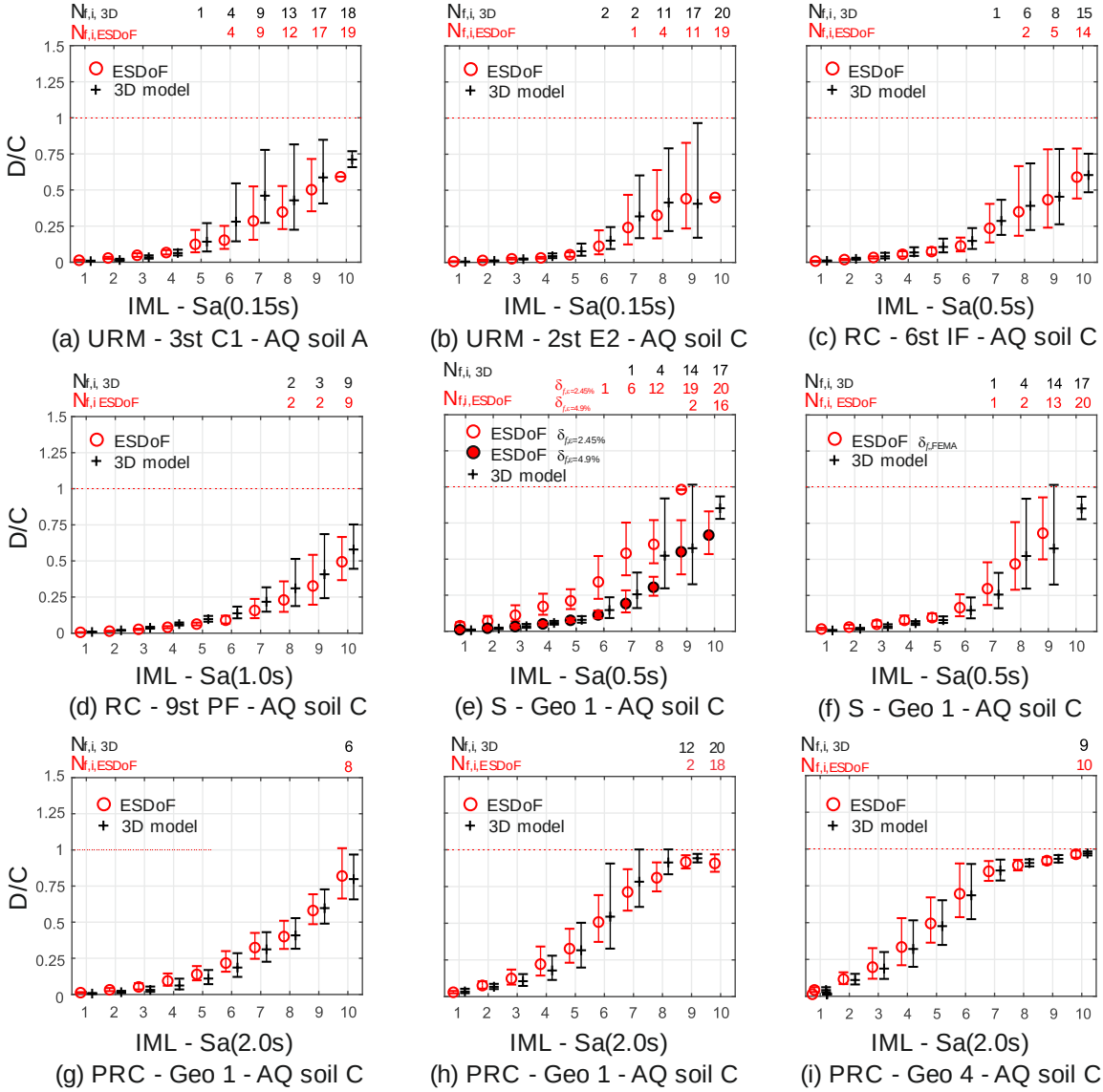

Figure 2-14 Comparisons of the computed D/C ratios (with error bars for non-failure cases).

Figure 2-14 shows the error bars indicating the mean plus/minus one standard deviation of the measured D/C ratios shown in Figure 2-13. It should be noted that, in order to fairly compare the variability of the responses between the 3D models and the ESDoF systems, they were computed excluding the failure cases (i.e., D/C exceeding 1), thus the variability of the response does not necessarily increase with the IM.[3] Though some discrepancies with the original structural models arose from the limitations of the ESDoF models and in the reference data from the original 3D models as discussed above, it can be considered that the computed ESDoF models under the above assumptions provided generally comparable estimates of structural responses of the original 3D models.

2.4 Design trends of structural features

This section examines certain structural features of the prototype buildings resulting from code-conforming design, that can help to explain the observed trend of seismic risk [Iervolino et al., 2017; 2018]. In particular, emphasis is herein placed on the actual (global) strength and ductility characteristics, which are critical in determining the seismic capacity of structures.

To discuss such structural features in relation to the seismic risk, it is worthy to rewrite Eq. (1-10) as Eq. (2-1) separating the seismic risk contributions into two terms: (i) the failure rate for earthquakes not causing the exceedance of the design seismic intensity im_d, $\lambda_{f,IM\le im_d}$; and (ii) the failure rate for earthquakes causing the exceedance of the design GM level, $\lambda_{f,IM>im_d}$.

$$\begin{aligned}\lambda_f &= \int_0^{im_d} P\left[F \mid IM = x\right]\left|d\lambda_{im}\right| + \int_{im_d}^{\infty} P\left[F \mid IM = x\right]\left|d\lambda_{im}\right| \\ &= \lambda_{f,IM\le im_d} + \lambda_{f,IM>im_d}\end{aligned} \tag{2-1}$$

It can be considered that, the first term, $\lambda_{f,IM\le im_d}$, is implicitly controlled through the code requirements, at least being expected to be smaller than the occurrence rate of earthquakes

[3] The reader must be cautioned against mistaking the presented means and standard deviations of the D/C ratios for the lognormal parameters of an EDP in Eq. (1-17), which are obtained from non-collapse data.

not causing the exceedance of the design level. However, the resulting risk still involves some degree of uncertainty given that the actual inelastic demands may vary from those assumed in the design, depending on the design assumptions pertaining to different structural types, configurations, and site hazard levels. On the contrary, the second term $\lambda_{f,IM>im_d}$, associated with failure due to an earthquake causing the exceedance, is beyond the control of the current seismic design code. This term is particularly dependent on the robustness and redundancy of structures and the seismic hazard at the site (i.e., the slope of the hazard curve). Thus, the dispersion in the seismic risk may arise from extreme events which are not considered in design.

Correspondingly to the two components in Eq. (2-1), the strength capacities of the examined structures are discussed herein in terms of strength reduction factors[4] (i) with respect to the design spectral accelerations for SLV, R_{SLV}, and (ii) with respect to a spectral acceleration level exceeding the design GM intensity, namely, *peak-over-threshold* (POT) intensity, $R_{POT,SLV}$. The former is defined as the ratio of the horizontal elastic spectral acceleration at T^* from the 475 year-return period elastic design spectrum (at the bottom of Figure 2-1b) to the yield acceleration of the ESDoF, i.e., $R_{SLV} = Sa_{SLV}\left(T^*\right) \big/ Sa_y\left(T^*\right)$, which can purely represent the degree of overstrength in design somewhat related to the trend of $\lambda_{f,IM\le im_d}$. The latter strength reduction factor refers to the expected value of spectral acceleration levels given the exceedance, i.e., $R_{POT,SLV} = E\left[Sa\left(T^*\right) > Sa_{SLV}\left(T^*\right)\right] \big/ Sa_y\left(T^*\right)$ (the computation to follow). This measure indicates seismic demands due to an extreme seismic event somewhat related to $\lambda_{f,IM>im_d}$. As regards the ductility capacity, failure (global collapse) ductility, μ_{GC} (evaluated according to the definitions in Sections 2.3.1) is considered herein as it is the normalizing term of the considered EDP.

Figure 2-15 schematically illustrates the examined structural features. In the figure, the design GM spectrum, the POT GM spectrum with the expected IM level given the exceedance $Sa(T) > Sa_{SLV}(T)$, and structural capacity curve, i.e., pushover curve of the ESDoF system

[4] In many US seismic design documents (e.g., ASCE/SEI 7-05, FEMA P695), the letter "*R*" is used to denote the response modification factor, which is equivalent to the behavior factor *.q*. of NTC and EC8; the reader is thus cautioned against mistaking its use herein, which is to denote the strength reduction factor as defined at the ESDoF system level in the text.

representing the structure, are plotted together in the acceleration-displacement (AD) format. Although strength reduction factors are often discussed considering separately the contributions from overstrength and purely from ductility and energy dissipation capacities of the structure, such distinction was not made in this study focusing on the ESDoF quantities.

The following first discusses the results of R_{SLV} and μ_{GC} for each structural type as their definitions have been already clarified above in the text. As regards the POT strength reduction factors, the definition of the expected intensity value $E\left[Sa\left(T^*\right) > Sa_{SLV}\left(T^*\right)\right]$ is provided, then the computed POT GM spectra are given for the considered three sites. The computed $R_{POT,SLV}$ values are discussed for each structural type.

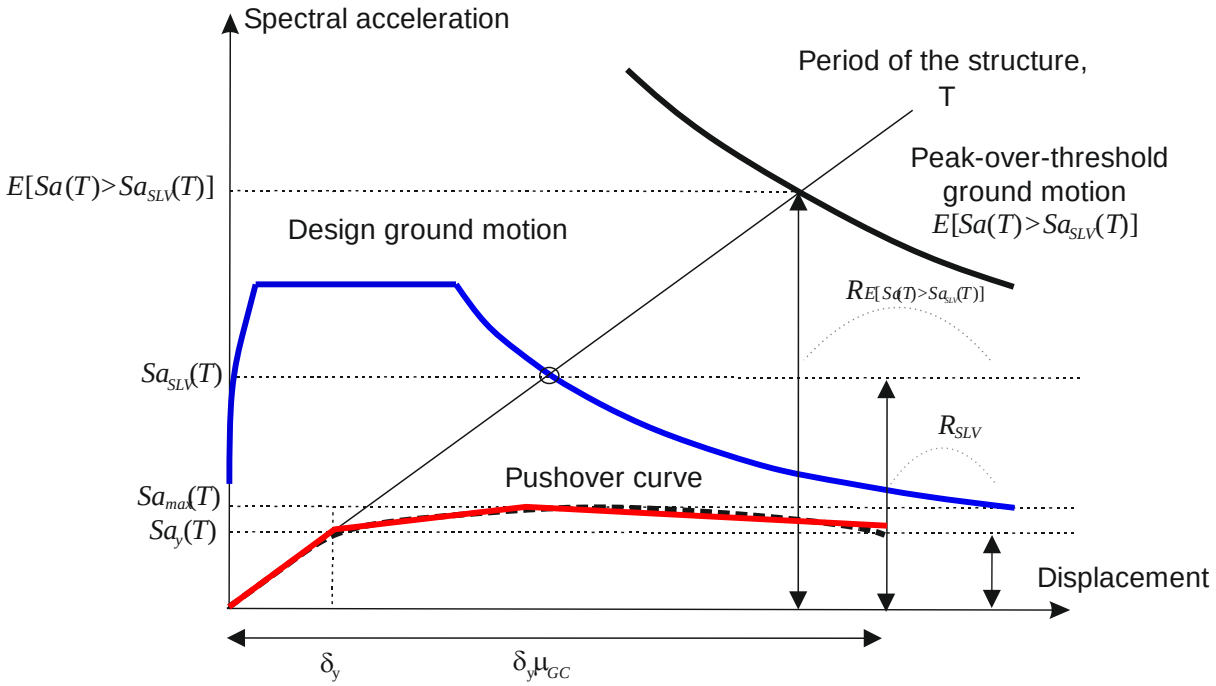

Figure 2-15 Illustration of seismic performance factors considered in this study.

2.4.1 Design level strength reduction factors and failure ductility factors

RC buildings

For the illustration sake, the results of the RC buildings are first discussed simply referring to the soil condition C only. The panels at the top of Figure 2-16 compare the strength reduction factors R_{SLV} of the RC buildings across the three different heights (number of stories), sites, and structural configurations. In each panel corresponding to each building height, the three

sites are aligned in the horizontal axis in order of seismicity level. It is observed that the strength reduction factor R_{SLV} ranges from 0.3 to 3.7 depending on the case at hand; it tends to increase with increasing hazard level at the site, when compared between the structures belonging to the same structural configuration and building height. In fact, the R_{SLV} factors computed among the buildings at L'Aquila, the site with the severest hazard, were approximately up to four times as large as the strength reduction factors of the buildings at Milan, the site with the mildest hazard. These results show that the structures at the sites with low seismicity, tend to exhibit lower reduction factors because of greater overstrength. This was to be expected, since at lower-hazard sites the strength reserves of a structure are more heavily dependent on the minimum requirements of the code's design provisions. An alternative way of highlighting this same effect, i.e., the fact that the structures designed for lower-hazard sites appear stronger than their higher-hazard counterparts, when lateral resistance is seen as a proportion of code-mandated elastic demand, is to monitor the return period of exceedance of the spectral acceleration causing nominal yield, $T_{R,Sa_y(T^*)}$. This is provided in Table 2-8 for the cases examined here; it can be observed that among counterpart structures, despite the increase of ESDoF yield force with increasing hazard, structures at higher-hazard levels are expected to experience excursions beyond their nominal yield point more frequently.

Meanwhile, the panels at the bottom of Figure 2-16 compare failure ductility, which was computed for the ESDoFs, from the piece-wise linear SPO parameters in Section 2.3.1.2 (see Figure 2-8). Contrary to the clear trend exhibited in R_{SLV}, no obvious trend was observed for μ_{GC} across the structures at different sites nor across those with the same building height. It appeared to be rather dependent on the configuration type.

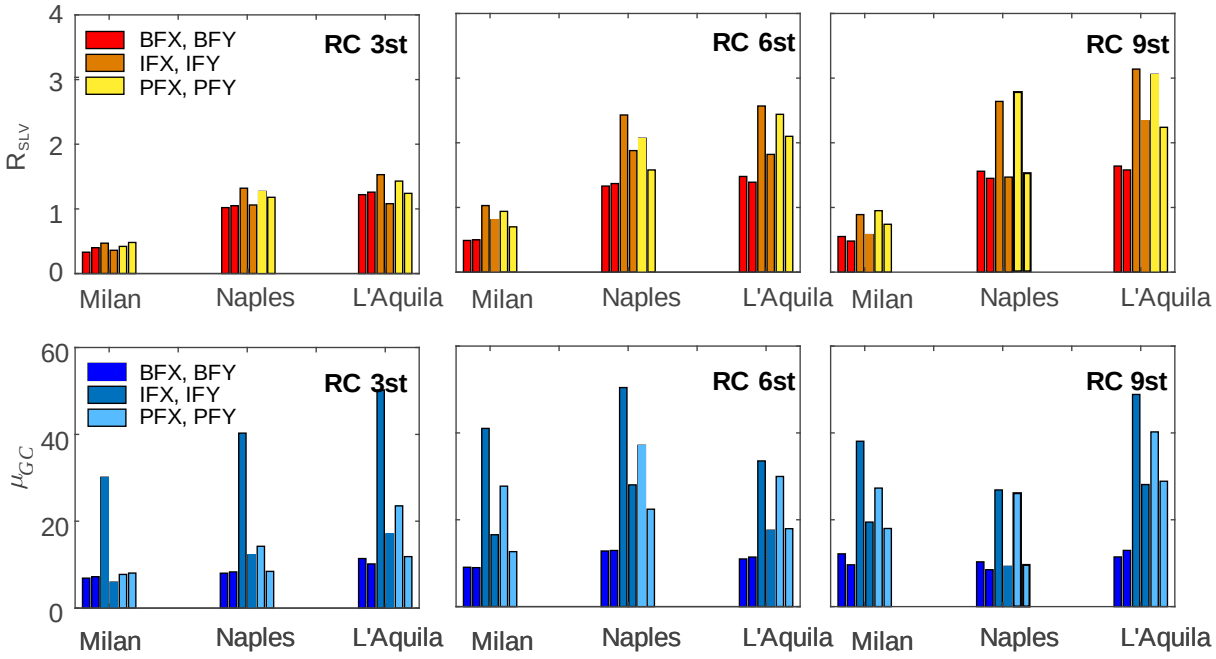

Figure 2-16 Comparison of inelastic capacity of the RC buildings; (top) strength reduction factor; (bottom) failure ductility.

Table 2-8 Spectral acceleration causing nominal yield $T_{R,Sa_y(T^*)}$ for the RC buildings.

Story	Site	Config./ dir BF X	BF Y	IF X	IF Y	PF X	PF Y
3-story	MI C	>10^5	38820	13319	36887	31686	14039
	NA C	1313	1058	346	589	553	663
	AQ C	431	401	179	379	309	414
6-story	MI C	34495	34771	1235	2319	1824	5565
	NA C	799	632	158	234	201	411
	AQ C	380	345	115	227	134	178
9-story	MI C	10627	22578	2169	9434	1666	4143
	NA C	725	829	136	488	93	302
	AQ C	553	516	104	162	100	177

Figure 2-17, Figure 2-18, and Figure 2-19 show the strength reduction/ductility factors for the other four structural types, URM, steel, and PRC, respectively. For all considered structural typologies, the similar trends of the strength reduction factor and the ductility factor were observed, i.e., the higher the site seismicity the larger strength reduction factor and comparable ductility capacity across the sites. The findings particular to each structural type are summarized in the following:

***URM*:** Figure 2-17 show the R_{SLV} and μ_{GC} factors for the URM buildings, at the top and bottom panels, respectively. The R_{SLV} factor ranges from 0.25 to 1.65, showing the clear increase with the site hazard. Particularly to the URM buildings, it can be considered that the observed trend is originally attributed to the different design approaches, as discussed in the RINTC project report [RINTC-Workgroup, 2018]. The most conservative design method LSA led to the R_{SLV} factors below 1, which were significantly smaller than those from the other two, SB and NLSA. On the contrary, the ductility capacity varied depending on the configurations (C, E2-9).

***Steel*:** The left and right panels of Figure 2-18 show the R_{SLV} and μ_{GC} factors (corresponding to 2.0% IDR suggested by FEMA 356) for the steel buildings, respectively. As presented in Section 2.3.1.3, the capacities of the structures with the same configuration are nearly identical in spite of the different hazard levels at the three sites, which resulted to form the clear trend of the increasing R_{SLV} factors with hazard ranging between 0.02 to 1.73. Especially a significant degree of overstrength can be seen in the site with lowest seismicity, Milan. The difference of the load-resisting systems in two horizontal directions was also reflected in the computed strength reduction factors and the ductility factors.

***PRC*:** Figure 2-19 show the R_{SLV} and μ_{GC} factors for the PRC buildings, respectively. Relatively smaller R_{SLV} values (all below 1) were observed in this typology presumably due to the fundamental vibration periods of the structures longer than those of the other typologies; the design seismic actions at the corresponding vibration periods are relatively small compared to those at shorter periods.

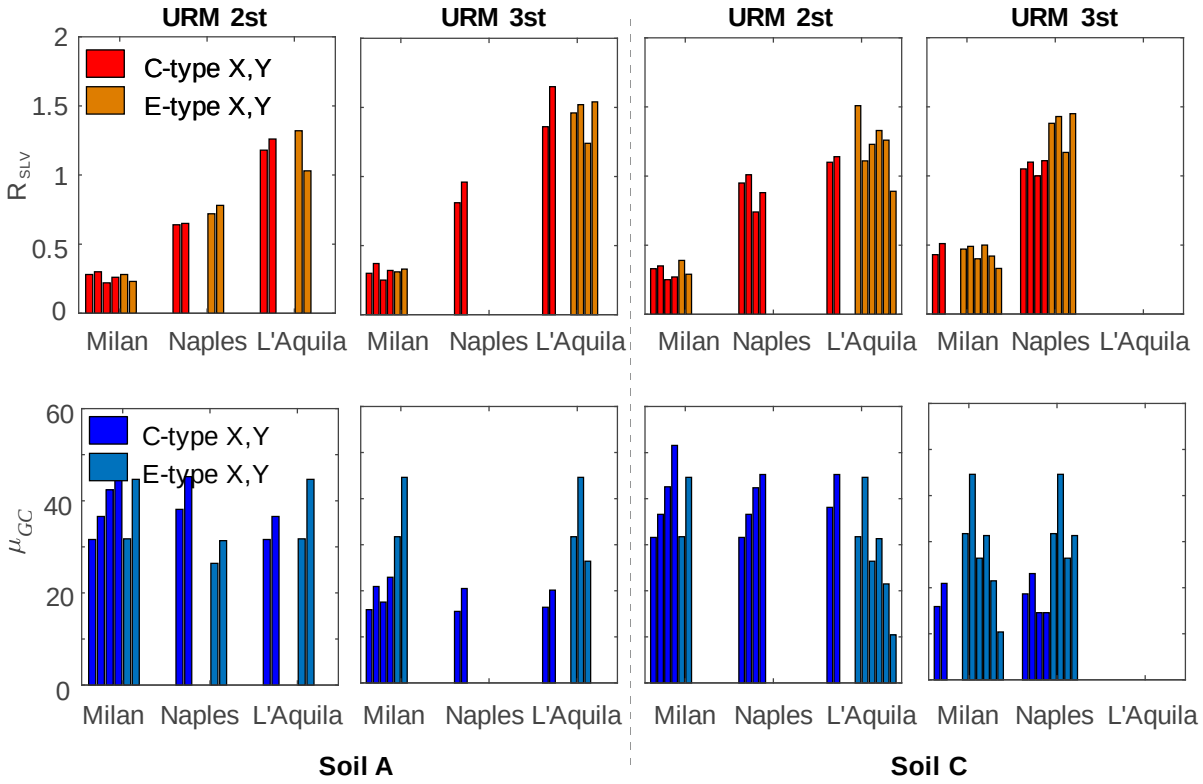

Figure 2-17 Comparison of inelastic capacity of the URM buildings; (top) strength reduction factor; (bottom) failure ductility.

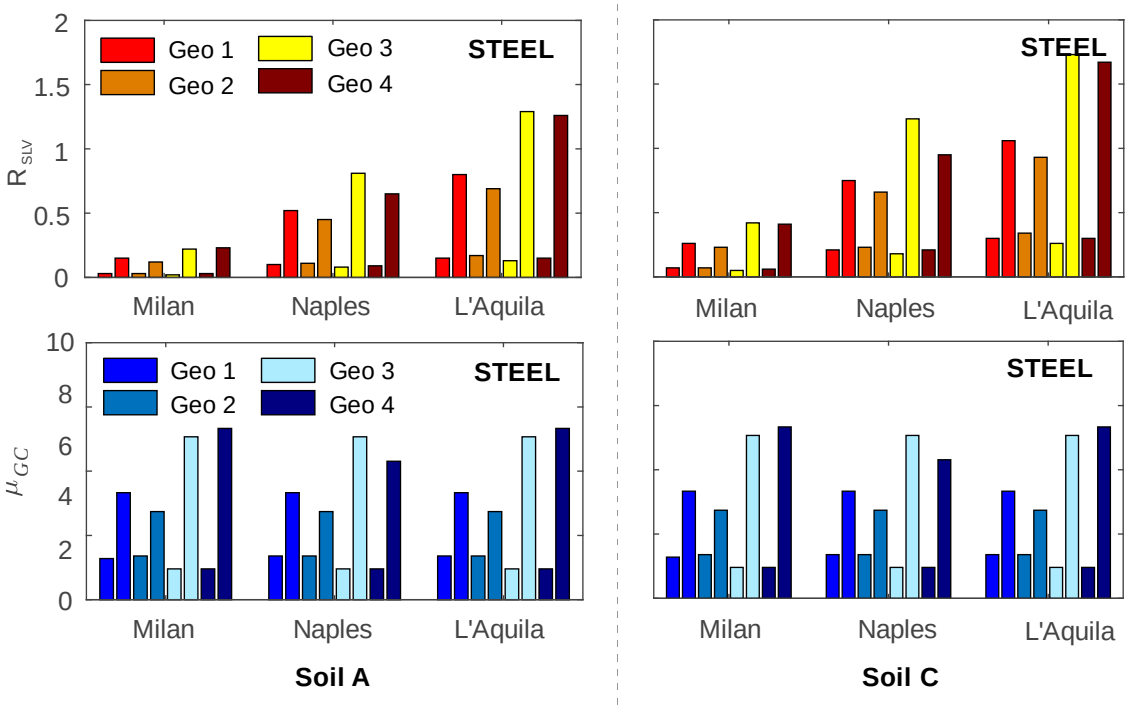

Figure 2-18 Comparison of inelastic capacity of the steel buildings; (top) strength reduction factor; (bottom) failure ductility.

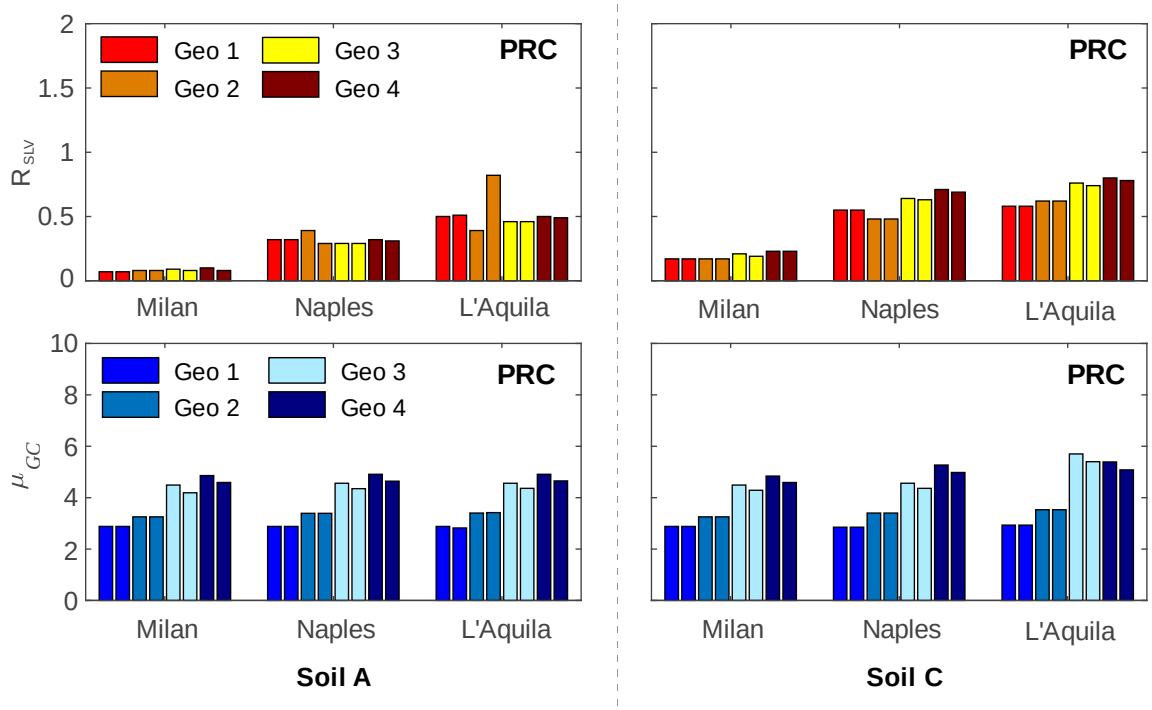

Figure 2-19 Comparison of inelastic capacity of the PRC buildings; (top) strength reduction factor; (bottom) failure ductility.

It should be noted that the absolute value of the computed ductility factor is highly dependent on the stiffness of the structure thus they cannot be fairly compared across different structural types or between the two horizontal directions in which the dynamic characteristics of the systems are different (i.e., the shorter period structures such as RC-IF/PF and URM show apparently larger ductility capacities, however, this does not mean larger deformation capacity; see the figures in Section 2.3 for the direct comparison of the deformation capacities).

2.4.2 Peak-over threshold strength reduction factors

2.4.2.1 Computation of peak-over threshold spectra

The computation of expected POT spectra is discussed in [Iervolino et al., 2018] which provides an Italian seismic hazard map in terms of the expected value of acceleration given the exceedance of the 475 year-return period elastic design spectrum, $E\left[Sa(T) > Sa_{SLV}(T)\right]$. In the cited paper, it can be computed with the following equation.

$$E\left[Sa(T) > Sa_{SLV}(T)\right] =$$

$$= \int_M \int_R e^{\mu_{\ln Sa(T)}(m,r)} \cdot \int_{\frac{\ln Sa_{SLV}(T) - \mu_{\ln Sa(T)}(m,r)}{\sigma_{\ln Sa(T)}}}^{\infty} e^{\sigma_{\ln Sa(T)} \cdot z} \cdot f_{M,R,\varepsilon|Sa(T)>Sa_{SLV}(T)}(m,r,z) \cdot dz \cdot dr \cdot dm \qquad (2\text{-}2)$$

The equation incorporates a GMPE which assumes a lognormal distribution of $Sa(T)$ characterized by $\ln Sa(T) = \mu_{\ln Sa(T)|M,R} + \sigma_{\ln Sa(T)} \cdot \varepsilon$: $\mu_{\ln Sa(T)|M,R}$ is the logarithmic mean of $Sa(T)$ conditional to a certain magnitude (M) and distance (R) scenario (m,r); $\sigma_{\ln Sa(T)}$ is the logarithmic standard deviation of $Sa(T)$; and ε is a standard normal variable, which is also interpreted as the number of standard deviations from $\mu_{\ln Sa(T)|M,R}$ predicted by the GMPE. $f_{M,R,\varepsilon|Sa(T)>Sa_{SLV}(T)}$ is the conditional joint probability density function of seismic magnitude, source-to-site distance, and residual $\{M, R, \varepsilon\}$, given the exceedance of $Sa_{SLV}(T)$. The equation is merely the integration of the products of the conditional random variable $Sa(T)$ and its distribution involving the GM characteristic variables over the domain of $Sa(T) > Sa_{SLV}(T)$.

It is noteworthy that $E\left[Sa(T) > Sa_{SLV}(T)\right]$ can be also obtained from the hazard curve in terms of $Sa(T)$ at a site of interest by normalizing the distribution of $Sa(T)$ given the occurrence of an earthquake over the domain of $Sa(T) > Sa_{SLV}(T)$. The integral of the random variable $Sa(T)$ and the normalized distribution of $Sa(T)$ given the exceedance yields the same solution as Eq. (2-2). For further details of the computation and the Italian POT hazard map, see [Iervolino et al., 2018].

2.4.2.2 Results of peak-over threshold strength reduction factors

Prior to the extreme value analysis via Eq. (2-2), PSHA was performed for the three sites under the two soil conditions A and C (see Chapter 1). The source model used for PSHA corresponds to branch 921 of the logic tree involved in the official Italian hazard model [Stucchi et al., 2011] with the GMPE developed by [Ambraseys et al., 1996] (the details to follow in the preceding chapters). This study utilized a computer software for PSHA, REASSESS [Chioccarelli et al., 2018] to perform the hazard disaggregation and the POT analyses with respect to the exceedance of the 475-year return period design seismic action altogether.

Figure 2-20 shows the computed expected POT acceleration response spectra

compared to the UHS for the 475-year return period earthquakes (which are actually approximated by the design spectra for the same sites at the bottom of Figure 2-1b). Corresponding to the findings in [Iervolino et al., 2018], the expected POT acceleration resulted in 1.5-2.0 times as large as the UHS at the highest seismicity site among the considered sites, L'Aquila. In particular, larger differences from the UHS were observed at short-to-intermediate periods corresponding to the peaks of the spectra. For the sites in Naples and Milan, the exceedance is expected to be approximately 1.5 times the UHS, yet no obvious trends across the vibration periods were observed.

From the obtained the expected POT spectra in Figure 2-20, the strength reduction factors, $R_{POT,SLV}$, were computed for all examined buildings. Figure 2-21 compares the POT strength reduction factors $R_{POT,SLV}$ of the RC buildings in the same manner as above. By its definition, the computed $R_{POT,SLV}$ factor for each building differs from the corresponding R_{SLV} by a factor of $E\left[Sa\left(T^*\right) > Sa_{SLV}\left(T^*\right)\right] \Big/ Sa_{SLV}\left(T^*\right)$, which is provided in Figure 2-22. Similarly to the observed differences between the expected POT and UHS spectra, the ratios $E\left[Sa\left(T^*\right) > Sa_{SLV}\left(T^*\right)\right] \Big/ Sa_{SLV}\left(T^*\right)$ are in the range of 0.8-1.3 for the cases in Milan and Naples and 1.1-1.9 for the cases in L'Aquila. This means that the POT strength reduction factors amplify the site-to-site differences, and, as a result, the trend observed above across the sites can be more clearly seen. In particular, the results highlighted significant increases of the seismic demands for the shorter period structures and/or at the most hazardous site, L'Aquila. It should be noted that, $E\left[Sa\left(T^*\right) > Sa_{SLV}\left(T^*\right)\right] \Big/ Sa_{SLV}\left(T^*\right)$ below 1 means that the design acceleration prescribed by the code much overestimates the UHS at the corresponding vibration period, thus exceeding the expected POT.

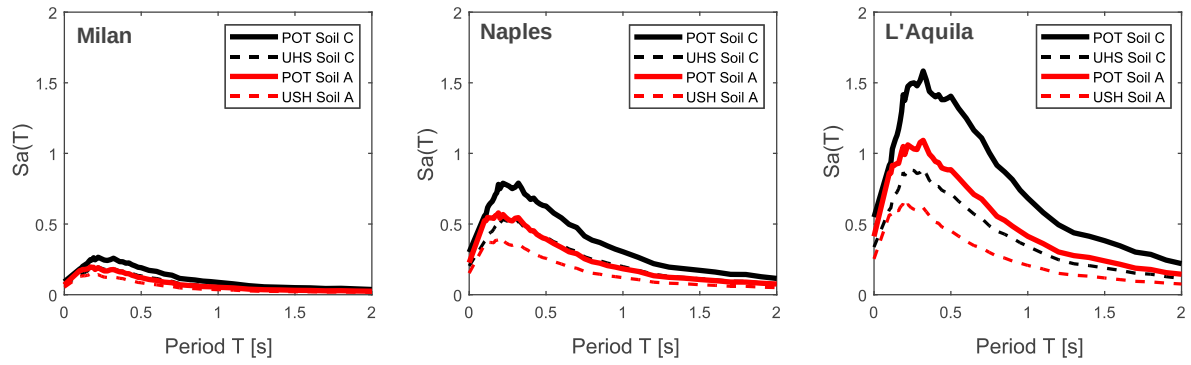

Figure 2-20 Comparisons of peak-over-threshold spectra and uniform hazard spectra at the three sites on the soil conditions A and C; (left) Milan (middle) Naples (right) L'Aquila.

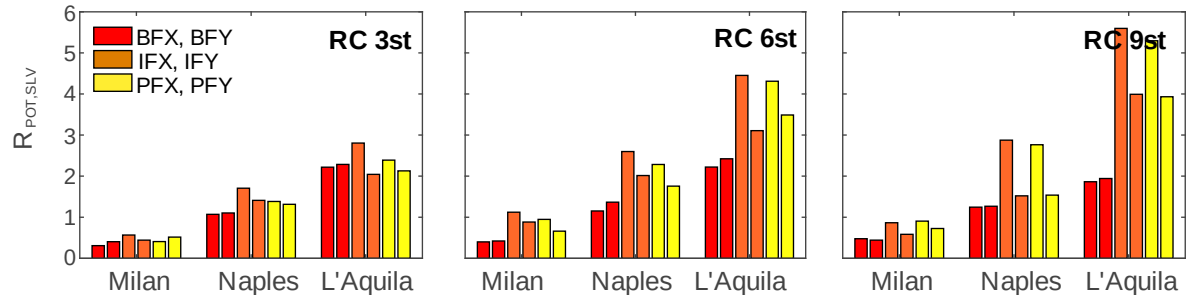

Figure 2-21 Strength reduction factors with respect to the expected spectral acceleration given the exceedance of the design seismic action (RC buildings; soil C).

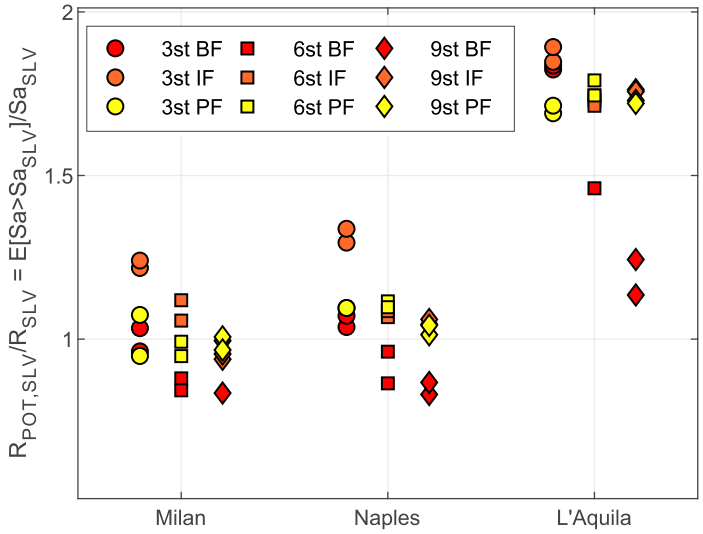

Figure 2-22 Ratios of the expected peak-over-threshold values to the design spectral accelerations (RC buildings; soil C).

Figure 2-23, Figure 2-24, and Figure 2-25 show the computed $R_{POT,SLV}$ factors for the other four structural types, URM, steel, and PRC, respectively. For all considered structural typologies, $R_{POT,SLV}$ increases with the seismic hazard level at the site at a steeper slope compared to R_{SLV}. The ratios of the expected POT to the design intensity level, $E\left[Sa\left(T^*\right) > Sa_{SLV}\left(T^*\right)\right] / Sa_{SLV}\left(T^*\right)$, are provided in Figure 2-26 for the rest of the examined buildings on the soil condition A and C. As for the RC buildings, the larger amplification can be seen for the higher seismicity sites and/or the structures with the shorter vibration periods, except the least hazardous site in Milan on the soil condition A. This is presumably because the design acceleration $Sa_{SLV}\left(T^*\right)$ is quite small for this site and a slight difference between UHS and $Sa_{SLV}\left(T^*\right)$ numerically led to the larger ratios than the other sites. Nonetheless, the investigations on the both strength factors, R_{SLV} and $R_{POT,SLV}$, indicate that the increasing trend of seismic risk with the site seismic hazard is ascribed not only to the degree of overstrength in the design, but also to local seismicity of extreme seismic events for which the structural safety is not controlled in the code-conforming design (corresponding to $T_R > 475 yrs$).

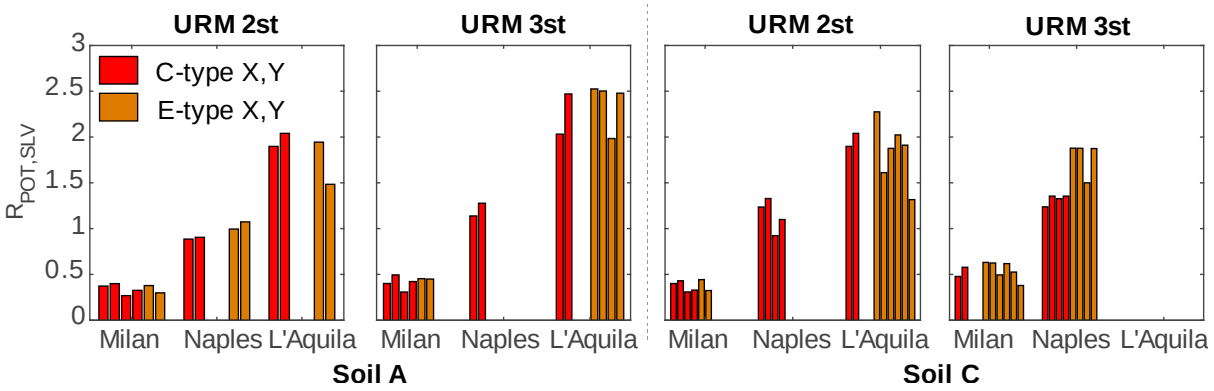

Figure 2-23 Strength reduction factors with respect to the expected spectral acceleration given the exceedance of the design seismic action (URM buildings).

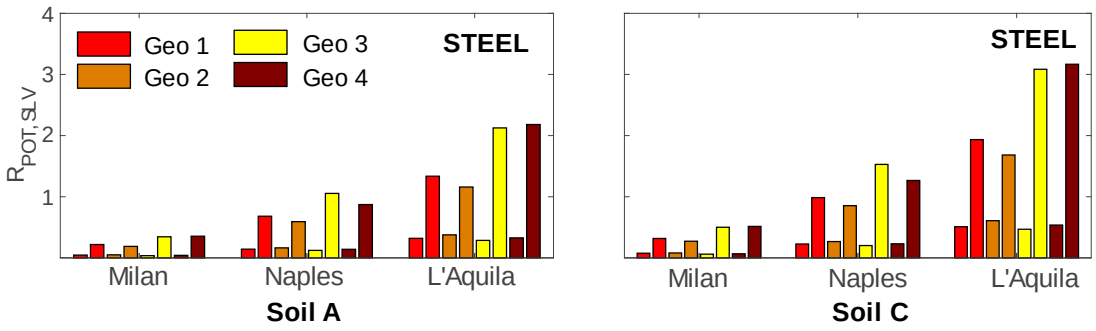

Figure 2-24 Strength reduction factors with respect to the expected spectral acceleration given the exceedance of the design seismic action (Steel buildings).

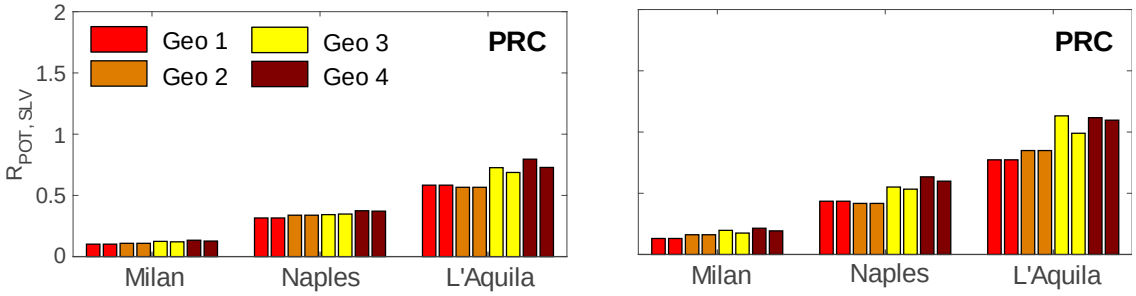

Figure 2-25 Strength reduction factors with respect to the expected spectral acceleration given the exceedance of the design seismic action (PRC buildings).

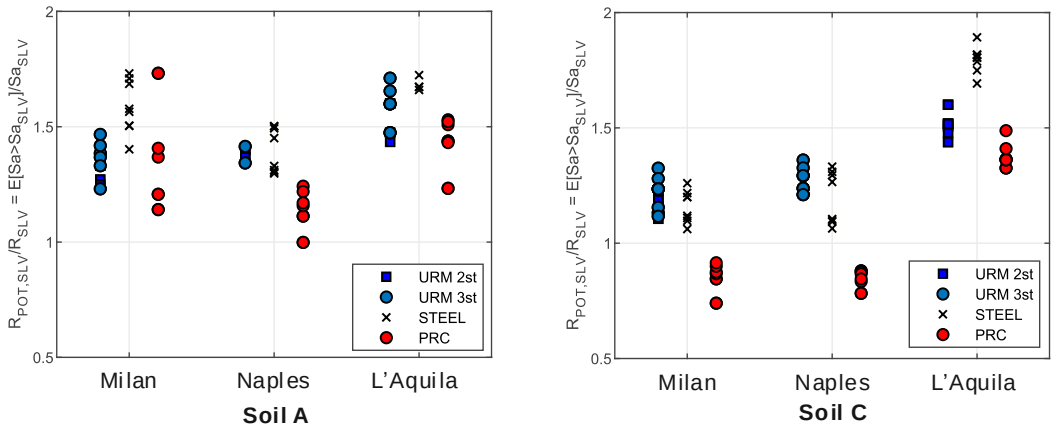

Figure 2-26 Ratios of the expected peak-over-threshold values to the design spectral accelerations (URM, Steel, and PRC buildings); (left) Soil A; (right) Soil C.

2.5 Conclusions

This chapter presented design structural features to explain the inhomogeneity of the collapse risk among the prototype buildings of the RINTC project, designed for several sites with different hazard levels. For the purposes of this investigation, this study exclusively examined some regular buildings belonging a variety of structural types (i.e., URM, RC, steel and PRC buildings) and located at three sites representing low-, mid- and high-hazard in Italy. The 3D structural models of the selected buildings were then converted into the ESDoF systems based on the SPO curves, which were verified through the comparisons of the structural responses obtained during NLDA. Through this approximation, design trends of inelastic capacities, such as strength reduction factors with respect to the design- and beyond-design GM levels and ductility capacity up to structural failure were examined. Notable remarks from this chapter are summarized below:

1. the structural response and collapse of the original 3D structural models were estimated using the calibrated ESDoF models, assuming the collapse criteria defined in a similar or fairly equivalent manner to the original models. In most of the cases, the calibrated ESDoF models provided fair estimates of the structural responses of the original 3D models in terms of the considered EDPs, particularly when the EDP was a global response measure which can be directly converted to an equivalent quantity. Relatively larger discrepancies arose by its nature from the limitations of the ESDoF models and/or the lack of the reference data from the original models.

2. the strength reduction factor for the ESDoFs, tends to increase with an increase of the hazard at the site; conversely, the computed ductility capacity shows a less clear trend with respect to site hazard. This indicates that the trend of strength reduction factor is one of the determining factors leading to the increasing seismic risk with the hazard level at the site. As expected, the computed inelastic capacities significantly varied depending on the structural types and configurations, thus the influences of those indices to the resulting seismic risk have to be further examined in the following chapters.

3. the study also showed that the reduction factor with respect to the expected spectral acceleration given the exceedance of the 475-year design GM intensity level increases with the seismic hazard level at the site. This possibly means the homogeneity of seismic risk across sites with different seismic hazard levels is ascribed not only to the degree of overstrength in the design, but also to local seismicity, which can cause the larger seismic demand relative to structural capacity in the more hazardous site, in case of the occurrence of an extreme earthquake beyond the design.

As expected from a multivariable function of seismic risk, there are other risk contributing factors potentially as significant as the actual design strength. For this issue, a further examination on the influences of the other risk contributing factors will be presented in the following chapters.

References

Altoontash, A., and Deierlein, G. G. [2004] "Simulation and Damage Models for Performance Assessment of Reinforced Concrete Beam-Column Joints," Ph.D. thesis, Stanford University, CA, USA.

Ambraseys, N. N., Simpson, K. A., and Bommer, J. J. [1996] "Prediction of horizontal response spectra in Europe," *Earthq. Eng. Struct. Dyn.*, 25(4), 371–400. DOI:10.1002/(SICI)1096-9845(199604)25:4<371::AID-EQE550>3.0.CO;2-A.

ASCE [2000] Prestandard And Commentary For The Seismic Rehabilitation Of Buildings, Report FEMA-356, Washington, DC, USA.

ASCE [2006] Minimum Design Loads for Buildings and Other Structures, ASCE Standard ASCE/SEI 7-05, including Supplement No. 1, American Society of Civil Engineers, Reston, Virginia, USA.

ATC [1978] Tentative provisions for the development of seismic regulations for buildings, ATC 3-06. National Bureau of Standards, Washington, DC, USA.

Baltzopoulos, G., Baraschino, R., Iervolino, I., and Vamvatsikos, D. [2017] "SPO2FRAG: software for seismic fragility assessment based on static pushover," *Bull. Earthq. Eng.*, 15(10), 4399–4425. DOI:10.1007/s10518-017-0145-3.

Camilletti, D., Cattari, S., Lagomarsino, S., Bonaldo, D., Guidi, G., Bracchi, S., Galasco, A., Magenes, G., Manzini, C. F., Penna, A., and Rota, M. [2017] "RINTC Project: Nonlinear dynamic analyses of Italian code-conforming URM buildings for collapse risk assessment," In *Proc. of 6th ECCOMAS Themat. Conf. Comput. Methods Struct. Dyn. Earthq. Eng.*, 1486–1502, Rhodes, Greece.

Cattari, S., Camilletti, D., Lagomarsino, S., Bracchi, S., Rota, M., Penna, A. [2018] "Masonry Italian code-conforming buildings. Part 2: nonlinear modelling and time-history analysis," *J. Earthq. Eng.*, 22(sup2), 2010-2040. doi:10.1080/13632469.2018.1541030.

CEN [2004] Eurocode 8: Design Provisions for Earthquake Resistance of Structures, Part 1.1: General rules, seismic actions and rules for buildings, EN1998-1.

Chioccarelli, E., Cito, P., Iervolino, I., and Giorgio, M. [2018] "REASSESS V2.0: software for single- and multi-site probabilistic seismic hazard analysis," *Bull. Earthq. Eng.*, 17(4), 1769-1793. DOI:10.1007/s10518-018-00531-x.

Christopoulos, C., Tremblay, R., Kim, H. J., and Lacerte, M. [2008] "Self-centering energy dissipative bracing system for the seismic resistance of structures: development and validation," *J. Struct. Eng.*, 134(1), 96–107. DOI:10.1061/(ASCE)0733-9445(2008)134:1(96).

CNR 10025/98 [2000] Istruzioni per il progetto, l'esecuzione ed il controllo delle strutture prefabbricate in calcestruzzo (in Italian).

CS.LL.PP., Decreto Ministeriale 14 gennaio [2008] Norme tecniche per le costruzioni (in Italian), Gazzetta Ufficiale della Repubblica Italiana, 29, Italy.

CS.LL.PP. [2018] Aggiornamento delle norme tecniche per le costruzioni, Gazzetta Ufficiale della Repubblica Italiana 42. (in Italian.)

De Luca, F., Vamvatsikos, D., and Iervolino, I. [2013] "Near-optimal piecewise linear fits of static pushover capacity curves for equivalent SDOF analysis," *Earthq. Eng. Struct. Dyn.*, 42(4), 523–543. DOI:10.1002/eqe.2225.

Dolšek M, Žižmond J, Kosič M, Lazar Sinković N [2017] Simplified reliability-based verification format, working material for Annex F to revised EN 1998-1. University of Ljubljana, Ljubljana.

Fajfar, P. [2000] "A nonlinear analysis method for performance-based seismic design," *Earthq. Spectra*, 16(3), 573–592. DOI:10.1193/1.1586128.

FEMA [2004] NEHRP Recommended Provisions for Seismic Regulations for New Buildings and Other Structures, FEMA 450-1/2003 Edition, Part 1: Provisions, Federal Emergency Management Agency, Washington, DC, USA.

FEMA [2009] Quantification of Building Seismic Performance Factors, FEMA P-695, Federal Emergency Management Agency, Washington. DC, USA.

FEMA [2013] Recommended Seismic Design Criteria For New Steel Moment-Frame Buildings: FEMA 350, Federal Emergency Management Agency, Washington, DC, USA.

Franchin, P., Ragni, L., Rota, M., and Zona, A. [2018] "Modelling uncertainties of Italian code-conforming structures for the purpose of seismic response analysis," *J. Earthq. Eng.*, 22(sup2), 1964-1989. DOI:10.1080/13632469.2018.1527262.

Hsiao, P., Lehman, D. E., and Roeder, C. W. [2013] "Evaluation of the response modification coefficient and collapse potential of special concentrically braced frames," *Earthq. Eng. Struct. Dyn.*, 42(10), 1547–1564. DOI:10.1002/eqe.2286.

Ibarra, L. F., Medina, R. A., and Krawinkler, H. [2005] "Hysteretic models that incorporate strength and stiffness deterioration," *Earthq. Eng. Struct. Dyn.*, 34(12), 1489–1511.

DOI:10.1002/eqe.495.

Iervolino, I., Giorgio, M., and Cito, P. [2018] "The peak over the design threshold in strong earthquakes," *Bull. Earthq. Eng.*, 17(3), 1145-1161.

Iervolino, I., Spillatura, A., Bazzurro, P. [2017] "RINTC Project: Assessing the (Implicit) Seismic Risk of Code-Conforming Structures In Italy," In Proc. of 6*th ECCOMAS Themat. Conf. Comput. Methods Struct. Dyn. Earthq. Eng.*, pp.1545–1557, Rhodes, Greece. DOI:10.7712/120117.5512.17282.

Iervolino, I., Spillatura, A., Bazzurro, P. [2018] "Seismic reliability of code-conforming Italian buildings," *J. Earthq. Eng.*, 22(sup2), 5–27. DOI:10.1080/13632469.2018.1540372.

Kohrangi, M., Vamvatsikos, D., and Bazzurro, P. [2017] "Site dependence and record selection schemes for building fragility and regional loss assessment," *Earthq. Eng. Struct. Dyn.*, 46(10), 1625–1643.

Lagomarsino, S., Penna, A., Galasco, A., Cattari, S. [2013] "TREMURI program: An equivalent frame model for the nonlinear seismic analysis of masonry buildings," *Eng. Struct.*, 56, 1787–1799. DOI:10.1016/j.engstruct.2013.08.002.

Lin, T., Haselton, C. B., and Baker, J. W. [2013] "Conditional spectrum-based ground motion selection. Part I: Hazard consistency for risk-based assessments," *Earthq. Eng. Struct. Dyn.*, 42(12), 1847–1865.

Magliulo, G., Bellotti, D., Cimmino, M. and Nascimbene, R. [2018] "Modeling and seismic response analysis of RC precast Italian code-conforming buildings," *J. Earthq. Eng.*, 22(sup2), 140-167, doi:10.1080/13632469.2018.1531093.

Manzini, C. F., Magenes, G., Penna, A., Rota, M., Camilletti, D., Cattari, S., Lagomarsino, S., Da Porto, F. [2018] "Masonry Italian code-conforming buildings: Part 1: case studies and design methods," *J. Earthq. Eng.*, 22(sup2):54-73. doi:10.1080/13632469.2018.1532358.

McKenna, F., Fenves, G. L., Scott, M. H., and Jeremic, B. [2000] Open System for Earthquake Engineering Simulation (OpenSees), Pacific Earthquake Engineering Research Center, University of California, Berkeley, CA, USA: http://opensees.berkeley.edu/; accessed on June 2019.

Ricci, P.; Manfredi, V., Noto, F., Terrenzi, M., Petrone, C., Celano, F., De Risi, M. T., Camata, G., Franchin, P., Magliulo, G., Masi, A., Mollaioli, F., Spacone, E., Verderame, G. M. [2018] "Modeling and seismic response analysis of Italian code-conforming reinforced concrete buildings," *J. Earthq. Eng.*, 22(sup2), 105-139.

doi:10.1080/13632469.2018.1527733.

RINTC-Workgroup [2018] Results of The 2015-2017 Implicit Seismic Risk Of Code-Conforming Structures In Italy (RINTC) Project. ReLUIS Report, Rete Dei Laboratori Universitari Di Ingegneria Sismica (ReLUIS), Naples, Italy.

Scozzese, F., Terracciano, G., Zona, A., Della Corte, G., Dall'Asta, A., Landolfo, R. [2018] "Modelling and seismic response analysis of Italian code-conforming single-storey steel buildings," *J. Earthq. Eng.*, 22(sup2):2104-2133. doi:10.1080/13632469.2018.1528913.

Shome, N., Cornell, A. C. [2000] "Structural seismic demand analysis: Consideration of "Collapse"," In Proc. of *PMC2000 - 8th ASCE Specialty Conference on Probabilistic Mechanics and Structural Reliability*. University of Notre Dame, South Bend, Indiana, USA, 24-26 July 2000.

Stucchi, M., Meletti, C., Montaldo, V., Crowley, H., Calvi, G. M., and Boschi, E. [2011] "Seismic hazard assessment (2003-2009) for the Italian building code," *Bull. Seismol. Soc. Am.*, 101(4), 1885–1911. DOI:10.1785/0120100130.

Tremblay, R., Lacerte, M., and Christopoulos, C. [2008] "Seismic response of multistory buildings with self-centering energy dissipative steel braces," *J. Struct. Eng.*, 134(1), 108–120. DOI:10.1061/ASCE0733-94452008134:1108.

Vamvatsikos, D., and Cornell, A. C. [2006] "Direct estimation of the seismic demand and capacity of oscillators with multi-linear static pushovers through IDA," *Earthq. Eng. Struct. Dyn.*, 35(9), 1097–1117. DOI:10.1002/eqe.573.

Chapter 3

Structure-site-specific fragility assessment of code-conforming buildings in Italy

Abstract

This chapter presents and discusses seismic fragility functions of code-conforming buildings in Italy. The structures under consideration are taken from those considered by a large Italian research project (RINTC), aiming at evaluating the seismic reliability of new-design buildings. Design refers to a variety of structural typologies (i.e., un-reinforced masonry, reinforced concrete, steel, and precast concrete buildings) and configurations (e.g., number of stories, floor plan, and the presence of infills), as well as to sites with different hazard levels and local site conditions. The main goal of the study presented in this chapter is to assess global collapse fragility of the code-conforming structures. The collapse fragility of the structures is evaluated via multiple-stripe nonlinear dynamic analysis using the equivalent-single-degree-of-freedom (ESDoF) systems calibrated based on pushover analysis of the three-dimensional structural models. This chapter primarily provides fragility curves for the buildings located at high-hazard sites and discusses the issues that significantly affect the collapse fragility assessment for low-to-mid hazard sites. The derived fragility functions are validated through comparisons with the original detailed models in terms of the estimated parameters and the resulting failure rates, when available. This chapter supplements the usability-preventing damage fragility functions as well, which are estimated from the structural responses of the original structural models analyzed in the RINTC project. The results of the estimated fragility functions confirmed that the buildings tend to be exposed to larger seismic risk at the sites with higher seismicity, which is one of the main outcomes of the RINTC project.

Keywords: *performance-based earthquake engineering; seismic risk; vulnerability.*

3.1 Introduction

There is a variety of procedures to derive fragility functions such as post-earthquake damage observations, numerical structural analysis, or expert judgement. Analytical approaches, in particular, have been developed in the last decades to help when viable data from real earthquake damage are unavailable or insufficient; e.g., [Pitilakis et al., 2014]. They can be broadly classified into two subclasses depending on whether they are based on nonlinear static or dynamic analyses. The former approach involves the characterization of a static capacity curve (i.e., a force-displacement relationship for the structure) via nonlinear static analysis and its comparison with a demand curve; i.e., Capacity Spectrum Method or so-called HAZUS methodology, e.g., [HAZUS-MH, 2003]. The latter characterizes the ground-motion versus seismic demand relationship via time-history response analysis using GM recordings, which allows to directly account for *record-to-record variability* of the structural response; e.g., [Rota et al., 2010]. A hybrid approach is also often applied, that is characterizing the static capacity curve via pushover analysis, then carrying out dynamic analysis with an equivalent single-degree-of-freedom (ESDoF) system; e.g., [D'ayala et al., 2014]. This combination has the advantage, especially when examining a large number of structures, of including the uncertainty of structural dynamic response with manageable computational demand.

The main goal of the study presented in this chapter is to derive seismic fragility curves for the selected prototype buildings studied in the RINTC project. In line with the scope of the project, seismic fragility is examined via nonlinear dynamic analysis (NLDA) with respect to global collapse and usability-preventing damage performance levels. The fragility functions are fitted through a maximum likelihood criterion utilizing structural response given spectral acceleration at a period close to the fundamental vibration periods of the corresponding structure. As regards collapse fragility, the study mainly provides fragility curves for the buildings located at high-hazard sites, which are estimated using the EDoFs' structural response obtained in Chapter 2, i.e., via multiple-stripe analysis (MSA) using hazard-consistent GM record sets. For the structures designed for the low-to-mid seismicity sites, some significant issues, related to the GM intensity causing failure, are addressed, as well as discussing the

resulting fragility functions. For all considered cases, the annual failure rates derived from the obtained seismic fragility curves are also compared with those of the original 3D models. The chapter also provides the usability-preventing damage fragility, which are estimated in the same approach but from the structural responses of the original structural models analyzed in the RINTC project.

The remainder of the chapter is structured such that the next section describes the adopted fragility assessment approach, specifying the structural models, failure criteria with respect to global collapse and usability-preventing damage, and fragility fitting method. The following section first presents the estimated collapse fragility parameters for the high and low-to-mid seismicity sites individually, which are validated through the comparison of the annual failure rates with the original 3D models. Particularly referring to the low-to-mid seismicity sites, the issues related to the low-to-mid hazard sites are described highlighting the sensitivity of the resulting fragility on the GM record selection. Furthermore, the usability-preventing fragility functions are provided as supplemental results of the RINTC project. A summary with final remarks closes the chapter.

3.2 Fragility assessment scheme

3.2.1 Structural models

Among the buildings designed in the RINTC project, this study exclusively examined some regular buildings specified in Chapter 2, i.e., belonging to four different structural types considered in the project (i.e., URM, RC, steel, and PRC buildings) and located at the three sites representing low-, mid- and high-hazard in Italy (i.e., Milan, Naples, and L'Aquila, hereafter denoted as MI, NA, AQ, respectively; on the two soil conditions A and C).

Their ESDoF systems, calibrated based on the pushover analysis of the 3D structural models, were used to develop structure-site-specific fragility curves with respect to the attainment of structural collapse, for reasons related to computability of seismic response at large GM intensity levels. With respect to the onset of usability-preventing damage, on the other hand, the structural response measures obtained from the original 3D models were used because

the local structural responses are more critical in this case. All structural models, both the ESDoFs and the originals, were constructed with OpenSees [McKenna et al., 2000] except the original structural models of the URM buildings for which TREMURI [Lagomarsino et al., 2013] was adopted. All in all, the number of the examined building-site combinations amounts to one-hundred-six (i.e., 31 URM, 27 RC, 24 steel, 24 PRC), for each of which two fragility curves with respect to usability-preventing damage onset and collapse limit states are provided herein. For the structural properties of the ESDoF systems examined for collapse fragility and those of the original 3D models providing damage-onset fragility, see the preceding chapter and [RINTC-Workgroup, 2018], respectively.

3.2.2 Failure criteria for the prototype buildings

In line with the RINTC project, the failure criteria for the fragility assessment were defined in a uniform manner among the structures belonging to the same typology, considering the structural characteristics of the four different structural types under consideration (URM, RC, steel, PRC). The following briefly summarizes the collapse criteria for the equivalent models defined consistently (or in a fairly equivalent manner) to the original 3D models, which were already discussed per typology in Chapter 2, as well as introducing the damage-onset criteria applied to the original 3D structural models.

3.2.2.1 Collapse limit states for the equivalent models

As illustrated in the left panel of Figure 3-1, the collapse criteria for the original 3D structural models were in general defined based on the deformation capacity corresponding to a certain level of strength deterioration, i.e., 50% of the maximum base-shear on the SPO curves of the structures for each horizontal direction. Accordingly, the same criteria were adopted for the equivalent models if the corresponding EDP was a global response measure. Otherwise an alternative or equivalent global EDP that can indicate the attainment of the considered local collapse condition was introduced. The former is the cases of the URM and RC, PRC buildings, however, there are some exceptions, adjustments, or additional considerations required for some structural typologies. The following briefly recalls the collapse criteria for the structural

types for which some adjustments or considerations on the global quantities were required (i.e., URM, steel, and PRC). For the detailed descriptions and the consistency with the original structural models; see Chapter 2.

***URM*:** For each of the original 3D structural models of the URM buildings, the collapse criteria were defined based on the maximum inter-story-drift ratio (IDR) of single-wall elements corresponding to a 50% drop of the maximum base-shear from pushover analysis. Assuming that the roof drift ratio (RDR) at that displacement is approximately equal to the maximum IDR measured in the original 3D models, the structural collapse for each ESDoF system was defined as the attainment of the displacement corresponding to a 50% drop of the maximum base-shear from pushover analysis.

Steel: Since the prototype steel buildings have different load-resisting systems in two horizontal directions, the collapse criteria of the RINTC project were originally defined individually for each direction: 10% IDR was selected for the direction with the moment-resisting frame (MRF) system, whereas the collapse in the concentrically braced frame (CBF) system corresponds to the attainment of the maximum strain range, defined as the difference between minimum and maximum strain responses measured at the cross sections of brace members, equal to 4.9%. Among the examined global quantities that can possibly indicate the local collapse condition in brace members (see the discussion in Section 2.3.1.3), 2.0% transient IDR suggested by FEMA 356 [ASCE, 2000] for the collapse prevention performance level of braced steel frames was considered for deriving the fragility functions because of the best estimates of the D/C ratios measured in dynamic analysis (Figure 2-13f).

PRC: Particularly to this structural type, the original detailed structural models accounted for a local collapse condition corresponding to the attainment of the maximum shear strength of the beam-column connections in addition to the aforementioned general collapse condition. In a similar manner, the ESDoF models refer to the shear strength ratio of the maximum base-shear recorded in dynamic analysis and connection shear capacity reported in [Magliulo et al., 2018] as an alternative response measure (Figure 2-13h,i).

3.2.2.2 Usability-preventing damage limit states for the original 3D structural models

The damage-onset criteria were defined based on a multi-criteria approach, considering the minimum displacement under multiple conditions that can jeopardize the building occupancy after a seismic event. As illustrated in Figure 3-1b, the damage conditions considered are: (a) a light-widespread damage condition corresponding to minor damage in 50% of the main non-structural elements; (b) a severe damage condition with at least one of non-structural elements reached a severe damage level leading to significant interruption of use; and (c) the attainment of a certain resistance level (e.g., 95% of the maximum base-shear of the structure). Remarks on each structural type are provided in the following. See [RINTC-Workgroup, 2018] for further details.

URM: The damage-onset criteria were defined considering the following conditions: (a) a light-widespread damage condition where more than 50% of masonry walls attained the maximum lateral strength in each main direction; (b) at least one of masonry walls reached the drift limit corresponding to a certain level of strength deterioration (e.g., a 40% drop for shear failure); and (c) the attainment of 95% strength of the maximum base-shear of the structure. It should be noted that, in cases of the URM buildings, the final threshold should be associated to a value of the base shear not lower than 85% of the peak resistance.

RC: The following conditions were defined as the damage-onset criteria for the IF/PF of the RC buildings: (a) light-widespread damage in 50% of masonry infills and partitions; (b) at least one of masonry infills and partitions reached 50% strength drop from its maximum resistance; and (c) the attainment of 95% strength of the maximum base-shear of the structure. For BFs without infills, the RDR threshold was constantly set to 0.05%.

Steel: The onset of usability-preventing damage was considered to have been reached when one of the following conditions was met: (a) light-widespread damage in 50% of sandwich panels in each horizontal direction, i.e., yielding in panel-to-frame connections; (b) at least one of panel-to-frame connections reached its maximum strength; or (c) the attainment of 95% strength of the maximum base-shear of the structure.

PRC: the damage-onset multi-criteria for PRC buildings were defined as follows: (a)

light-widespread damage corresponding to the attainment of 50% of the maximum shear strength in the panel-structure connection (i.e., at the yielding of the bolts or nuts); (b) at least one of cladding panels reached the maximum strength of the panel-structure connection, i.e., failure of the bolt or opening of the channel lips. The general condition (c) above was not applied for this structural type because the collapse in panel-structure connections occurs much earlier than the onset of strength deterioration.

A summary of the failure criteria considered in this study is provided in Table 3-1.

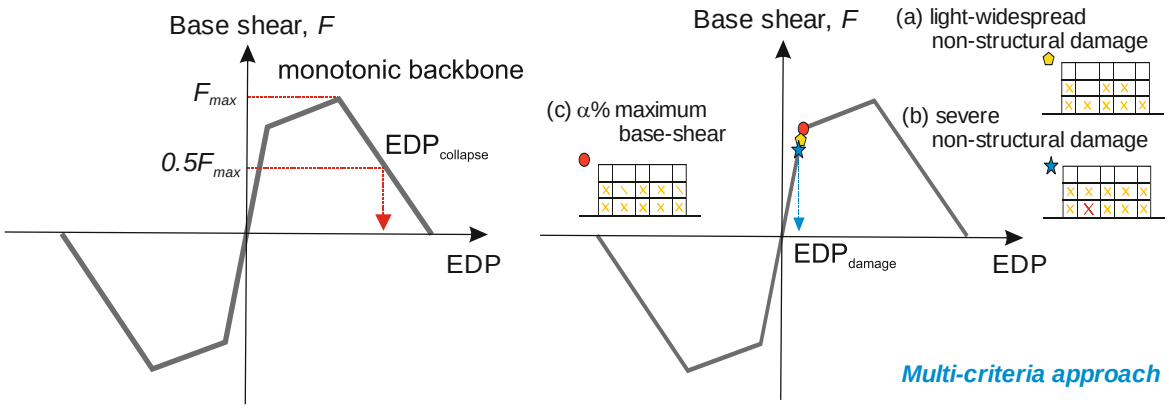

Figure 3-1 General definitions of failure criteria (RC, URM, PRC); (left) with respect to collapse; (right) with respect to usability-preventing damage onset.

Table 3-1 Summary of the adopted failure criteria for fragility estimation.

	Performance levels		
Structural type	**Usability-preventing damage (3D models)**		**Global collapse (ESDoF models)**
	Multiple criteria	**main non-structural components**	**Criteria**
URM	(a) light-widespread damage in main non-structural components (b) severe damage in at least one of main non-structural components (c) strength reduction from the maximum resistance (except PRC)	masonry walls	RDR corresponding to a 50% drop from the maximum resistance
RC		masonry infills	
Steel		sandwich panels panel-to-frame connections	X: 10% IDR (RDR) Y: 2% IDR (RDR)
PRC		panel-to-structure connections	(d) RDR corresponding to a 50% drop from the maximum resistance (e) maximum beam-column connection resistance [Magliulo et al., 2018]

3.2.3 Probabilistic structural response analysis

In this study, the fragility function parameters were estimated using the structural response given $Sa(T)$ obtained through MSA (in Chapter 2.3.2). Among the estimation methods introduced in Chapter 1, this study adopted the EDP-based parametric approach estimating lognormal fragility parameters via maximum likelihood estimation criterion via Eq. (3-1). Though the equation is merely an extension of Eq. (1-15) to spectral acceleration-based IMs, it is worth recalling the formulation that is the framing equation of this chapter. In the equation, the median and logarithmic standard deviation of IM, that is, $Sa(T)$, are denoted as $\left\{\hat{\theta}_{Sa(T)}, \hat{\beta}_{Sa(T)}\right\}$.

$$P\left[F \middle| Sa(T) = sa\right] = \Phi\left(\frac{\ln sa - \ln \hat{\theta}_{Sa(T)}}{\hat{\beta}_{Sa(T)}}\right) \tag{3-1}$$

where $\left\{\hat{\theta}_{Sa(T)}, \hat{\beta}_{Sa(T)}\right\}$

$$= \underset{\hat{\theta}_{Sa(T)}, \hat{\beta}_{Sa(T)}}{\arg\max}\left[\sum_{i=1}^{m} \ln\binom{N_{tot,i}}{N_{f,i}} + N_{f,i} \ln\left\{\Phi\left[\frac{\ln\left(sa_i/\theta_{Sa(T)}\right)}{\beta_{Sa(T)}}\right]\right\} + \left(N_{tot,i} - N_{f,i}\right) \cdot \ln\left\{1 - \Phi\left[\frac{\ln\left(sa_i/\theta_{Sa(T)}\right)}{\beta_{Sa(T)}}\right]\right\}\right]$$

As discussed in Section 2.3.2, MSA was performed at the ten discrete levels of spectral acceleration at one of the following five discrete periods, $T = \{0.15\text{s}, 0.5\text{s}, 1.0\text{s}, 1.5\text{s}, 2.0\text{s}\}$, of which the closest to the fundamental vibration periods of the corresponding structure was considered. For each IM level, 20 records were selected consistently to the hazard disaggregation given the occurrence of the corresponding IM level for the site of interest, i.e., $N_{tot,i} = 20$. For further details of the methodology and the MSA results of the examined structures, see Chapter 1 and Chapter 2, respectively.

Figure 3-2 shows an example of the described EDP-based fragility fitting using the MSA results (i.e., AQ soil C, URM 2st C3). Identifying the number of failure cases observed in MSA at each of the ten IMLs ($N_{f,i}$ in the left panel), the failure probabilities computed as the fractions of the failure cases, $N_{f,i}/N_{tot,i}$ (denoted with the triangle scatters in the right panel), are thoroughly fitted by a lognormal CDF (denoted with the red solid line in the right) via Eq. (3-1).

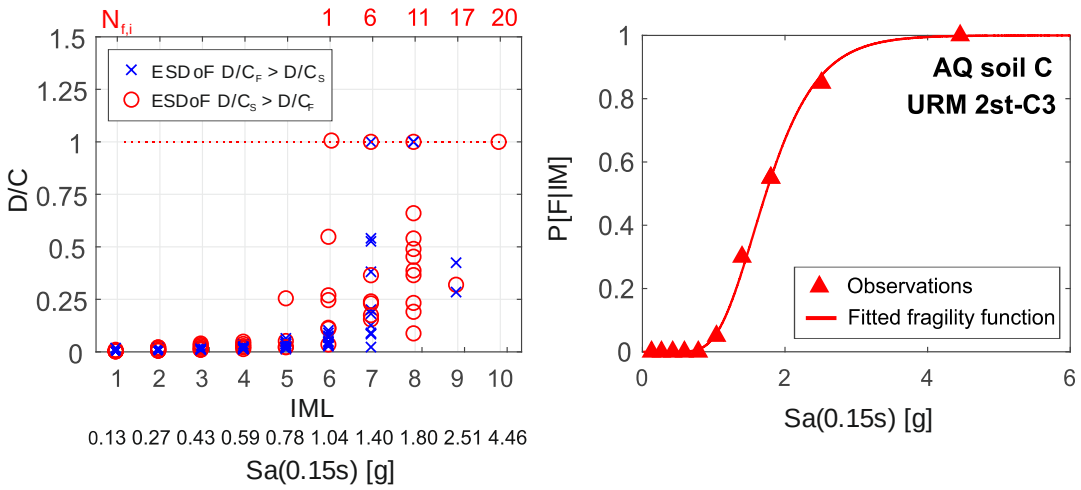

Figure 3-2 Example of EDP-based fragility fitting using MSA results for URM 2st C3 at AQ on soil C; (a) measured D/C ratios at multiple levels of $Sa(0.15s)$, the GM records causing $D/C \geq 1$ are counted as the number of failure cases $N_{f,i}$ (b) observed fractions of failure as a function of IM and the estimated fragility function with Eq. (3-1).

3.3 Collapse fragility estimation

3.3.1 Collapse fragility curves for high hazard sites

This section presents the seismic fragility functions of the case study buildings derived for the most hazardous site, i.e., AQ, using the structural EDP responses obtained from MSA of the ESDoF systems. The derived fragility curves were also compared with those from the original 3D structural models at the end of this section. For relevant scientific issues related to the fragility derivation (to follow), fragilities for the structures at the low- and mid-hazard sites are not discussed herein.

3.3.1.1 Results of URM buildings

The fragility functions for the URM buildings were estimated as a function of $Sa(0.15s)$ for all building cases. The presented fragility functions assume the worst damage case (i.e., the larger value of the D/C ratios) of the flexure- and shear-dominated hysteresis models, which mimic the structural response of the original detailed models (Figure 2-11). The estimated fragility function parameters are summarized in Table 3-2, which compares the results from the

ESDoF systems with those from the original 3D models. In agreement with the discussion given in Section 2.3.2, the ESDoF systems show lower values of the median spectral acceleration causing structural failure, that is $\hat{\theta}_{Sa(T)}$, than the original 3D models, especially for the buildings with the E-type configuration where the error ranges between 24-60%. The same type of error for the C type configuration is between 1-6%. The estimated values of $\hat{\beta}_{Sa(T)}$ are in the range between approximately 0.25–0.50, for both the two modelling approaches.

3.3.1.2 Results of RC buildings

The fragility functions for the RC buildings were estimated as a function of spectral acceleration at the conditioning period varying for each configuration (i.e., number of stories, with or without infills). The estimated fragility function parameters and the considered IMs are provided in Table 3-3. It should be noted that, for some RC buildings (whose results are denoted in italic in the table), the failure probability given the IML corresponding to the maximum return period, i.e., $T_R = 10^5$ years, resulted to be smaller than 50%, leading to the fitted parameters only governed by the failure observations at the smaller IMLs, i.e., $P\left[F \mid Sa(T) = sa_{T_R=10^5} \right] < 0.50$. In such cases, the fragility parameters were *re-estimated* by performing some additional analyses up to $Sa(T) = sa$, $sa > sa_{T_R=10^5}$, at which the failure probability had exceeded $P\left[F \mid Sa(T) = sa \right] > 0.9$, using the same GM set for the tenth IML (denoted as 10^+IML in the table; the past study on the efficient strategies for fragility function fitting in [Baker, 2015] recommends, when the number of stripes is limited, to run the analysis up to IMLs corresponding to probabilities of 0.7 and 0.9, for estimating median and standard deviation parameters, respectively; herein the larger between these values was considered to re-estimate sets of fragility parameters). Nonetheless, the results show that the fragility parameters from the ESDoFs have the maximum error of 25% in $\hat{\theta}_{Sa(T)}$ (excluding the cases in italic) with respect to those obtained from the original models. The values of $\hat{\beta}_{Sa(T)}$ vary approximately from 0.3 to 0.7.

3.3.1.3 Results of steel buildings

Table 3-4 shows the fragility function parameters for the steel buildings, which were estimated

as a function of $Sa(0.5s)$ and $Sa(1.0s)$ for the Geo 1-2 and Geo 3-4 buildings, respectively, given the FEMA 356 criterion [ASCE, 2000] for the CBF systems. It is observed that, in most cases, the $\hat{\theta}_{Sa(T)}$ values differ by 2-26% with respect to the 3D models.

For Geo 3,4 on soil A, the failure probability conditional to the largest investigated IML did not exceed 50%, thus the parameters were re-estimated as described. For Geo 3,4 on soil C, the fragility resulted to be very steep because the lower IMs, at which failures are not observed, are abruptly separated from the higher IMs where failure is almost certain, according to the response sample. The parameters for such cases were re-estimated including the sample additionally obtained at the intermediate IMs using the GM set for the closet IML. In both cases re-estimated parameters showed the similar median but larger $\hat{\beta}_{Sa(T)}$ values.

Excluding such special cases, the values of $\hat{\beta}_{Sa(T)}$ from the ESDoFs with the equivalent global EDPs were all around 0.30, generally smaller than the results from the 3D models using the local strain-based failure criterion.

3.3.1.4 Results of PRC buildings

The fragility functions parameters for the PRC buildings were estimated as a function of $Sa(2.0s)$ and are given in Table 3-5 for both the displacement-based and connection-shear-based global collapse conditions. In most cases, the collapse fragility curves associated with the two different EDPs showed similar trends due to the proximity of the EDP thresholds on the pushover curves, yet the local collapse mechanism appeared still more critical. It should be noted that most of the cases required to re-estimate the parameters as the initial ones were governed by the failure observations at the smaller IMLs (see the previous section), though it didn't significantly affect the median trend. The ESDoF-based estimates of fragility parameters show good consistency with the original models except ones associated with the connection collapse for Geo 1,2 because of the difference in mass assumption. The range of $\hat{\theta}_{Sa(T)}$ is approximately 0.70-1.20 for both the collapse conditions. With respect to $\hat{\beta}_{Sa(T)}$, the re-estimated values range from 0.2 to 0.4.

Table 3-2 Collapse fragility function parameters for the URM buildings (soil A and C).

$IM = Sa(0.15s)$	**Site**	**AQ soil A**						**AQ soil C**		
Model	**Config.**	**C1 2st**	**C1 3st**	**E2 2st**	**E2 3st**	**E8 3st**	**C3 2st**	**E2 2st**	**E8 2st**	**E9 2st**
3D model	$\hat{\theta}_{Sa(T)}$ [g]	1.44	1.32	2.04	1.52	1.64	1.68	1.80	1.84	1.34
	$\hat{\beta}_{Sa(T)}$	0.41	0.51	0.48	0.48	0.42	0.24	0.32	0.33	0.38
ESDoF	$\hat{\theta}_{Sa(T)}$ [g]	1.52	1.31	2.55	1.88	2.26	1.73	2.44	2.32	2.14
	$\hat{\beta}_{Sa(T)}$	0.40	0.44	0.50	0.51	0.52	0.33	0.34	0.37	0.30

Table 3-3 Collapse fragility function parameters for the RC buildings (soil C).

Model	**Story**	**3st**			**6st**			**9st**		
	Config.	**BF**	**IF**	**PF**	**BF**	**IF**	**PF**	**BF**	**IF**	**PF**
	IM	$Sa(1.0s)$	$Sa(0.15s)$	$Sa(0.5s)$	$Sa(1.5s)$	$Sa(0.5s)$	$Sa(0.5s)$	$Sa(2.0s)$	$Sa(1.0s)$	$Sa(1.0s)$
3D model	$\hat{\theta}_{Sa(T)}$ [g]	*4.56**	*5.67**	5.84	1.72	4.47	4.57	*1.14**	*3.64**	*3.76**
	$\hat{\beta}_{Sa(T)}$	*0.51**	*0.52**	0.49	0.35	0.67	0.65	*0.62**	*0.72**	*0.71**
ESDoF	$\hat{\theta}_{Sa(T)}$ [g]	3.01	*4.89**	5.44	1.83	5.59	5.59	*1.87**	*3.81**	*3.88**
	$\hat{\beta}_{Sa(T)}$	0.30	*0.44**	0.47	0.33	0.55	0.55	*0.73**	0.61*	0.70*
ESDoF	$\hat{\theta}_{Sa(T)}$ [g]	-	6.88	-	-	-	-	1.56	4.20	4.23
10^{+}IML	$\hat{\beta}_{Sa(T)}$	-	0.73	-	-	-	-	0.47	0.72	0.74

* $P\left[F \mid Sa(T) = sa_{T_R=10^5}\right] < 0.50$

Table 3-4 Collapse fragility function parameters for the steel buildings (soil A and soil C).

Model	IM	Soil A				Soil C			
		$Sa(0.5s)$		$Sa(1.0s)$		$Sa(0.5s)$		$Sa(1.0s)$	
	Config.	Geo 1	Geo2	Geo 3	Geo4	Geo 1	Geo2	Geo 3	Geo4
3D model	$\hat{\theta}_{Sa(T)}$ [g]	3.49	5.08*	2.11	2.34*	3.67	4.47	2.56	2.04
	$\hat{\beta}_{Sa(T)}$	0.42	0.10*	0.37	0.57*	0.52	0.29	0.45	0.39
ESDoF	$\hat{\theta}_{Sa(T)}$ [g]	3.55	3.67	2.14*	2.26*	3.40	3.53	1.90**	1.92**
	$\hat{\beta}_{Sa(T)}$	0.35	0.32	*0.08**	*0.10**	0.32	0.29	*0.06***	*0.06***
ESDoF	$\hat{\theta}_{Sa(T)}$ [g]	-	-	2.19	2.30	-	-	2.09	2.24
10+IML	$\hat{\beta}_{Sa(T)}$	-	-	0.28	0.27	-	-	0.28	0.27

* $P\left[F \mid Sa(T) = sa_{T_R=10^5}\right] < 0.50$; ** the lack of samples at intermediate IMLs where $0 < P\left[F \mid Sa(T) = sa_i\right] < 1$

Table 3-5 Collapse fragility function parameters for the PRC buildings (soil A and soil C).

$IM = Sa(2.0s)$		Site	Soil A				Soil C			
EDP	Model	Config.	Geo 1	Geo2	Geo 3	Geo4	Geo 1	Geo2	Geo 3	Geo4
Disp.	**3D model**	$\hat{\theta}_{Sa(T)}$ [g]	0.69**	0.76*	0.75*	0.76*	1.13*	1.07**	1.18*	1.07**
		$\hat{\beta}_{Sa(T)}$	0.08**	0.09*	0.09*	0.09*	0.09*	0.08**	0.11*	0.08**
	ESDoF	$\hat{\theta}_{Sa(T)}$ [g]	0.67	0.82*	0.75*	0.76*	1.10*	1.12*	1.18*	1.12*
		$\hat{\beta}_{Sa(T)}$	0.33	0.11*	0.09*	0.09*	0.08*	0.09*	0.11*	0.09*
	ESDoF	$\hat{\theta}_{Sa(T)}$ [g]	-	0.93	0.89	0.89	1.03	1.22	1.30	1.20
	10+IML	$\hat{\beta}_{Sa(T)}$	-	0.26	0.29	0.29	0.22	0.17	0.18	0.19
Conn.	**3D model**	$\hat{\theta}_{Sa(T)}$ [g]	0.49*	0.38**	0.75*	0.76*	0.56**	0.56**	1.20*	1.09*
		$\hat{\beta}_{Sa(T)}$	0.24*	0.05**	0.09*	0.09*	0.05**	0.05**	0.11*	0.08*
	ESDoF	$\hat{\theta}_{Sa(T)}$ [g]	0.67	0.74*	0.75*	0.77*	0.79	1.09*	1.12*	1.08*
		$\hat{\beta}_{Sa(T)}$	0.33	0.08*	0.09*	0.09*	0.24	0.08*	0.09*	0.08*
	ESDoF	$\hat{\theta}_{Sa(T)}$ [g]	-	0.80	0.85	0.98	-	1.06	1.18	1.09
	10+IML	$\hat{\beta}_{Sa(T)}$	-	0.21	0.28	0.42	-	0.23	0.15	0.19

* $P\left[F \mid Sa(T) = sa_{T_R=10^5}\right] < 0.50$; ** the lack of samples at intermediate IMLs where $0 < P\left[F \mid Sa(T) = sa_i\right] < 1$

3.3.1.5 Verification of collapse fragility models

This section verifies the fragility models presented above, through the comparisons of the failure rates with the 3D structural models. Since seismic hazard at each site of interest was computed only up to the IM value corresponding to $T_R = 10^5$ year exceedance return period (to avoid a large extrapolation of the hazard), that is $sa_{T_R=10^5}$, the failure rates of the RINTC project were computed with Eq. (3-2). This equation gives a conservative approximation of the *true* rate in Eq. (1-10), assuming $P[F \mid IM = im] = 1$ for larger IMs corresponding to an exceedance return period larger than 10^5 years. $P[F \mid IM = im]$ at each IM level was computed using the measured EDP response (D/C) via Eq. (1-17).

$$\lambda_f = \int_0^{im_{T_R=10^5}} P[F \mid IM = im] \cdot |d\lambda_{im}| + 10^{-5} \tag{3-2}$$

In a similar manner, the failure rates were evaluated also using the fragility functions estimated from the ESDoF systems via Eq. (3-1) and Eq. (3-2), i.e., substituting $P[F \mid Sa(T) = sa_i] = \Phi\left[\ln\left(sa_i / \hat{\theta}_{Sa(T)}\right) \Big/ \hat{\beta}_{Sa(T)}\right]$ where $i = \{1, 2, ..., 10\}$ into Eq. (3-2). The obtained results (using the re-estimated parameters where applicable) are compared in Figure 3-3 with those computed from the original 3D structural models. The results show that, in general, the failure rates computed using the ESDoF models are of the same order of magnitude as those from 3D model's fragilities.

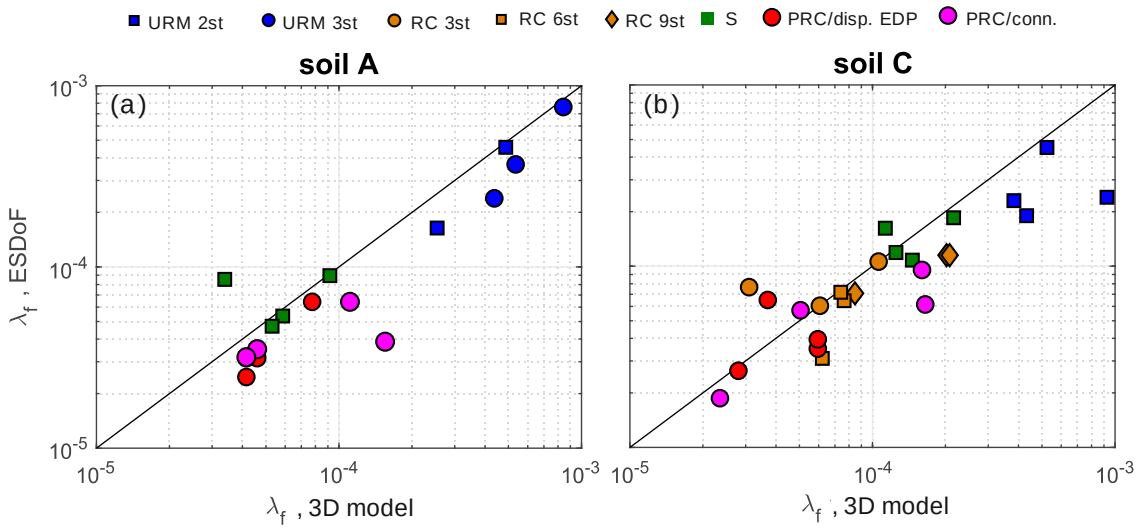

Figure 3-3 Verification of the ESDoF-based fragility models (AQ).

3.3.2 Collapse fragility curves for low-to-mid hazard sites

The issue concerning the structures designed at low-to-mid seismicity sites is there is a lack of failure cases from the dynamic analyses. In fact, it was not possible to obtain fragility curves for the MI and NA sites from the structural response at the investigated IMLs neither from the 3D structural models nor the ESDoF systems. Hence, this section investigates the fragility functions of the structures by performing MSA at additional IMLs utilizing the ESDoF systems. The following first introduces the issues on GM record selection for the additional IMLs, followed by the resulting fragility curves and failure rates.

3.3.2.1 Issues on ground motion record selection

Considering that no or quite few failure cases had been observed up to the largest IML corresponding to $T_R = 10^5$ years, it is expected to perform MSA at additional – much larger in fact – GM intensity levels for deriving fragility functions for the structures designed for the low-to-mid seismicity sites. In order to deepen the effects of selection and scaling of GM records on the resulting seismic fragility and risk, two strategies for GM selection were pursued. The first strategy was (1) to scale the hazard-consistent (CS-based) record sets corresponding to $T_R = 10^5$ up to larger IMLs without any reselection of GM records for the site at hand. The results from this strategy are hereafter referred to as CS-scaled. The second strategy was (2) to use an unique set of twenty GM records representing large seismic events (moment magnitude within 6.5-6.9, recorded on firm soil [Vamvatsikos and Cornell, 2006]; see Appendix) for any further IMLs. The major reason for utilizing this record set (denoted as PEER after the database), even despite the different rupture features from those expected, is the comparability with many studies and applications in the literature, in the context of collapse fragility assessment via incremental dynamic analysis (IDA). Regardless of the GM selection, the analyses were performed until observing failure in more than 90% of the records at the last analyzed IML.

In Figure 3-4a,b the mean GM response spectra of these two cases are compared at the two arbitrarily selected IMLs of $Sa(0.5s)$ corresponding to $T_R = 7.4\times10^4$ and $T_R = 4.4\times10^7$ years for the site NA soil C, as well as with the corresponding conditional mean spectrum (CMS) from PSHA, which should be the target for record selection. For both the

return periods, the mean spectrum (of the maximum horizontal component) of the PEER GM features larger spectral ordinates than the CS-scaled GM set and the target CMS.) Correspondingly, MSA had to be carried out, in the cases of using the CS-based records for some RC structures, up to an IM with 10^8 years – much larger than in cases of using the PEER GM set – for observing failure in more than 90% of records. These differences are expected to be reflected on the estimates of fragility parameters; therefore, the fragility functions estimated using Eq. (3-1) under the two different GM scenarios are discussed herein.[5]

The following presents the fragility functions for the low-to-mid hazard sites, each of which is expressed in terms of the same IM as that used for the corresponding structural type and configuration of the AQ buildings.

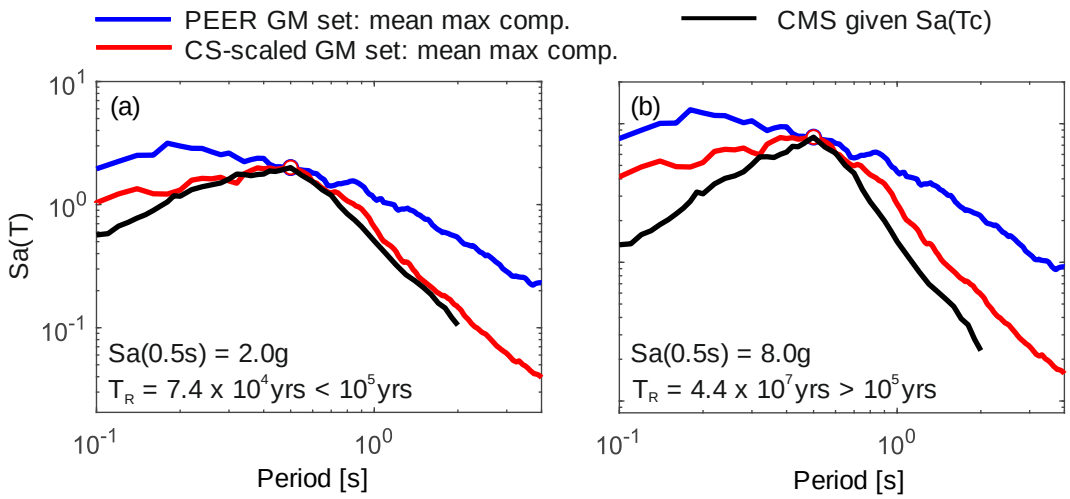

Figure 3-4 Comparisons of the GM response spectra for the mid-hazard site (NA, soil C).

3.3.2.2 Results of URM buildings

Table 3-6 and Table 3-7 provide the fragility functions of the URM buildings located at the sites,

[5] Note that, at the IM level corresponding $T_R = 4.4\times10^7$ years, the scaling factors were quite large; this is inevitable due to the acceleration values to observe a significant number of failures in the buildings designed at the low-to-mid hazard sites. In fact, the average of the scaling factors the CS-based record set was 17, while the average for the PEER GM set was equal to 26. The effects of scaling on structural response is discussed in literature; see for example Luco and Bazzurro [2007], where similar ranges of scaling factors are investigated. However, note that very large accelerations have little impact on the failure rate because of nearly-zero occurrence probability of such large IM levels for these sites, which is to be confirmed in the text.

NA and MI. As expected from the spectral shapes shown in Figure 3-4, the PEER GM set provided the lower estimates of $\hat{\theta}_{Sa(T)}$ than the CS-scaled one for both of the sites (even by 54%). The $\hat{\beta}_{Sa(T)}$ parameter also becomes larger when estimated using the CS-scaled GM set, ranging between 0.40-0.70 under the CS-scaled set and between 0.30-0.50 under the PEER GM set.

3.3.2.3 Results of RC buildings

It is for the RC buildings that the choice of GM records affected most significantly the estimated fragility function parameters (Table 3-8). Especially for some short period structures (e.g., 3st PF, 6st IF/PF), $\hat{\theta}_{Sa(T)}$ from the CS-scaled GM set is more than 60% larger than the corresponding value from the PEER GM set. It is considered that, for the RC frames with the masonry infills, the lateral stiffness changes as damage in the masonry infills progresses, thus the collapse fragility could possibly be more sensitive to the spectral ordinates in the range of vibration periods longer than T^*, as argued by specific literature; e.g., O'Reilly and Sullivan [2018]. The same trend is observed in this group for $\hat{\beta}_{Sa(T)}$.

3.3.2.4 Results of steel buildings

The same trends are observed also for the steel buildings. As summarized in Table 3-9, the difference in $\hat{\theta}_{Sa(T)}$ between the two GM sets varies approximately between 20-40%. The $\hat{\beta}_{Sa(T)}$ parameter ranges between 0.2-0.4. It is peculiar for this structural type that the fragility parameters from the PEER GM set are similar across the sites, which arises from the fact that the site hazard made little difference in the seismic design, as seismic loads were not the design-ruling action.

3.3.2.5 Results of PRC buildings

Table 3-10 summarizes the estimated fragility parameters for the PRC buildings with respect to the collapse conditions based on the two different EDPs. It should be noted that, as reported in Magliulo et al., [2018], the maximum connection shear capacities of the Geo 3 and/or 4 buildings for the sites NA and MI are attained within the elastic branch of the pushover curve

due to the low design demand for the sites, thus resulting in $\hat{\theta}_{Sa(T)} < 0.20g$. Compared to the other structural types, the choice of the GM sets did not apparently affect the resulting fragility parameters presumably because of the GM scaling at a relatively longer conditioning period.

Table 3-6 Collapse fragility function parameters for the URM buildings (NA).

$IM = Sa(0.15s)$	Site	NA soil A			NA soil C					
GM type	**Config.**	**C3 2st**	**C4 3st**	**E8 2st**	**C1 2st**	**C4 2st**	**C3 3st**	**C5 3st**	**E2 3st**	**E8 3st**
CS-scaled	$\hat{\theta}_{Sa(T)}$ [g]	2.53	1.96	3.96	2.44	2.69	2.01	2.10	4.29	4.91
	$\hat{\beta}_{Sa(T)}$	0.50	0.51	0.62	0.47	0.46	0.40	0.43	0.69	0.61
PEER	$\hat{\theta}_{Sa(T)}$ [g]	1.91	1.53	2.61	1.68	1.88	1.48	1.53	2.12	2.27
	$\hat{\beta}_{Sa(T)}$	0.35	0.34	0.46	0.37	0.34	0.34	0.33	0.44	0.47

Table 3-7 Collapse fragility function parameters for the URM buildings (MI).

$IM = Sa(0.15s)$	Site	MI soil A						MI soil C						
GM type	**Config.**	**C3 2st**	**C4 2st**	**C2 3st**	**C6 3st**	**E2 2st**	**E2 3st**	**C1 2st**	**C7 2st**	**C2 3st**	**E2 2st**	**E2 3st**	**E8 3st**	**E9 3st**
CS-scaled	$\hat{\theta}_{Sa(T)}$ [g]	2.04	2.30	1.86	1.92	4.28	3.64	2.41	2.60	2.14	4.78	4.08	4.35	1.95
	$\hat{\beta}_{Sa(T)}$	0.40	0.36	0.42	0.36	0.56	0.62	0.44	0.39	0.49	0.61	0.59	0.68	0.40
PEER	$\hat{\theta}_{Sa(T)}$ [g]	1.68	1.88	1.57	1.58	2.63	2.12	1.68	1.89	1.57	2.62	2.12	2.27	1.67
	$\hat{\beta}_{Sa(T)}$	0.37	0.34	0.38	0.36	0.44	0.44	0.37	0.35	0.38	0.44	0.44	0.47	0.30

Table 3-8 Collapse fragility function parameters for the RC buildings (NA and MI, soil C).

Site	**GM type**	**Story Config.**	**3st**			**6st**			**9st**		
			BF	**IF**	**PF**	**BF**	**IF**	**PF**	**BF**	**IF**	**PF**
		IM	$Sa(1.0s)$	$Sa(0.15s)$	$Sa(0.5s)$	$Sa(1.5s)$	$Sa(0.5s)$	$Sa(0.5s)$	$Sa(2.0s)$	$Sa(1.0s)$	$Sa(1.0s)$
NA	**CS-scaled**	$\hat{\theta}_{Sa(T)}$ [g]	2.66	11.7	5.64	2.08	9.75	10.7	1.14	2.42	2.23
		$\hat{\beta}_{Sa(T)}$	0.22	0.84	0.50	0.31	0.54	0.55	0.24	0.25	0.25
	PEER	$\hat{\theta}_{Sa(T)}$ [g]	1.58	3.17	2.78	1.41	3.94	4.09	0.97	1.30	1.30
		$\hat{\beta}_{Sa(T)}$	0.39	0.46	0.37	0.36	0.41	0.49	0.06	0.45	0.53
MI	**CS-scaled**	$\hat{\theta}_{Sa(T)}$ [g]	2.72	5.08	4.93	2.21	5.58	6.47	1.78	5.09	4.38
		$\hat{\beta}_{Sa(T)}$	0.44	0.55	0.69	0.33	0.69	0.65	0.35	0.40	0.37
	PEER	$\hat{\theta}_{Sa(T)}$ [g]	1.30	2.39	1.93	1.00	1.89	1.88	0.85	1.81	1.41
		$\hat{\beta}_{Sa(T)}$	0.40	0.48	0.35	0.33	0.34	0.44	0.29	0.54	0.60

Table 3-9 Collapse fragility function parameters for the steel buildings (NA and MI, soil C).

		Soil A				Soil C			
Site	**IM**	$Sa(0.5s)$		$Sa(1.0s)$		$Sa(0.5s)$		$Sa(1.0s)$	
/GM type	**Config.**	**Geo 1**	**Geo2**	**Geo 3**	**Geo4**	**Geo 1**	**Geo2**	**Geo 3**	**Geo4**
NA	$\hat{\theta}_{Sa(T)}$ [g]	4.10	4.13	2.20	2.39	4.00	4.09	2.51	2.74
/CS-scaled	$\hat{\beta}_{Sa(T)}$	0.45	0.40	0.22	0.24	0.39	0.36	0.34	0.35
NA	$\hat{\theta}_{Sa(T)}$ [g]	3.02	3.16	1.82	1.91	3.02	3.16	1.82	1.91
/PEER	$\hat{\beta}_{Sa(T)}$	0.27	0.25	0.38	0.30	0.27	0.25	0.38	0.30
MI	$\hat{\theta}_{Sa(T)}$ [g]	4.49	4.59	2.36	2.49	4.51	4.58	2.95	3.08
/CS-scaled	$\hat{\beta}_{Sa(T)}$	0.37	0.36	0.24	0.25	0.36	0.35	0.39	0.31
MI	$\hat{\theta}_{Sa(T)}$ [g]	3.02	3.16	1.82	1.90	3.02	3.16	1.82	1.90
/PEER	$\hat{\beta}_{Sa(T)}$	0.27	0.25	0.38	0.30	0.27	0.25	0.38	0.30

Table 3-10 Collapse fragility function parameters for the PRC buildings (NA and MI, soil C).

				Soil A				Soil C			
EDP	**Site**	**GM type**	**Config.**	**Geo 1**	**Geo2**	**Geo 3**	**Geo4**	**Geo 1**	**Geo2**	**Geo 3**	**Geo4**
Disp.	**NA**	**CS-scaled**	$\hat{\theta}_{Sa(T)}$ [g]	0.79	0.93	1.09	1.09	1.06	1.28	1.35	1.35
			$\hat{\beta}_{Sa(T)}$	0.29	0.29	0.31	0.31	0.23	0.15	0.25	0.25
		PEER	$\hat{\theta}_{Sa(T)}$ [g]	0.65	0.83	1.00	1.00	0.78	1.07	1.00	1.01
			$\hat{\beta}_{Sa(T)}$	0.27	0.22	0.20	0.24	0.20	0.14	0.20	0.21
	MI	**CS-scaled**	$\hat{\theta}_{Sa(T)}$ [g]	0.99	0.77	1.26	1.30	1.09	1.22	1.47	1.52
			$\hat{\beta}_{Sa(T)}$	0.30	0.26	0.28	0.26	0.35	0.23	0.27	0.27
		PEER	$\hat{\theta}_{Sa(T)}$ [g]	0.63	0.68	0.86	0.88	0.63	0.77	0.89	0.88
			$\hat{\beta}_{Sa(T)}$	0.21	0.23	0.27	0.26	0.21	0.26	0.28	0.26
Conn.	**NA**	**CS-scaled**	$\hat{\theta}_{Sa(T)}$ [g]	0.80	0.93	0.20	1.16	1.06	1.17	1.25	1.34
			$\hat{\beta}_{Sa(T)}$	0.29	0.29	0.14	0.37	0.23	0.21	0.25	0.22
		PEER	$\hat{\theta}_{Sa(T)}$ [g]	0.67	0.83	0.23	1.13	0.81	1.03	0.99	1.06
			$\hat{\beta}_{Sa(T)}$	0.25	0.22	0.11	0.30	0.22	0.13	0.21	0.22
	MI	**CS-scaled**	$\hat{\theta}_{Sa(T)}$ [g]	0.90	0.75	0.14	0.14	0.99	1.08	0.19	0.20
			$\hat{\beta}_{Sa(T)}$	0.25	0.27	0.04	0.04	0.30	0.25	0.02	0.14
		PEER	$\hat{\theta}_{Sa(T)}$ [g]	0.57	0.64	0.20	0.14	0.57	0.73	0.20	0.21
			$\hat{\beta}_{Sa(T)}$	0.24	0.18	0.14	0.04	0.24	0.23	0.14	0.12

3.3.2.6 Comparisons of failure rates

The failure rates of the considered buildings for the sites NA and MI were also computed using Eq. (3-2). Figure 3-5 presents the computed rates for the NA and MI sites with different colors and markers corresponding to different structural typologies and configurations, models, GM record sets, and collapse conditions.

Although the estimated fragility parameters showed a substantial dependency on the used GM records set, it can be observed that the resulting failure rates, thanks to the filtering effect of low exceedance rates of the largest IM values, are relatively close between the two GM selection strategies. Note that the markers aligned on the 10^{-5} rate mean that, regardless the used GM set, only an upper bound to the failure rate could be provided because the integral part of such an equation was negligible.

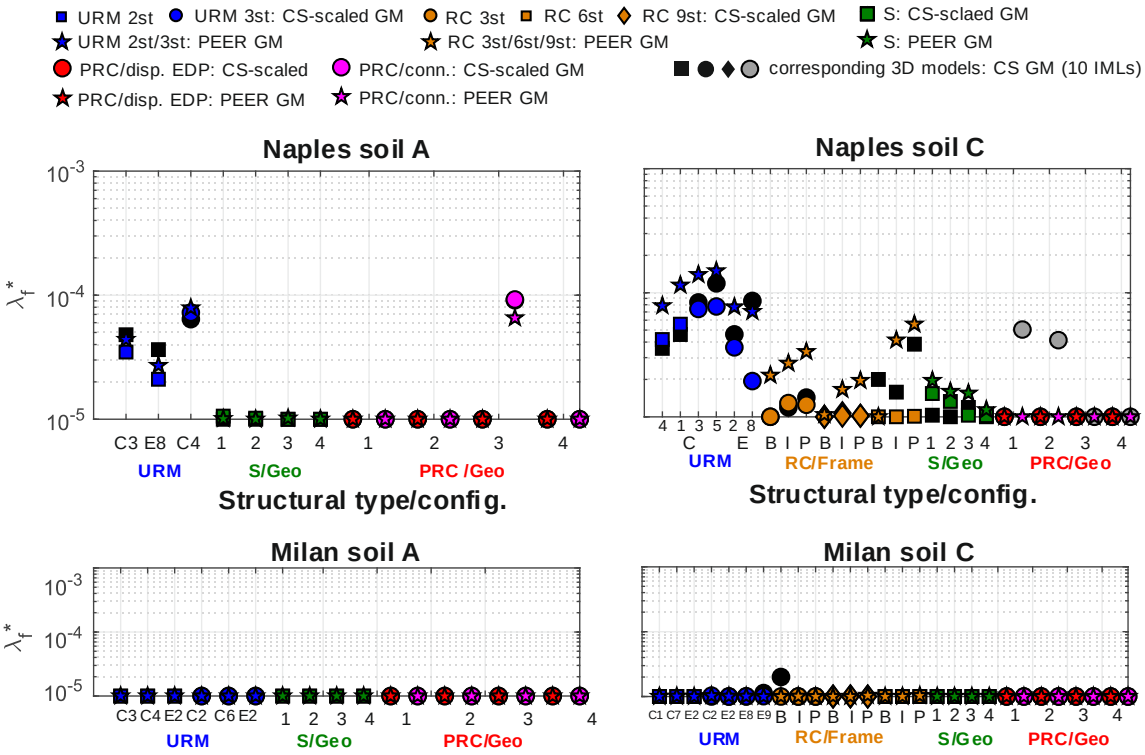

Figure 3-5 Comparisons of failure rates for the low-to-mid hazard sites (MI and NA) computed with fragilities from the two different record sets.

3.4 Usability-preventing damage onset fragility curves

In the RINTC project, the usability-preventing damage onset fragilities were computed using Eq. (3-2) in the same manner as for the global collapse damage level. As briefly mentioned above, $P\left[F \mid IM = im\right]$ at each IM levels was computed via Eq. (1-17) summing a lognormal fragility model and a non-parametric collapse fragility. The former is constructed from non-collapse data with the measured D/C ratios with respect to the failure criteria specified in Section 3.2.2.2, while the latter is represented as the the fractions of collapse cases. Since Eq. (1-17) expresses structural fragility as a probability mass function, it is worthwhile to provide parametric (lognormal) fragility functions estimated via Eq. (3-1). Although this thesis does not provide the details of the original structural numerical models, readers can find further details, such as the descriptions on the numerical modelling of the structures and the results of NLDAs, in the project report [RINTC-Workgroup, 2018].

3.4.1.1 Results of URM buildings

The damage-onset fragility functions for masonry buildings were estimated as a function of $Sa\left(0.15s\right)$ using the original 3D structural models given the failure criteria described above. The obtained parameters are listed in Table 3-11. It should be noted that the issue related to the aforementioned limitations for low seismicity sites arose even for this performance limit state, hence the parameters for some MI buildings are not available or likely to be biased due to few failure cases concentrated at the lower tail of the fragility function. Such cases are indicated in the table. As observed in the previous section, generally the C type configuration buildings resulted in the smaller median spectral acceleration causing the onset of the usability-preventing damage (in the range between 0.34-0.57g), $\hat{\theta}_{Sa(T)}$ than the E-type configuration buildings (in the range between 0.77-1.01g). Although the trend of the median $\hat{\theta}_{Sa(T)}$ is not that clear due to the lack of the results for the MI buildings, it can be seen that those values for the buildings with the same configuration type are comparable across the three sites with different hazard levels. As it regards to the standard deviation, it ranges approximately from 0.19 to 0.48 showing less significant trend across different sites or configurations.

3.4.1.2 Results of RC buildings

Table 3-12 summarizes the estimated parameters for damage-onset fragility functions for the RC buildings for each number of story and each configuration. Similarly to the collapse fragility, it can be observed that the median $\hat{\theta}_{Sa(T)}$ does not necessarily increases with the seismicity of the site. In fact, the damage onset fragility for the BF and some IF/PF buildings showed the comparable median dynamic capacities between the three sites. Particularly to this structural type, the median values of $\hat{\theta}_{Sa(T)}$ causing the onset of usability-preventing damage were found to be much smaller than those with respect to global collapse reported in Table 3-3 and Table 3-8 (i.e., below the quarter of the median collapse capacity of the same building). It is indicated from the comparisons between the two performance levels that mitigating the damage onset risk under moderate earthquake events is more critical for this structural type.

3.4.1.3 Results of steel buildings

Table 3-13 shows the fragility function parameters for the steel buildings, which were estimated as a function of $Sa(0.5s)$ for the buildings Geo 1, 2 and $Sa(1.0s)$ for the ones Geo 3 and 4. The median $\hat{\theta}_{Sa(T)}$ resulted to be between 0.4-0.5g for $Sa(0.5s)$ and 0.3-0.4g for $Sa(1.0s)$, which are comparable among the different sites. It shows even a slightly decrease with the increasing hazard level at the site. The logarithmic standard deviation for Geo 1 and 2 corresponding to $Sa(0.5s)$ ranges between 0.3-0.45 while those for Geo 3 and 4 show slightly higher values, 0.5-0.6.

3.4.1.4 Results of PRC buildings

Table 3-14 shows the fragility function parameters for the PRC buildings, which were estimated as a function of $Sa(2.0s)$ for all considered cases. The results showed that the median $\hat{\theta}_{Sa(T)}$ causing failure are between 0.08-0.11 and do not differ between the AQ and NA sites nor between the soil conditions. On the other hand, $\hat{\beta}_{Sa(T)}$ varies from 0.05-0.45 showing the increasing trend with the site hazard. Due to few collapse cases, this study was not able to obtain the parameters for the lowest seismicity site, MI, as for some buildings belonging to the other structural types.

Table 3-11 Usability-preventing damage onset fragility function parameters for the URM buildings (soil A and C).

GM type	AQ	Soil A					Soil C			
		C1-2st	C1-3st	E2-2st	E2-3st	E8-3st	C3-2st	E2-2st	E8-2st	E9-2st
CS GM $IM = Sa(0.15s)$	$\hat{\theta}_{Sa(T)}$ [g]	0.43	0.34	0.95	0.80	0.77	0.57	1.01	0.82	0.88
	$\hat{\beta}_{Sa(T)}$	0.29	0.19	0.32	0.33	0.33	0.34	0.24	0.27	0.24
	NA	**Soil A**			**Soil C**					
		C3-2st	**C4-3st**	**E8-2st**	**C1-2st**	**C4-2st**	**C3-3st**	**C5-3st**	**E2-3st**	**E8-3st**
	$\hat{\theta}_{Sa(T)}$ [g]	0.51	0.37	0.90	0.46	0.56	0.41	0.40	0.92	0.86
	$\hat{\beta}_{Sa(T)}$	0.48	0.36	0.30	0.24	0.31	0.24	0.19	0.46	0.40
	MI	**Soil A**			**Soil C**									
		C1-2st	**C4-2st**	**C2-3st**	**C6-3st**	**E2-2st**	**E2-3st**	**C1-2st**	**C7-2st**	**C2-3st**	**E2-2st**	**E2-3st**	**E8-3st**	**E9-3st**
	$\hat{\theta}_{Sa(T)}$ [g]	NaN	NaN	0.38	NaN	NaN	NaN	*0.75**	NaN	0.39	NaN	NaN	*0.48**	*0.46**
	$\hat{\beta}_{Sa(T)}$	NaN	NaN	0.33	NaN	NaN	NaN	*0.52**	NaN	0.24	NaN	NaN	*0.06**	*0.05**

*****NaN =no failure cases; *italic** = a few failure cases, i.e., $P\left[F \mid Sa(T) = sa_{T_R=10^5}\right] < 0.50$; these cases are excluded in Figure 3-7.

Table 3-12 Usability-preventing damage onset fragility function parameters for the RC buildings (soil C).

	Story	3st			6st			9st		
	Config.	BF	IF	PF	BF	IF	PF	BF	IF	PF
Site/GM type	IM	$Sa(1.0s)$	$Sa(0.15s)$	$Sa(0.5s)$	$Sa(1.5s)$	$Sa(0.5s)$	$Sa(0.5s)$	$Sa(2.0s)$	$Sa(1.0s)$	$Sa(1.0s)$
AQ/CS GM	$\hat{\theta}_{Sa(T)}$ [g]	0.18	0.67	0.80	0.11	0.74	0.95	0.08	0.15	0.15
	$\hat{\beta}_{Sa(T)}$	0.55	0.42	0.40	0.46	0.47	0.54	0.25	0.06	0.06
NA/CS GM	$\hat{\theta}_{Sa(T)}$ [g]	0.15	0.92	0.58	0.10	0.42	0.65	0.08	0.25	0.30
	$\hat{\beta}_{Sa(T)}$	0.43	0.62	0.36	0.36	0.44	0.61	0.39	0.27	0.35
MI/CS GM	$\hat{\theta}_{Sa(T)}$ [g]	0.15	NaN	*0.52**	0.09	*0.53**	0.66	0.08	0.26	0.24
	$\hat{\beta}_{Sa(T)}$	0.37	NaN	*0.06**	0.18	*0.07**	0.60	0.26	0.06	0.35

NaN =no failure cases; *italic** = a few failure cases, i.e., $P\left[F \mid Sa(T) = sa_{T_R=10^5}\right] < 0.50$; these cases are excluded in Figure 3-7.

Table 3-13 Usability-preventing damage onset fragility function parameters for the steel buildings (soil A and C).

Site/GM type	Soil type	Soil A				Soil C			
	IM	$Sa(0.5s)$		$Sa(1.0s)$		$Sa(0.5s)$		$Sa(1.0s)$	
	Config.	Geo 1	Geo2	Geo 3	Geo4	Geo 1	Geo2	Geo 3	Geo4
AQ/CS GM	$\hat{\theta}_{Sa(T)}$ [g]	0.49	0.42	0.28	0.26	0.47	0.44	0.31	0.29
	$\hat{\beta}_{Sa(T)}$	0.33	0.28	0.56	0.49	0.29	0.44	0.52	0.52
NA/CS GM	$\hat{\theta}_{Sa(T)}$ [g]	0.44	0.49	0.40	0.35	0.42	0.44	0.42	0.37
	$\hat{\beta}_{Sa(T)}$	0.43	0.39	0.61	0.48	0.43	0.41	0.58	0.52
MI/CS GM	$\hat{\theta}_{Sa(T)}$ [g]	*0.35**	*0.36**	NaN	*0.18**	0.45	0.45	*0.30**	*0.29**
	$\hat{\beta}_{Sa(T)}$	*0.07**	*0.08**	NaN	*0.08**	0.30	0.26	*0.08**	*0.08**

NaN =no failure cases; *italic** = a few failure cases, i.e., $P\left[F \mid Sa(T) = sa_{T_R=10^5}\right] < 0.50$; these cases are excluded in Figure 3-7.

Table 3-14 Usability-preventing damage onset fragility function parameters for the PRC buildings (soil A and C).

Site/GM type	Soil type	Soil A				Soil C			
	Config.	Geo 1	Geo2	Geo 3	Geo4	Geo 1	Geo2	Geo 3	Geo4
AQ/CS GM	$\hat{\theta}_{Sa(T)}$ [g]	0.08	0.08	0.09	0.09	0.09	0.08	0.11	0.10
	$\hat{\beta}_{Sa(T)}$	0.05	0.32	0.28	0.26	0.31	0.33	0.45	0.39
NA/CS GM	$\hat{\theta}_{Sa(T)}$ [g]	0.09	0.09	0.10	0.10	0.09	0.11	0.10	0.11
	$\hat{\beta}_{Sa(T)}$	0.14	0.21	0.17	0.19	0.21	0.33	0.24	0.25
MI/CS GM	$\hat{\theta}_{Sa(T)}$ [g]	NaN	NaN	NaN	NaN	*0.11***	*0.11***	*0.11***	*0.11***
	$\hat{\beta}_{Sa(T)}$	NaN	NaN	NaN	NaN	*0.06***	*0.06***	*0.06***	*0.06***

NaN =no failure cases; ** the lack of samples at intermediate IMLs where $0 < P\left[F \mid Sa(T) = sa_i\right] < 1$; these cases are excluded in Figure 3-7.

3.5 Quantifications of structural safety margins

The estimated collapse and usability-preventing damage onset fragility functions of the prototype buildings were compared between the three cities with different levels of seismicity. Figure 3-6 and Figure 3-7 show the median and variability of the estimated collapse and damage onset fragility functions, which are normalized by the elastic horizontal spectral acceleration at the conditioning period of the structure with respect to the corresponding design limit state $Sa_{SLV}(T)$ and $Sa_{SLD}(T)$ (475 year- and 50 year- GM levels; Figure 2-1b), respectively. In the figure, the computed safety margins are aligned in the ascending order of the design hazard for the sake of illustration.

It is clearly observed that the so-called collapse margin ratio $\hat{\theta}_{Sa(T)} / Sa_{SLV}(T)$ tends to decrease with the increasing hazard at the site due to the comparable median capacities and site-dependent design seismic actions. When compared between the results from the CS-scaled/-based GM sets, the $\hat{\theta}_{Sa(T)} / Sa_{SLV}(T)$ ratios of the same structural type for AQ are smaller than those for MI, approximately by a factor of 3-9 in most cases, mainly ascribed to the differences in the design seismic actions (see Figure 2-1b). Besides the seismic performance factors presented in Chapter 2, these results support that the structures designed for the more hazardous site AQ are generally more vulnerable relative to the site hazard then those for the other two sites. This may be another interpretation to explain the observed trend of the seismic risk, namely, increasing seismic risk with the increase of the hazard at the site [Iervolino et al., 2017; 2018].

Although the results have lack of usability-preventing damage fragilities for some buildings at the less hazardous sites (MI), $\hat{\theta}_{Sa(T)} / Sa_{SLD}(T)$ also show the same trend as the collapse fragilities. Generally, smaller safety margin ratios were observed for the usability-preventing damage fragilities than the global collapse ones (except the URM buildings).

As regards the trend across the various typologies, the URM buildings turned out to be the most vulnerable, followed by the steel, PRC and RC buildings, as far as the prototype buildings examined under particular assumptions on design, modelling, and collapse criteria are concerned. On the contrary, the safety margin ratios with respect to damage onset are

comparable among the four different structural types. Particularly, it is noteworthy that some RC buildings, which turned out to be less exposed to the collapse risk, exhibited smaller safety margin ratios than the other typologies. These are also consistent to the project's findings in the project.

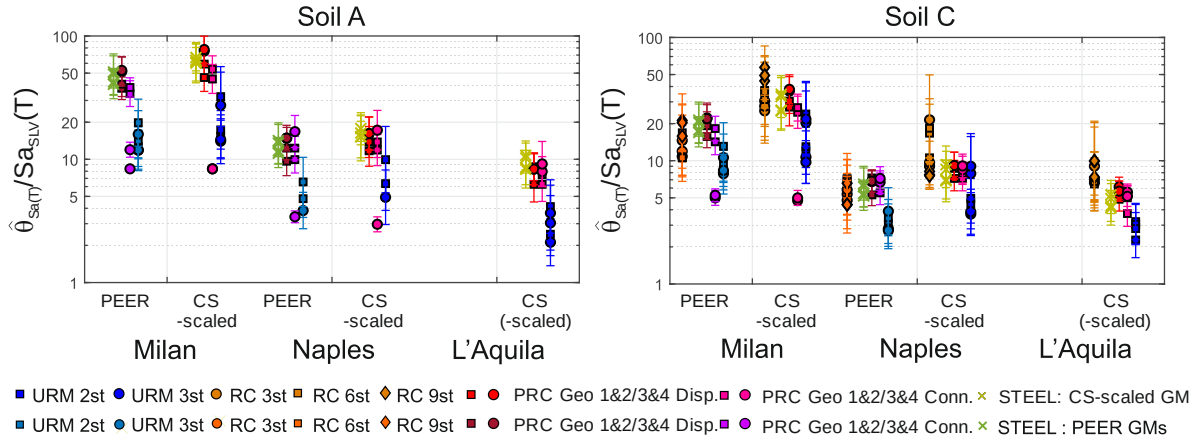

Figure 3-6 Estimated collapse margin ratios with respect to global collapse.

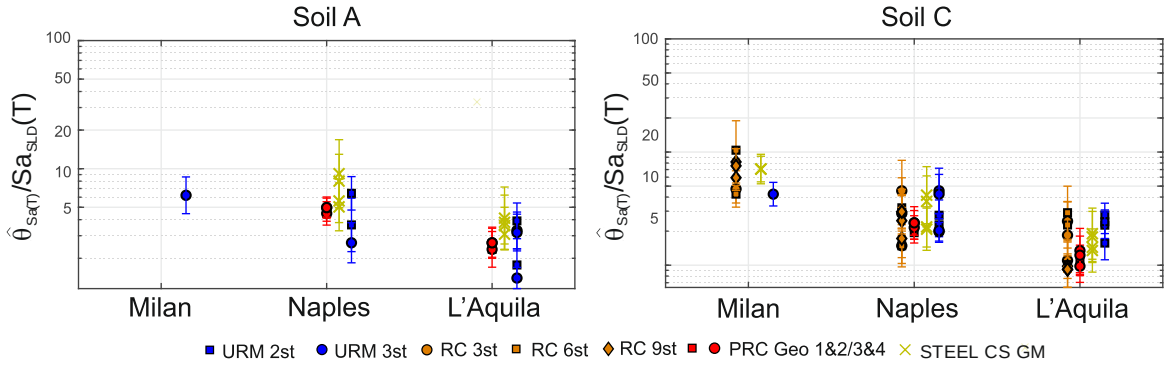

Figure 3-7 Estimated safety margin ratios with respect to usability-preventing damage onset.

3.6 Conclusions

This study presented in this chapter developed seismic fragility functions of the Italian NTC code-conforming buildings of the RINTC project with respect to two performance limit states, i.e., collapse and usability -preventing damage onset limit states. For the purposes of this investigation, some regular buildings belonging to four different structural types common in Italy and located at three Italian cities were selected. Seismic fragility with respect to collapse limit state was examined via NLDA using the ESDoF systems equivalent to the detailed

structural models while that with respect to the damage onset limit state was analyzed in a similar manner but using the structural responses of the original 3D models. The fragility functions, expressed in terms of spectral acceleration at a period close to the fundamental vibration periods of the corresponding structure, were constructed through an EDP-based approach in conjunction with maximum likelihood estimation fitting method. In the course of investigations, it turned out that a large extrapolation of hazard models was required in estimating collapse fragility functions for new buildings at the sites with low-to-mid seismicity in Italy, therefore the fragility functions with respect to collapse limit states were estimated under two different assumptions on hazard characterization aiming to identify the possible ranges of the collapse margins. The ESDoF systems and computed fragilities were validated through the comparison with the 3D models, in terms of dynamic structural response (i.e., demand-to-capacity ratio of the EDP of interest) and annual collapse rate. The main findings are summarized as:

1. It is observed that, the safety margin ratio with respect to the elastic response for design earthquake, that is, the ratio of the median spectral acceleration causing structural failure (collapse and usability-preventing damage onset), to the elastic horizontal spectral acceleration ($\hat{\theta}_{Sa(T)}/Sa_{SLV}(T)$ and $\hat{\theta}_{Sa(T)}/Sa_{SLD}(T)$, respectively) tends to decrease with the increasing hazard.

2. As regards the collapse margin ratios $\hat{\theta}_{Sa(T)}/Sa_{SLV}(T)$, those of the same structural type belonging to the highest seismicity site, L'Aquila, are smaller than those for the lowest seismicity site, Milan, approximately by a factor of 3-9 in most of the cases, mainly ascribed to the differences in the design seismic actions (i.e. comparable median collapse capacities, $\hat{\theta}_{Sa(T)}$).

3. As far as the prototype buildings examined in this study are concerned, the results of the collapse margin ratios showed that the URM buildings turned out to be the most vulnerable across the different structural types, followed by the steel/PRC and RC

buildings. On the contrary, the safety margin ratios with respect to usability-preventing damage onset were comparable among the four different structural types.

In conjunction with the findings in Chapter 2, the findings from this study revealed the fact that the current code-conforming design tends to prescribe smaller safety margins for the more hazardous sites.

References

ASCE [2000] Prestandard And Commentary For The Seismic Rehabilitation Of Buildings, Report FEMA-356, Washington, DC, USA.

Baker, J. W. [2015] "Efficient analytical fragility function fitting using dynamic structural analysis," *Earthq. Spectra*, 31(1), 570–599.

D'ayala, D. F., Vamvatsikos, D., and Porter, K. [2014] GEM Guidelines For Analytical Vulnerability Assessment Of Low/Mid-Rise Buildings, Vulnerability Global Component Project. DOI:10.13117/GEM.VULN-MOD.TR2014.12.

HAZUS-MH [2003] Multi-hazard Loss Estimation Methodology: Earthquake Model – Technical Manual. (https://www.fema.gov/hazus; accessed on June 2019).

Iervolino, I., Spillatura, A., and Bazzurro, P. [2017] "RINTC Project: Assessing the (Implicit) Seismic Risk of Code-Conforming Structures In Italy," In *6th ECCOMAS Themat. Conf. Comput. Methods Struct. Dyn. Earthq. Eng.*, pp.1545–1557, Rhodes, Greece. DOI:10.7712/120117.5512.17282.

Iervolino, I., Spillatura, A., and Bazzurro, P. [2018] "Seismic reliability of code-conforming Italian buildings," *J. Earthq. Eng.*, 22(sup2), 5–27. DOI:10.1080/13632469.2018.1540372.

Lagomarsino, S., Penna, A., Galasco, A., and Cattari, S. [2013] "TREMURI program: An equivalent frame model for the nonlinear seismic analysis of masonry buildings," *Eng. Struct.*, 56, 1787–1799. DOI:10.1016/j.engstruct.2013.08.002.

Luco, N., and Bazzurro, P. [2007] "Does amplitude scaling of ground motion records result in biased nonlinear structural drift responses?" *Earthq. Eng. Struct. Dyn.*, 36(13), 1813–1835.

Magliulo, G., Bellotti, D., Cimmino, M. and Nascimbene, R. [2018] "Modeling and seismic response analysis of RC precast Italian code-conforming buildings," *J. Earthq. Eng.*, 22(sup2), 140-167, doi:10.1080/13632469.2018.1531093.

McKenna, F., Fenves, G. L., Scott, M. H., and Jeremic, B. [2000] Open System for Earthquake Engineering Simulation (OpenSees), Pacific Earthquake Engineering Research Center, University of California, Berkeley, CA, USA: http://opensees.berkeley.edu/; accessed on June 2019.

O'Reilly, G. J., and Sullivan, T. J. [2018] "Quantification of modelling uncertainty in existing Italian RC frames," *Earthq. Eng. Struct. Dyn.*, 47(4), 1054–1074. DOI:10.1002/eqe.3005.

Pitilakis, K., Crowley, H., and Kaynia, A. M. [2014] SYNER-G: Typology Definition And Fragility Functions For Physical Elements At Seismic Risk, Vol. 27, Springer, Dordrecht, Netherlands. DOI:10.1007/978-94-007-7872-6.

RINTC-Workgroup [2018] Results of The 2015-2017 Implicit Seismic Risk Of Code-Conforming Structures In Italy (RINTC) Project. ReLUIS Report, Rete Dei Laboratori Universitari Di Ingegneria Sismica (ReLUIS), Naples, Italy.

Rota, M., Penna, A., and Magenes, G. [2010] "A methodology for deriving analytical fragility curves for masonry buildings based on stochastic nonlinear analyses," *Eng. Struct.*, 32(5), 1312–1323. DOI:10.1016/j.engstruct.2010.01.009.

Vamvatsikos, D., and Cornell, A. C. [2006] "Direct estimation of the seismic demand and capacity of oscillators with multi-linear static pushovers through IDA," *Earthq. Eng. Struct. Dyn.*, 35(9), 1097–1117. DOI:10.1002/eqe.573

Chapter 4

Intensity measure conversion of seismic structural fragility curves

Abstract

In seismic risk assessment of structures, fragility functions are the probabilistic characterization of vulnerability at the component and/or structural level, expressing the probability of *failure* as a function of a ground motion intensity measure (IM). The fragility curves, in general, are structure- and site-specific, thus a comparison of fragility curves, and of vulnerability, is not straightforward across multiple structures and/or sites. Also, it could be the case that hazard at the site of interest is not available for the IM of the fragility. These situations require to convert fragility curves from an original IM to a target one. The present study addresses the hazard-consistent probabilistic framework for converting spectral acceleration-based IMs from an original IM to a target IM at a given site. In particular, three conversion cases, under different assumptions on the explanatory power of the involved IMs with respect to structural failure, are discussed: (i) a vector-valued IM consisting of the original and target IMs, magnitude, and source-to-site distance, (ii) a vector-valued IM consisting of the original and target IMs, and (iii) the original (scalar) IM only, assuming that structural response given the IM is statistically-independent of the other ground motion characteristics. In this framework, the original fragility functions are characterized utilizing the state-of-the-art methods in performance-based earthquake engineering, then the fragility curves as a function of the target IM are evaluated through applications of the probability calculus rules ensuring consistency with the seismic hazard at the site of interest. The conversion strategy is illustrated through the applications to three-, six-, nine-story Italian code-conforming reinforced concrete buildings designed for a high-hazard site in Italy. The study showed the converted fragility curves have agreement with the reference curves directly estimated from the structural response analysis using the target IM

in the most of cases, whereas the conversions between spectral acceleration-based IMs at two vibration periods, relatively close or far from each other, resulted in larger discrepancies under the adopted fragility assessment procedures in this study.

Keywords**:** *performance-based earthquake engineering; seismic vulnerability; vector-valued intensity measures; probabilistic seismic risk assessment.*

4.1 Introduction

Probabilistic seismic risk assessment of structures evaluates the rate of earthquakes capable of causing structural failure. As an application of the total probability theorem, the *failure rate* is obtained by integrating seismic fragility and seismic hazard, both expressed in terms of the same ground motion (GM) intensity measure (IM) serving as a link between the two probabilistic models. The choice of the IM to be employed in the risk analysis is mainly determined by some desired properties, e.g., *sufficiency*, *efficiency* [Luco and Cornell, 2002] and *scaling robustness* [Tothong and Luco, 2007] besides *hazard computability* [Giovenale et al., 2004]. A sufficient IM is defined as one that yields the structural response given IM statistically independent of earthquake magnitude and source-to-site distance, while an efficient IM is defined as one that provides a comparatively low conditional *record-to-record variability* of structural response. With respect to scaling robustness, it is desirable to employ an IM which leads to unbiased structural response under scaled GM records compared to the results from as-recorded GMs. Hazard computability refers to the possibility of deriving the hazard curve in terms of the IM.

IMs for fragility assessment have been extensively investigated in research. Among all, time-domain peak GM characteristics, such as peak ground acceleration (PGA), are classic IMs and still widely used in practice, also because developed seismic hazard models are typically expressed in terms of these IMs. Currently, elastic spectral acceleration at the first mode vibration period of the structure is the most common IM. This is supported by studies which claim that it is usually more efficient than PGA and sufficient in several practical cases [Shome and Cornell, 2000]. Nonetheless, other studies have discussed that $Sa(T)$ can be neither efficient nor sufficient in specific situations [Luco and Cornell, 2002; Shome and Cornell, 1999]. Advances with respect to $Sa(T)$ include vector-valued IMs or, in general, spectral-shape-based IMs [Baker and Cornell, 2005; Baker, 2007; Vamvatsikos and Cornell, 2005; Bojórquez and Iervolino, 2011; Eads et al., 2015]. Some other studies also explored IMs based on non-linear structural response of simple systems [Tothong and Luco, 2007], yet the usages of those advanced IMs, both scalar and vector-valued, is still not widespread in practice.

Although a meaningful structure-to-structure seismic reliability comparison should be made in terms of annual failure rate or probability, it could be still needed to translate fragilities into a common IM; for example when hazard is only available in terms of a particular IM [Giardini et al., 1999], or to compare seismic structural vulnerability removing as much as possible the hazard contribution to the failure risk. To address this issue, some studies discuss the IM conversion of fragility curves. For example, Ohtori and Hirata [2007] explored the IM conversion from spectral velocity at the first mode vibration period of the structure to PGA based on the *first-order second moment* approximation [Melchers and Beck, 2018], although the relationship between original and target IMs is not fully characterized with respect to site's hazard. Michel et al. [2018] convert fragility curves between spectral accelerations at different periods, yet the consistency of the proposed approach with the rules of probability calculus is not totally clear.

Extending preliminary research on the subject [Suzuki and Iervolino, 2019], the study presented in this chapter addresses a probabilistic framework for converting spectral acceleration-based IMs of seismic fragility curves. In fact, it explores possible conversion cases under different assumptions on the explanatory power of the concerned IMs. The fragility curve of a structure in terms of the target intensity (IM_2) is obtained through hazard-consistent conversion of a fragility function derived from structural response given the original intensity (IM_1). The probabilistic framework considers three different cases about the IMs involved: (i) a vector-valued IM consisting of $.IM_1.$, $.IM_2.$, magnitude (M) and source-to-site distance (R), $\{IM_1, IM_2, M, R\}$; (ii) a vector-valued IM consisting of IM_1 and IM_2, $\{IM_1, IM_2\}$; and (iii) the original IM_1 which is supposed to be a sufficient IM, not only with respect to M and R, but also with respect to IM_2. The IM conversion is performed using the equivalent single-degree-of-freedom (ESDoF) systems of multiple-story Italian code-conforming RC buildings, varying the fundamental vibration periods of the structure from 0.3s to 2.0s. All the original fragility functions are obtained with the state-of-the-art methods for structural response analysis within the PBEE framework [Cornell and Krawinkler, 2000]; e.g., the multiple-stripe analysis method [Jalayer and Cornell, 2003] (MSA) with hazard-consistent record selection based on the *conditional spectra* [Lin et al., 2013] (CS). For the sake of hazard computability,

the original IM herein is the spectral acceleration at a period close to the fundamental period of the corresponding structure and the structural response data are utilized to perform the IM conversion for the following two situations: IM_2 is (i) PGA and (ii) spectral acceleration at a period longer than that for the original IM. For comparison, a *reference* fragility curve expressed in terms of IM_2 is also directly evaluated performing nonlinear dynamic analyses (NLDAs) using records selected directly considering IM_2 as the (original in this case) IM.

The remainder of the chapter is structured such that the next section introduces the framework for converting fragility curves, followed by the models for estimating seismic fragility adopted in the study. In particular, regression models, involving the original and target IMs and GM characteristics, are utilized for the original fragility assessment. The next section describes the examined IM conversions including the structural models and seismic hazard under consideration. The results of the original fragility assessment of the examined structures and site-specific seismic functions are then discussed. Subsequently, reference fragilities, whose parameters are estimated via a maximum likelihood estimation approach, are described. Finally, the results of the converted fragility curves for all IM conversion conditions/cases are discussed. Notable remarks and findings conclude the study presented in this chapter.

4.2 Methodology

This section introduces the probabilistic framework for converting IMs for seismic fragility curves. The framework assumes that structural response data are preliminary obtained through NLDA to assess the fragility in terms of the original IM_1 and aims at converting to the target IM_2 without carrying out further structural analyses. The IM conversion involves probabilistic modelling of seismic hazard and fragility, through which the fragility in terms of the target IM_2 is evaluated. In particular, this study addresses the conversion between spectral acceleration-based IMs, considering three conversion cases under different assumptions on the IM involved in probabilistic calculus rules. The following provides the derivation of the conversion equations as well as the PSHA results required by the conversion.

4.2.1 Conversion equations

Assuming that the probability of *failure* (denoted as F) conditional to the joint occurrence of IM_1 and IM_2, $P\left[F\left|IM_1 = im_1 \cap IM_2 = im_2\right.\right]$, is available for a structure supposed to be located at a site of interest, the probability of failure given a certain $\left(im_2\right)$ value of IM_2, that is $P\left[F\left|IM_2 = im_2\right.\right]$, can be computed as per Eq. (4-1) based on the total probability theorem:

$$P\left[F\left|IM_2 = im_2\right.\right] = \int_{IM_1} P\left[F\left|IM_1 = im_1 \cap IM_2 = im_2\right.\right] \cdot f_{IM_1|IM_2}\left(im_1 \mid im_2\right) \cdot dim_1 \tag{4-1}$$

where $f_{IM_1|IM_2}\left(im_1 \mid im_2\right)$ is the conditional distribution of IM_1 given IM_2, in one earthquake of unspecified other characteristics.

The term $P\left[F\left|IM_1 = im_1 \cap IM_2 = im_2\right.\right]$ is a fragility surface evaluated through structural analysis, while $f_{IM_1|IM_2}\left(im_1 \mid im_2\right)$ is computed via the fools of PSHA [Cornell, 1968]. Because PSHA typically considers earthquake magnitude and source-to-site distance as random variables (RVs), Eq. (4-1) can be further extended to Eq. (4-2):

$$\begin{aligned} & P\left[F\left|IM_2 = im_2\right.\right] \\ & = \int_{IM_1}\int_{M}\int_{R} P\left[F\left|IM_1 = im_1 \cap IM_2 = im_2 \cap M = m \cap R = r\right.\right] \cdot f_{IM_1,M,R|IM_2}\left(im_1, m, r \mid im_2\right) \cdot dr \cdot dm \cdot dim_1 \\ & = \int_{IM_1}\int_{M}\int_{R} P\left[F\left|IM_1 = im_1 \cap IM_2 = im_2 \cap M = m \cap R = r\right.\right] \cdot f_{IM_1|M,R,IM_2}\left(im_1 \mid m, r, im_2\right) \cdot f_{M,R|IM_2}\left(m, r \mid im_2\right) \cdot dr \cdot dm \cdot dim_1 \end{aligned} \tag{4-2}$$

In the equation, the first term of the integrands $P\left[F\left|IM_1 = im_1 \cap IM_2 = im_2 \cap M = m \cap R = r\right.\right]$ is the failure probability conditional to the joint occurrence of $\left\{IM_1, IM_2, M, R\right\}$; the second term $f_{IM_1,M,R|IM_2}\left(im_1, m, r \mid im_2\right)$ is a site-specific function that can be seen as the product of the two probability density functions (PDFs): $f_{IM_1|M,R,IM_2}\left(im_1 \mid m, r, im_2\right)$ and $f_{M,R|IM_2}\left(m, r \mid im_2\right)$. As discussed in the following, the former can be obtained from a ground motion prediction equation (GMPE) considering the statistical dependency between IM_1 and IM_2 conditional to M and R; i.e., via *conditional hazard* [Baker and Cornell, 2006]. The latter is computed through seismic hazard disaggregation [Bazzurro and Cornell, 1999] that provides the probability (density) of a certain M and R scenario given the occurrence of IM_2. Eq. (4-2) yields the failure probability conditional only to the target IM by marginalizing out the other

three variables from a multi-variable fragility function. It can be considered the framing equation as it involves all the basic RVs involved in the conversion problem.

4.2.2 Vector-valued IM consisting of IM_1 and IM_2

If it cannot be rejected that the vector-valued IM $\{IM_1, IM_2\}$ is sufficient, then the structural response given the IM can be considered, by definition, statistically-independent of M and R. This means that the GM charcateristics have negligible influence in predicting the structural response, that is to say, the conditional failure probability $P\left[F \middle| IM_1 = im_1 \cap IM_2 = im_2 \cap M = m \cap R = r\right]$ can be assumed to be equal to $P\left[F \middle| IM_1 = im_1 \cap IM_2 = im_2\right]$. Hence, Eq (4-2) reduces to:

$$P\left[F \middle| IM_2 = im_2\right] = \\ = \int_{IM_1} P\left[F \middle| IM_1 = im_1 \cap IM_2 = im_2\right] \iint_{M\ R} f_{IM_1|M,R,IM_2}\left(im_1 \mid m, r, im_2\right) \cdot f_{M,R|IM_2}\left(m, r \mid im_2\right) \cdot dr \cdot dm \cdot dim_1 \quad (4\text{-}3)$$

This conversion equation considering a two-parameter-vector-valued fragility function is useful when adding IM_2 lets the structural assessment easier and/or more effective, as discussed in the past studies endorsing the use of vector-valued IMs for seismic risk assessment of structures.

4.2.3 Single intensity measure

If the original IM_1 is a sufficient IM not only with respect to the GM characteristics but also with respect to IM_2, Eq. (4-3) can be further simplified as per Eq. (4-4), where $P\left[F \middle| IM_1 = im_1\right]$ is the original fragility curve of the structure.

$$P\left[F \middle| IM_2 = im_2\right] = \\ = \int_{IM_1} P\left[F \middle| IM_1 = im_1\right] \iint_{M\ R} f_{IM_1|M,R,IM_2}\left(im_1 \mid m, r, im_2\right) \cdot f_{M,R|IM_2}\left(m, r \mid im_2\right) \cdot dr \cdot dm \cdot dim_1 \quad (4\text{-}4)$$

The multi- or single-variable fragility functions in Eqs. (4-2)-(4-4) can be derived via a numerical approach, and there is a variety of methods for assessing probabilistic seismic fragility. For the sake of generality of the conversion framework, the fragility evaluation models considered particularly in this study will be separately introduced in Section 4.3.

4.2.4 Hazard conversion terms

This subsection describes the procedures to characterize the terms that depend on the probabilistic seismic hazard of the site in the IM conversion equations, Eqs. (4-2)-(4-4); i.e., the probability distributions conditional to the target IM_2, $f_{IM_1|M,R,IM_2}$ and $f_{M,R|IM_2}$, corresponding to the second and third integrands, respectively.

The calculations to obtain the PDFs of IM_1 conditional to IM_2 and a specific magnitude and distance scenario, $f_{IM_1|M,R,IM_2}$, have been discussed in previous research [Baker and Cornell, 2005; Iervolino et al., 2010]. Given that GMPEs exist for the two IMs, the following equations hold:

$$\begin{cases} \ln IM_1 = \mu_{\ln IM_1|M,R} + \sigma_{\ln IM_1} \cdot \varepsilon_{\ln IM_1} \\ \ln IM_2 = \mu_{\ln IM_2|M,R} + \sigma_{\ln IM_2} \cdot \varepsilon_{\ln IM_2} \end{cases}, \tag{4-5}$$

where $\mu_{\ln IM_1|M,R}$ $\left(\mu_{\ln IM_2|M,R}\right)$ is the logarithmic mean of IM_1 (IM_2) conditional to a certain magnitude and distance scenario (m,r) (as well as to some variables, for example, related to the local site condition); $\sigma_{\ln IM_1}$ $\left(\sigma_{\ln IM_2}\right)$ is the logarithmic standard deviation for the selected IM_1 $\left(IM_2\right)$; and $\varepsilon_{\ln IM_1}$ $\left(\varepsilon_{\ln IM_2}\right)$ is a standard normal variable, also known as the *standardized residual*. Eq. (4-5) typically allows to assume that the two IMs are (marginally) lognormally distributed conditional to (m,r).

Under the assumptions that the logarithms of the two IMs, conditional to the magnitude and source-to-site distance, are jointly normal, then the conditional distribution $f_{IM_1|M,R,IM_2}$ is also lognormal. For certain (im_2,m,r) values of the target IM_2, magnitude, and distance, the parameters of the Gaussian distribution associated to $f_{IM_1|M,R,IM_2}$ are:

$$\begin{cases} \mu_{\ln IM_1|\ln IM_2,M,R} = \mu_{\ln IM_1|M=w,R=z} + \rho_{\ln IM_1,\ln IM_2} \cdot \sigma_{\ln IM_1} \cdot \dfrac{\ln IM_2 - \mu_{\ln IM_2|M,R}}{\sigma_{\ln IM_2}} \\ \sigma_{\ln IM_1|\ln IM_2} = \sigma_{\ln IM_1} \cdot \sqrt{1-\rho^2_{\ln IM_1,\ln IM_2}} \end{cases}, \tag{4-6}$$

where $\mu_{\ln IM_1|\ln IM_2,M,R}$ is the mean value of $\ln IM_1$ given the joint occurrence of the other three parameters $\left\{\ln IM_2 = im_2, M = m, R = r\right\}$. The correlation coefficient $\rho_{\ln IM_1,\ln IM_2}$ can be obtained, for example, from literature studying the correlation between spectral acceleration values at different periods, e.g., [Baker and Jayaram, 2008].

The other term depending on the hazard, namely, the conditional distribution $f_{M,R|IM_2}$ can be computed via hazard *disaggregation*. Based on the Bayes theorem, the $f_{M,R|IM_2}$ can be computed from the fundamental PSHA results for the site of interest, i.e., the hazard curve in terms of IM_2 and distributions of variables related to the GM characteristics. For more details, see [Bazzurro and Cornell, 1999].

4.3 Fragility assessment

The fragility functions in the integrals at the right-hand sides of Eqs. (4-2)-(4-4) can be obtained through NLDA using a numerical model of the structure and a set of GM records. In the state-of-the-art approach of PBEE, there is a variety of structural analysis methods to obtain the relationship between a specific IM and a structural response measure, i.e., an EDP. Among all, common approaches in earthquake engineering research are cloud analysis [Cornell et al., 2002], incremental dynamic analysis (IDA) [Vamvatsikos and Cornell, 2002], and MSA. The cloud method typically performs dynamic analysis using a set of unscaled GM records collected so as to over wide ranges of the concerned IMs. IDA collects EDP values under a single set of GM records incrementally scaled up to a certain IM level. The MSA method also involves dynamic analyses at multiple IM levels using scaled GM records, yet it employs different record sets selected consistently to the hazard disaggregation results for different IM levels (*stripes*).

Fragility modelling strategies for various structural analysis methods have been comprehensively discussed in literature [Baker, 2007; Iervolino, 2017]. From a statistical inference perspective, fragility assessment approaches can be broadly classified into *parametric* and *non-parametric* ones. For the original and reference fragility assessment of the examined structures, this study adopts one of the possible assessment approaches using parametric models. In particular, the approaches discussed hereafter assume structural response analysis methods that warrant hazard consistency at a site of interest; e.g., cloud analysis and MSA methods.

Supposing that structural failure is expressed as the exceedance a certain performance threshold in terms of an EDP of interest $\left(EDP_f\right)$, that is, $F \equiv EDP > EDP_f$, log-linear regression models are often employed to calibrate the relationship between the EDP and the IM.

In case the considered IM is $\{IM_1, IM_2, M, R\}$, for example, the logarithm of the EDP can be given in the simplest form of Eq. (4-7) [Baker and Cornell, 2005; Baker, 2007]:

$$\begin{aligned} \ln EDP &= \ln \overline{EDP} + \eta_{\ln EDP} \cdot \sigma_\eta = \\ &= \beta_0 + \beta_1 \cdot \ln im_1 + \beta_2 \cdot \ln im_2 + \beta_3 \cdot m + \beta_4 \cdot \ln r + \eta_{\ln EDP} \cdot \sigma_\eta \end{aligned} \tag{4-7}$$

where $\ln \overline{EDP}$ is the conditional mean given the explanatory variables $\{IM_1, IM_2, M, R\}$, $\{\beta_0, \beta_1, \beta_2, \beta_3, \beta_4, \sigma_\eta\}$ are regression parameters, and $\eta_{\ln EDP}$ (i.e., the regression residual) is the standard normal variable. Note that this is merely an extension of the single parameter model of Eq. (1-11).

The model defined by Eq. (4-7) is equivalent to assume a lognormal distribution of EDP conditional to $\{IM_1, IM_2, M, R\}$, with the mean equal to $\beta_0 + \beta_1 \cdot \ln im_1 + \beta_2 \cdot \ln im_2 + \beta_3 \cdot m + \beta_4 \cdot \ln r$ and standard deviation σ_η. Then, the exceedance probability of EDP with respect to the failure threshold value, EDP_f, conditional to $\{IM_1, IM_2, M, R\}$ can be given by Eq. (4-8), where $\Phi(\bullet)$ is a standard normal cumulative distribution function:

$$P\left[F \,|\, IM_1 = im_1 \cap IM_2 = im_2 \cap M = m \cap R = z\right] = 1 - \Phi\left(\frac{\ln EDP_f - \ln \overline{EDP}}{\sigma_\eta}\right). \tag{4-8}$$

It should be noted that there are some disadvantages in estimating a fragility function through linear regression as some assumptions are often not appropriate when nonlinear structural response is concerned (e.g., ones related to a constant variance of response over a wide IM domain, *homoscedasticity* and to interactions between predictor variables); see [Baker, 2007]. In case of performing MSA, the fragility function can be modelled estimating different regression parameters for each IM_1 stripe, which can help at least to reduce some of these problems. Although this option is not considered in this study, relevant issues will be altogether discussed later in the application.

Another issue that often arises in structural fragility analysis is that the numerical model of the structure does not yield meaningful EDP values in cases of *numerical instability*, or *collapse* according to the definition by [Shome and Cornell, 2000]. However, in such cases, one can derive a fragility model that accounts for the contribution from collapses using a logistic

regression model with a binary variable, C: it is equal to 1 if the collapse of the structure is observed, and 0 otherwise [Baker and Cornell, 2005; Elefante et al., 2010]. In this case, the probability of collapse can be evaluated as:

$$P\left[C\left|IM_1=im_1\cap IM_2=im_2\cap M=m\cap R=r\right.\right]=\frac{\exp\left(\beta_{0,\mathrm{L}}+\beta_{1,\mathrm{L}}\ln im_1+\beta_{2,\mathrm{L}}\ln im_2+\beta_{3,\mathrm{L}}m+\beta_{4,\mathrm{L}}\ln r\right)}{1+\exp\left(\beta_{0,\mathrm{L}}+\beta_{1,\mathrm{L}}\ln im_1+\beta_{2,\mathrm{L}}\ln im_2+\beta_{3,\mathrm{L}}m+\beta_{4,\mathrm{L}}\ln r\right)} \tag{4-9}$$

where $\beta_{0,\mathrm{L}}$, $\beta_{1,\mathrm{L}}$, $\beta_{2,\mathrm{L}}$, $\beta_{3,\mathrm{L}}$, and $\beta_{4,\mathrm{L}}$ are logistic regression coefficients. The probability of failure given a vector-valued IM, that is $\{IM_1, IM_2, M, R\}$, can be then reformulated considering the contributions from both non-collapse (NC) and collapse data from Eq. (4-8) and Eq. (4-9), respectively. It is given by the following application of the total probability theorem:

$$P\left[F\left|IM\right.\right]=P\left[C\left|IM\right.\right]+P\left[EDP>EDP_f\left|NC,IM\right.\right]\cdot\left(1-P\left[C\left|IM\right.\right]\right). \tag{4-10}$$

4.4 Investigated conversions and structural models

IM conversions under various conditions were explored with respect to different combinations of Sa-based IMs and structural performance levels. To this aim, this study considered a series of multiple-story RC frame buildings discussed in the preceding chapters, i.e., three-, six-, and nine-story (3st, 6st, 9st) RC moment-resisting frame (MRF) buildings featuring three different structural configurations (i.e., bare-, infilled-, and *pilotis*-frames, hereafter denoted as BF, IF, and PF, respectively). Seismic design of these buildings refers only to the site of L'Aquila on the local soil condition C. Thanks to the variety of the structural configurations, the fundamental vibration periods of the considered buildings is approximately in the range between 0.3 and 2.0s. Consistently to the studies presented in the previous chapter, $Sa(T)$ at the closest to the fundamental vibration period of the structure among the five discrete periods, $T=\{0.15s, 0.5s, 1.0s, 1.5s, 2.0s\}$, was considered as IM_1.

The IM conversion of the fragility curves was performed with respect to the exceedance of two performance levels (PLs), usability-preventing damage (UPD) and global collapse (GC). For each performance level, this study explored: (1) the conversion from

$IM_1 = Sa(T)$ to $IM_2 = PGA$ for all nine buildings; (2) only for the 6st IF building whose IM_1 is $Sa(0.5s)$, the original IM is converted to a spectral acceleration at each of the three discrete periods longer than 0.5s; i.e., $T = \{1.0s, 1.5s, 2.0s\}$. As summarized in Table 4-1, this study considered twelve conversions for each of the two performance levels.

Table 4-1 IM conversions under consideration.

PL	UPD, GC											
Story config.	**3st**			**6st**			**9st**			**6st**		
	BF	**IF**	**PF**	**BF**	**IF**	**PF**	**BF**	**IF**	**PF**	**IF**		
$IM_1 = Sa(T)$	1.0s	0.15s	0.5s	1.5s	0.5s	0.5s	2.0s	1.0s	1.0s	0.5s	0.5s	0.5s
$IM_2 = Sa(T)$	0s (PGA)									1.0s	1.5s	2.0s

To reduce the computational complexity in seismic response analysis for fragility evaluation, this study utilized equivalent single degree-of-freedom (ESDoF) systems calibrated in Chapter 2 for both the two performance levels. The failure criteria with respect to the GC and UPD performance levels are consistent to those adopted in the RINTC project, as described in Section 3.2.2. The collapse ductility μ_{GC} (see Section 3.5) was considered for GC, while, with respect to UPD, the equivalent failure ductility corresponding to the failure displacement considered for the original 3D models, δ_{UPD}, was introduced only for the purpose of this study. The ESDoF failure ductility was computed by translating the failure roof-top displacement δ_{UPD} of a 3D structural model into the ESDoF quantity through a modal participation factor (Γ), i.e., $\mu_{UPD} = \delta_{UPD} / \delta_y^* \Gamma = \delta_{UPD}^* / \delta_y^*$. Since this parameter as well as other ESDoF parameters are relevant to the reproductivity of the study, they are summarized for the considered nine RC buildings in Table 4-2. An example of the ESDoF systems (i.e., 6st PF) and their failure thresholds is illustrated in Figure 4-1. For more detailed information on ESDoF modelling, see Chapter 2.

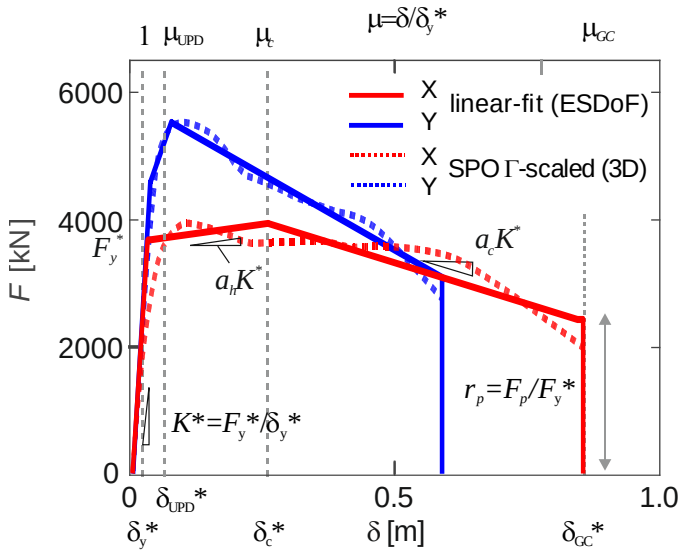

Figure 4-1 Examples of case study RC buildings and failure criteria, μ_{UPD} and μ_{GC} (6st PF).

Table 4-2 Dynamic and SPO parameters of the ESDoF systems.

Config.	Dir.	T^* [s]	m^* [ton]	Γ	$Sa_y(T^*)$ [g]	ξ^* [%]	F_y^* [kN]	δ_y^* [m]	a_h	μ_c	a_c	r_p	μ_{UPD}	μ_{GC}
3st BF	**X**	0.68	534	1.30	0.51	5	2668	0.06	0.003	7.0	-0.11	0.51	0.62	11.4
	Y	0.69	543	1.29	0.49	5	2600	0.06	0.006	5.8	-0.12	0.52	0.64	10.2
3st IF	**X**	0.30	580	1.26	0.54	5	3059	0.01	0.07	4.6	-0.02	0.90	1.20	50.2
	Y	0.33	590	1.25	0.76	5	4422	0.02	0.04	3.1	-0.10	0.75	1.66	17.1
3st PF	**X**	0.47	730	1.09	0.58	5	4119	0.03	0.01	6.4	-0.03	0.61	1.31	23.5
	Y	0.50	731	1.09	0.66	5	4753	0.04	0.01	2.6	-0.04	0.60	1.21	11.8
6st BF	**X**	1.13	1177	1.31	0.25	5	2923	0.08	0.01	7.5	-0.15	0.54	0.88	11.0
	Y	0.87	1147	1.33	0.35	5	3941	0.07	0.02	5.1	-0.08	0.59	1.05	11.4
6st IF	**X**	0.57	1230	1.30	0.29	5	3485	0.02	0.03	4.7	-0.03	0.90	2.71	33.6
	Y	0.54	1247	1.30	0.43	5	5269	0.03	0.09	3.1	-0.07	0.86	1.98	17.6
6st PF	**X**	0.65	1401	1.26	0.27	5	3671	0.03	0.01	9.0	-0.02	0.66	2.51	30.0
	Y	0.57	1251	1.33	0.37	5	4581	0.03	0.17	2.2	-0.03	0.67	1.77	17.9
9st BF	**X**	1.86	1774	1.31	0.14	5	2423	0.12	0.01	7.3	-0.10	0.56	0.87	11.4
	Y	1.68	1725	1.34	0.16	5	2707	0.11	0.02	7.8	-0.08	0.68	0.91	12.9
9st IF	**X**	0.78	1728	1.31	0.17	5	2936	0.03	0.03	4.7	-0.02	0.85	2.64	48.8
	Y	0.84	1695	1.36	0.22	5	3589	0.04	0.12	2.6	-0.02	0.56	1.75	28.1
9st PF	**X**	0.87	2012	1.30	0.16	5	3140	0.03	0.02	4.2	-0.02	0.89	2.42	40.2
	Y	0.89	1853	1.33	0.21	5	3859	0.04	0.002	9.0	-0.02	0.62	1.47	28.9

4.5 Original fragility assessment

Original fragilities were obtained by means of MSA, performed in terms of IM_1 of the described ESDoF systems. The details of the analyses, such as the GM record selection and the number of stripes can be found in Section 2.3.2. It should be noted that, the demand-over-capacity (D/C) ratio of the roof-top displacement was considered as the EDP for both the two

performance levels such that $EDP_f = 1$ in any case (hereafter, the EDPs for UPD and GC are denoted as D/C_{UPD} and D/C_{GC}, respectively, to make a distinction between the two; note that the latter corresponds to D/C in the preceding chapters).

As an example, Figure 4-2a,b show the mean spectra of the GM records for the ten stripes and the obtained collapse D/C ratios (D/C_{GC}) against IM_1 and IM_2 for the 6st PF building (shown in Figure 4-1), for the case when the target IM_2 is PGA. In this case, MSA was performed up to $Sa(0.5s)$ equal to 7.64g that corresponds to the largest return period of exceedance considered. The response data corresponding to the failure cases (denoted with blue markers) and the number of the observations are provided in Figure 4-2b.

Because, even for the same structure, the assessment of the original fragility needs to be performed for each pair of $\{IM_1, IM_2\}$, the following discusses the fragility results separately for the IM conversions to PGA and those to a spectral acceleration at a larger period than that of the original IM.

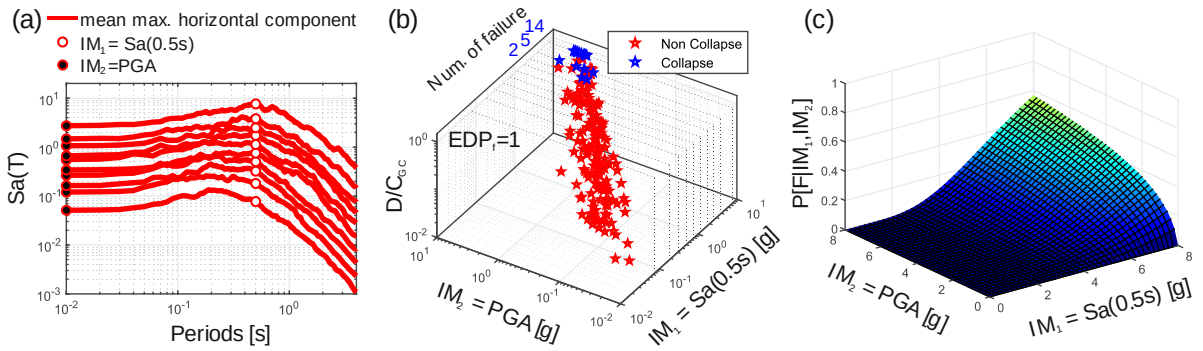

Figure 4-2 Results of original fragility assessment; (a) mean spectra of GM records;(b) collapse D/C ratios against the two IMs; (c) computed collapse fragility surfaces using $\{IM_1, IM_2\}$.

4.5.1 Fragility assessment for PGA as the target IM

This subsection discusses original fragilities when $IM_2 = \text{PGA}$. Multiple linear regression analyses were performed via Eq. (4-9) using the EDP response data obtained from MSA (e.g., Figure 4-2b). For each structure and each performance level, the linear regression models

involving the three IMs, $\{IM_1, IM_2, M, R\}$, $\{IM_1, IM_2\}$, and IM_1, were obtained.[6] In fact, these linear regression models varying the candidate variables were also utilized to examine the efficiency and sufficiency criteria for the candidate IMs. The efficiency of an IM can be measured by the standard deviation of the regression analysis, σ_η. One can establish the sufficiency of IM based on the effectiveness of the GM characteristics, though a comparison with the regression model involving the GM characteristics, additionally to the IM, as the explanatory variables. It is the case that the regression coefficients for the GM characteristic variables are statistically insignificant and/or the standard deviation of the regression, σ_η is improved from the simple regression model on the IM [Jalayer and Cornell, 2003; Elefante et al., 2010]. To this aim, the regression analysis using $\{IM_1, M, R\}$ was additionally performed via Eq. (4-9) (under $\beta_2 = 0$) to examine the sufficiency of IM_1 for each conversion.

Table 4-3 provides the regression results for the three IM cases with respect to the GC and UPD performance levels, as well as those for the additional IMs intended for the sufficiency tests. In all considered cases, the joint consideration of all four variables resulted, as expected, in the lowest σ_η values. Nonetheless, IM_1 alone generally provided σ_η values comparable to the vector-valued IMs, showing its efficiency (i.e., 3st PF, 6st IF/PF, all 9st frames). In such cases, IM_1 appeared to be also a sufficient IM, which is supported by the regression models considering $\{IM_1, M, R\}$; comparable σ_η values to those of the simple regression models using IM_1 and small regression coefficients for magnitude and distance (since the regression coefficients in the table tell changes in terms of logarithm of EDP due a unit change in each variable, the latter was also confirmed through standardized regressions eliminating the unit scale problem).

[6] It should be noted that, as a possible alternative to fit the fragility functions, logistic regression analyses were also performed; however, the log-linear model setting the EDP values equal to 1, in case of numerical instabilities, was found more effective to assess the GC fragility functions.

Table 4-3 Multiple linear regression analysis results of collapse fragility assessment ($IM_2 = PGA$).

Con-fig.	PL	UPD - $EDP = D/C_{UPD}$						GC - $EDP = D/C_{GC}$					
	IM	β_0	β_1	β_2	β_3	β_4	σ_η	β_0	β_1	β_2	β_3	β_4	σ_η
3st BF	$\{Sa(1.0s), PGA, M, R\}$	1.14	0.62	0.35	0.06	0.02	0.27	-1.63	0.66	0.34	0.05	0.01	0.27
	$\{Sa(1.0s), PGA\}$	1.52	0.68	0.32	-	-	0.27	-1.27	0.71	0.31	-	-	0.28
	$\{Sa(1.0s), M, R\}$	1.55	0.95	-	-0.02	0.01	0.33	-1.27	0.97		-0.02	0.004	0.32
	$Sa(1.0s)$	1.42	0.93	-	-	-	0.32	-1.38	0.95	-	-	-	0.32
3st IF	$\{Sa(0.15s), PGA, M, R\}$	0.94	-0.45	1.43	0.11	-0.0003	0.49	-2.09	-0.56	1.55	0.13	-0.03	0.51
	$\{Sa(0.15s), PGA\}$	1.50	-0.36	1.45	-	-	0.50	-1.46	-0.44	1.57	-	-	0.52
	$\{Sa(0.15s), M, R\}$	-0.24	1.04	-	0.12	-0.004	0.62	-3.32	1.07	-	0.14	-0.03	0.66
	$Sa(0.15s)$	0.38	1.16	-	-	-	0.63	-2.65	1.22	-	-	-	0.67
3st PF	$\{Sa(0.5s), PGA, M, R\}$	0.23	0.90	0.10	0.04	-0.04	0.26	-2.32	0.80	0.19	0.07	-0.09	0.33
	$\{Sa(0.5s), PGA\}$	0.38	0.94	0.10	-	-	0.26	-2.06	0.87	0.20	-	-	0.35
	$\{Sa(0.5s), M, R\}$	0.23	0.99	-	0.03	-0.05	0.26	-2.32	0.97	-	0.05	-0.10	0.34
	$Sa(0.5s)$	0.31	1.02	-	-	-	0.26	-2.19	1.04	-	-	-	0.36
6st BF	$\{Sa(1.5s), PGA, M, R\}$	1.26	0.67	0.29	0.05	0.003	0.26	-1.13	0.68	0.30	0.05	-0.007	0.27
	$\{Sa(1.5s), PGA\}$	1.63	0.72	0.26	-	-	0.26	-0.80	0.73	0.28	-	-	0.27
	$\{Sa(1.5s), M, R\}$	1.81	0.94	-	-0.02	-0.01	0.31	-0.57	0.95	-	-0.03	-0.02	0.31
	$Sa(1.5s)$	1.63	0.93	-	-	-	0.31	-0.80	0.94	-	-	-	0.32
6st IF	$\{Sa(0.5s), PGA, M, R\}$	-0.34	0.80	0.13	0.13	-0.10	0.37	-2.65	0.74	0.20	0.14	-0.11	0.40
	$\{Sa(0.5s), PGA\}$	0.22	0.95	0.11	-	-	0.40	-2.04	0.91	0.19	-	-	0.43
	$\{Sa(0.5s), M, R\}$	-0.35	0.92	-	0.12	-0.10	0.37	-2.65	0.93	-	0.12	-0.12	0.41
	$Sa(0.5s)$	0.15	1.04	-	-	-	0.40	-2.16	1.07	-	-	-	0.43
6st PF	$\{Sa(0.5s), PGA, M, R\}$	-0.37	0.74	0.17	0.15	-0.10	0.39	-2.76	0.71	0.22	0.16	-0.12	0.41
	$\{Sa(0.5s), PGA\}$	0.25	0.91	0.14	-	-	0.42	-2.05	0.90	0.20	-	-	0.45
	$\{Sa(0.5s), M, R\}$	-0.38	0.90	-	0.13	-0.11	0.40	-2.77	0.91	-	0.14	-0.13	0.42
	$Sa(0.5s)$	0.16	1.03	-	-	-	0.43	-2.18	1.07	-	-	-	0.45
9st BF	$\{Sa(2.0s), PGA, M, R\}$	1.93	0.86	0.10	0.01	0.01	0.23	-0.65	0.89	0.10	0.02	0.01	0.25
	$\{Sa(2.0s), PGA\}$	2.05	0.87	0.10	-	-	0.23	-0.50	0.90	0.09	-	-	0.25
	$\{Sa(2.0s), M, R\}$	2.15	0.97	-	-0.01	0.01	0.24	-0.45	0.98	-	-0.005	0.02	0.26
	$Sa(2.0s)$	2.08	0.95	-	-	-	0.24	-0.47	0.97	-	-	-	0.26
9st IF	$\{Sa(1.0s), PGA, M, R\}$	0.56	0.78	0.17	0.10	-0.03	0.32	-2.29	0.80	0.18	0.11	-0.04	0.36
	$\{Sa(1.0s), PGA\}$	1.15	0.88	0.13	-	-	0.33	-1.62	0.91	0.13	-	-	0.37
	$\{Sa(1.0s), M, R\}$	0.74	0.93	-	0.06	-0.04	0.33	-2.10	0.96	-	0.08	-0.04	0.37
	$Sa(1.0s)$	1.10	0.99	-	-	-	0.33	-1.66	1.02	-	-	-	0.38
9st PF	$\{Sa(1.0s), PGA, M, R\}$	0.46	0.80	0.09	0.12	-0.04	0.31	-2.46	0.84	0.10	0.13	-0.03	0.36
	$\{Sa(1.0s), PGA\}$	1.16	0.93	0.04	-	-	0.32	-1.65	0.97	0.05	-	-	0.37
	$\{Sa(1.0s), M, R\}$	0.56	0.88	-	0.10	-0.05	0.31	-2.35	0.93	-	0.11	-0.03	0.36
	$Sa(1.0s)$	1.14	0.96	-	-	-	0.32	-1.67	1.01	-	-	-	0.37

However, there are a few exceptional cases. In the cases of the 3st and 6st BFs, the regression results suggest that the two-parameter model $\{IM_1, IM_2\}$ may be the optimal choice with respect to the other options investigated. For each structure, the two-parameter model's σ_η was comparable to that of the four-parameter regression model, while it was improved by more than 15% with respect to the regression model involving IM_1 only . The use of $\{IM_1, IM_2\}$ improved the performance of the model with respect to IM_1 presumably because these structures have their T^* periods relatively apart from T_1 at least in one horizontal direction (see Table 4-1). Another exception is the case of 3st IF: the estimates of the regression coefficients for IM_1 resulted to be negative, possibly because of the correlation of the IMs at close vibration periods. The trends discussed above were also observed regardless the performance level considered.[7]

Based on the regression results, fragility functions were derived using Eqs. (4-7) and (4-8). As an example, Figure 4-2c illustrates the computed GC fragility surfaces using $\{IM_1, IM_2\}$ for the 6st PF building of Figure 4-1 and Figure 4-2a, b. It can be seen that the failure probability increases principally with IM_1, yet showing a slight increase with IM_2 for a given IM_1.

4.5.2 Fragility assessment for spectral acceleration as the target IM

This subsection presents the results of the fragility assessment for converting $IM_1 = Sa(0.5s)$ to spectral acceleration at a longer period, $T = \{1.0s, 1.5s, 2.0s\}$. Table 4-4 provides the multiple regression results of D/C_{UPD} and/or D/C_{GC} for these conversion cases. Generally, it is observed that $\{IM_1, IM_2\}$ reduces σ_η by approximately 20% from that estimated by the regression model considering IM_1 only. No significant change in σ_η between the four- and two-parameter regression models supports the sufficiency hypothesis of $\{IM_1, IM_2\}$.

It should be noted that, when IM_2 is spectral acceleration at a period longer than the

[7] This study also examined the sufficiency and efficiency of the candidate IMs by performing the regression of the residual EDP given IM on each of the GM characteristics (the approach set forth by [Luco and Cornell, 2007]). The similar results on the explanatory power of the candidate IMs were also observed for each structure.

fundamental period(s) of the structure, one challenge is to appropriately model the interaction between IM_1 and IM_2 in a linear regression. For example, as discussed in [Baker, 2007], structural response can be less sensitive to IM_2 levels at low IM_1 levels when the structure behaves in the linear range, while the sensitivity of structural response to IM_2 (or *practicality* [Giovenale et al., 2004] of IM_2) increases at large IM_1 levels; i.e., in the non-linear range.

As a matter of fact, the multiple linear regression results in the table show that the regression coefficients corresponding to the four explanatory variables remain almost the same between the UPD and GC performance levels, and only the intercept β_0 shifts. This means that the difference in the corresponding EDP per-unit increase of each explanatory variable does not change. To handle this issue, this study also attempted some alternative solutions, among which a logistic regression model using the collapse data was the most effective. The computed two-parameter logistic regression models using the sufficient and efficient $\{IM_1, IM_2\}$ fit the observed non-collapse and collapse data with a relatively large logistic R-squared measure, R_L^2 [Efron, 1978]. Hence, the fragility surface modelled using Eqs. (4-9)-(4-10) was additionally examined through the conversion case using $\{IM_1, IM_2\}$ for all considered periods of IM_2.[8] Conversely to the linear regression models, the logistic regression models showed the dominant effect of IM_2 on the EDP rather than that of IM_1; see the estimates of the regression coefficients in Table 4-4.

As in the conversion to PGA, the original fragility functions with respect to the two performance levels were principally derived via Eqs. (4-7)-(4-8) using the three IMs. For each different IM_2, the models combining linear and logistic regression models (defined by Eqs. (4-7)-(4-10); hereafter denoted as *hybrid*) were also additionally explored using $\{IM_1, IM_2\}$ only with respect to GC. In the general (linear regression) models, the collapse data were included assigning the corresponding EDP values equal to 1 instead of performing the logistic regression.

[8] In MSA for the 6st IF building, 21 collapse cases were observed in total (similar as Figure 4-2), thus the logistic regression on more than two predictor variables were not performed in this study following *ten-events-per-variable* rule).

Table 4-4 Multiple regression analysis results cases; ($IM_2 = Sa(T > 0.5s)$).

Con-fig.	PL	UPD - $EDP = D/C_{UPD}$						GC - $EDP = D/C_{GC}$					
	IM	β_0	β_1	β_0	β_1	β_0	β_1	β_0	β_1	β_0	β_1	β_0	β_1
6st IF	$\{Sa(0.5s), Sa(1.0s), M, R\}$	0.56	0.52	0.46	0.01	-0.05	0.29	-1.75	0.51	0.47	0.01	-0.06	0.33
	$\{Sa(0.5s), Sa(1.0s)\}$	0.57	0.53	0.48			0.29	-1.76	0.52	0.50	-	-	0.33
	$\{Sa(0.5s), Sa(1.5s), M, R\}$	1.11	0.63	0.39	-0.05	-0.05	0.30	-1.23	0.63	0.38	-0.05	-0.06	0.34
	$\{Sa(0.5s), Sa(1.5s)\}$	0.71	0.64	0.36	-	-	0.31	-1.61	0.64	0.36	-	-	0.35
	$\{Sa(0.5s), Sa(2.0s), M, R\}$	1.36	0.67	0.36	-0.06	-0.05	0.28	-1.00	0.66	0.36	-0.06	-0.06	0.33
	$\{Sa(0.5s), Sa(2.0s)\}$	0.87	0.67	0.33	-	-	0.29	-1.46	0.67	0.33	-	-	0.34
	$Sa(0.5s)$	0.15	1.04	-	-	-	0.40	-2.16	1.07	-	-	-	0.43
	IM	$\beta_{0,L}$	$\beta_{1,L}$	$\beta_{2,L}$	$\beta_{3,L}$	$\beta_{4,L}$	R_L^2	$\beta_{0,L}$	$\beta_{1,L}$	$\beta_{2,L}$	$\beta_{3,L}$	$\beta_{4,L}$	R_L^2
	$\{Sa(0.5s), Sa(1.0s)\}$	-	-	-	-	-	-	-5.06	0.14	4.10	-	-	0.67
	$\{Sa(0.5s), Sa(1.5s)\}$	-	-	-	-	-	-	-4.33	0.82	5.21	-	-	0.72
	$\{Sa(0.5s), Sa(2.0s)\}$	-	-	-	-	-	-	-2.70	1.39	4.50	-	-	0.76

4.5.3 Site-specific seismic hazard functions for conversion

PSHA was performed for the site in L'Aquila, in order to characterize the site-specific hazard functions required in the IM conversion framework (Section 4.2.4). The source model used for PSHA corresponds to *branch 921* of the logic tree involved in the official Italian hazard model [Stucchi et al., 2011]. For all target IMs, the hazard disaggregation results given IM_2 $\left(f_{M,R|IM_2}\right)$ were obtained via REASSESS [Chioccarelli et al., 2018]. In order to obtain a fragility function in terms of IM_2, the disaggregation was repeatedly performed at each step of IM_2 up to an upper limit value of the target IM. For all possible combinations of $\{IM_2, M, R\}$, the conditional PDF of $f_{IM_1|M,R,IM_2}$ was computed via Eq. (4-6) using the parameters from the cited GMPEs with the correlation model developed by [Baker and Jayaram, 2008]. The correlation coefficients for the considered combinations of the IMs are summarized in Table 4-5. The correlation coefficients between PGA and the candidate $Sa(T)$ ranges between approximately 0.35 and 0.89, decreasing with an increase of the vibration period. Those between $Sa(0.5s)$ and $Sa(T)$ at a period longer than 0.5s are from 0.51 to 0.75. The closer two vibration periods, the higher the correlation coefficients for the two IMs.

To better understand this issue, Figure 4-3a shows hazard disaggregation conditional to PGA equal to 0.9g (corresponding to $T_R = 5.6\times10^3$) at the site of interest, L'Aquila. Against the spectral acceleration measures at the shortest and longest periods, Figure 4-3b,c present the

Table 4-5 Correlation coefficients between IM_1 and IM_2.

$\rho_{\ln IM_1,\ln IM_2}$	$Sa(0.15s)$	$Sa(0.5s)$	$Sa(1.0s)$	$Sa(1.5s)$	$Sa(2.0s)$	$\rho_{\ln IM_1,\ln IM_2}$	$Sa(1.0s)$	$Sa(1.5s)$	$Sa(2.0s)$
PGA	0.8876	0.6862	0.5243	0.4255	0.3539	$Sa(0.5s)$	0.7490	0.6087	0.5141

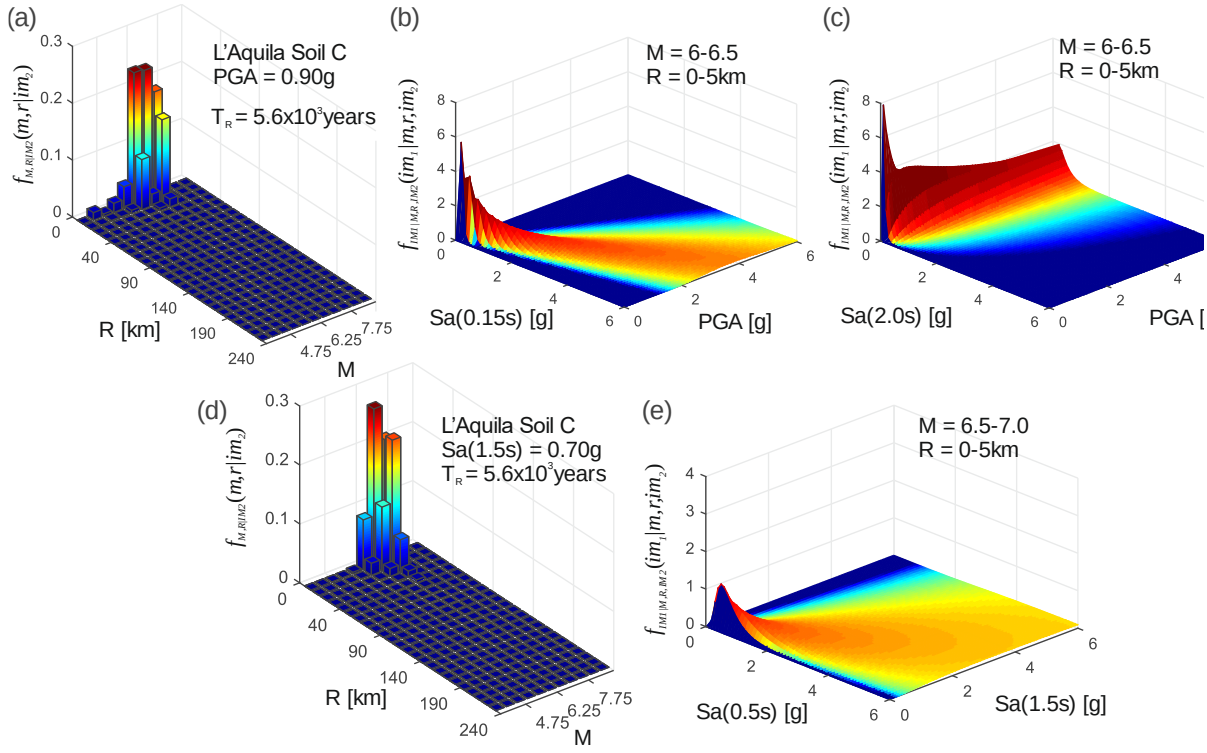

Figure 4-3 PSHA results;(a) hazard disaggregation for PGA = 0.90g corresponding to $T_R = 5.6\times10^3$ yrs at L'Aquila; examples of conditional PDF of (b) $Sa(0.15s)$ and (c) $Sa(2.0s)$ given PGA; (d) hazard disaggregation for $Sa(1.5s)$ = 0.70g corresponding to $T_R = 5.6\times10^3$ yrs at L'Aquila; examples of conditional PDF of (e) $Sa(0.5s)$ given $Sa(1.5s)$

.

conditional distribution $f_{IM_1|M,R,IM_2}$ given a certain PGA value, magnitude $M \in (6.0, 6.5)$ and $R \in (0\text{km}, 5\text{km})$, which is the scenario dominating the hazard being disaggregated in Figure 4-3a. It can be clearly seen from these figures that, the area exhibiting a comparatively large probability density shifts from the proximity of the diagonal of the $IM_1 - IM_2$ domain (the warm-colored area in Figure 4-3b) to the corner corresponding to low IM_1 levels (Figure 4-3c) with an increase of the fundamental period of the structure (i.e., an decrease of the correlation coefficient between two periods; see Table 4-5). Given that the original fragility

functions are weighted by the corresponding hazard function through the conversion integral, it is indicated that the reliability of the adopted fragility model is particularly important in the $IM_1 - IM_2$ range showing a relatively large value of the PDF of IM_1 given IM_2. Figure 4-3d,e provides similar results for one of the conversions from $Sa(0.5s)$ to spectral acceleration at a period longer than 0.5s; i.e., hazard disaggregation conditional to $Sa(1.5s)$ equal to 0.7g at the same site and the conditional distribution $f_{IM_1|M,R,IM_2}$ given $Sa(1.5s)$ and the dominating scenario in the disaggregation. On the contrary to Figure 4-3b,c, the area corresponding to the mid-to-high value of the conditional PDF widely spreads over the $IM_1 - IM_2$ domain due to moderate correlations between the two IMs.

4.5.4 Reference fragility analyses

As illustrated in Figure 4-4a,b, the reference fragility assessment involves MSA performed in a similar manner as for the original fragility assessment (Figure 4-2a,b), yet considering seismic input based on site's hazard in terms of IM_2. Since record sets selected based on PGA hazard were not available from the datasets of the RINTC project, ad-hoc GM record sets were selected for the multiple PGA levels (i.e., stripes; see Appendix). The target CS given a certain PGA value was computed using the hazard models used in PSHA, then twenty GM records were selected from the NEES database [Luzi et al., 2016; Pacor et al., 2018] so as to match the target CS pertaining to each stripe (Figure 4-4a). It should be noted that the PGA domain was discretized via the exceedance return periods specified above, plus two additional return periods corresponding to $T_R = 10^6$ and $T_R = 10^7$ years (i.e., twelve stripes in total). The additional two PGA levels were considered so as to render the reference fragility up to a large PGA level. In fact, generally a small number of the collapse cases was observed even at the tenth PGA level in the majority of the cases (e.g., 5 collapse cases, as shown in Figure 4-4b), then the analysis was continued until the number of the collapse cases had reached more than 50% of the total number of the records per stripe (i.e., more than 10). As it regards the cases when the target IM is Sa at $T = \{1.0s, 1.5s, 2.0s\}$, the GM record sets collected in the RINTC project (i.e., those used above for the original fragility assessment of the BF and/or 9st buildings) were used.

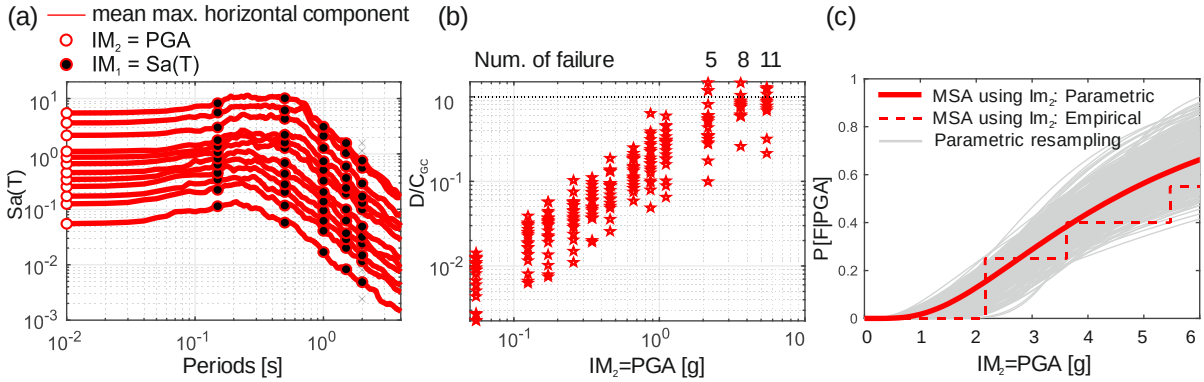

Figure 4-4 MSA for reference target fragility; (a) mean spectra of GM records; (b) collapse D/C ratios and number of failure cases; (c) reference target fragility estimated via maximum likelihood.

Whereas the original fragility assessment (Sections 4.5.1, 4.5.2) employed only parametric one, the reference fragility functions were evaluated by both (i) non-parametric and (ii) parametric approaches (Figure 4-4c). The former was adopted to interpret as-observed probability distributions without involving any particular assumption on the probabilistic model. The latter was used to make the converted and reference curves comparable by means of a few parameters, including uncertainty of estimation. For each ($i-th$) stripe of $IM_2 = im_{2,i}$, non-parametric fragility was given by Eq. (1-16) while parametric fragility was estimated using (1-15). For further computational details, see Chapter 1.

Table 4-6 shows the results of the estimated fragility parameters with respect to PGA for the nine structures, and Table 4-7 provides those with respect to spectral acceleration at the three periods examined for the 6st IF building. To assess the estimation uncertainties, the expected value and standard deviation of each fragility parameter were estimated through parametric resampling [Iervolino, 2017]. In each table, the expected values $(E[\bullet])$ and coefficients of variation (CoV) of $\{\hat{\theta}, \hat{\beta}\}$ are provided. In Table 4-6, it can be seen that the low-rise structures with relatively short fundamental vibration periods, tend to show a smaller value of median PGA causing failure, $E[\hat{\theta}_{PGA}]$, compared to the taller buildings featuring relatively long vibration periods. This trend is clearly seen in θ_{PGA} particularly with respect to GC (3.3g of the shortest period vs 8.4g of the longest period structures), and its dispersion,

evaluated by its CoV, evolves with an increase of the vibration periods of the structure. The logarithmic standard deviation also shows the increasing trends of the mean and variance with the vibration period of the structure and with the performance level: $E\left[\hat{\beta}_{PGA}\right]$ varies between 0.37-0.52 for the UPD and 0.49-0.89 for the GC fragilities, being associated with the CoVs of 13-15% and 19-30%, respectively.

Table 4-7 shows the lognormal fragility parameters of the same building but expressed in terms of $Sa(T)$ at the three different periods, $T=\{1.0s,1.5s,2.0s\}$, i.e., $\left\{\hat{\theta}_{Sa(T)},\beta_{Sa(T)}\right\}$. $E\left[\hat{\theta}_{Sa(T)}\right]$ decreases with an increase of the vibration period of the target IM, while $E\left[\hat{\beta}_{Sa(T)}\right]$ increases with it. For both of the two parameters, larger estimation uncertainties (the CoVs) were observed particularly with respect to the GC performance levels, as expected.

The plots of the reference fragility curves, obtained via non-parametric, parametric, and parametric sampling approaches, are all provided in the following section in comparison with the IM conversion results. As an example, the resampled fragility curves, corresponding to 500 simulations are given as grey lines in Figure 4-4c.

Table 4-6 Estimated lognormal fragility parameters in reference analyses (IM_2 =PGA).

	PL config.	**UPD**						**GC**					
		BF		**IF**		**PF**		**BF**		**IF**		**PF**	
Story	Parameter	$E[\bullet]$	**CoV**	$E[\bullet]$	**CoV**	$E[\bullet]$	**CoV**	$E[\bullet]$	**CoV**	$E[\bullet]$	**CoV**	$E[\bullet]$	**CoV**
3st	$\hat{\theta}_{PGA}$ **[g]**	0.29	7%	0.32	5%	0.45	6%	3.90	11%	3.34	9%	3.91	11%
	$\hat{\beta}_{PGA}$	0.51	13%	0.37	15%	0.43	14%	0.62	20%	0.49	19%	0.55	19%
6st	$\hat{\theta}_{PGA}$ **[g]**	0.44	6%	0.62	6%	0.56	6%	5.32	20%	4.67	15%	4.54	14%
	$\hat{\beta}_{PGA}$	0.41	14%	0.41	14%	0.40	14%	0.74	25%	0.69	21%	0.69	22%
9st	$\hat{\theta}_{PGA}$ **[g]**	0.54	6%	0.50	6%	0.47	7%	8.37	39%	7.41	33%	7.37	34%
	$\hat{\beta}_{PGA}$	0.49	13%	0.40	14%	0.52	13%	0.89	30%	0.75	30%	0.81	29%

Table 4-7 Estimated lognormal fragility parameters in reference analyses ($IM_2 = Sa(T>0.5s)$).

	PL IM_2	**UPD**						**GC**					
		$Sa(1.0s)$		$Sa(1.5s)$		$Sa(2.0s)$		$Sa(1.0s)$		$Sa(1.5s)$		$Sa(2.0s)$	
	Parameter	$E[\bullet]$	**CoV**	$E[\bullet]$	**CoV**	$E[\bullet]$	**CoV**	$E[\bullet]$	**CoV**	$E[\bullet]$	**CoV**	$E[\bullet]$	**CoV**
6st IF	$\hat{\theta}_{Sa(T)}$ **[g]**	0.58	6%	0.29	9%	0.19	9%	3.42	10%	1.88	9%	1.85	70%
	$\hat{\beta}_{Sa(T)}$	0.30	20%	0.61	14%	0.59	14%	0.27	61%	0.25	55%	0.46	78%

4.6 Results and discussion

4.6.1 IM Conversion to PGA

This subsection presents the results of the IM conversion from $Sa(T)$ to PGA for both the UPD and collapse fragility curves. For each of the nine buildings, the three conversion cases were compared with the results from the reference analyses.

4.6.1.1 Usability-preventing damage fragility

The PGA-based fragility curves were derived from the original fragility functions and site-specific hazard functions through the conversion formulas of Eqs. (4-2)-(4-4). The results of the three conversion cases, each involving $\{IM_1, IM_2, M, R\}$, $\{IM_1, IM_2\}$ and IM_1, are presented in Figure 4-5 for the nine building cases, together with the reference analysis results. It can be observed that all three conversion cases show apparently comparable results in the cases where the scalar IM_1 is a sufficient and comparably efficient measure with respect to the vector IMs.

Conversely, it can be seen that the curves converted using the vector-valued IMs have better agreement with the reference curves (empirical and parametric) at upper tails in the cases where the two-parameter vector $\{IM_1, IM_2\}$ is sufficient and more efficient than IM_1 (3st and 6st BF). As it regards the reference fragilities, the lognormal fragility fits the empirical one, except the longest period structure (9st BF) where some discrepancies start to arise at larger PGA levels. In this case, the converted fragility curves apparently track better the empirical one than the set of parametric fragility curves. It can be also seen that most of the conversion cases rendered the fragility estimates within the band of the resampled fragility curves indicating estimation uncertainties. Particularly, the conversion involving the optimal IM led to the median estimates $\left(\hat{\theta}_{PGA}\right)$ with 1–34% difference with respect to the expected values from the parametric resampling.

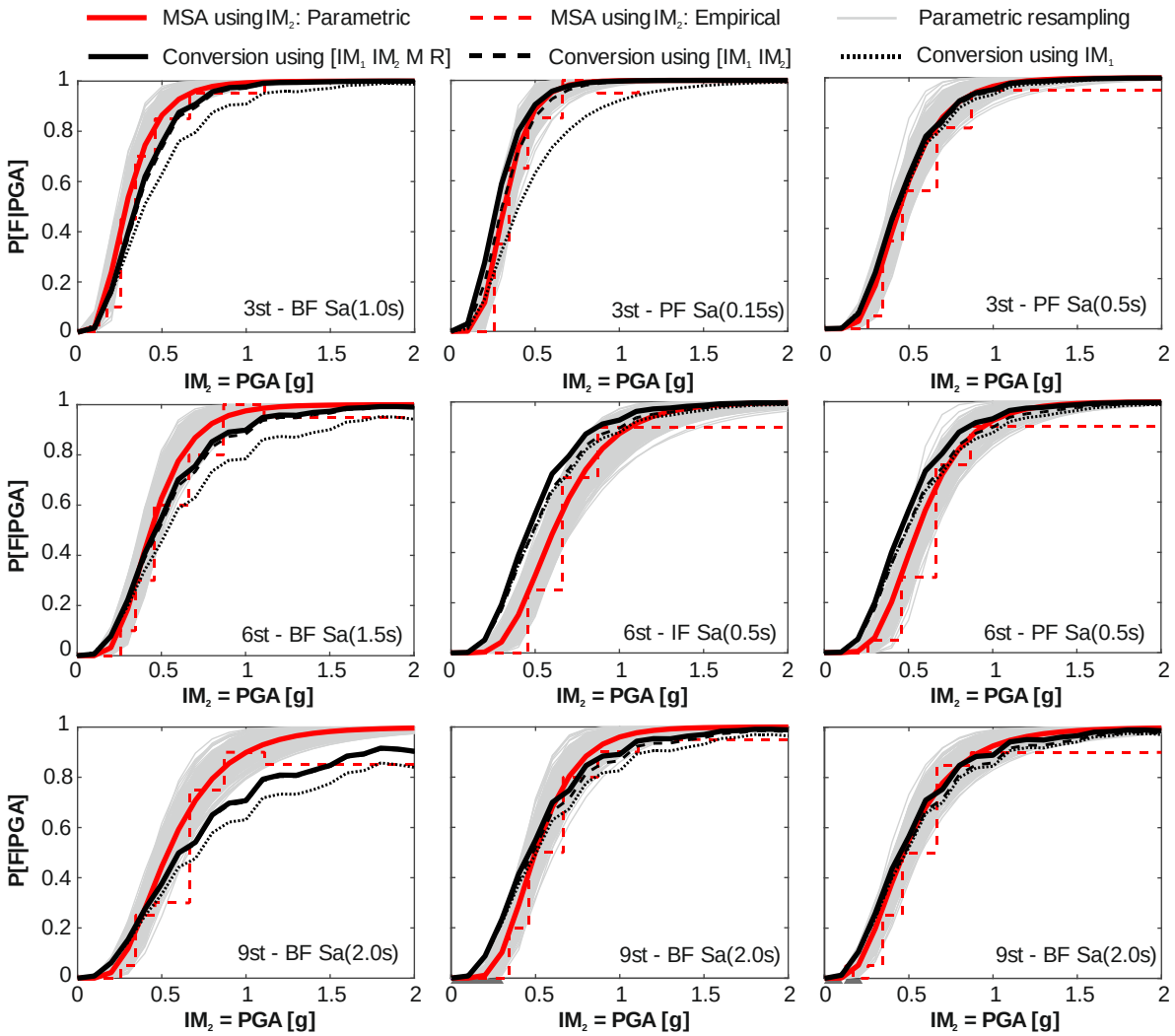

Figure 4-5 Comparison of converted and reference fragility curves with respect to UPD ($IM_2 = PGA$).

4.6.1.2 Collapse fragility

The results of the collapse fragility curves in terms of PGA are presented in Figure 4-6 for the nine building cases. The results not only show somewhat similar trends as the UPD fragilities but also may support that the performance of the IM conversion depends on the combination of the original and target IMs. In cases of converting from an intermediate period ranging from 0.5s to 1.5s, all three conversion cases showed apparently comparable results to the reference curves when the appropriate IM was considered. Indeed, the median estimates $\left(\hat{\theta}_{PGA}\right)$ feature 2%-25% differences with respect to the expected value estimated from the resampled parametric fragilities, $E\left[\hat{\theta}_{PGA}\right]$.

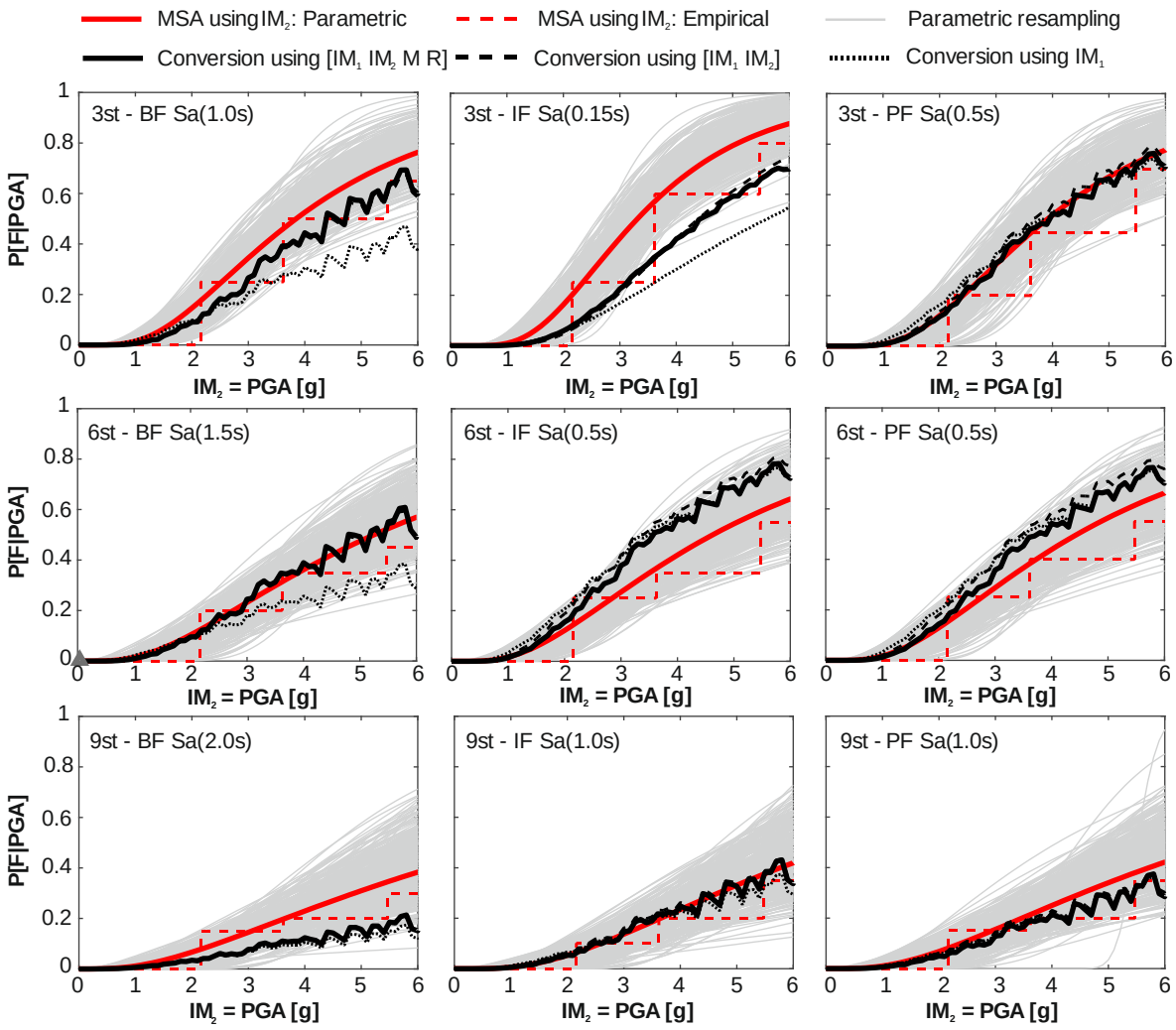

Figure 4-6 Comparison of converted and reference fragility curves with respect to GC ($IM_2 = PGA$).

On the contrary, larger discrepancies with the target fragility estimates were observed in the IM conversion from the spectral acceleration at the shortest and the longest periods (i.e., 3st IF and 9st BF where IM_1 is $Sa(0.15s)$ and $Sa(2.0s)$, respectively). With respect to the former, all conversion cases led to an optimistic estimation of the reference fragility functions presumably because of involving relatively more correlated IMs ($\rho_{\ln IM_1, \ln IM_2} \simeq 0.9$), which also seem to have affected somewhat the estimates for the UPD fragility curves.

Regarding the conversion from $Sa(2.0s)$, it is considered the larger discrepancies are associated with the extrapolation of the regression model. As shown in Figure 4-4c, the major PDF contribution comes from a quite limited range of the $IM_1 - IM_2$ domain (i.e.,

corresponding to low values of IM_1). In fact, the structural response data at large IM_2 levels are rarely obtained under the seismic input conditioned with respect to IM_1 due to a weak correlation between the two IMs ($\rho_{\ln IM_1, \ln IM_2} \simeq 0.35$). In this case, the choice of regression models and/or fragility assessment procedures is also an issue. The resulting converted fragility can be sensitive to the form of the fragility surface in the local area with dominant hazard contribution.

Figure 4-7 illustrates the abovementioned issues showing the fragility surfaces in the $Sa(T) - PGA$ domain with respect to the considered two performance levels. In each panel of the figure, the data points used for the regression analyses are plotted together with the iso-probability lines for the fragility surfaces (for the sake of illustration, the plotted models correspond to the surfaces computed using $\{IM_1, IM_2\}$), as well as with $f_{IM_1|M,R,IM_2}$, namely, the hazard function of IM_1 conditional to the magnitude-distance scenario dominating the hazard disaggregation in Figure 4-4a. The left panel corresponds to the conversion from $Sa(0.5s)$ to PGA ($\rho_{\ln IM_1, \ln IM_2} \simeq 0.67$), while the right one shows the probabilistic models for the conversion from $Sa(2.0s)$. It can be clearly observed that, when the two IMs are moderately correlated (corresponding to the former), the data points defining the fragility surfaces (blue dots) cover the range corresponding to a high occurrence probability of IM_1 given IM_2 (dashed and solid black lines), and the model extrapolation does not significantly matter as its effect is compensated by the integration with the seismic hazard. Conversely, most of the data points in the right panel lie beyond the $IM_1 - IM_2$ range corresponding to a large value of the conditional PDF, thus extrapolation can substantially affect the converted fragility, in particular, with respect to the collapse performance level. Furthermore, unconservative underestimation of the collapse fragility in this conversion can be also ascribed to nearly-zero probabilities at the corners predicted by the adopted linear regression model.

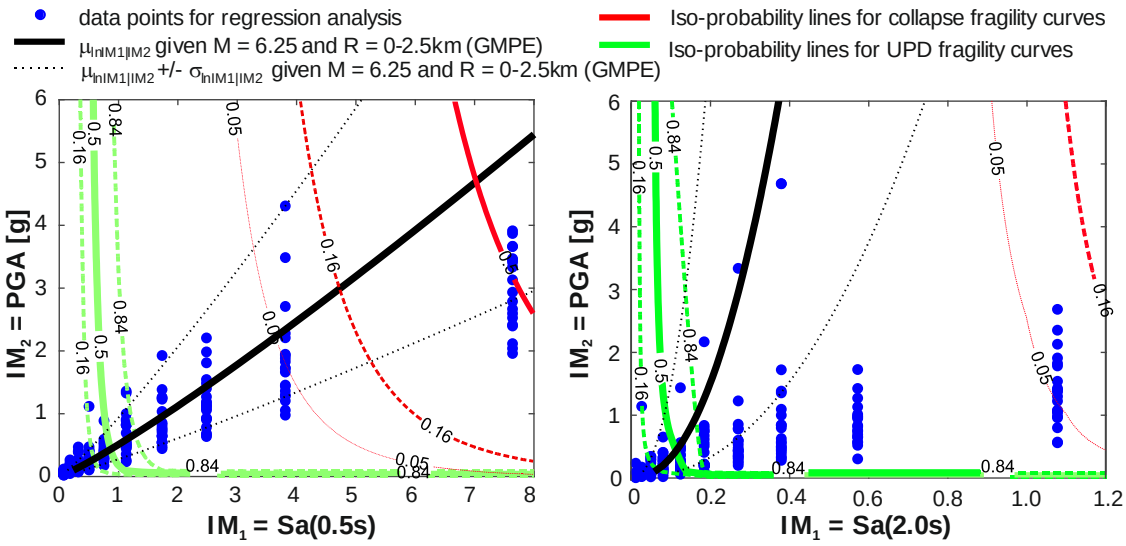

Figure 4-7 Comparisons of the fragility surfaces with respect to the two performance levels and the GMPE models; (left) 6st IF; (right) 9st BF.

4.6.2 IM conversion to spectral acceleration at a longer period

The IM conversions from $Sa(0.5s)$ to $Sa(T>0.5s)$ were also performed in a similar manner. The results for the IM conversions to the two performance levels are shown in Figure 4-8 for all three cases. Regarding the fragilities with respect UPD, all converted fragility curves derived from the linear regression models are generally in agreement with the reference curves, although the curves in terms of $Sa(1.0s)$ are located slightly at the left side to the group of the reference fragilities. When the collapse probability is concerned, however, all log-linear regression-driven fragility curves (denoted LR in the figure) resulted to underestimate the reference analysis at large IM_2 levels (e.g., beyond the ninth stripe corresponding to $Sa(1.5s)=1.0g$ or $T_R>10^4$ years in the figure). In such cases, the hybrid models utilizing the logistic regression apparently capture better the target curves from the reference MSA up to the largest IM_2 level corresponding to $T_R=10^5$ years ($Sa(1.5s)=2.0g$). Although large discrepancies at extremely large IM levels for a long period spectral acceleration generally may not significantly matter when integrated with a hazard curve, the resulting GC fragility significantly depends on the functional form adopted in the original fragility assessment.

It should be noted that the GC fragility conversion to $Sa(2.0s)$, again, turned out to be an exception due to the extension of the regression model far beyond the observation range

(see the previous subsection).

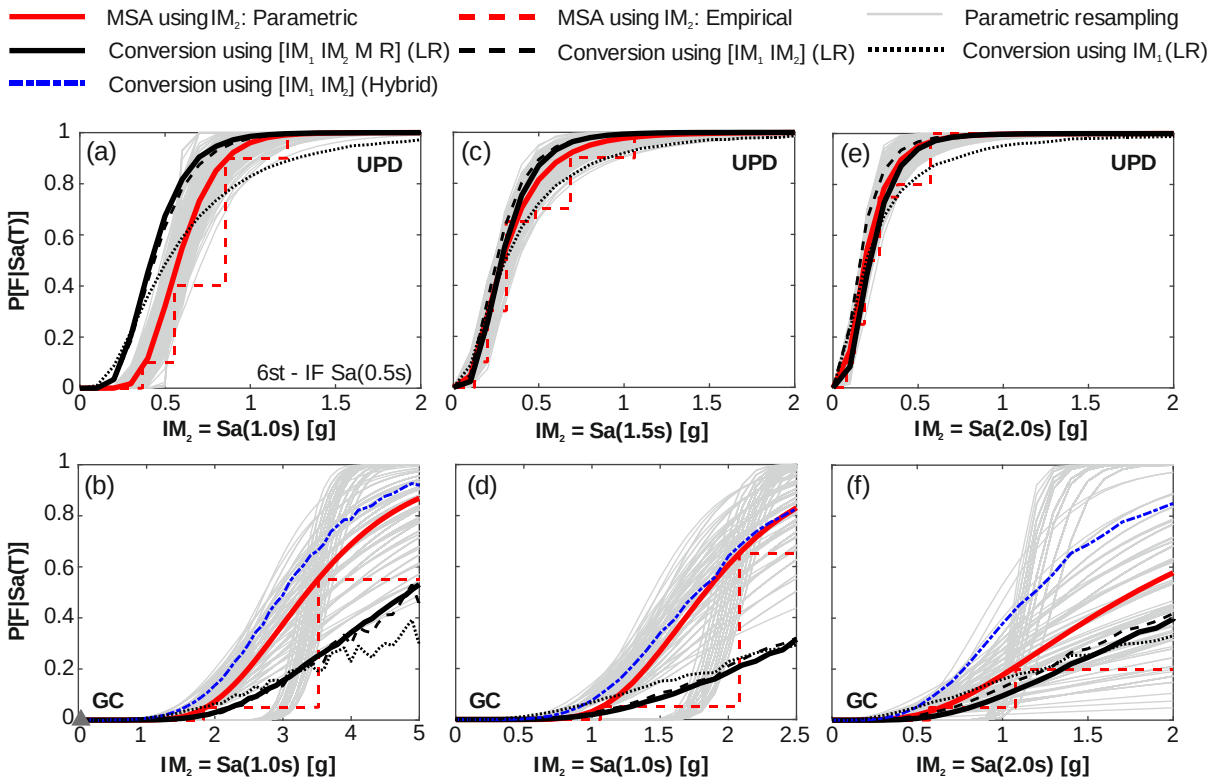

Figure 4-8 Comparison of converted and reference fragility curves in cases of the IM conversions to $IM_2 = Sa(T > 0.5s)$; (a,b) to $Sa(1.0s)$; (c,d) to $Sa(1.5s)$; (e,f) to $Sa(2.0s)$.

4.7 Application to the RINTC prototype buildings

4.7.1 Structural models

In order to compare the fragilities of the examined code-conforming buildings, this section applies the IM conversion framework to the other structural types as well. As with the RC buildings, the structures designed for the site of L'Aquila (soil C) were selected from each structural type (i.e., URM, RC, steel; PRC), aiming to obtain the collapse fragility curves expressed in terms of PGA. Table 4-8-Table 4-10 show the selected case study buildings and the structural properties (for the identification tags and the detailed structural properties, see Chapter 2), for which the conversion conditions are summarized in Table 4-11. In total, ten (four URM – 2st C3, E2, E8, E9 -, two steel Geo 1- Geo 2; and four PRC -Geo 1- Geo 4)

buildings were examined in addition to the nine RC buildings in the previous section. The selected EDP measures are basically analogous to those defined in Chapter 2 (the demand-to-capacity ratio, i.e., μ/μ_{GC}) for all structural types, except that the collapse in the beam-column connections was not considered for the PRC buildings in this application study; only the displacement-based collapse limit thresholds were considered for this structural type. As the study using the RC buildings revealed that the considerations on magnitude and distance give little improvement in the IM conversion in most of the cases, the results from the conversion cases involving the two-parameter vector-valued IMs will be discussed hereafter in order to optimize the computational cost and estimation accuracy.

Table 4-8 Dynamic and SPO parameters of the ESDoF systems (URM).

Story Config.	Dir.	T^* [s]	m^* [ton]	Γ	$Sa_y(T^*)$ [g]	ξ^* [%]	F_y^* [kN]	δ_y^* [m]	a_h	μ_c	a_c	r_p	μ_{GC}
2st C3	**X**	0.07	317	1.22	0.49	3	1523	6.57E-04	0	27.3	-0.40	0.65	38.1
	Y	0.07	323	1.25	0.48	3	1505	7.97E-04	0	26.9	-0.40	0.66	45.3
2st E2	**X**	0.13	322	1.22	0.47	3	1481	1.88E-03	0.006	30.2	-0.38	0.60	31.7
	Y	0.11	322	1.22	0.58	3	1846	1.81E-03	0.001	40.6	-0.09	0.69	44.6
2st E8	**X**	0.12	476	1.20	0.55	3	2584	1.99E-03	0.006	20.9	-0.10	0.55	26.4
	Y	0.12	475	1.20	0.51	3	2373	1.75E-03	0.006	27.8	-0.11	0.76	31.3
2st E9	**X**	0.12	535	1.20	0.54	3	2832	2.01E-03	0.017	20.6	-0.41	0.98	21.5
	Y	0.08	557	1.18	0.64	3	3483	1.02E-03	0.084	6.5	-0.21	0.63	10.4

Table 4-9 Dynamic and SPO parameters of the ESDoF systems (steel).

Config.	Dir.	T^* [s]	m^* [ton]	Γ	$Sa_y(T^*)$ [g]	ξ^* [%]	F_y^* [kN]	δ_y^* [m]	a_h	μ_c	a_c	r_p	μ_{GC}
Geo 1	**X**	0.51	73	1	2.73	5	1967	0.18	0.047	2.33	-0.041	1.02	3.4
	Y	0.27	73	1	0.77	5	557	0.01	0.003	-	-	-	8.3
Geo 2	**X**	0.58	95	1	2.10	5	1956	0.17	0.045	2.36	-0.09	0.96	3.4
	Y	0.28	95	1	0.88	5	820	0.02	0.003	-	-	-	6.9

Table 4-10 Dynamic and SPO parameters of the ESDoF systems (PRC).

Config.	Dir.	T^* [s]	m^* [ton]	Γ	$Sa_y(T^*)$ [g]	ξ^* [%]	F_y^* [kN]	δ_y^* [m]	a_h	μ_c	a_c	r_p	μ_{GC}
Geo 1	**X**	1.53	398	1	0.48	5	1865	0.28	0.214	2.08	-0.72	0.62	2.93
	Y	1.53	398	1	0.48	5	1865	0.28	0.214	2.08	-0.72	0.62	2.93
Geo 2	**X**	1.50	566	1	0.45	5	2513	0.25	0.197	2.57	-0.68	0.66	3.53
	Y	1.50	566	1	0.45	5	2513	0.25	0.197	2.57	-0.68	0.66	3.53
Geo 3	**X**	1.17	543	1	0.46	5	2473	0.16	0.048	3.40	-0.24	0.56	5.70
	Y	1.31	543	1	0.44	5	2324	0.18	0.050	3.29	-0.26	0.56	5.44
Geo 4	**X**	1.31	802	1	0.39	5	3097	0.17	0.045	3.31	-0.26	0.55	5.39
	Y	1.46	802	1	0.36	5	2870	0.19	0.048	3.17	-0.29	0.55	5.08

Table 4-11 Conversions under consideration.

Structural type	**URM**				**Steel**		**PRC**			
Story/ config.	**2st C3**	**2st E2**	**2st E8**	**2st E9**	**Geo 1**	**Geo 2**	**Geo 1**	**Geo 2**	**Geo 3**	**Geo 4**
$IM_1 = Sa(T)$	0.15s	0.15s	0.15s	0.15s	0.5s	0.5s	2.0s	2.0s	2.0s	2.0s
$IM_2 = Sa(T)$	0s (i.e., PGA)									

4.7.2 Definitions of fragility and hazard models

In order to characterize a multi-variable fragility function, this study utilized the D/C ratios of the adopted EDP obtained in Chapter 2. Using the sampled data of each case study, multi-variable regression analysis and logistic regression analysis were performed through Eq. (4-7) and Eq. (4-9), respectively, varying the number of the explanatory variables including the interaction term between the two IMs (i.e., $\beta_{12} \ln IM_1 \cdot \ln IM_2$; reasons to follow). Among all regression models corresponding to the candidate IMs, the results from the regression model with the optimal IM (i.e., sufficient and efficient) are provided in Table 4-12-Table 4-14. Since the URM and steel buildings have the fundamental periods intermediate between 0 and T corresponding to IM_1, the regression models indicated that the effect of PGA (IM_2) on structural response is comparable to or greater than $Sa(T)$. Particularly in cases of these two typologies, the linear regression models involving PGA and $Sa(T)$ (and their interaction) led to the smallest standard deviation, σ_η, and the logistic regressions at least including IM_2 resulted in a satisfactory goodness of fitting for all examined buildings ($R_L^2 > 0.77$). As regards the PRC buildings, conversely, the logistic regression models were rejected for a low test's accuracy presumably because of the small explanatory power of IM_2 on structural response (the same for the RC buildings). Hence, this study included the collapse data in the multiple linear regression by setting their EDP values equal to 1 (Table 4-14). As shown in the table, the two-parameter-vector-IM without the interaction term was selected as the optimal choice for all considered four cases.

It should be noted that, unlike the 3st IF RC building, the problems in the linear regressions between two periods with a relatively high correlation were not observed as far as the case study URM buildings are concerned.

Table 4-12 Multiple regression analysis results (URM).

EDP	Story/ Config.	IM	β_0	β_1	β_2	β_{12}	σ_η
D/C_{GC}	**2st C3**	$\{Sa(0.15s), PGA\}$	-1.38	1.12	1.63	0.53	0.5228
	2st E2	$\{Sa(0.15s), PGA\}$	-1.63	0.99	0.94	0.23	0.4420
	2st E8	$\{Sa(0.15s), PGA\}$	1.50	1.01	1.06	0.31	0.4297
	2st E9	$\{Sa(0.15s), PGA\}$	1.29	0.82	0.93	0.25	0.4066
EDP	**Story/ Config.**	**IM**	β_0	β_1	β_2	β_{12}	R_L^2
D/C_{GC}	**2st C3**	$\{Sa(0.15s), PGA\}$	1.22	-	9.88	-	0.8212
	2st E2	$\{Sa(0.15s), PGA\}$	-1.60	-	7.45	-	0.7712
	2st E8	$\{Sa(0.15s), PGA\}$	-1.38	-	9.51	-	0.8034
	2st E9	$\{Sa(0.15s), PGA\}$	-0.77	-	11.59	-	0.8522

Table 4-13 Multiple linear regression analysis results (Steel).

EDP	Story/ Config.	IM	β_0	β_1	β_2	β_{12}	σ_η
D/C_{GC}	**Geo 1**	$\{Sa(0.5s), PGA\}$	-1.48	0.64	0.62	0.11	0.3332
	Geo 2	$\{Sa(0.5s), PGA\}$	-1.44	0.60	0.62	0.11	0.3163
EDP	**Story/ Config.**	**IM**	$\beta_{0,L}$	$\beta_{1,L}$	$\beta_{2,L}$	$\beta_{12,L}$	R_L^2
D/C_{GC}	**Geo 1**	$\{Sa(0.5s), PGA\}$	-6.08	3.94	2.83	-	0.7762
	Geo 2	$\{Sa(0.5s), PGA\}$	8.13	5.30	3.04	-	0.8224

Table 4-14 Multiple linear regression analysis results (PRC).

EDP	Story/ Config.	IM	β_0	β_1	β_2	β_{12}	σ_η
D/C_{GC}	**Geo 1**	$\{Sa(2.0s), PGA\}$	-0.10	0.75	0.25	-	0.2620
	Geo 2	$\{Sa(2.0s), PGA\}$	-0.20	0.75	0.25	-	0.2635
	Geo 3	$\{Sa(2.0s), PGA\}$	-0.42	0.67	0.36	-	0.2902
	Geo 4	$\{Sa(2.0s), PGA\}$	-0.31	0.73	0.28	-	0.2779

For each building case, the fragility surface, namely, the two-parameter-vector-valued fragility function, was derived from the regression models in Table 4-12-Table 4-14 using Eqs.

(4-7)-(4-10). Figure 4-9 shows the results for some representative building cases from the three structural type.

The reference analysis is also analogous to Section 4.5.4 but adopted non-parametric resampling of fragilities, as some fragility surfaces were defined as the combination of the two different types of regression models (i.e., URM and steel). In particular, failure and non-failure cases were generated at each PGA level assuming a binominal distribution with the failure probability computed from the observed number of failure cases (i.e., $p_i = N_{f,IM_2=im_{2,i}} / N_{tot,M_2=im_{2,i}}$), instead of that used in parametric-resampling.

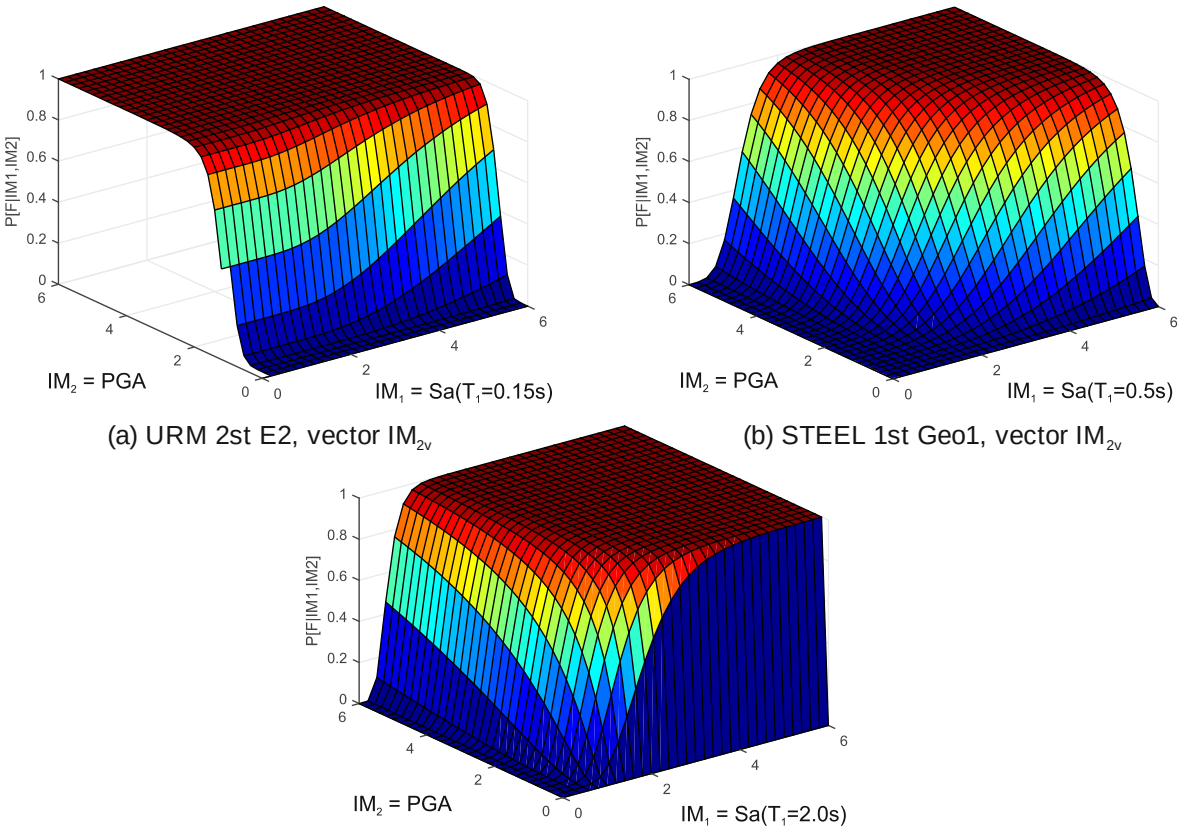

(a) URM 2st E2, vector IM_{2v}

(b) STEEL 1st Geo1, vector IM_{2v}

(c) PRC 1st Geo1, vector IM_{2v}

Figure 4-9 Fragility surfaces in the two IM domain for the representative building cases: (a) URM 2st E2; (b) steel Geo 1, (c) PRC Geo 1.

4.7.3 Results

The PGA fragility curves were derived from the multi-variable fragility functions and hazard models presented in the previous section, using Eq. (4-2). Figure 4-10 compares the converted

fragility curves with the non-parametric reference fragilities and the resampled fragility functions for some representative building cases (i.e., URM 2st C3, 2st E2, Steel Geo 1, and PRC Geo1). As shown in the figure, the converted fragility curves are consistent to the reference target fragility functions over the range of PGA. In all cases, the converted curves were located within the possible estimation ranges identified by the resampling analyses. For the rest of the examined building cases, the obtained PGA-based fragility functions showed good agreement with the reference analyses.

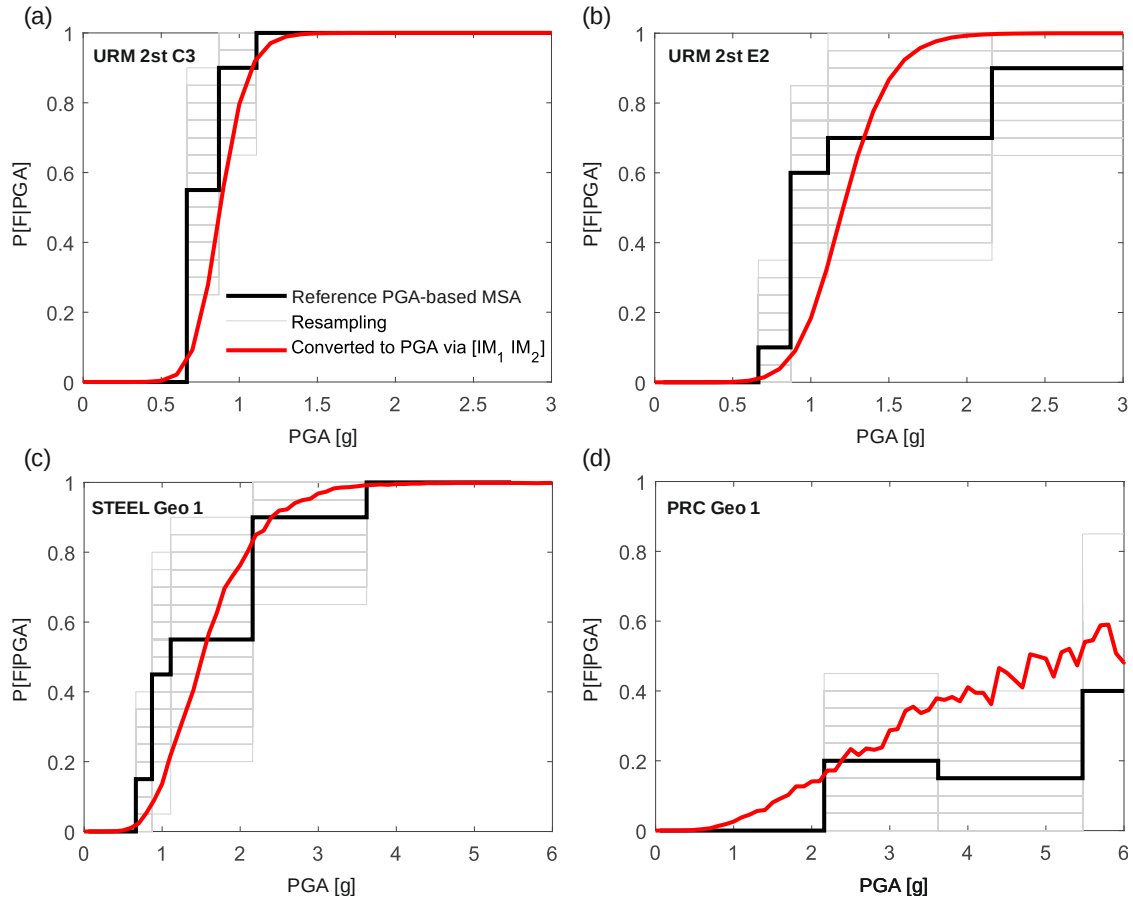

Figure 4-10 Comparison of converted and reference collapse fragility curves for the representative cases (L'Aquila on soil C); (a) URM 2st C3; (b) URM 2st E2; (c) Steel Geo 1; (d) PRC Geo 1.

Finally, Figure 4-11 compares the PGA-based fragility curves of all the buildings examined in this chapter, which were estimated all using $\{IM_1, IM_2\}$. In the figure, the different

structural types and configurations are denoted with different colors and markers. Correspondingly to the observation on the safety margin ratios presented in Chapter 3, it can be seen that the most vulnerable structural type among those examined in the RINTC project is URM, followed by the steel and PRC (side-sway collapse), and RC buildings. However, it is noteworthy that the comparison of these hazard-consistent fragility curves is based on the CS of a certain IM, thus providing a different interpretation of seismic structural fragility from other types of comparisons, for instance, in terms of failure rate or safety margin ratio as presented in the preceding chapters. In this study considering the CS given PGA, the fragility curves resulted to be aligned in the order of the increasing fundamental period of the structure, which means the shorter period structures appear to be more vulnerable than the long period structures corresponding to the spectral shapes of the CS given PGA.

It should be also noted that the steel buildings examined in the project appear to be more vulnerable relative to the other structural types even with the similar geometry (e.g., PRC). This is mainly because the estimated collapse fragility curves for this structural type exceptionally refer to the local failure condition of the bracing members (see Chapter 2 for the details) instead of the global (side-sway) collapse considered for the other structural types.

In the figure, the curves are also compared to the current first and second maximum recorded horizontal PGA values in Italy (i.e., at the Amatrice station from the 2016 Central Italy and at the Sant'Eusaino station from the 2009 L'Aquila aftershock, equal to of 0.87g and 0.67g, respectively; see [Suzuki and Iervolino, 2017] for the details). It is observed that some URM and steel structures have the failure probabilities given these recorded PGA values above 1%. Given that the irregular URM buildings examined in the RINTC project exibited much higher seismic risk than the regular ones considered in this thesis [Iervolino et al., 2018], it can be stated that collapse risk of generic URM buildings, even code-conforming, may not be sufficiently small in case of the occurrence of an rare seismic event comparable to the record-breaking events ever observed in the history.

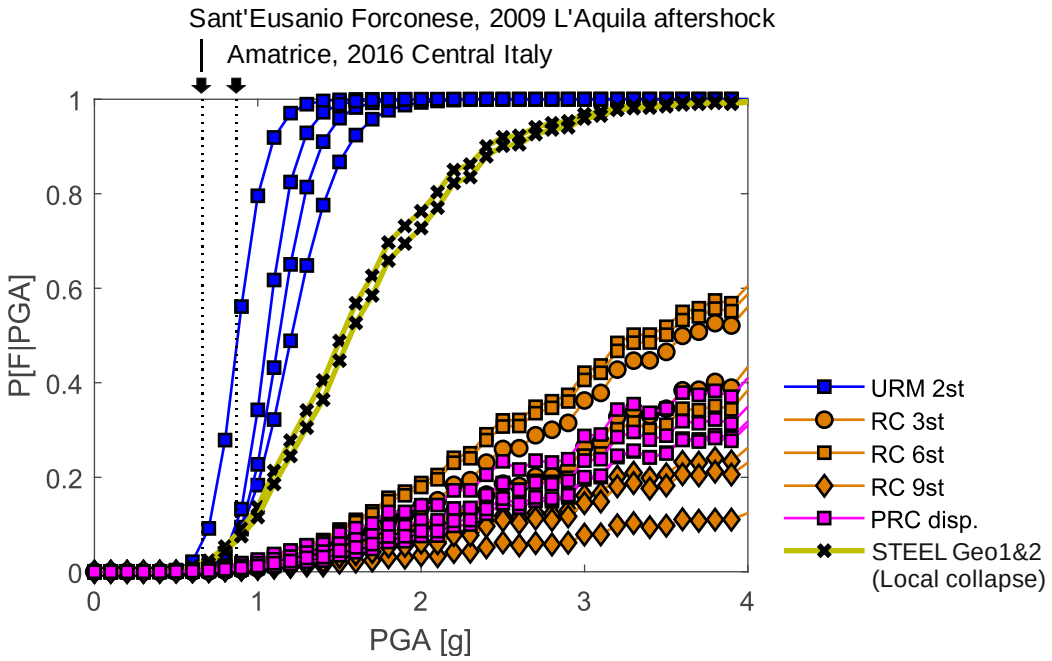

Figure 4-11 PGA fragility curves of the selected RINTC prototype buildings.

4.8 Conclusions

The study discussed the probabilistic framework for converting spectral acceleration IMs of fragility curves with the aid of the state-of-the art methods within PBEE. On the premise that structural response given an IM is available from a preliminary structural response analysis, the presented framework aims to express the fragility curve in terms of a target IM without any additional structural analyses. In particular, the study discussed three possible conversion cases with different assumptions on the IMs involved. The IM conversion cases were explored using the ESDoF systems of multi-story Italian code-conforming RC buildings featuring a wide range of the fundamental vibration period of the structure (from 0.3s to 2.0s). For each structure, the original IM was defined as spectral acceleration at a period close to the fundamental period of the structure, $Sa(T)$, then the IM conversions were performed with respect to two performance levels (i.e., usability-preventing damage and near-collapse) and under the following two different conditions: (i) the target IM is PGA for all considered structure and (ii) the target IM is to spectral acceleration at a longer periods for the selected intermediate period building. For all IM conversion cases, the fragility curves expressed in terms of the target IM

were obtained from the regressions of the structural response given $Sa(T)$ on the involved IM variables and the products of PSHA for the construction site. The converted fragility functions were compared with the results of the reference fragility analysis accounting for the estimation uncertainties, which were also hazard-consistent with respect to the target IM. Notable remarks are summarized here.

1. As it regards the variables to be involved in assessing the original fragility, the study showed that generally the effects of magnitude and source-to-site distance did not affect significantly the structural response prediction, neither the resulting converted fragility functions. On the other hand, the use of a two-parameter-vector IM consisting the original and target IMs improved the IM conversion performance in some cases compared to the model only accounting for the original IM. These results are consistent to the past literature.

2. In cases of converting to PGA, the fragility curves converted through the examined IM conversion framework were in agreement with both the empirical and parametric fragility functions computed via a conventional approach in PBEE. Most of the considered IM conversions provided the fragility curves within the possible ranges of parametric fragility functions including estimation uncertainties, when the optimal (sufficient and efficient) IM was considered.

3. As far as the conversions to PGA were concerned, the larger discrepancies with the reference analysis results were observed in the conversions from spectral acceleration at the closest period or the farthest period among those considered. In particular, this trend was clearly observed when the attainment of global collapse of the structure was of interest. The former can be due to the used regression model to link structural response including to spectral accelerations at close periods, while the latter can be related to the use of the fragility model beyond the domain where response data belong.

4. In cases of converting to spectral acceleration at a longer period than the original IM, usability-preventing-damage fragility curves derived from multiple linear regression models showed consistency with the reference curves (both empirical and parametric), while the hybrid models including the logistic regression showed better agreement with the reference collapse fragility curves.

5. The comparison of the PGA-based fragility curves of the Italian code-conforming buildings revealed that the group of the URM buildings was the most vulnerable, among the four structural types examined in this thesis. In fact, the fragility functions of some URM buildings showed global collapse probabilities greater than 1% given the first two largest horizontal PGA values in Italy (recorded in the region belonging to the site of interest).

6. The presented hazard-consistent IM conversion framework allows to examine multiple structures under the same conditions of seismic input, thus providing another interpretation of seismic structural fragility from other types of comparisons presented in Chapters 2 and 3, i.e., in terms of failure rate and safety margin ratios. Corresponding to the spectral shapes of the CSs given PGA, the converted fragility curves of the code-conforming buildings were aligned in ascending order of the fundamental vibration period of the structure. In other words, the shorter the structural vibration period, the more vulnerable the structure appeared given the PGA hazard for the site.

Since the study considered the ESDoF systems only, it is expected for future work to further consolidate the findings above through applications using some MDoF structural numerical models. Nonetheless, the conversion procedure presented in this chapter can be of help to structural engineers dealing with multiple fragility functions in terms of different IMs. Besides other comparable metrics, such as failure rate or spectra-shape-based IMs, this allows an informative comparison of structural vulnerability.

References

Baker, J. W. [2007] "Probabilistic structural response assessment using vector-valued intensity measures," *Earthq. Eng. Struct. Dyn*., 36(13), 1861–1883. DOI:10.1002/eqe.700.

Baker, J. W., and Cornell, A. C. [2005] "A vector-valued ground motion intensity measure consisting of spectral acceleration and epsilon," *Earthq. Eng. Struct. Dyn.*, 34(10), 1193–1217. DOI:10.1002/eqe.474.

Baker, J. W., and Cornell, A. C. [2006] "Spectral shape, epsilon and record selection," *Earthq. Eng. Struct. Dyn*., 35, 1077–1095. DOI:10.1002/eqe.571.

Baker, J. W., and Jayaram, N. [2008] "Correlation of spectral acceleration values from NGA ground motion models," *Earthq. Spectra*, 24(1), 299–317. DOI:10.1193/1.2857544.

Bazzurro, P., and Cornell, A. C. [1999] "Disaggregation of seismic hazard," *Bull. Seismol. Soc. Am.*, 89(2), 501–520. DOI:10.1785/0120060093.

Bojórquez, E., and Iervolino, I. [2011] "Spectral shape proxies and nonlinear structural response," *Soil Dyn. Earthq. Eng.*, 31(7), 996–1008. DOI:10.1016/j.soildyn.2011.03.006.

Chioccarelli, E., Cito, P., Iervolino, I., and Giorgio, M. [2018] "REASSESS V2.0: software for single- and multi-site probabilistic seismic hazard analysis," *Bull. Earthq. Eng*., 17(4), 1769-1793. DOI:10.1007/s10518-018-00531-x.

Cornell, A. C. [1968] "Engineering seismic risk analysis," *Bull. Seismol. Soc. Am.*, 58(5), 1583–1606.

Cornell, A. C., Jalayer, F., Hamburger, R. O., and Foutch, D. A. [2002] "Probabilistic basis for 2000 SAC federal emergency management agency steel moment frame guidelines," *J. Struct. Eng.*, 128(4), 526–533. DOI:10.1061/ASCE0733-94452002128:4526.

Cornell, A. C., and Krawinkler, H. [2000] Progress And Challenges In Seismic Performance Assessment, PEER Center News, 3, 1-3, CA, USA.

Eads, L., Miranda, E., and Lignos, D. G. [2015] "Average spectral acceleration as an intensity measure for collapse risk assessment," *Earthq. Eng. Struct. Dyn.*, 44(12), 2057–2073. DOI:10.1002/eqe.2575.

Efron, B. [1978] "Regression and ANOVA with zero-one data: measures of residual variation," *J. Am. Stat. Assoc.*, 73(361), 113–121. DOI:10.1080/01621459.1978.10480013.

Elefante, L., Jalayer, F., Iervolino, I., and Manfredi, G. [2010] "Disaggregation-based response weighting scheme for seismic risk assessment of structures," *Soil Dyn. Earthq. Eng.*, 30(12), 1513–1527. DOI:10.1016/j.soildyn.2010.07.003.

Giardini, D., Giardini, D., Grünthal, G., Shedlock, K. M., and Zhang, P. [1999] "The GSHAP Global Seismic Hazard Map," *Ann. Geophys*., 42(6). DOI:10.4401/ag-3784.

Giovenale, P., Cornell, A. C., and Esteva, L. [2004] "Comparing the adequacy of alternative ground motion intensity measures for the estimation of structural responses," *Earthq. Eng. Struct. Dyn.*, 33(8), 951–979. DOI:10.1002/eqe.386.

Iervolino, I. [2017] "Assessing uncertainty in estimation of seismic response for PBEE," *Earthq. Eng. Struct. Dyn.*, 46(10), 1711–1723. DOI:10.1002/eqe.2883.

Iervolino, I., Giorgio, M., Galasso, C., and Manfredi, G. [2010] "Conditional hazard maps for secondary intensity measures," *Bull. Seismol. Soc. Am.*, 100(6), 3312–3319. DOI:10.1785/0120090383.

Iervolino, I., Spillatura, A., and Bazzurro, P. [2018] "Seismic reliability of code-conforming Italian buildings," *J. Earthq. Eng.*, 22(sup2), 5–27. DOI:10.1080/13632469.2018.1540372.

Jalayer, F. and Cornell, A. [2003] "Direct probabilistic seismic analysis: implementing non-linear dynamic assessments," Ph.D Thesis, Stanford University, California, USA.

Lin, T., Haselton, C. B., and Baker, J. W. [2013] "Conditional spectrum-based ground motion selection. Part I: Hazard consistency for risk-based assessments," *Earthq. Eng. Struct. Dyn.*, 42(12), 1847–1865. DOI:10.1002/eqe.2301.

Luco, N. and Cornell, A. C. [2002] "Probabilistic seismic demand analysis, SMRF connection fractures, and near-source effects," Ph.D Thesis, Stanford University, California, USA.

Luco, N., and Cornell, A. C. [2007] "Structure-specific scalar intensity measures for near-source and ordinary earthquake ground motions," *Earthq. Spectra*, 23(2), 357–392. DOI:10.1193/1.2723158.

Luzi, L., Pacor, F., and Paolucci, R. [2016] Italian Accelerome-tric Archive v 2.1. Istituto Nazionale di Geofisica e Vulcanologia, Dipartimento della Protezione Civile Nazionale. DOI:10.13127/ITACA/2.1.

Melchers, R. E., and Beck, A. T. [2018].Structural reliability analysis and prediction. John Wiley & Sons.

Michel, C., Crowley, H., Hannewald, P., Lestuzzi, P., and Fäh, D. [2018] "Deriving fragility functions from bilinearized capacity curves for earthquake scenario modelling using the

conditional spectrum," *Bull. Earthq. Eng.*, 16(10), 4639–4660. DOI:10.1007/s10518-018-0371-3.

Ohtori, Y., and Hirata, K. [2007] Conversion Methods Of Ground Motion Index For Fragility Curve, CRIEPI Civil Engineering Research Laboratory Report No.N05053, Tokyo, Japan.

Pacor, F., Felicetta, C., Lanzano, G., Sgobba, S., Puglia, R., D' Amico, M., Russo, E., Baltzopoulos, G., and Iervolino, I. [2018] NESS1: A Worldwide Collection of Strong‐Motion Data to Investigate Near‐Source Effects, Seismol. Res. Lett., 89(6), 2299‐2313. DOI:10.1785/0220180149.

Shome, N. and Cornell, A. C. [1999] "Probabilistic Seismic Demand Analysis of Nonlinear Structures," Ph.D. Thesis, Stanford University, California, USA.

Shome, N., Cornell, A. C. [2000] "Structural seismic demand analysis: Consideration of "Collapse"," In Proc. of *PMC2000 - 8th ASCE Specialty Conference on Probabilistic Mechanics and Structural Reliability*. University of Notre Dame, South Bend, Indiana, USA, 24-26 July 2000.

Stucchi, M., Meletti, C., Montaldo, V., Crowley, H., Calvi, G. M., and Boschi, E. [2011] "Seismic hazard assessment (2003-2009) for the Italian building code," *Bull. Seismol. Soc. Am.*, 101(4), 1885–1911. DOI:10.1785/0120100130.

Suzuki, A., and Iervolino, I. [2017] "Italian vs. worldwide history of largest PGA and PGV," *Ann. Geophys.*, 60(5), S0551.

Suzuki, A., and Iervolino, I. [2019a] "Hazard-consistent intensity meamure conversion of fragility curves," In Proc. of *13th Int. Conf. Appl. Stat. Probab. Civ. Eng.*, Seoul, South Korea.

Tothong, P., and Luco, N. [2007] "Probabilistic seismic demand analysis using advanced ground motion intensity measures," *Earthq. Eng. Struct. Dyn.*, 36(13), 1837–1860. DOI:10.1002/eqe.696.

Vamvatsikos, D., and Cornell, A. C. [2002] "Incremental dynamic analysis," *Earthq. Eng. Struct. Dyn.*, 31(3), 491–514. DOI:10.1002/eqe.141.

Vamvatsikos, D., and Cornell, A. C. [2005] "Developing efficient scalar and vector intensity measures for IDA capacity estimation by incorporating elastic spectral shape information," *Earthq. Eng. Struct. Dyn.*, 34(13), 1573–1600. DOI:10.1002/eqe.496.

Chapter 5

Markovian modelling of damage accumulation of structures in seismic sequences

Abstract

In the performance-based earthquake engineering framework, seismic loss assessment of structures typically neglects the progressive attainment of a certain loss level due to damage accumulation in multiple earthquakes. However, this issue can be relevant in cases of the occurrence of a mainshock-aftershock sequence during which repair cannot be promptly enforced. The study presented herein develops a homogeneous Markov-chain model for damage accumulation in structures due to mainshock-aftershock seismic sequences. In particular, a discrete-time and discrete-state Markovian process is characterized by a stationary transition matrix which collects the probabilities the structure changes its state during a seismic sequence. The occurrence rate of sequences is modelled as a homogeneous Poisson process via sequence-based probabilistic seismic hazard analysis. The proposed seismic reliability model is illustrated through applications to six-story reinforced-concrete moment-resisting-frame buildings designed for three sites with different seismic hazard levels in Italy. For each structure, a unit-time transition matrix is computed by integrating *state-dependent* fragility curves, derived using the equivalent-single-degree-of-freedom systems of the examined buildings, and sequence-based probabilistic hazard at the building site. The resulting time-variant seismic risk is compared to the similar Markov-chain model neglecting the effects of aftershocks and across the different sites. The study shows that the sequence effects significantly affect the long-term seismic risk assessment results when the structure is already damaged to some extent and/or prone to high seismicity. On the contrary, the effects are irrelevant for new structures and/or located at a mid-to-low seismicity site, which supports the classical design assumptions in the modern seismic codes.

Keywords: *state-dependent fragility, aftershocks, code-conforming design, sequence-based probabilistic seismic hazard analysis.*

5.1 Introduction

In the PBEE framework, seismic risk analysis of structures aims to assess the structural safety against potentially damaging earthquakes given a time interval [Cornell and Krawinkler, 2000]. In its classical form, seismic risk analysis lies on two main hypotheses that are also at the base of modern seismic design philosophy: (i) the exceedance of a given performance limit state (i.e., *structural failure*) is due to a single shock, that is to say, no progressive attainment of limit state due to damage accumulations is considered; and (ii) only mainshock events, which are the largest magnitude earthquakes within a sequence of events clustered in space and time, are capable of damaging the structure. These hypotheses support a mathematically convenient time-invariant representation of the seismic threat according to which the occurrence of the mainshocks on each seismic source is modelled via a homogeneous Poisson process (HPP) characterized by a constant-in-time mean annual value (i.e., rate) of seismic events. On these premises, classical PSHA [Cornell, 1968] evaluates the rate of mainshocks exceeding a specific ground motion intensity measure (IM) at the site of the structure. On the structural side, fragility functions are used to model the failure probability of the structure as a function of the ground motion IM. Fragilities are typically developed for the undamaged structure on the assumption that minor or below-threshold structural damage due to a single shock is negligible or instantaneously repaired before the occurrence of the following (main-) shock (leading to the assumption (i) above). Thus, the mean annual rate of exceeding a given structural performance level (e.g., *failure rate*), which is the main outcome of the seismic risk assessment, does not account for damage accumulated in structures nor effects of seismic sequences.

This classical formulation, framing the PBEE approach, come into question in cases strong seismic shocks are closely clustered in time and space. In fact, sequential effects of strong seismic shocks to structural damage have been discussed among earthquake engineering research communities in the last decade (e.g., [Li and Ellingwood, 2007], [Iervolino et al., 2017]). For structural design and life-cycle assessment purposes, it is argued in a number of studies that the occurrence of seismic sequences can be treated in a similar fashion as the conventional PSHA, namely, given that each seismic sequence contain, by definition, a single

mainshock, the occurrence rate of the whole sequence is equal to the occurrence rate of the mainshock; Toro and Silva [2001] and Boyd [2012] developed sequential seismic hazard models including foreshocks and aftershocks. In the same direction of research, the analytical formulation of sequence-based PSHA (SPSHA) has been developed by [Iervolino et al., 2014] considering mainshock-aftershock sequences. The latter study is established based on the hypotheses that the temporal distribution of mainshock events is modeled as a HPP, whereas that of aftershocks is modeled as a conditional non-homogeneous Poisson process (NHPP) dependent on the mainshock ground motion (GM) features (i.e., a time-variant decreasing rate), as in aftershock PSHA (APSHA) [Yeo and Cornell, 2009].

Originated from a life-cycle performance point of view, stochastic modelling of degrading structures has been developed and discussed in literature. In general, two types of deterioration mechanism are accounted for engineering structures: (i) gradual deterioration of material characteristics (i.e., *aging*) and (ii) instantaneous damage due to the external loads of natural hazard. When seismic loading, belonging to the second type of deterioration phenomena, is of concern, the most of pioneering studies adopt an analytically convenient reliability model assuming independent damage increments in subsequent shocks. In other words, damage accumulated in the previous shocks does not affect the increment due to the following shock. For example, Iervolino et al. [2013] developed Gamma degradation models of structures subjected to both mainshocks and aging for long-term risk assessment of structures. A similar fragility model for seismic shocks was further extended to short-term aftershock reliability problems based on APSHA in [Iervolino et al., 2014], as well as to a long-term risk context considering mainshock-aftershock clusters via SPSHA in [Iervolino et al., 2015a]. To simulate damage progression in a more realistic fashion, a modelling alternative is *state-dependent* fragility representing damage increments dependent on the state of the structure at the time of the seismic shock and has been also adopted in the past literature. For instance, Iervolino et al. [2016] incorporated state-dependent seismic fragility functions into a long term seismic risk assessment of structures degrading structures subjected to mainshock events through a (discrete-time homogeneous) Markov-chain-based approach (see also [Iervolino et al., 2015b] combining aging and seismic damage). Yeo and Cornell [2009] developed a Markov process

framework for financial life-cycle cost analysis of buildings based on homogeneous Poisson mainshocks and non-homogeneous Poisson aftershocks. While Jia and Gardoni [2018, 2019] developed a stochastic framework using state-dependent stochastic models of multiple deterioration processes including their interactions. Nonetheless, the number of researches addressing a long-term seismic risk assessment of structures considering mainshock-aftershock sequences is still limited.

Starting from the past studies [Iervolino et al., 2015a, 2016], this chapter presents Markovian modelling of damage accumulation in structures accounting for mainshock-aftershock sequences. Figure 5-1 illustrates structural reliability issues under seismic sequences to be addressed in this chapter. It can be supposed that the structure is expected to encounter for its lifetime a number of mainshock -aftershock sequences, whose occurrence is a random process. In this study, such random occurrence of mainshock-aftershock sequences is modelled by a HPP, and GM intensity given the occurrence of a single shock is also considered as a random variable for both mainshock and aftershock events. On the structural side, random damage increments in the structure are represented by state-dependent fragility models. In particular, the structural performance is discretized into a set of damage states (DSs), then the damage progression from one to another DS is characterized in the Markov-chain. The proposed seismic reliability model is illustrated through applications to a series of six-story reinforced-concrete (RC) moment-resisting-frame buildings, which were designed for three Italian cities with different levels of seismic hazard according to the current seismic design code in Italy [CS.LL.PP., 2008; 2018] (Chapter 2). The resulting time-variant seismic risk is compared to the model neglecting the sequence effects [Iervolino et al., 2016] as well as across the sites with different seismic hazard levels.

The chapter is structured in such a way that the Markov-chain-based reliability formulation of damage accumulation of structures due to mainshock events is first given, recalling the basis of the classic PSHA. Subsequently, the reformulated solution for mainshock-aftershock sequence reliability problems is derived. An analytical solution to compute state-dependent fragility functions is discussed. The illustrative applications are then presented referring to the Italian code-conforming RC frame buildings and the sequence-based seismic

hazard at the different sites. Through the application studies, an analytical solution to compute state-dependent fragility functions is also illustrated. The resulting sequence-based seismic risk is then discussed in comparison with the conventional approach and/or across the different seismicity levels at the building site. Finally, conclusions and findings close the chapter.

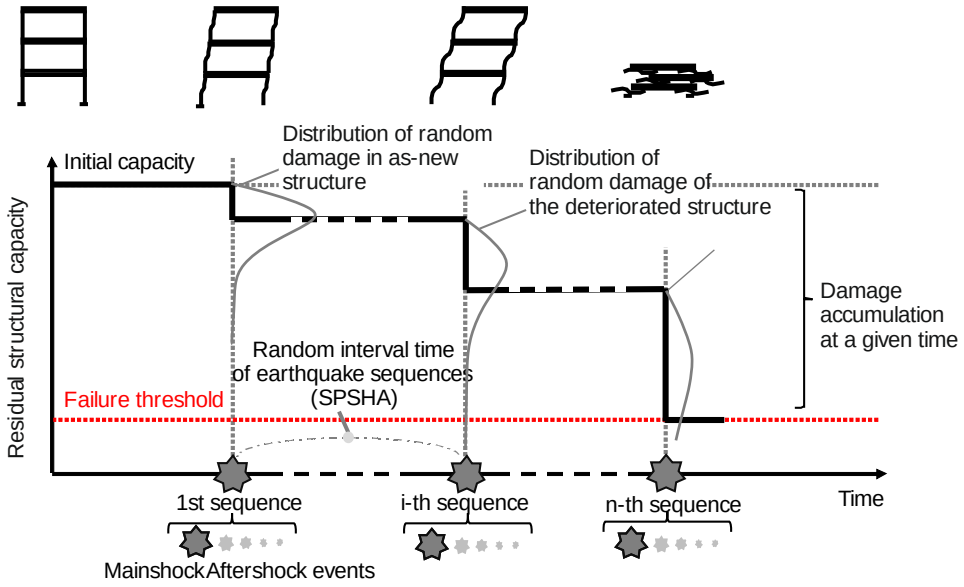

Figure 5-1 Schematic diagram for damage accumulation of structures due to multiple mainshock-aftershock sequences.

5.2 Markov-chain model for seismic damage accumulation process in mainshock events

This section recalls the Markov-type reliability model of damage progression in structures subjected to mainshock events, which is originally formulated by [Iervolino et al., 2016]. The hazard model in this reliability formulation refers to the classical PSHA. Structural damage is modelled such that considered limit state (i.e., failure) can be attained not only in a single earthquake, as typically assumed in the conventional PBEE approaches, but also in multiple seismic shocks producing progressive damage on the structure. This is achieved by the following hypotheses: (i) structural damage, which should be in principle described by a continuous variable, is simplified in discrete states of damage, with respect to which the state-dependent fragility functions [Luco et al., 2004a]; (ii) the time is discretized in intervals of a

fixed width which can be considered to be the unit time (e.g., one year); and (iii) it is assumed that the structural response during each earthquakes depends on the earthquake intensity and on the damage state of the structure at the time of the seismic event. Thus, the seismic damage process is modelled as a Markov chain. The following first briefly recalls the basis of PSHA and then derives the reliability formulation for the Markov-chain-based damage accumulation process.

5.2.1 Occurrence of mainshocks

The classic format of PSHA models the occurrence of seismic events on a particular source as a the *memory-less* HPP, that is, the unit-time occurrence rate of mainshocks, ν_E, is constant in time and independent on the history of previous shocks. In the earthquake engineering context, of particular interest is often the exceedance of a certain IM threshold, say im. The occurrence rate of mainshocks exceeding im at the site of the structure, $\lambda_{im,E}$, is given by Eq. (5-1), in which the subscript (E) is added to distinguish the obtained rate and variables from the ones by SPSHA (to follow).

$$\lambda_{im,E} = \nu_E \int_{R_E} \int_{M_E} P\left[IM_E > im \,|\, m_E, r_E\right] \cdot f_{M_E,R_E}\left(m_E, r_E\right) \cdot dm_E \cdot dr_E \tag{5-1}$$

In the equation, $P\left[IM_E > im \,|\, m_E, r_E\right]$ is the probability that the intensity threshold is exceeded given a mainshock of magnitude $M_E = m_E$ which is separated from the site by a distance $R_E = r_E$. Such a probability can be obtained from a ground motion prediction equation (GMPE). $f_{M_E,R_E}\left(m_E, r_E\right)$ is the joint probability density function (PDF) of mainshock magnitude and source-to-site distance random variables (RVs). For each source, these two RVs are usually considered stochastically independent. The products of the two terms are integrated over the whole domain of the possible magnitude and source-to-site distance values to obtain the exceedance probability of IM_E based on the total probability theorem. The resulting $\lambda_{im,E}$ is the unit-time rate of a new (filtered) HPP describing the im exceedance at the site. Eq. (5-1) is written, for simplicity, for the case of a single seismic source zone; when multiple $\left(N_s\right)$ seismic sources affect the seismic hazard at the site, the exceedance rate can be computed summing the result of Eq. (5-1) computed for each source: $\lambda_{im,E} = \sum_{n_s=1}^{N_s} \lambda_{im,E,n_s}$.

5.2.2 Markov-chain-based damage accumulation process due to mainshocks

The model developed in [Iervolino et al., 2016] refers to a discrete-time and discrete-state Markov-chain: time t is discretized in intervals of a fixed width equal to Δt, which is typically defined as $\Delta t = 1$ corresponding to a time unit (e.g., one year). The domain of the considered damage index (structural performance measure) is partitioned to have a finite number (n) of damage states (DS). The various DS_i, $i = \{1, 2, ...n\}$ from an as-built condition to the complete loss of the load-bearing capacity are factually limit states, identifying the intervals of the considered damage metric the structure passes through (not necessarily one-by-one) to reach the structural collapse.

In this context, the probabilities that the structure in a certain $i-th$ DS excurses to a worse $j-th$ DS given the occurrence of an earthquake, denoted as $P_{i,j}$, can be arranged in the form of a matrix containing those for all possible combinations of the DS. As per Eq. (5-2), the resulting matrix is the Markovian transition matrix in case of event occurrence.

$$[P] = \begin{bmatrix} 1-\sum_{j=2}^{n} P_{1,j} & P_{1,2} & \dots & \dots & P_{1,n} \\ 0 & 1-\sum_{j=3}^{n} P_{2,j} & \dots & \dots & P_{2,n} \\ \dots & \dots & \dots & \dots & \dots \\ 0 & \dots & 0 & 1-P_{n-1,n} & P_{n-1,n} \\ 0 & \dots & \dots & 0 & 1 \end{bmatrix} \tag{5-2}$$

The row and column of the transition probability matrix corresponds to the original and attained *DS* (the state before and after the shock), respectively; the elements at the first row, for example, represent the transition probabilities from the as-built condition up to the collapse represented by the $n-th$ state. The diagonal elements stand for the probabilities of the earthquake-affected structure remaining in the original *DS* (i.e., no transition), which are computed as the probability of the complement of the event that the structure moves to any of worse *DS*s. In particular, the $n-th$ state is the *absorbing state* in this Markov-chain context, which cannot be left once entered (i.e., $P_{n,n} = 1$). Elements in the lower triangle of the matrix are set to zeros for the irreversible nature of damage progression.

When an IM is *sufficient*, i.e., structural response given the IM is statistically

independent on magnitude and source-to-site distance, the individual elements of the matrix in Eq. (5-2) can be computed according to Eq. (5-3). In the latter equation, $P\left[\, j-th\ state \,|\, i-th\ state\,, IM = im \,\right]$ is the probability that the structure in the $i-th$ *DS* moves to the worse $j-th$ *DS* conditional to a specific im value of the GM intensity and is derived from a state-dependent fragility function. The other term in Eq. (5-3), $f_{IM_E|E}$ is the PDF of IM_E conditional to the event occurrence:

$$P_{i,j} = \int_{IM_E} P\left[\, j-th\ state \,|\, i-th\ state\,, IM_E = im \,\right] \cdot f_{IM_E|E}\left(im\right) \cdot dz \tag{5-3}$$

Note that, according to the hypotheses of PSHA, the RVs representing GM intensities of different earthquakes are independently and identically distributed (i.i.d.). Furthermore, if the structure is not affected by continuous degradation (e.g., aging), $P\left[\, j-th\ state \,|\, i-th\ state\,, IM = im \,\right]$ does not change in time. This leads to the time-invariance of $P_{i,j}$, and, consequently, of the whole transition matrix in Eq. (5-2).

The definition of the time-invariant transition matrix in Eq. (5-2) makes possible to probabilistically describe the transition between any two *DS*s from a certain time step $t = k$ to the next time step $t + \Delta = k + 1$, leading to $\left[P_E\left(k, k+1\right)\right]$ given by Eq. (5-4). The equation stands on the premise that the unit-time rate of occurrence of earthquake shocks is small enough such that the probability of observing more than one seismic event in the unitary time interval is negligible. Thus, in Eq. (5-4), the first term $\nu_E \cdot \left[P\right]$ provides the probabilities that the structure attains each damage state if one earthquake occurs; the second term, $\left(1-\nu_E\right)\cdot\left[I\right]$, represents the probabilities that the structure remains at the same state if no earthquakes occur in the unit-time interval, which is the product of the probability of not observing an earthquake in the unit-time interval $\left(1-\nu_E\right)$ and the certitude that the structure remains in the same state under the circumstance of no earthquakes. Note that the identity matrix $\left[I\right]$ is assigned to the latter assuming no repair actions are considered in the unit time (i.e., $P_{i,j} = 0$ where $i > j$).

$$\left[P_E(k,k+1)\right]=\nu_E\cdot\left[P\right]+\left(1-\nu_E\right)\cdot\left[I\right]=$$

$$=\begin{bmatrix} 1-\sum_{j=2}^{n}\nu_E\cdot P_{1,j} & \nu_E\cdot P_{1,2} & \cdots & \cdots & \nu_E\cdot P_{1,n} \\ 0 & 1-\sum_{j=2}^{n}\nu_E\cdot P_{1,j} & \cdots & \cdots & \nu_E\cdot P_{2,n} \\ \cdots & \cdots & \cdots & \cdots & \cdots \\ 0 & \cdots & 0 & 1-\nu_E\cdot P_{n-1,n} & \nu_E\cdot P_{n-1,n} \\ 0 & \cdots & \cdots & 0 & 1 \end{bmatrix}=\left[P_E\right] \quad (5\text{-}4)$$

Once the unit-time transition matrix, $\left[P_E\right]$, is known, the stochastic damage accumulation process, that is a homogeneous Markov chain, is completely defined. The transition probabilities at m time units after time k, $\left[P_E(k,k+m)\right]$ can be computed through the unit-time transition matrix to the $m-th$ power, $\left[P_E\right]^m$. This accounts for all possible transition paths between any two DS s within a time interval of interest.

5.3 Markov-chain model for seismic damage accumulation process in mainshock and aftershock sequences

In this section, the Markov-chain-based reliability model accounting for the effects of mainshock-aftershock sequences is formulated. The main difference from the original model in [Iervolino et al., 2016] is that, in accordance with the hypotheses at the base of SPSHA, the occurrence of a whole seismic sequence (i.e., mainshock and following aftershocks) is considered instantaneous. Thus, a new unit-time transition matrix accounting for the sequence effects is derived herein.

The following provides a brief overview of SPSHA and then formulates the transition matrices in the context of seismic sequences. Note that variables related to an aftershock are indicated with the superscript A in order to distinguish from those for a mainshock.

5.3.1 Occurrence of mainshock and aftershock sequences based on SPSHA

Similarly to PSHA, the main goal of SPSHA is to evaluate the occurrence rate of sequences (mainshock and following aftershocks) in which at least one seismic shock causes the

exceedance of im at the site. In fact, the occurrence rate of seismic sequences, hereafter denoted as λ_{im}, is equal to that of mainshocks, ν_E, thus being described by a HPP. As demonstrated in [Iervolino, et al., 2014], λ_{im} can be computed via Eq. (5-5).

$$\lambda_{im} = \nu_E \cdot \left\{ 1 - \iint_{R_E M_E} P\left[IM_E \le im \,|\, m_E, r_E\right] \cdot P\left[IM_{\cup A} \le im \,|\, m_E, r_E\right] \cdot f_{M_E,R_E}\left(m_E, r_E\right) \cdot dm_E \cdot dr_E \right\} \quad (5\text{-}5)$$

where $P\left[IM_{\cup A} \le im \,|\, m_E, r_E\right] = e^{-E\left[N_{A|M_E=m_E}(0,\Delta T_A)\right] \cdot \iint_{R_A M_A} P[IM_A > im | m_A, r_A] \cdot f_{M_A,R_A|M_E,R_E}(m_A, r_A) \cdot dm_A \cdot dr_A}$

In the equation, $P\left[IM_E \le im \,|\, m_E, r_E\right]$ is the complement to one of $P\left[IM_E > im \,|\, m_E, r_E\right]$ that is defined in Eq. (5-1) together with ν_E and $f_{M_E,R_E}\left(m_E, r_E\right)$. The terms not defined in the previous equations are introduced to compute the probability that none of the aftershocks, following the mainshock features $\left\{M_E = m_E, R_E = r_E\right\}$, cause the exceedance of *im* (i.e., the maximum IM of aftershocks belonging to a sequence $IM_{\cup A}$ is smaller than *im*). This probability depends on $P\left[IM_A > im \,|\, m_A, r_A\right]$, the probability that *im* is exceeded given an aftershock of magnitude $M_A = m_A$ and source-to-site distance $R_A = r_A$, which can be also obtained from a GMPE. The term $f_{M_A,R_A|M_E,R_E}$ is the distribution of magnitude and distance of aftershocks, which are conditional on the features $\left\{M_E, R_E\right\}$ of the mainshock. The aftershock magnitude is bounded by a minimum magnitude, $m_{A,\min}$, and the mainshock magnitude, i.e., $M_E = m_E$ (note that $m_{A,\min}$ may coincide with the minimum mainshock magnitude; i.e., $m_{A,\min} \equiv m_{E,\min}$). Given the location of the site, the aftershock distance, $R_A \in \left(r_{A,\min}, r_{A,\max}\right)$, depends on the magnitude and location of the mainshock (see [Iervolino et al., 2014], for details). $E\left[N_{A|M_E=m_E}\left(0,\Delta T_A\right)\right]$ is the expected number of aftershocks, conditional to the mainshock of magnitude $M_E = m_E$, in the time interval of ΔT_A, which defines the considered length of the aftershock sequence from the mainshock occurrence at (local) time $\tau = 0$. This number, consistently with APSHA, can be computed with Eq. (5-6), where $\left\{a, b, c, p\right\}$ are the parameters of the modified Omori law [Yeo and Cornell, 2009].

$$E\left[N_{A|M_E=m_E}\left(0,\Delta T_A\right)\right] = \frac{10^{a+b\cdot(m_E - m_{\min})} - 10^a}{p-1} \cdot \left[c^{1-p} - \left(\Delta T_A + c\right)^{1-p}\right] \quad (5\text{-}6)$$

5.3.2 Markov-chain-based damage accumulation process due to mainshock-aftershock sequences

This section derives the Markov-chain damage formulation process accounting for mainshock and following aftershocks. According to the hypotheses of SPSHA, it is assumed that the sequence can be approximated as an instantaneous damaging event because its duration is negligible with respect to the lifespan of the structure. Herein, a unit time transition probability matrix, equivalent to the one of Eq. (5-4) but accounting for the effect of the whole sequence, is derived. To this aim it is useful to first compute a transition probability matrix conditional to a mainshock of a given magnitude and distance, $\left[P_{M_E,R_E}\right]$, collecting the conditional transition probabilities between any two DSs given $M_E = m_E$ and $R_E = r_E$, $P_{i,j|M_E,R_E}$. The latter can be computed as shown in Eq. (5-7) in which $f_{IM_E|M_E,R_E}$ is the PDF of IM_E provided by the GMPE and $P\left[\, j-th\ state \,|\, i-th\ state, IM_E = im, M_E = m_E, R_E = r_E \right]$ is independent on M_E and R_E due to the statistical sufficiency of IM_E already introduced in Eq. (5-3).

$$\begin{aligned} P_{i,j|M_E,R_E} &= P\left[\, j-th\ state \,|\, i-th\ state, M_E = m_E, R_E = r_E \right] = \\ &= \int_{IM_E} P\left[\, j-th\ state \,|\, i-th\ state, IM_E = im, M_E = m_E, R_E = r_E \right] \cdot f_{IM_E|M_E,R_E}(im) \cdot dim = \\ &= \int_{IM_E} P\left[\, j-th\ state \,|\, i-th\ state, IM_E = im \right] \cdot f_{IM_E|M_E,R_E}(im) \cdot dim \end{aligned} \tag{5-7}$$

The transition probability matrix conditional to the occurrence of one of the aftershocks triggered by a mainshock featuring $\{M_E, R_E\}$, that is $\left[P_{A,M_E,R_E}\right]$, is also needed. Its elements are the probabilities that the structure in a certain $(i-th)$ DS excurses to a worse $(j-th)$ DS given the occurrence of an aftershock of the sequence, $P_{i,j|A,M_E,R_E}$, which can be computed via Eq. (5-8).

$$P_{i,j|A,M_E,R_E} = \int_{IM_A} P\left[\, j-th\ state \,|\, i-th\ state, IM = im \right] \cdot f_{IM_A|M_E,R_E}(im) \cdot dim \tag{5-8}$$

In the equation, $f_{IM_A|M_E,R_E}$ is the PDF of the aftershock IM given the features of the mainshock. It can be computed with Eq. (5-9) in which $f_{IM_A|M_A,R_A}$ is the PDF of IM_A conditional to known values of aftershock magnitude and distance provided by the GMPE and $f_{M_A,R_A|M_E,R_E}$ is defined in Eq. (5-5).

$$f_{IM_A|M_E,R_E}(im) = \iint_{R_A M_A} f_{IM_A|M_A,R_A,M_E,R_E}(im)\cdot f_{M_A,R_A|M_E,R_E}(m_A,r_A)\cdot dm_A\cdot dr_A = \\ = \iint_{R_A M_A} f_{IM_A|M_A,R_A}(im)\cdot f_{M_A,R_A|M_E,R_E}(m_A,r_A)\cdot dm_A\cdot dr_A \tag{5-9}$$

Note that, according to the APSHA formulation, the RVs representing aftershock features, M_A and R_A, are both i.i.d. conditional to the M_E, R_E values. Thus, not only $P_{i,j|E,M_E,R_E}$ but also $P_{i,j|A,M_E,R_E}$ are time-independent probabilities. Consequently, both $\left[P_{M_E,R_E}\right]$ and $\left[P_{A,M_E,R_E}\right]$ are time-independent and the transition probabilities due to a number of aftershocks of the sequence, say n_A, are obtained by $\left[P_{A,M_E,R_E}\right]^{n_A}$. Considering the number of aftershocks a RV, the transition probability given the occurrence of the whole sequence constituted by the mainshock featuring $\{M_E,R_E\}$ and the following aftershocks in the time interval $(0,\Delta T_A)$ can be comprehensively represented as $\left[P_{S,M_E,R_E}\right]$ given by Eq. (5-10) in which the total probability theorem is applied.

$$\left[P_{S,M_E,R_E}\right] = \left[P_{M_E,R_E}\right]\cdot\left(\sum_{n_A=0}^{+\infty}\left[P_{A,M_E,R_E}\right]^{n_A}\cdot P\left[N_A(\Delta T_A)=n_A\middle|M_E=m_E\right]\right) \tag{5-10}$$

In the equation, $P\left[N_A(\Delta T_A)=n_A\middle|M_E=m_E\right]$ is the probability that exactly n_A aftershocks are generated by the mainshock of magnitude $M_E=m_E$ and can be computed according to the non-homogeneous Poisson process described in [Yeo and Cornell, 2009]. For simplicity , an approximation of the rigorous formulation of Eq. (5-10) can be also employed as per Eq. (5-11) considering the expected number of aftershock $E\left[N_A(\Delta T_A)\middle|M_E=m_E\right]$ provided by Eq. (5-6).

$$\left[P_{S,M_E,R_E}\right] = \left[P_{M_E,R_E}\right]\cdot\left[P_{A,M_E,R_E}\right]^{E\left[N_A(\Delta T_A)\middle|M_E=m_E\right]} \tag{5-11}$$

The total probability theorem allows to compute the transition probability given the occurrence of any sequences, $\left[\overline{P}\right]$, by integrating over the range of mainshock features:

$$\left[\overline{P}\right] = \iint_{R_E M_E}\left[P_{E,M_E,R_E}\right]\cdot\left[P_{S,M_E,R_E}\right]\cdot f_{M_E,R_E}(m_E,r_E)\cdot dm_E\cdot dr_E \tag{5-12}$$

In the context of damage accumulation due to mainshock-aftershock sequences, one can apply Eq. (5-12) in the Markov-chain as the equivalent of Eq. (5-2) in the mainshock-driven (5-4), unit-time damage transition probability matrix for seismic sequences $\left[P_S(k,k+1)\right]$ is

given by Eq. (5-13).

$$\left[P_S\left(k,k+1\right)\right]=\nu_E\cdot\left[\overline{P}\right]+\left(1-\nu_E\right)\left[I\right]=\left[P_S\right] \tag{5-13}$$

When multiple seismic source zones affect the seismic hazard at the building site, the unit-time damage transition matrix in Eq. (5-13) can be rewritten as Eq. (5-14), considering the contribution from each source zone being associated with the occurrence rate, ν_{E,n_s} and the corresponding transition matrix $\left[\overline{P}_{n_s}\right]$. Then the transition probabilities at m time units after time $t=k$, $\left[P_S\left(k,k+m\right)\right]$ can be computed through the unit-time transition matrix to the $m-th$ power with Eq. (5-15):

$$\left[P_S\left(k,k+1\right)\right]=\sum_{n_s=1}^{N_s}\nu_{E,n_s}\cdot\left[\overline{P}_{n_s}\right]+\left(1-\sum_{n_s=1}^{N_s}\nu_{E,n_s}\right)\cdot\left[I\right]=\left[P_S\right] \tag{5-14}$$

$$\left[P_S\left(k,k+m\right)\right]=\left[P_S\right]^m \tag{5-15}$$

5.4 Illustrative application

In this section, the proposed Markovian modelling of degrading structures due to mainshock-aftershock sequences is illustrated through the application to a set of Italian code-conforming RC buildings. In particular, the structural design refers to three Italian sites with different seismic hazard levels. In order to investigate the effects of sequential shocks, for a high seismicity site, the results of the long-term seismic risk assessment are first compared to the conventional approach that neglects the effects of aftershocks (i.e., Section 5.2). Subsequently, the trends across different sites are discussed.

5.4.1 Structural model and damage states

Among the code-conforming buildings examined in the preceding chapters, this study selected the six-story RC IF buildings designed for the three sites, Milan, Naples, and L'Aquila (on the soil condition C) as a case study, for which the state-dependent seismic fragilities were examined using their ESDoF models calibrated in Chapter 2. Table 5-1 provides the structural features and SPO backbone parameters for the considered three RC buildings.

The damage index under consideration is a *displacement-related* one, in particular, the maximum transient displacement ever recorded throughout a series of seismic events[9]. Including the two performance levels examined in the aforementioned RINTC project, this study specified five DSs based on the backbone characteristics of the considered building. Those considered are: as-new (AN), usability-preventing damage (UPD), *life safety* (LS), *collapse prevention* (CP), and global collapse (GC), partitioned in the displacement (δ) domain of the pushover curve (Figure 5-2).

Following the general failure criteria adopted in the RINTC project, this study first defined the attainments of the two *DS*s, UPD and GC (their displacement lower thresholds are identified as δ_1 and δ_4, respectively). Using the original 3D structural models, the UPD failure thresholds were identified through a multi-criteria approach, i.e., considering the minimum displacement under multiple damage conditions that can jeopardize the building occupancy after a seismic event. In particular, these conditions refer to the damage in main non-structural elements, i.e., masonry infills in case of RC residential buildings (see the definitions for the ESDoF systems in Section 4.4 and for the 3D original structural models in Section 2.2.6). As regards global collapse, the displacement limit threshold, δ_4, corresponds to a certain level of strength deterioration; i.e., a 50% from the maximum base-shear on the SPO curve of the original structural model in each horizontal direction. The additional two intermediate performance levels, i.e., LS and CP, were also defined as follows: the attainment of the LS performance level (δ_2) corresponds to the excursion to the residual plateau, indicating the masonry infilled walls have no contribution to the lateral load-bearing capacity of the structure; the CP performance level initiates from the two-third of the collapse displacement defined above (δ_3), according to the indication for the capacity of the components in NTC [CS.LL.PP., 2008, 2018]. The AN state is consequently specified from no damage (zero displacement) up to the attainment of UPD. In Figure 5-2, these displacement thresholds are illustrated for the three

[9] Damage indices are broadly categorized into two groups, *displacement-related* and *energy-related ones*. In the former case, the damage state of the structure is labeled based on the exceedance of a certain displacement threshold during a seismic shock, while the latter quantifies the amount of energy dissipation in the dynamic hysteretic behavior of the structure. For further information on damage indices used for stochastic modelling of damage accumulation in structures, see [Iervolino et al., 2016].

buildings, particularly referring to the L'Aquila building to specify the DS intervals identified on the backbones of the ESDoF systems. See also Table 5-2 for the corresponding displacement threshold values.

Table 5-1 Dynamic and SPO parameters of the ESDoF systems.

Config.	Dir.	T^* [s]	m^* [ton]	Γ	$Sa_y(T^*)$ [g]	ξ^* [%]	F_y^* [kN]	δ_y^* [m]	a_h	μ_c	a_c	r_p	μ_{GC}
Milan	**X**	0.53	1161	1.32	0.16	5	1865	0.01	0.08	4.2	-0.03	0.80	41.1
	Y	0.58	1165	1.31	0.19	5	2164	0.02	0.29	3.3	-0.16	0.87	16.5
Naples	**X**	0.53	1265	1.31	0.23	5	2842	0.02	0.02	7.2	-0.04	0.90	50.5
	Y	0.57	1262	1.31	0.28	5	3419	0.02	0.09	3.4	0.08	0.85	28.0
L'Aquila	**X**	0.57	1230	1.30	0.29	5	3485	0.02	0.03	4.7	-0.03	0.90	33.6
	Y	0.54	1247	1.30	0.43	5	5269	0.03	0.09	3.1	-0.07	0.86	17.6

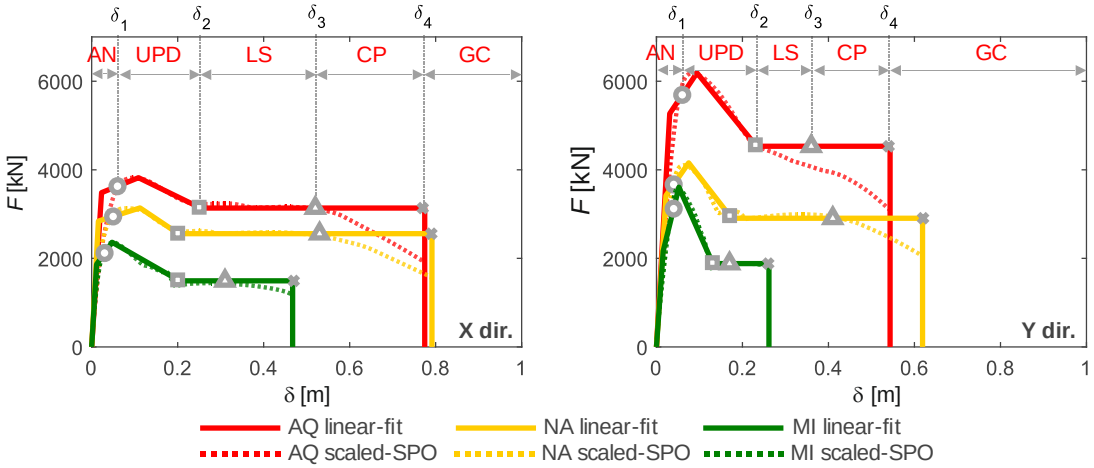

Figure 5-2 Damage states and limit state thresholds defined for the ESDoF systems.

Table 5-2 Definitions of five discretized damage states (Milan, Naples, L'Aquila).

Building site (soil C)	Dir.	δ_1 [m]	δ_2 [m]	δ_3 [m]	δ_4 [m]
Milan	**X**	0.0349	0.2040	0.3115	0.4673
	Y	0.0412	0.1310	0.1745	0.2617
Naples	**X**	0.0451	0.2016	0.5276	0.7914
	Y	0.0419	0.1748	0.4126	0.6189
L'Aquila	**X**	0.0626	0.2537	0.5164	0.7746
	Y	0.0610	0.2328	0.3623	0.5434

5.4.2 State-dependent fragility curves obtained via nonlinear dynamic analyses

To obtain the transition probabilities $P\left[j-th\ state \,|\, i-th\ state, IM_E = im \right]$ in Eq. (5-3) and Eq. (5-7), state-dependent fragility curves can be computed through state-of-the-art structural

response analysis methods of PBEE. Using a numerical model of the structure and a suite of GM records, the transition probabilities of the as-new structure $(i=1)$ can be computed via incremental dynamic analysis (IDA) from response of the intact structure under a single shock [Vamvatsikos and Cornell, 2002]. For those from any worse damaged states $(i>1)$, *back-to-back incremental dynamic analysis* (B2BIDA) [Luco et al., 2004] can be performed to simulate the response of the structure progressively damaged under sequential earthquake excitation.[10] More specifically, this method involves two-step nonlinear dynamic analysis (NLDA) using two suites of GM records: the intact structure is first damaged to a target DS by a scaled GM record from the first GM record set, then damage increments given the target DS are obtained by further exciting the damaged structure by one of the second record set scaled to a certain IM level. Although this process requires a more elaborate calibration process compared to conventional fragility estimation methods in PBEE (see Chapter 1), it renders the conditional distribution of random damage increments given DS considering *record-to-record variability* in successive seismic shocks.

For the three case study buildings and the defined five *DS*s, the state-dependent fragility curves, $P\left[\, j-th\ state \,|\, i-th\ state\,, IM=im \right]$, were computed utilizing an open-source graphical user interface for dynamic analysis of SDoF systems in OpenSees (DYANAS) [Baltzopoulos et al., 2018]. In accordance with the RINTC project, the selected IM for all the three buildings was the maximum spectral acceleration of the two horizontal components at 0.5s, i.e., $IM=\max\left(Sa_x\left(0.5s\right), Sa_y\left(0.5s\right)\right)$, referring to the equivalent periods in the two horizontal directions (see Table 5-1). It should be noted that, according to the previous chapters, structural responses in the two horizontal directions were examined independently by considering the two uncoupled ESDoF systems for each structure, then being merged into a single fragility function to represent the probability of the structure exceeding a given performance level at least in one direction. In IDA or B2BIDA, the two ESDoF systems in the

[10] It should be noted that there is also an alternative to render the transition probabilities given the occurrence of an event, $P_{i,j}$, which is based Monte Carlo simulation of structural response subjected to earthquake sequences. However, this is the option that is not adopted in this study. See [Iervolino et al., 2016] for more details.

same DS were excited by a pair of two horizontal components of a GM record with $IM = \max\left(Sa_x\left(0.5s\right), Sa_y\left(0.5s\right)\right)$, then the smallest IM level causing the change of the DS in either direction was obtained to derive the state-dependent fragility curves (to follow).

To obtain the structural fragility from AN to the other damage states, IDA was first performed using twenty GMs to represent large seismic events (moment magnitude within 6.5-6.9, recorded on firm soil and selected from the record set; the PEER GM set in Chapter 3; see Appendix). As mentioned above, the two uncoupled ESDoFs for the X and Y directions were individually excited by one of the horizontal components of a GM record scaled incrementally to a certain $Sa\left(0.5s\right)$ level. The spectral acceleration values causing the undamaged structure (in the AN state; $i=1$) to exceed the displacement threshold value of a worse DS (δ_{j-1} where $j>1$) in either of the two horizontal directions, $Sa^{1,j}$, were collected from all GM records.

Subsequently, B2BIDA was carried out using the same GM record set in IDA for both the first and second excitation groups. All possible combinations of the first and second shocks were considered from the twenty GM records with repetition, thus leading to four-hundred (20×20) sequential excitations in total for each pair of *DS*s. For the sake of simplicity in this kind of dynamic analysis using the two uncoupled systems, this study assumed the following conditions regarding structural response and damage progression in two horizontal directions: (i) the interactions between the two directions are negligible, thus the IM level causing the transition from one to a worse DS in one horizontal direction, say $Sa_x^{i,j}$, is independent to that in the other, $Sa_y^{i,j}$; and (ii) when the structure travels from one to a worse DS, it means that the structure initially stays in the same DS in the two directions then attains a worse DS at least in one direction. Although it quite often happens that the earthquake-affected structure is damaged to different DSs in the two directions, the latter was adopted in order to simply assess the bidirectional state-dependent fragility with the adopted IM. Starting from these assumptions, each ESDoF system was excursed to the lower bound of a certain DS (from UPD to CP) in the corresponding direction by one component of the first shock[11], then being further damaged by

[11] Different scaling factors were applied to the two horizontal directions of the first shock in order to attain the target damage

the same component of the second shock. Figure 5-3 illustrates the sampled IM values from four-hundred two-component B2BIDA curves, as an example, those given UPD as the initial DS for the building designed for the L'Aquila site. As shown in Figure 5-3a, a pair of two-component B2BIDA curves were obtained individually for each GM record, and the spectral acceleration values intersecting the displacement thresholds in the corresponding direction ($Sa_x^{i,j}$ or $Sa_y^{i,j}$; denoted with round or x-cross markers) were sampled. For each record and for each initial ($i-th$) DS, the minimum values of $Sa(0.5s)$ causing to a worse DS in either direction, $Sa^{i,j}=\min\left(Sa_x^{i,j},Sa_y^{i,j}\right)$ denoted with round markers in the figure, were then collected. For the sake of completeness, the obtained response data for all 400 simulations are provided in Figure 5-3b.

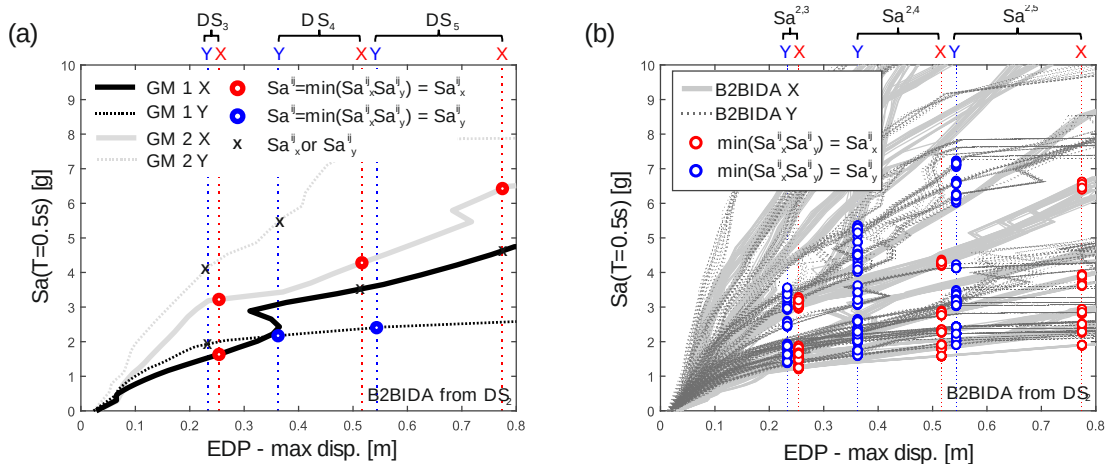

Figure 5-3 Back-to-back incremental dynamic analysis; (a) sampling $Sa^{i,j}$ values from two horizontal directions; (b) using 20 mainshock and 20 aftershock records (400 simulations).

Assuming a lognormal distribution for the IM causing the transition between any DSs, the median and the logarithmic standard deviation of the sampled $Sa^{i,j}$, denoted as $\tilde{S}a^{i,j}$ and $\sigma_{\ln Sa^{i,j}}$, respectively, were estimated. Using the estimated lognormal parameters, the state-dependent fragility curves were computed using Eq. (5-16) for all examined buildings.

state in each direction.

$$P\left[\, j-th\ state\ or\ worse \,\middle|\, i-th\ state\ , IM = im \,\right] = \Phi\left(\frac{\ln im - \ln \tilde{S}a^{i,j}}{\sigma_{\ln Sa^{i,j}}} \right) \tag{5-16}$$

The results of the lognormal parameters for all cases shown in Table 5-3, and a set of the curves for the L'Aquila building is provided in Figure 5-4. It can be generally seen that, under the same seismic inputs, the median capacity given the same initial DS increases with the seismic hazard at the site in accordance with the structural design reflecting the local seismicity, although the transition probabilities from some intermediate DS to a worse depend on the width of the interval (i.e., $\delta_j - \delta_i$) and/or the slope within the interval identified on the backbone of the ESDoF system at hand. As expected, the worse the initial state is, the smaller spectral acceleration level causing the transition to a worse DS $\left(\tilde{S}a^{i,j}\right)$ can be observed for all examined buildings cases. Compared with the lognormal fragility parameters for the AN state $\left(\tilde{S}a^{1,n}\right)$, for instance, the median spectral acceleration causing global collapse $\left(\tilde{S}a^{i,n}\right)$ did not change much until UPD, then gradually dropped accordingly to the damage extent of the initial state (by approximately 15-40% if $DS_i = \text{LS}$ and by approximately 90% if $DS_i = \text{CP}$). Regarding the logarithmic standard deviation, it changes suddenly when the initial DS of the structure is above LS.

From the computed state-dependent fragility curves, the transition probabilities between any two DSs can be retrieved as Eq. (5-17), i.e., taking the differences between the two adjacent fragilities for a given IM.

$$\begin{aligned} &P\left[\, j-th\ state \,\middle|\, i-th\ state\ , IM = im \,\right] = \\ &= P\left[\, j-th\ state\ or\ worse \,\middle|\, i-th\ state\ , IM = im \,\right] - P\left[\, j+1-th\ state\ or\ worse \,\middle|\, i-th\ state\ , IM = im \,\right] \end{aligned} \tag{5-17}$$

Table 5-3 State-dependent fragility parameters.

Building site	To	UPD		LS		CP		GC	
	From	$\tilde{S}a^{i,j}$	$\sigma_{\ln Sa^{i,j}}$	$\tilde{S}a^{i,j}$	$\sigma_{\ln Sa^{i,j}}$	$\tilde{S}a^{i,j}$	$\sigma_{\ln Sa^{i,j}}$	$\tilde{S}a^{i,j}$	$\sigma_{\ln Sa^{i,j}}$
Milan	**AN**	0.45	0.21	1.10	0.27	1.25	0.30	1.49	0.37
	UPD	-	-	1.07	0.28	1.23	0.30	1.47	0.36
	LS	-	-	-	-	0.13	0.25	0.85	0.51
	CP	-	-	-	-	-	-	0.14	0.26
Naples	**AN**	0.53	0.20	1.44	0.32	2.39	0.43	3.20	0.47
	UPD	-	-	1.38	0.32	2.32	0.41	3.19	0.47
	LS	-	-	-	-	1.79	0.41	2.73	0.47
	CP	-	-	-	-	-	-	0.34	1.01
L'Aquila	**AN**	0.75	0.23	1.96	0.33	2.61	0.38	3.34	0.43
	UPD	-	-	1.83	0.32	2.53	0.35	3.28	0.41
	LS	-	-	-	-	0.86	0.66	2.61	0.39
	CP	-	-	-	-	-	-	0.45	0.87

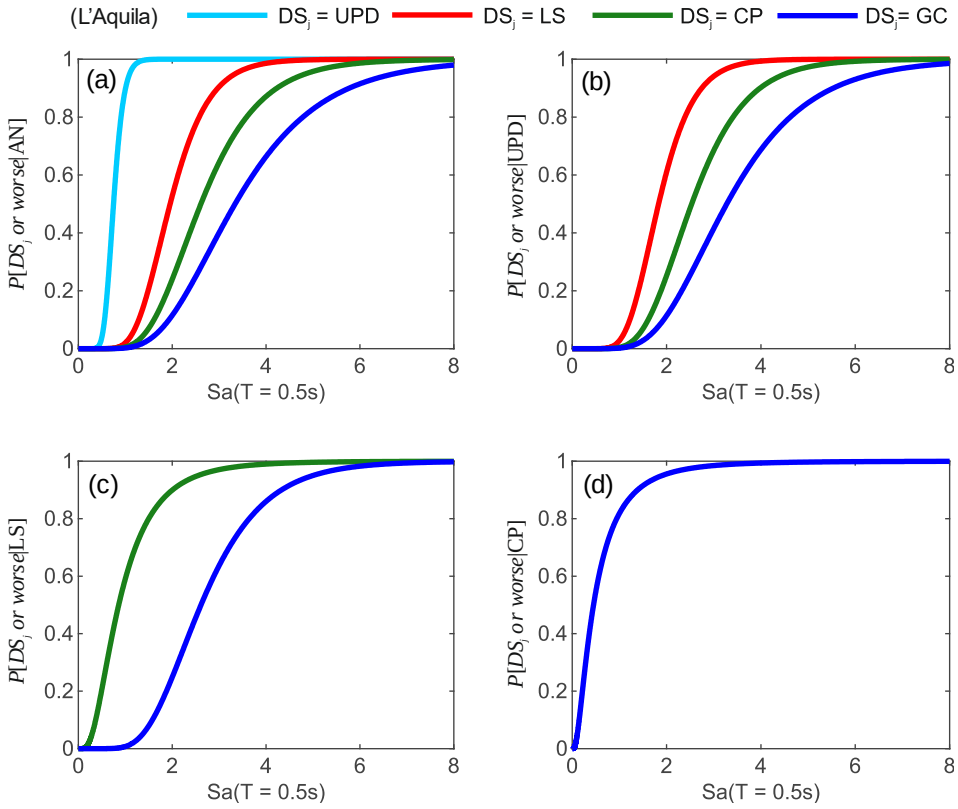

Figure 5-4 State-dependent fragility curves for the building in L'Aquila; from AN; (b) from UPD; (c) from LS; and (d) from CP.

5.4.3 Seismic source models and seismic hazard curves

As discussed in Section 5.3, the proposed Markovian modelling of degrading structures due to mainshock-aftershock sequences requires the conditional PDFs for mainshock and aftershock

events in a seismic sequence ($f_{IM_E|M_E,R_E}$ and $f_{IM_A|M_E,R_E}$) and the occurrence rate of sequences (ν_E) for each seismic source zone affecting the site of interest. To this aim, PSHA and SPSHA were performed for each of the considered three sites, L'Aquila, Naples, and Milan (Figure 5-5a), via a computer software for advanced seismic hazard assessment, REASESS [Chioccarelli et al., 2018]. According to the NLDAs presented above, the selected IM was the spectral acceleration at 0.5s. The seismic source model for each site was the one by [Meletti et al., 2008] which features 36 seismic source zones, and only those dominantly contributing to the seismic hazard at the site were considered as specified in Figure 5-5a. According to [Stucchi et al., 2011] in which PSHA had been performed using the same source model via a logic tree, this study considered the branch named 921 and the GMPE by [Ambraseys et al., 1996] as it renders the closest hazard results to those from the full logic tree. According to the GMPE, the mainshock magnitude between 4.0 and 7.5 and the Joyner Boore distance (i.e., the shortest distance from the site to the surface projection of the fault plane) up to 200km were considered. The joint PDF of mainshock magnitude and source-to-site distance, $f_{M_E,R_E}(m_E,r_E)$, was computed assuming the magnitude and distance of an earthquake are stochastically independent: for each zone, the magnitude-frequency distribution for each seismic zone was modelled based on the annual activity rates for discrete magnitude bins spanning from 4.15 to 7.45 (reported in [Iervolino et al., 2018]) while the location of a seismic source was assumed to be uniformly distributed within the seismogenic zone.

Aftershock parameters used in the modified Omori law of Eq. (5-6) are from [Lolli and Gasperini, 2003] for generic aftershock sequences in Italy: ($a=-1.66$, $b=0.96$, $c=0.03$, and $p=0.93$). The minimum magnitude of aftershock ($m_{A,\min}$) corresponds to that for the mainshock events [Iervolino et al., 2018]. The locations of aftershocks were assumed to be uniformly distributed within a circular area centered on the mainshock location, which size was also determined by the size of the mainshock [Utsu, 1970]. The duration of the aftershock sequence (ΔT_A) was defined arbitrarily equal to 90 days from the occurrence of the mainshock although, in principle, this duration could be mainshock magnitude dependent. For further details about the models adopted for seismic hazard assessment, see [Iervolino et al., 2018].

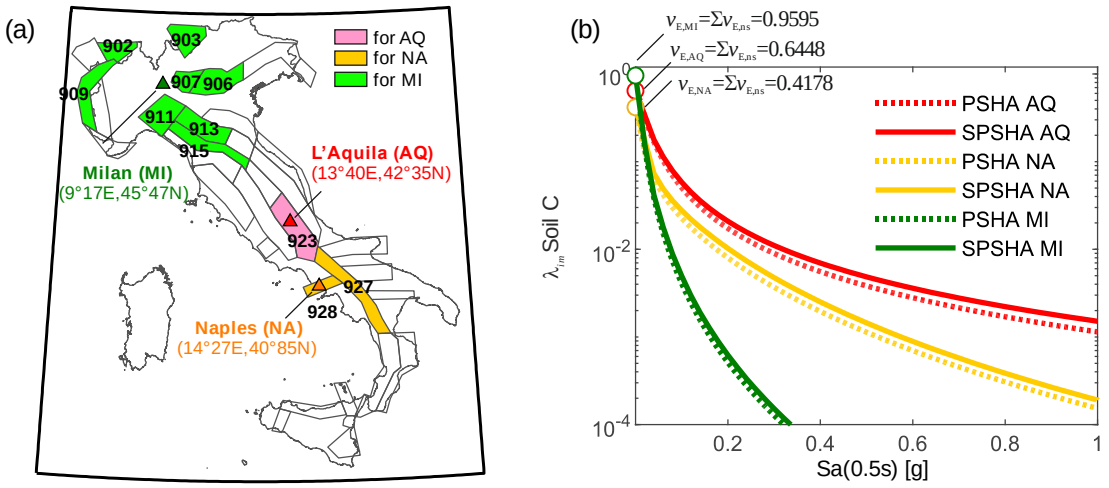

Figure 5-5 Considered sites and hazard curves; (a) Locations and source zones; (b) annual exceedance rates of $Sa(0.5s)$ computed via PSHA and via SPSHA for the three sites.

Figure 5-5b provides the hazard curves derived by PSHA, Eq. (5-1), and SPSHA, Eq. (5-5), for the three considered sites. For the sites in Naples and Milan, the sum of the hazard curves from the multiple seismogenic zones are plotted for the sake of illustration, which jointly characterize the time-unit damage transition matrix in Eq. (5-14). For each site, both PSHA and SPSHA curves start from the same value which is the sum of the annual rates of mainshocks/sequences producing at least one exceedance of zero IM at the site from the considered sources. It should be noted that, one or a few hazard-dominating seismic sources were considered for the higher seismicity sites (L'Aquila and Naples), their hazard curves apparently are exceeded by those for the lowest seismicity site (Milan) at the lower IM levels, nevertheless, it was confirmed that these values do not affect the resulting risk as nearly zero failure probabilities at the corresponding IM levels (see Figure 5-4). For each site, the difference between the PSHA and SPSHA curves increases with the IM and the seismic hazard at the site. For example, for a return period of 475 year, the increment of the spectral acceleration due to SPSHA with respect to PSHA is about 8-16%. Further details about PSHA and SPSHA for the sites can be found in the authors' previous studies [Iervolino et al., 2018; Chioccarelli et al., 2018].

5.4.4 Transition probability matrices and time-variant seismic risk

This section provides the resulting transition probability matrices and the resulting time-variant seismic risk for the considered three sites. The following first presents the results of the sequence-based seismic risk for the highest seismicity site, L'Aquila, in comparison with those only accounting for mainshock events. Subsequently, the trends across the three sites with different seismic hazard levels are discussed.

High seismicity site, L'Aquila

Table 5-4 shows the results of the annual damage transition matrices for the building designed for the highest seismicity site, L'Aquila on the soil condition C. Since the seismogenic zone (Zone 923) was only considered for this site, the annual (unit-time) transition matrix $\left[P_E\right]$ was computed simply using Eqs. (5-12)-(5-13), involving the transition matrix given the occurrence of a seismic sequence $\left[\overline{P}\right]$, and the annual occurrence of earthquake clusters of the source, ν_E . In this case study, the resulting matrix $\left[\overline{P}\right]$ considered $\left[P_{S,M_E,R_E}\right]$ through the approximation via Eq. (5-11), which will be later verified through a comparison with the rigorous formulation of Eq. (5-10). For the sake of comparison, Table 5-4 also provides the transition matrix $\left[P_E\right]$ given by Eqs. (5-3)-(5-4) considering the effects of mainshocks only through the PSHA results. Although the damage transition rates of the two matrices generally show the same order of magnitude for a given pair of the two DSs, the results show that the annual damage transition matrix for seismic sequences $\left[P_S\right]$ have the smaller rates of events causing no change from the initial DS (i.e., at the diagonals of the matrices) compared to $\left[P_E\right]$. In turn, larger transition rates to the worse DSs, particularly to the ultimate (GC) DS, can be observed in $\left[P_S\right]$ than $\left[P_E\right]$. In fact, the transition rate from the AN to GC state, that is equivalent to the annual collapse rate for new design buildings in the classical risk assessment, increases from 1.45E-04 (0.7% exceedance in 50 years) to 3.63E-04 (1.8% exceedance in 50 years). This indicates that the consideration of the sequence effects may require to revise the structural design of some new buildings, if target-risk-based structural design is implemented; for example, 1% collapse probability in 50 years.

Table 5-4 Unit-time damage transition matrices for the building in L'Aquila soil C.

[year] (Hazard type/site)		AN	UPD	LS	CP	GC
$[P_S]$ (sequences/AQ)	AN	9.97E-01	2.14E-03	1.29E-04	4.19E-05	3.63E-04
	UPD	-	9.99E-01	1.58E-04	4.67E-05	3.81E-04
	LS	-	-	9.96E-01	2.03E-03	1.88E-03
	CP	-	-	-	9.85E-01	1.51E-02
	GC	-	-	-	-	1.00E+00
$[P_E]$ (mainshocks/AQ)	AN	9.98E-01	1.68E-03	1.56E-04	8.09E-05	1.45E-04
	UPD	-	1.00E+00	1.97E-04	8.64E-05	1.46E-04
	LS	-	-	9.97E-01	2.55E-03	2.31E-04
	CP	-	-	-	9.88E-01	1.15E-02
	GC	-	-	-	-	1.00E+00

Figure 5-6 provides the time-variant probabilities of the structure staying in a certain DS, which were computed through Eq. (5-4) and Eqs. (5-13), (5-15) for the PSHA- and for SPSHA-based reliability models, respectively. Herein the sequence-based results from the approximated $\left[P_{S,M_E,R_E}\right]$ given by Eq. (5-11) are compared not only to the PSHA-based one but also to those derived from the rigorous solution of Eq. (5-10). In the each panel, the horizontal axis is the elapsed time t from $t=0$, which can be interpreted as the construction time for the AN-state building otherwise corresponds to the time when structural damage state is somehow identified as one of the possible DSs (e.g., post-earthquake damage inspection by means of structural health monitoring). The sum of the transition probabilities starting from the same DS is unity at any points of time. It can be generally observed that the probability of the structure remaining at the initial DS decreases as time elapses due to seismic damage accumulated in the structure. Particularly, the worse the initial DS is, (i) the more rapidly it moves to a worse DS and (ii) the larger effects of the sequential seismic shocks can be observed. For the sake of quantitative comparison, Table 5-5 provides the transition probability matrices at the fiftieth years, $\left[P_S(0,50)\right]$ and $\left[P_E(0,50)\right]$, referring to the expected lifespan prescribed for ordinary structures in the NTC code. For the both reliability models, the transition probabilities to worse DSs resulted to evolve by approximately orders of magnitude of 2 after 50 years, compared to the annual transition probabilities (see Table 5-4). Also, the sequence-based reliability model $\left[P_S(0,50)\right]$ resulted to differ the one neglecting the effects of

aftershocks $\left[P_E(0,50)\right]$ at maximum by about an order of magnitude; especially larger discrepancies were observed in the transition probabilities to the GC state.

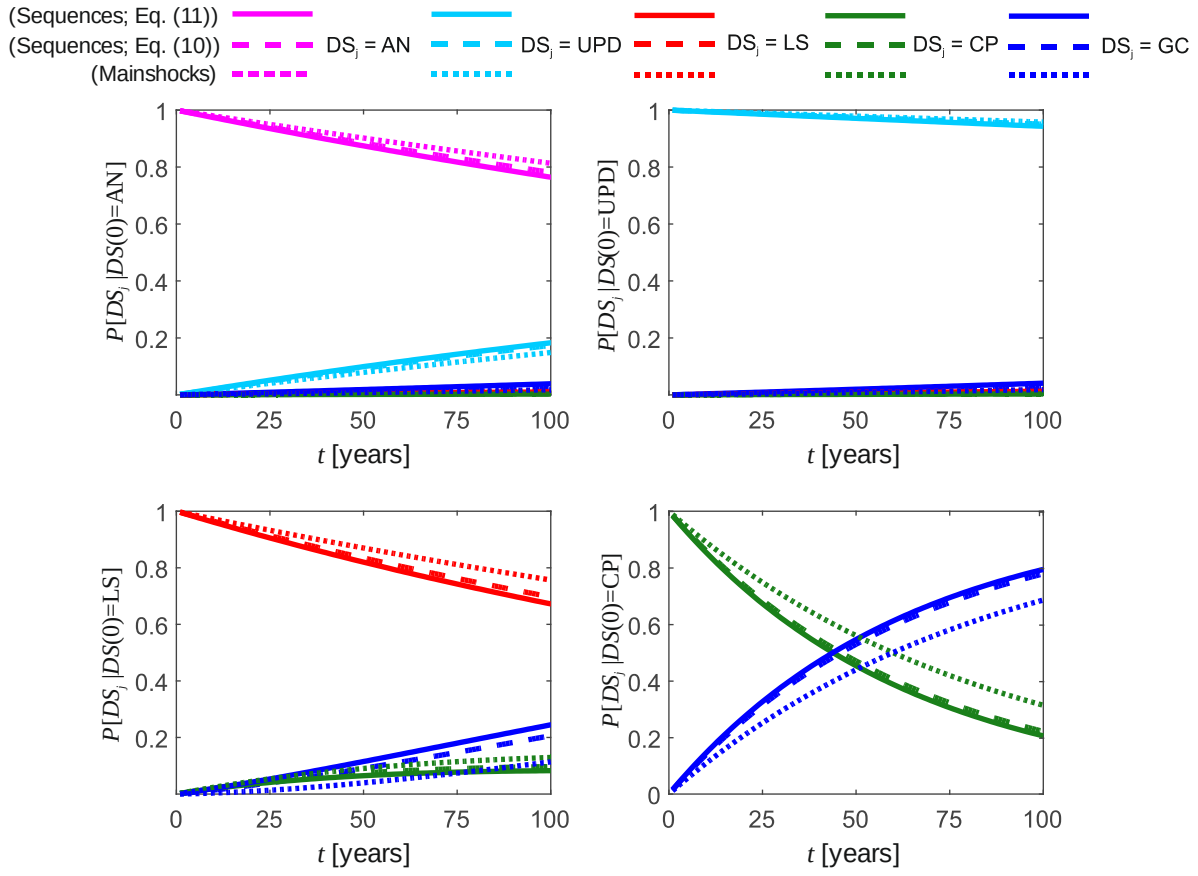

Figure 5-6 Time variant damage transition probabilities (6st IF L'Aquila Soil C).

Table 5-5 Damage transition matrices at a time of 50 years for the building in L'Aquila soil C.

[year] (Hazard type/site)		AN	UPD	LS	CP	GC
$\left[P_S(0,50)\right]$ (sequences/AQ)	**AN**	8.74E-01	9.93E-02	5.84E-03	1.69E-03	1.89E-02
	UPD	-	9.71E-01	7.10E-03	1.90E-03	1.99E-02
	LS	-	-	8.20E-01	6.49E-02	1.15E-01
	CP	-	-	-	4.54E-01	5.46E-01
	GC	-	-	-	-	1.00E+00
$\left[P_E(0,50)\right]$ (mainshocks/AQ)	**AN**	9.02E-01	7.92E-02	7.30E-03	3.46E-03	8.24E-03
	UPD	-	9.79E-01	9.09E-03	3.75E-03	8.40E-03
	LS	-	-	8.70E-01	9.04E-02	3.96E-02
	CP	-	-	-	5.60E-01	4.40E-01
	GC	-	-	-	-	1.00E+00

As far as the shown time frame is concerned, the two sequence-based results show that the approximation solution with Eq. (5-11) has agreement with the rigorous solution over the time. Hence, the sequence-based reliability models for the low-to-mid seismicity sites are presented in the following only referring to the approximated solution for the transition matrix $\left[P_{S,M_E,R_E}\right]$.

Low-to-mid seismicity sites, Milan and Naples

For the building designed for the low-to-intermediate seismicity zones, Milan and Naples, the transition matrices given an earthquake occurrence $\left[\overline{P}\right]$ were first computed integrating the state-dependent fragility curves (Table 5-3) and the site-specific sequence-based seismic hazard functions for the considered seismogenic zones (Figure 5-5) via Eqs. (5-11)-(5-12). Subsequently, the annual transition matrix $\left[P_S\right]$ was obtained via Eq. (5-14), summing up the contributions from all considered seismogenic zones for each site. Table 5-6 provides the results of the annual damage transition matricies for mainshock-aftershock sequences in comparison with those for mainshocks, $\left[P_E\right]$, computed via Eq. (5-3) and the equivalent of Eq. (5-14) in the PSHA context. Correspondingly to the findings from the RINTC project, the transition matrices for the buildings in Milan and Naples show much smaller transition probabilities to worse DSs than those for L'Aquila. In particular, large discrepancies across the three sites are related to the transitions to intermediate-to-severe DSs. For instance, the transition probabilities to the UPD-LS states for the Naples building have a similar order of magnitude as those for the L'Aquila building (Table 5-4), while those to the CP-GC states resulted to be smaller by approximately 1-2 orders of magnitude.

Similarly to the case for the L'Aquila building, differences between the two reliability models, $\left[P_S\right]$ and $\left[P_E\right]$, mainly lie in the transition probabilities to the GC state, but they appear quite small in terms of the other of magnitude.

Table 5-6 Unit-time damage transition matrices for the building in Naples and Milan soil C.

Model (Hazard type/site)		AN	UPD	LS	CP	GC
$[P_S]$ (sequences/NA)	**AN**	9.99E-01	1.30E-03	6.82E-05	8.13E-06	1.88E-05
	UPD	-	1.00E+00	8.10E-05	7.91E-06	1.88E-05
	LS	-	-	1.00E+00	2.612-05	4.02E-05
	CP	-	-	-	9.86E-01	1.39E-02
	GC	-	-	-	-	1.00E+00
$[P_E]$ (mainshocks/NA)	**AN**	9.99E-01	1.05E-03	5.49E-05	1.21E-05	9.76E-06
	UPD	-	1.00E+00	6.55E-05	1.19E-05	9.74E-06
	LS	-	-	1.00E+00	3.69E-05	1.67E-05
	CP	-	-	-	9.91E-01	9.27E-03
	GC	-	-	-	-	1.00E+00
$[P_S]$ (sequences/MI)	**AN**	1.00E+00	4.21E-05	3.85E-07	2.43E-07	5.82E-07
	UPD	-	1.00E+00	4.90E-07	3.05E-07	5.87E-07
	LS	-	-	9.97E-01	2.65E-03	8.46E-05
	CP	-	-	-	9.98E-01	2.27E-03
	GC	-	-	-	-	1.00E+00
$[P_E]$ (mainshocks/MI)	**AN**	1.00E+00	3.66E-05	3.88E-07	1.98E-07	4.91E-07
	UPD	-	1.00E+00	4.92E-07	2.47E-07	4.89E-07
	LS	-	-	9.98E-01	2.32E-03	1.45E-05
	CP	-	-	-	9.98E-01	1.94E-03
	GC	-	-	-	-	1.00E+00

Figure 5-7 and Figure 5-8 show the time-variant probabilities of damage states for the Naples and Milan buildings, respectively, which were computed through Eq. (5-15) both in the PSHA and SPSHA contexts. For the sake of comparison, the results for L'Aquila shown in Figure 5-6 are also plotted with grey lines in the same panels. As indicated with the unit-time transition matrices, it can be generally seen that structural damage is expected to proceed at a slower rate mainly due to the milder seismicity at these sites, and, in some cases, due to structural fragility comparable to that of the L'Aquila case. Particularly, this trend can be clearly seen in the cases where the structure is in the AN state $t=0$, while the transition from an intermediate state depends not only on the local seismicity but also on the intervals of the DSs specified on the backbone curves. Moreover, smaller discrepancies between the two reliability models were observed compared to the L'Aquila site, unless the structure is heavily damaged or in the near collapse (CP) state and prone to not low seismicity at the site.

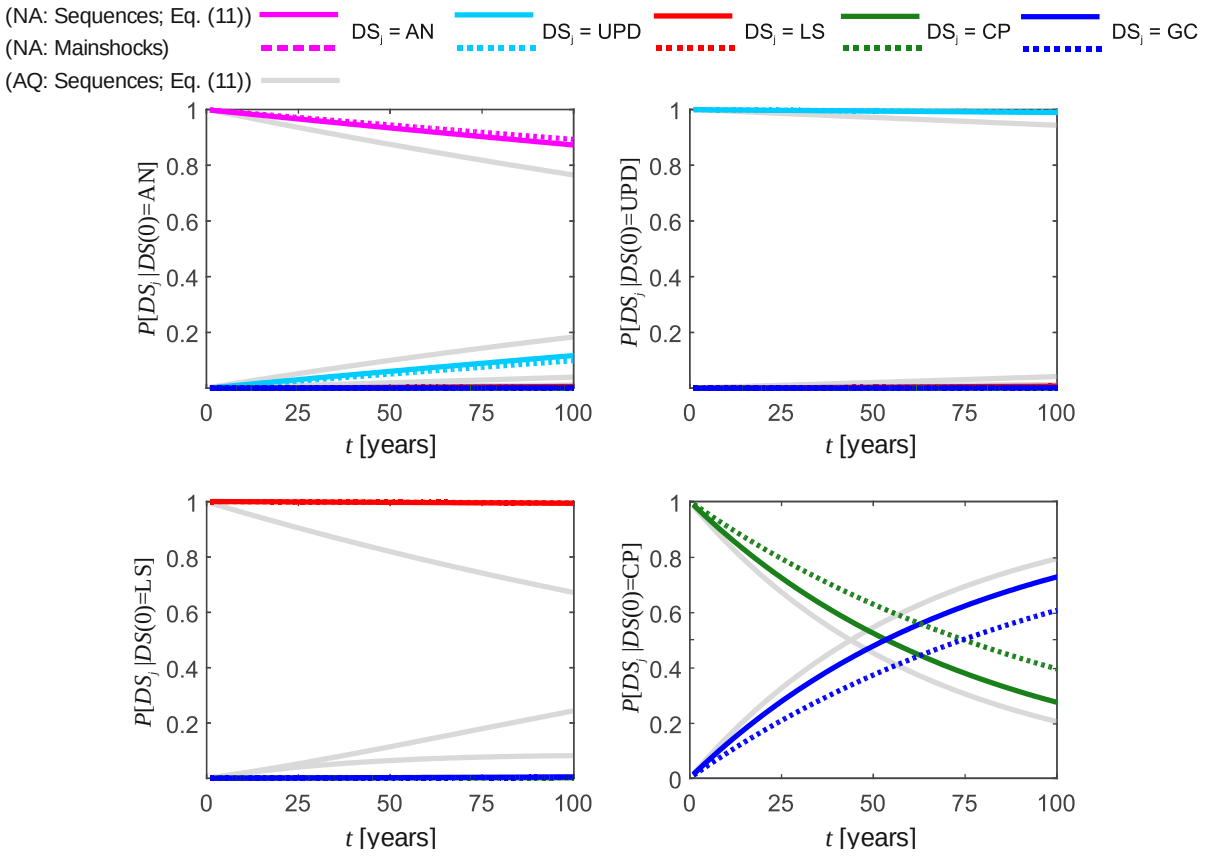

Figure 5-7 Time variant damage transition probabilities (6st IF Naples Soil C).

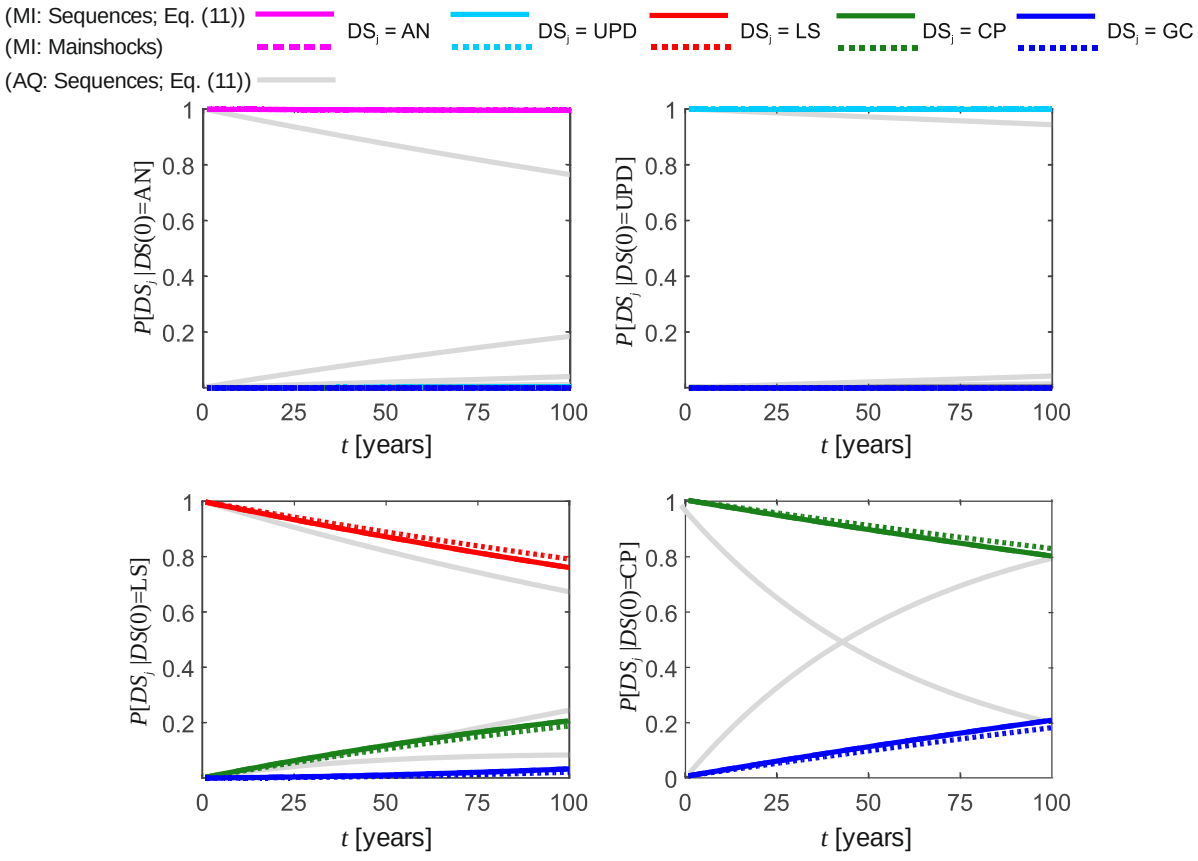

Figure 5-8 Time variant damage transition probabilities (6st IF Milan Soil C).

5.5 Conclusions

This chapter presented a Markov-chain-based reliability model of damage accumulation in structures subjected to mainshock-aftershock sequences. The model considered herein is a discrete-time and discrete-state Markovian process, being extended from the reliability model for deteriorating structures subjected to mainshocks in the authors' past study. Different structural performance levels are represented by a finite number of damage states from the intact state to collapse of a structure, and structural damage due to a single shock depends on the state of the structure at the time (state-dependent). The damage progression in the structure due to seismic sequences is modelled using a stationary transition matrix consisting of the probabilities that the structure changes the state between any possible pair of DSs. This probability matrix is derived from state-dependent fragility curves and SPSHA for the construction site of the structure. The proposed methodology was illustrated through application studies using the ESDoF systems of Italian code-conforming RC frame buildings, which were supposed to be located at three Italian sites representing different seismic hazard levels in Italy. For each building, five damage states from as-new to global collapse states were defined in terms of the maximum transient displacement, referring to the desired structural performance levels indicated in the performance-based Italian design code. The state-dependent fragility curves were obtained through back-to-back incremental dynamic analyses in terms of spectral acceleration at a period close to the fundamental periods of the structure. Using the same IM, the seismic hazard of earthquake sequences for each site was assessed via SPSHA considering the neighboring source zones dominating the seismic hazard at each site, as well as the conventional PSHA. The resulting sequence-based time-variant seismic risk was compared to that from the similar Markovian modelling of damage accumulation process accounting for mainshock events only, as well as across the different sites. Notable remarks are summarized as follows:

As far as this study's illustrative applications are concerned,

1. The computed state-dependent fragility curves under the same GM inputs for the three different sites generally show the median IM level causing the transition between any

two DSs increases with the seismic hazard at the site in accordance with the structural design reflecting the local seismicity. As expected, the worse the initial state is, the smaller spectral acceleration level causing the transition to a worse DS can be observed for all examined buildings cases. Compared with the lognormal fragility parameters for the AN state, for instance, the median spectral acceleration causing global collapse did not change much until the attainment of UPD which occurs slightly before the attainment of the maximum resistance. Then, it suddenly dropped by approximately 15-40% at the LS state due to the complete loss of load-bearing contributions from the masonry infills, eventually by approximately 90% at the CP state.

2. Given the five DS defined in a uniform manner, the unit-time transition probabilities between any DSs increase with the increasing seismic hazard at the site, which is consistent to the findings from RINTC project. Moreover, the larger discrepancies between the three sites were observed particularly in predicting the transition probabilities to intermediate-to-near-collapse DSs.

3. Compared to the mainshock-occurrence-based models, the consideration of seismic sequences generally led to major increases in the unit-time transition probabilities to the ultimate DS (i.e., global collapse) for the examined buildings in this study. Particularly, larger discrepancies between the two reliability models were observed when: (a) the seismic hazard at the site is higher and/or (b) the structure is already damaged to some extent (i.e., in intermediate DSs at the initial time). Among the sites considered, the collapse probability increased due to the sequence effects at maximum by approximately one order of magnitude for the damaged structure in the highest seismicity site, L'Aquila, while no notable changes were observed for the building in Milan.

4. The time-variant seismic risk was computed using the obtained unit-time transition matrices in (ii). The transition probabilities to any worse DSs evolved as time elapsed, showing for the mid-to-high seismicity sites increases by approximately 1-2 orders of

magnitude for 50 years, for example, from those at the first year. Correspondingly to the observations above, structural damage evolved at a more rapid pace for the building at the L'Aquila site, mainly ascribed to the higher seismic hazard.

All things considered, the results presented in this study may suggest to account for sequence effects in a long-term risk assessment of degrading structures if: (a) the structure is located at a high seismicity region, (b) suspicious to strucutral deteriotation, and/or (c) structural safety for a long time interval is of interst.

References

Ambraseys, N. N., Simpson, K. A., and Bommer, J. J. [1996] "Prediction of horizontal response spectra in Europe," *Earthq. Eng. Struct. Dyn.*, 25(4), 371–400. DOI:10.1002/(SICI)1096-9845(199604)25:4<371::AID-EQE550>3.0.CO;2-A.

Baltzopoulos, G., Baraschino, R., Iervolino, I., and Vamvatsikos, D. [2018] "Dynamic analysis of single-degree-of-freedom systems (DYANAS): A graphical user interface for OpenSees," *Eng. Struct.*, 177(December), 395–408. DOI:10.1016/J.ENGSTRUCT.2018.09.078.

Boyd, O. S. [2012] "Including foreshocks and aftershocks in time-independent probabilistic seismic-hazard analyses," *Bull. Seismol. Soc. Am.*, 102(3), 909–917. DOI:10.1785/0120110008.

Chioccarelli, E., Cito, P., Iervolino, I., and Giorgio, M. [2018] "REASSESS V2.0: software for single- and multi-site probabilistic seismic hazard analysis," *Bull. Earthq. Eng*., 17(4), 1769-1793. DOI:10.1007/s10518-018-00531-x.

Cornell, A. C., and Krawinkler, H. [2000] Progress And Challenges In Seismic Performance Assessment, PEER Center News, 3, 1-3, CA, USA.

CS.LL.PP., Decreto Ministeriale 14 gennaio [2008] Norme tecniche per le costruzioni (in Italian), Gazzetta Ufficiale della Repubblica Italiana, 29, Italy.

CS.LL.PP. [2018] Aggiornamento delle norme tecniche per le costruzioni, Gazzetta Ufficiale della Repubblica Italiana 42. (in Italian.)

Iervolino, I., Baltzopoulos, G., Chioccarelli, E., and Suzuki, A. [2017] "Seismic actions on structures in the near-source region of the 2016 central Italy sequence," *Bull. Earthq. Eng.*, no. i, 1–19.

Iervolino, I., Chioccarelli, E., and Giorgio, M. [2018] "Aftershocks' Effect on Structural Design Actions in Italy," *Bull. Seismol. Soc. Am.*, 108(4), 2209–2220. DOI:10.1785/0120170339.

Iervolino, I., Giorgio, M., and Chioccarelli, E. [2013] "Gamma degradation models for earthquake-resistant structures, *Structural Safety*, 45, 48-58.

Iervolino, I., Giorgio, M., and Chioccarelli, E. [2014] "Closed-form aftershock reliability of damage-cumulating elastic-perfectly-plastic systems," *Earthq. Eng. Struct. Dyn.*, 43(4),

613–625. DOI:10.1002/eqe.2363.

Iervolino, I., Giorgio, M., and Chioccarelli, E. [2015b] "Age- and state-dependent seismic reliability of structures," In *12th Int. Conf. Appl. Stat. Probab. Civ. Eng.*, Vancouver, Canada. DOI:10.14288/1.0076087.

Iervolino, I., Giorgio, M., and Chioccarelli, E. [2016] "Markovian modeling of seismic damage accumulation," *Earthq. Eng. Struct. Dyn.*, 45(3), 441–461. DOI:10.1002/eqe.2668.

Iervolino, I., M. Giorgio, and B. Polidoro [2014] "Sequence-based probabilistic seismic hazard analysis," *Bull.Seismol.Soc.Am.*, 104, 1006–1012. DOI:10.1785/0120130207.

Iervolino, I., Giorgio, M., and Polidoro, B. [2015a] "Reliability of structures to earthquake clusters," *Bull. Earthq. Eng.*, 13(4), 983–1002. DOI:10.1007/s10518-014-9679-9.

Jia, G., and Gardoni, P. [2018] "State-dependent stochastic models: A general stochastic framework for modeling deteriorating engineering systems considering multiple deterioration processes and their interactions," *Struct. Saf.*, 72(May), 99–110. DOI:10.1016/J.STRUSAFE.2018.01.001.

Jia, G., and Gardoni, P. [2019] "Stochastic life-cycle analysis: renewal-theory life-cycle analysis with state-dependent deterioration stochastic models," *Struct. Infrastruct. Eng.*, , March, 1–14. DOI:10.1080/15732479.2019.1590424.

Li, Q., and Ellingwood, B. R. [2007] "Performance evaluation and damage assessment of steel frame buildings under main shock–aftershock earthquake sequences," *Earthq. Eng. Struct. Dyn.*, 36(3), 405–427. DOI:10.1002/eqe.667.

Lolli, B., and Gasperini, P. [2003] "Aftershocks hazard in Italy Part I: Estimation of time-magnitude distribution model parameters and computation of probabilities of occurrence," *J. Seismol.*, 7(2), 235–257. DOI:10.1023/A:1023588007122.

Luco, N., Bazzurro, P., and Cornell, A. C. [2004] "Dynamic versus static computation of the residual capacity of a mainshock-damaged building to withstand an aftershock," In Proc.of *13th World Conf. Earthq. Eng. Vancouver, Canada*, , no. 2405.

Meletti, C., Galadini, F., Valensise, G., Stucchi, M., Basili, R., Barba, S., Vannucci, G., and Boschi, E. [2008] "A seismic source zone model for the seismic hazard assessment of the Italian territory," *Tectonophysics*, 450(1–4), 85–108. DOI:10.1016/J.TECTO.2008.01.003.

Stucchi, M., Meletti, C., Montaldo, V., Crowley, H., Calvi, G. M., and Boschi, E. [2011] "Seismic hazard assessment (2003-2009) for the Italian building code," *Bull. Seismol. Soc. Am.*, 101(4), 1885–1911. DOI:10.1785/0120100130.

Toro, G. R., and Silva, W. J. [2001] "Scenario earthquakes for Saint Louis, MO, and Memphis, TN, and seismic hazard maps for the central United States region including the effect of site conditions, Final Technical Report, Boulder, Colorado: Risk Engineering.

Utsu T. [1970] "Aftershocks and earthquake statistics (1): Some parameters which characterize an aftershock sequence and their interrelations," *J Faculty Sci, Hokkaido Univ.*, **3**(3): 129–195.

Vamvatsikos, D., and Cornell, A. C. [2002] "Incremental dynamic analysis," *Earthq. Eng. Struct. Dyn.*, 31(3), 491–514. DOI:10.1002/eqe.141.

Yeo, G. L., and Cornell, A. C. [2009] "A probabilistic framework for quantification of aftershock ground-motion hazard in California: Methodology and parametric study," *Earthq. Eng. Struct. Dyn.*, 38(1), 45–60. DOI:10.1002/eqe.840.

Yeo, G. L., and Cornell, C. A. [2009]. "Building life-cycle cost analysis due to mainshock and aftershock occurrences," *Structural Safety*, 31(5), 396-408.

Chapter 6

Summary

This thesis addressed the structural seismic fragility of the current Italian code-conforming buildings in relation to structural design features and to the degree of the resulting structural reliability in line with the PBEE framework. To this aim, the seismic performance factors of some representative buildings designed, modeled and analyzed within the RINTC project, belonging to a variety of structural types and configurations and site hazard levels, were examined using the simplified models equivalent to the original 3D structural models. Through the seismic performance factors computed based on the SDoF approximation, the structural design features that are related to the resulting seismic risk were examined (Chapter 2). Using the calibrated equivalent systems, the fragility functions were estimated principally with respect to collapse limit states in order to quantify the possible ranges of the collapse safety margins, as well as those related to the usability-preventing damage onset limit states (Chapter 3). This thesis also explored possible approaches to convert GM intensity measures (IMs) of fragility curves, which were applied to the selected prototype buildings (Chapter 4). Furthermore, the effects of earthquake sequences in long-term seismic risk assessment of new constructions were examined using the selected case studies for the sites exposed to different seismic hazard levels (Chapter 5). The conclusions and remarks from each chapter are summarized in the following.

Chapter 2: Seismic performance evaluation of Italian code-conforming buildings based on SDoF approximation

Chapter 2 presented design structural features to explain heterogeneity of seismic risk among the prototype buildings of the RINTC project, designed for several sites with different hazard levels in Italy. For the purposes of this investigation, this study exclusively examined some

regular buildings belonging to a variety of structural types (i.e., URM, RC, steel, and PRC buildings) and located at three sites representing low-, mid- and high-hazard in Italy. The 3D structural models of the selected buildings were then converted into the ESDoF systems based on the SPO curves, which were verified through comparisons of structural responses obtained through NLDAs. Through SDoF approximation, structural response and collapse of the original 3D structural models were estimated assuming the collapse criteria defined in a similar or fairly equivalent manner to the original models. Although some discrepancies inevitably arose due to the SDoF approximation unsuitable for local structural response prediction, the calibrated ESDoF systems provided fair estimates of the structural responses of the original 3D models. Using the validated ESDoF systems, design trends of inelastic capacities such as strength reduction factors with respect to the 475-year design GM levels and ductility capacity up to global collapse of the structure were examined. One of the main findings from this chapter is that the strength reduction factor with respect to a 475-year design GM level tends to increase with an increase of the hazard at the site, while ultimate ductility capacity appeared less related to seismic hazard at the site. The study also showed that the reduction factor with respect to the expected spectral acceleration given the exceedance of the 475-year design GM intensity level increases with the seismic hazard level at the site. This possibly means the inhomogeneity of seismic risk across sites with different seismic hazard levels is ascribed not only to the degree of overstrength imposed in seismic design, but also to the seismic hazard level associated with extreme events at the building site.

Chapter 3:

Structure-site-specific fragility assessment of code-conforming buildings in Italy

This chapter developed seismic fragility functions of the Italian NTC code-conforming buildings of the RINTC project with respect to two performance limit states, i.e., global collapse and usability -preventing damage onset limit states. Seismic fragilities with respect to global collapse limit state were examined via NLDA principally using the ESDoF systems calibrated in Chapter 2, while those with respect to the damage onset limit state were assessed using structural responses of the original 3D models. Fragility functions, expressed in terms of

spectral acceleration at a period close to the fundamental vibration periods of the corresponding structure, were estimated through an EDP-based approach in conjunction with maximum likelihood estimation fitting method. The study first validated the estimated collapse fragility functions for the highest seismicity site, L'Aquila, through a comparison with those estimated using the original 3D models. In the course of investigations, it emerged that some relevant issues related to GM scaling significantly affect the resulting collapse fragility functions for the sites exposed to low- and intermediate seismicity. Therefore, the collapse fragility functions were estimated using the ESDoF systems under two different assumptions on hazard characterization. For all examined cases, the computed fragilities were validated through the comparisons of annual collapse rates computed from the 3D models. The safety margin ratios, defined as the ratio of the median spectral acceleration causing the violation of the desired performance level to the 475-year design GM level, were also provided with respect to collapse and usability-preventing damage onset limit states. The results revealed that the estimated safety margin ratios with respect to SLD and SLV tend to decrease with the increasing hazard, correspondingly to the findings on the trends of strength reduction factors in Chapter 2. In particular, the collapse safety margin ratios of the same structural type belonging to the highest seismicity site, L'Aquila, resulted to be smaller than those for the lowest seismicity site, Milan, approximately by a factor of 3-9 in most of the cases. Such differences are mainly ascribed to the difference in the design seismic actions and the estimated median collapse capacities appeared comparable across the sites. As it regards the collapse margin ratios across the different structural types, the URM buildings turned out to be the most vulnerable, followed by the steel/PRC and RC buildings. On the contrary, the safety margin ratios with respect to damage onset were comparable among the four different structural types. These findings, consistent to the results in Chapter 2, revealed the fact that the current code-conforming design tend to prescribe smaller safety margins for the more hazardous sites.

Chapter 4:

Intensity measure conversion of seismic structural fragility curves

This chapter explored hazard-consistent IM conversions for fragility curves with the aid of the state-of-the art methods in PBEE. Assuming that structural response given an IM is available from preliminary structural response analysis, the presented framework allows one to estimate the fragility curve in terms of a target IM without any additional structural analyses. Particularly, three possible conversion cases were examined varying the assumptions on the sufficiency of the IMs involved. The IM conversion cases were explored using the ESDoF systems of multi-story Italian code-conforming RC buildings featuring a wide range of the fundamental vibration period of the structure (from 0.3s to 2.0s). For each structure, the original IM was defined as spectral acceleration at a period close to the fundamental period of the structure, $Sa(T)$, then the IM conversions were performed with respect to two performance levels (i.e., usability-preventing damage and global collapse) accounting for the following two different conditions: (i) the target IM is PGA and (ii) the target IM is spectral acceleration at a longer period then the fundamental period of the structure. The former was explored for all considered structures while the latter exclusively referred to an intermediate period building selected from them. For all IM conversion cases, the fragility curves expressed in terms of the target IM were obtained from the regressions of the structural response given $Sa(T)$ on the involved IM variables and the PSHA results for the building site. The converted fragility functions were compared with the results from the reference fragility analysis accounting for the estimation uncertainties, which were also hazard-consistent with respect to the target IM. Particularly in cases of converting to PGA, the fragility curves converted through the examined IM conversion framework were in agreement with both the empirical and parametric fragility functions computed via a conventional approach in PBEE. Most of the considered IM conversions provided the fragility curves within the possible ranges of parametric fragility functions including estimation uncertainties, when the optimal (sufficient and efficient) IM was considered. As it regards the variables to be involved in assessing the original fragility, the study showed, the effects of magnitude and source-to-site distance did not affect significantly the structural response prediction, neither the resulting converted fragility functions, which is consistent or expected

from the past literature. On the other hand, the use of a two-parameter-vector IM consisting the original and target IMs returned the closest estimate to the reference analysis results in some cases. However, it should be noted that larger discrepancies with the reference analysis results were observed in the conversion between two IMs whose periods are relatively close or far to each other, particularly when referring to the attainment of structural collapse. The presented conversion framework was also applied to a series of the prototype code-conforming buildings belonging to the site, L'Aquila on soil C. The PGA-based converted fragility curves of the code-conforming buildings showed that the structures with a shorter vibration period appeared the more vulnerable, corresponding to the CS shapes given PGA. This means that the presented hazard-consistent IM conversion framework allows to examine multiple structures under the same conditions of seismic input, thus providing a different interpretation of seismic structural fragility from other types of comparisons in the preceding chapters, such as in terms of failure rate or safety margin ratios.

Chapter 5:

Markovian modelling of damage accumulation of structures in seismic sequences

This chapter presented a Markov-chain-based reliability model of damage accumulation in structures subjected to mainshock-aftershock sequences. The model considered herein is a discrete-time and discrete-state Markovian process. Different structural performance levels are represented by a finite number of damage states from an intact state to collapse of the structure, and structural damage due to a single shock depends on the state of the structure at the time (state-dependent). Damage progression in the structure subjected to seismic sequences is modelled using a stationary transition matrix consisting of the probabilities that the structure changes the state between any possible pair of DSs. This probability matrix is derived from state-dependent fragility curves of the structure and sequenced-based probabilistic seismic hazard (via SPSHA) for the building site. The proposed methodology was illustrated through application studies using the ESDoF systems of the Italian code-conforming RC frame buildings at the three Italian sites examined in the preceding chapters. For each building, five damage states from as-new to global collapse states were defined in terms of the maximum

transient displacement, referring to the desired structural performance levels indicated in the PBSD code. The state-dependent fragility curves were obtained through back-to-back incremental dynamic analyses in terms of spectral acceleration at a period close to the fundamental periods of the structure. Using the same IM, the seismic hazard of earthquake sequences for each site was assessed via SPSHA considering the neighboring source zones dominating the seismic hazard at each site. The resulting sequence-based time-variant seismic risk was compared to that from the PSHA-based reliability model neglecting the effects of aftershocks. The results in this chapter illustrated that the effects of seismic sequences are relevant especially for structures located at a high seismicity region and/or suspicious to any strucutral deteriotation.

Appendix

Ground motion record sets (Chapters 2-4)

Examined IM levels in MSA (Soil A)

Table A1 IM levels in MSA (L'Aquila Soil A).

	IML									
IM	**1**	**2**	**3**	**4**	**5**	**6**	**7**	**8**	**9**	**10**
$Sa(0.15s)$ [g]	0.107	0.22	0.352	0.493	0.658	0.858	1.132	1.417	2.056	3.417
$Sa(0.5s)$ [g]	0.050	0.114	0.202	0.319	0.485	0.720	1.074	1.529	2.387	4.830
$Sa(1.0s)$ [g]	0.018	0.044	0.083	0.138	0.221	0.340	0.514	0.732	1.115	2.117
$Sa(2.0s)$ [g]	0.007	0.017	0.032	0.052	0.081	0.122	0.180	0.253	0.382	0.731

Table A2 IM levels in MSA (Naples Soil A).

	IML									
IM	**1**	**2**	**3**	**4**	**5**	**6**	**7**	**8**	**9**	**10**
$Sa(0.15s)$ [g]	0.055	0.127	0.219	0.322	0.434	0.56	0.728	0.907	1.173	1.806
$Sa(0.5s)$ [g]	0.028	0.076	0.142	0.214	0.297	0.393	0.523	0.66	0.871	1.409
$Sa(1.0s)$ [g]	0.010	0.032	0.064	0.099	0.140	0.189	0.252	0.317	0.418	0.659
$Sa(2.0s)$ [g]	0.005	0.014	0.027	0.042	0.058	0.076	0.100	0.128	0.167	0.260

Table A3 IM levels in MSA (Milan Soil A).

	IML									
IM	**1**	**2**	**3**	**4**	**5**	**6**	**7**	**8**	**9**	**10**
$Sa(0.15s)$ [g]	0.032	0.057	0.081	0.102	0.126	0.151	0.181	0.214	0.266	0.373
$Sa(0.5s)$ [g]	0.015	0.029	0.044	0.059	0.076	0.098	0.127	0.157	0.208	0.33
$Sa(1.0s)$ [g]	0.005	0.011	0.017	0.024	0.033	0.044	0.058	0.074	0.101	0.166
$Sa(2.0s)$ [g]	0.002	0.005	0.008	0.011	0.015	0.02	0.026	0.034	0.046	0.073

Table A4 IM levels in MSA (L'Aquila Soil C).

	IML											
IM	**1**	**2**	**3**	**4**	**5**	**6**	**7**	**8**	**9**	**10**	**11**	**12**
PGA	0.055	0.125	0.172	0.257	0.345	0.459	0.664	0.870	1.11	2.16	3.62	5.47
$Sa(0.15s)$ [g]	0.128	0.267	0.425	0.589	0.784	1.039	1.397	1.801	2.512	4.456	-	-
$Sa(0.5s)$ [g]	0.077	0.181	0.322	0.503	0.754	1.129	1.733	2.481	3.810	7.639	-	-
$Sa(1.0s)$ [g]	0.029	0.073	0.139	0.232	0.365	0.558	0.855	1.217	1.837	3.520	-	-
$Sa(1.5s)$ [g]	0.015	0.039	0.075	0.126	0.200	0.309	0.478	0.689	1.062	2.080	-	-
$Sa(2.0s)$ [g]	0.011	0.026	0.049	0.08	0.124	0.184	0.27	0.379	0.572	1.077	-	-

Table A5 IM levels in MSA (Naples Soil C).

	IML									
IM	**1**	**2**	**3**	**4**	**5**	**6**	**7**	**8**	**9**	**10**
$Sa(0.15s)$ [g]	0.065	0.154	0.265	0.384	0.526	0.696	0.893	1.095	1.42	2.092
$Sa(0.5s)$ [g]	0.043	0.119	0.226	0.343	0.48	0.637	0.834	1.051	1.393	2.114
$Sa(1.0s)$ [g]	0.017	0.053	0.106	0.166	0.235	0.313	0.411	0.532	0.693	1.055
$Sa(1.5s)$ [g]	0.01	0.031	0.061	0.094	0.134	0.18	0.235	0.292	0.383	0.573
$Sa(2.0s)$ [g]	0.007	0.021	0.041	0.063	0.089	0.119	0.155	0.195	0.256	0.384

Table A6 IM levels in MSA (Milan Soil C).

	IML									
IM	**1**	**2**	**3**	**4**	**5**	**6**	**7**	**8**	**9**	**10**
$Sa(0.15s)$ [g]	0.039	0.07	0.099	0.126	0.154	0.187	0.226	0.261	0.314	0.446
$Sa(0.5s)$ [g]	0.023	0.045	0.07	0.094	0.122	0.154	0.197	0.248	0.328	0.521
$Sa(1.0s)$ [g]	0.009	0.018	0.028	0.04	0.053	0.071	0.096	0.123	0.165	0.271
$Sa(1.5s)$ [g]	0.005	0.01	0.016	0.023	0.031	0.041	0.055	0.071	0.097	0.155
$Sa(2.0s)$ [g]	0.004	0.008	0.012	0.017	0.023	0.031	0.04	0.052	0.071	0.114

A.1.1 – GM record sets for MSA (L'Aquila, soil A), $Sa(0.15s)$

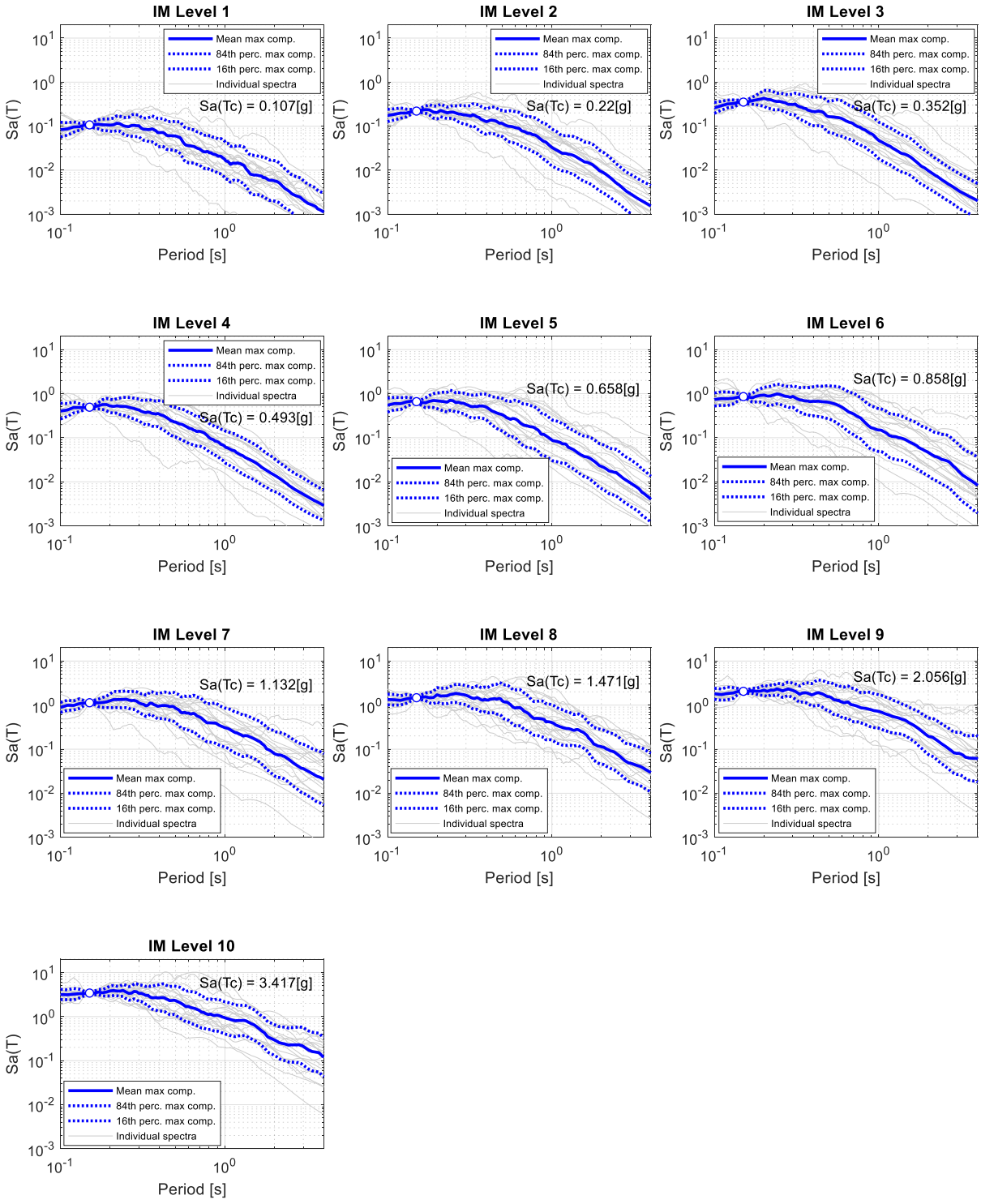

A.1.2 GM record sets for MSA (L'Aquila, soil A), $Sa(0.5s)$

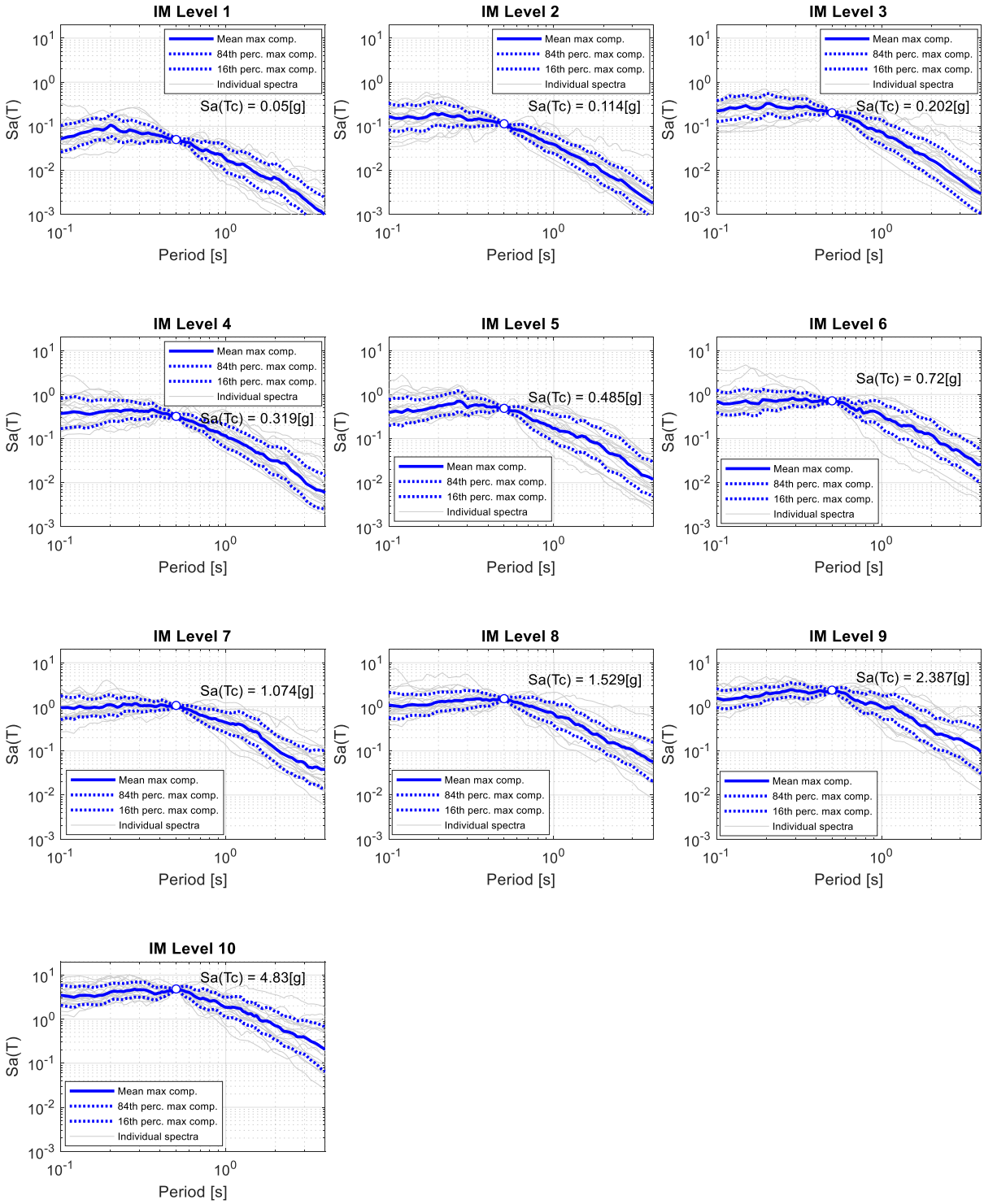

A.1.3 GM record sets for MSA (L'Aquila, soil A), $Sa(1.0s)$

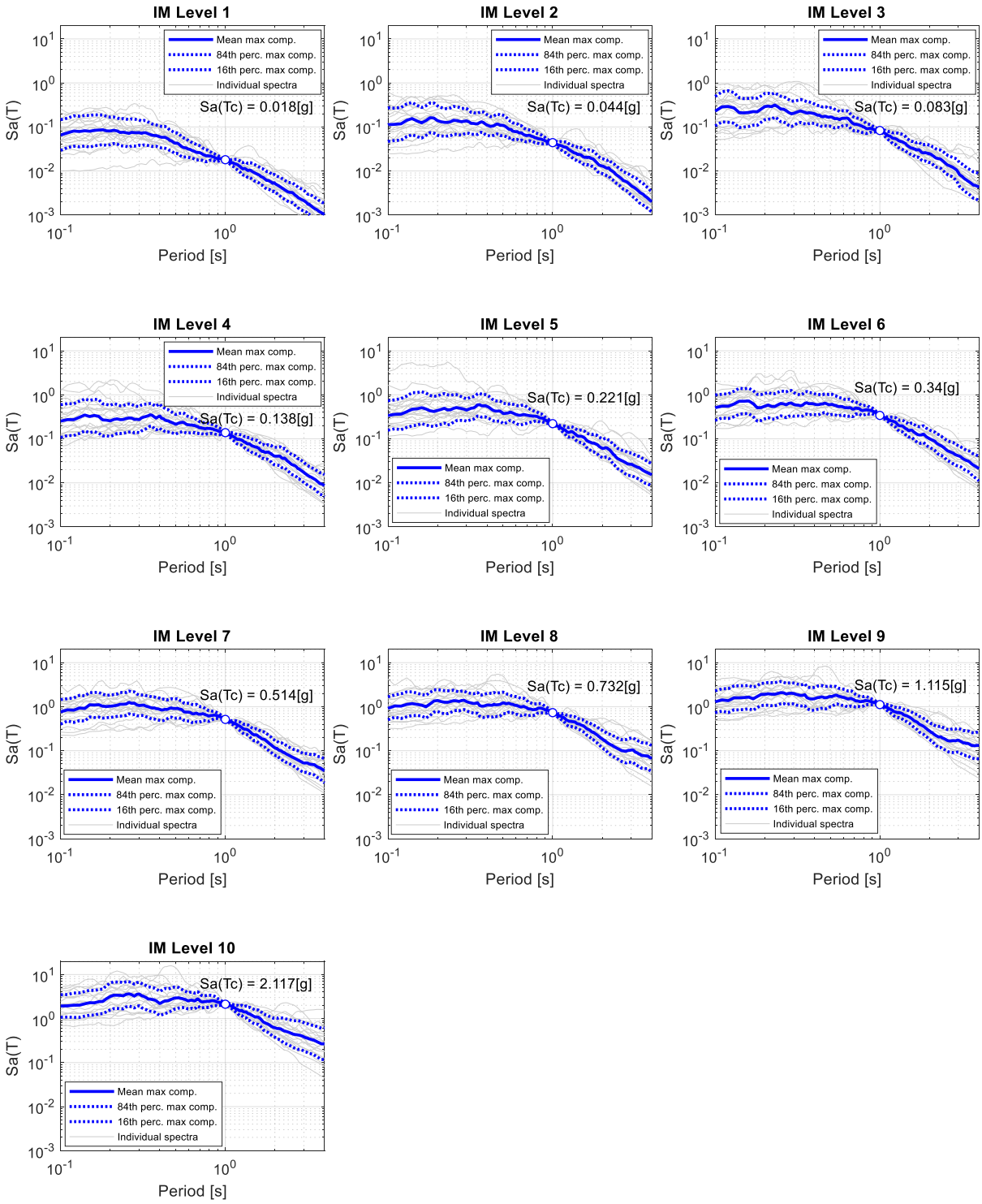

A.1.4 GM record sets for MSA (L'Aquila, soil A), $Sa(2.0s)$

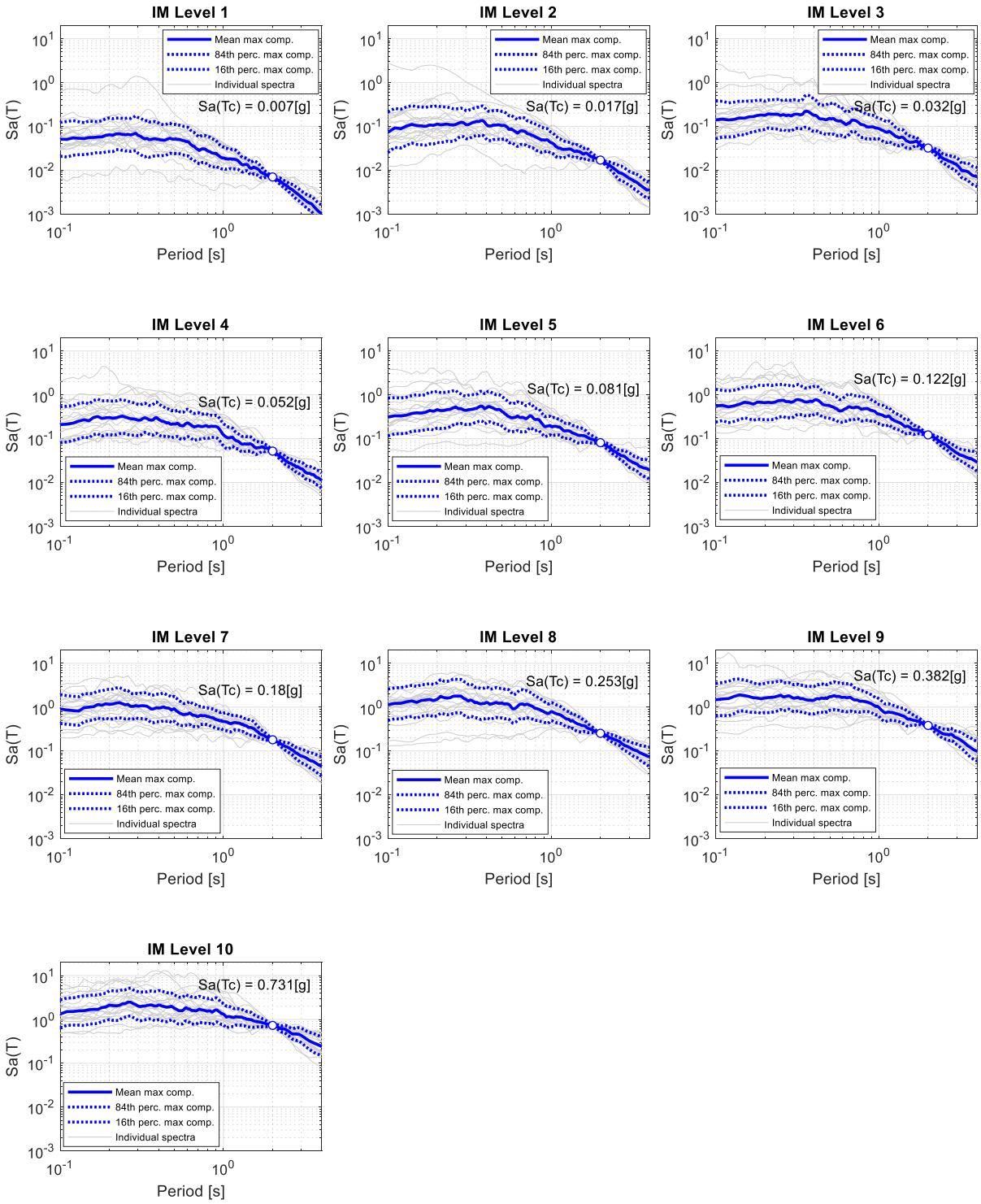

A.2.1 GM record sets for MSA (Naples, soil A), $Sa(0.15s)$

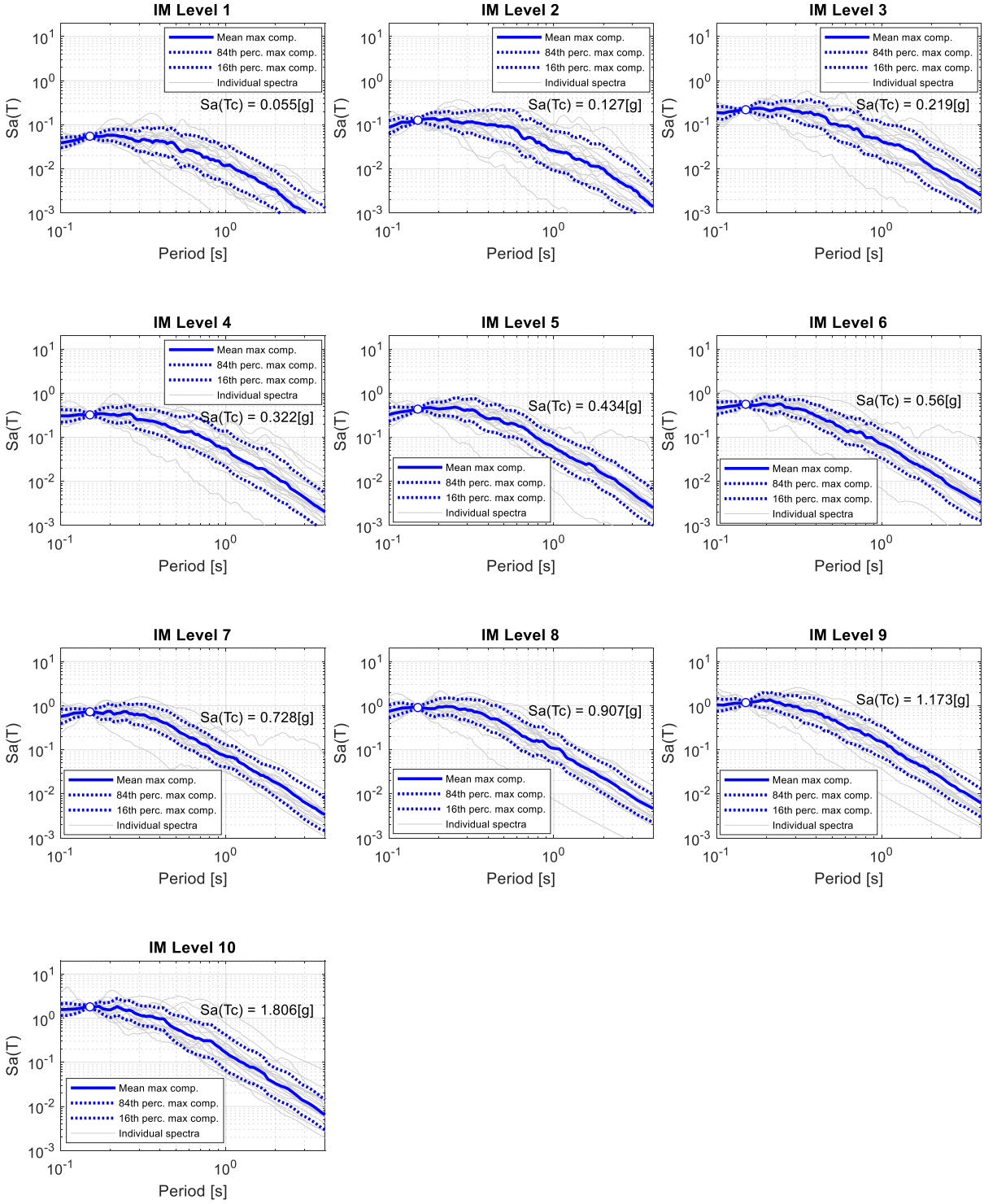

A.2.2 GM record sets for MSA (Naples, soil A), $Sa(0.5s)$

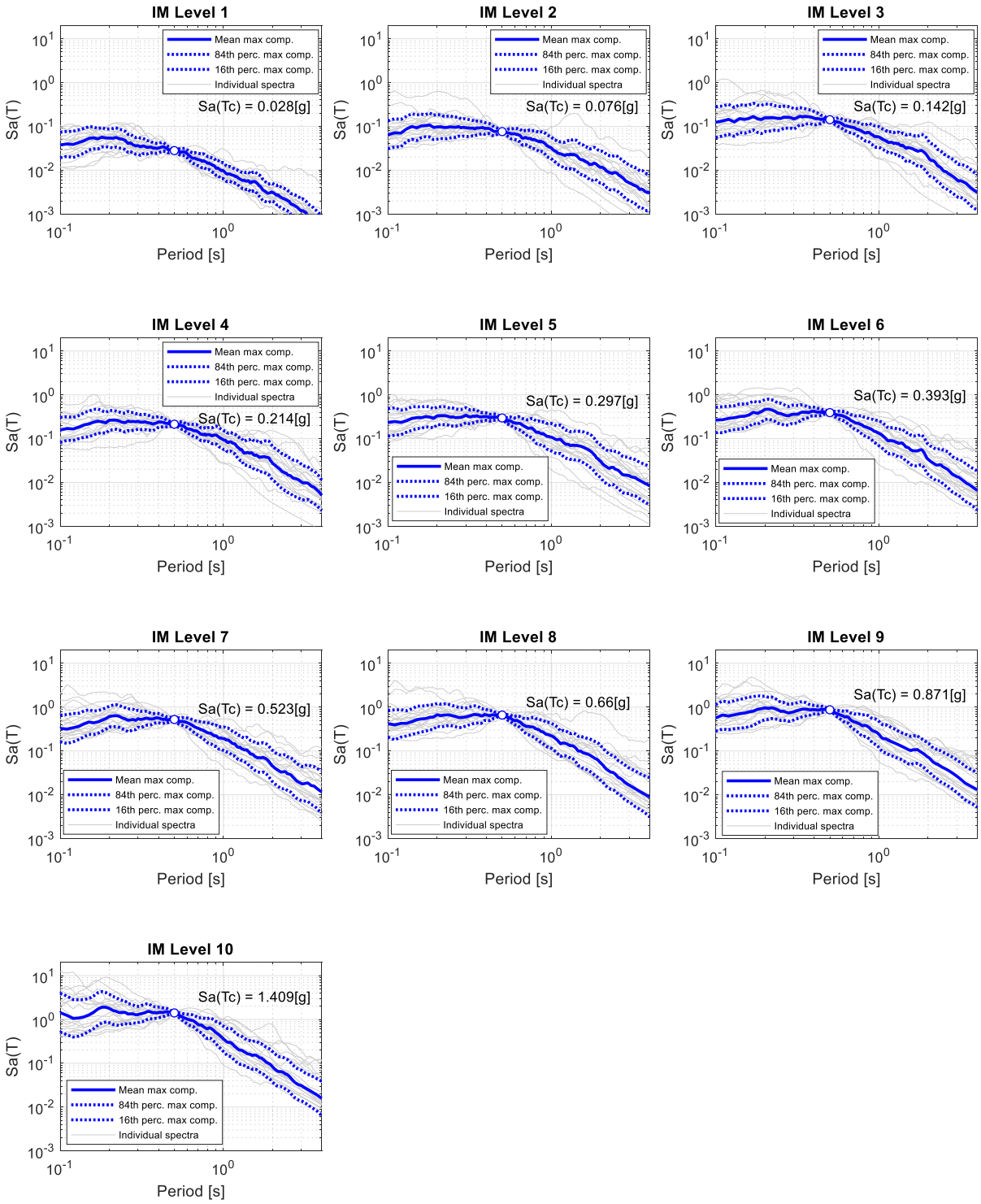

A.2.3 GM record sets for MSA (Naples, soil A), $Sa(1.0s)$

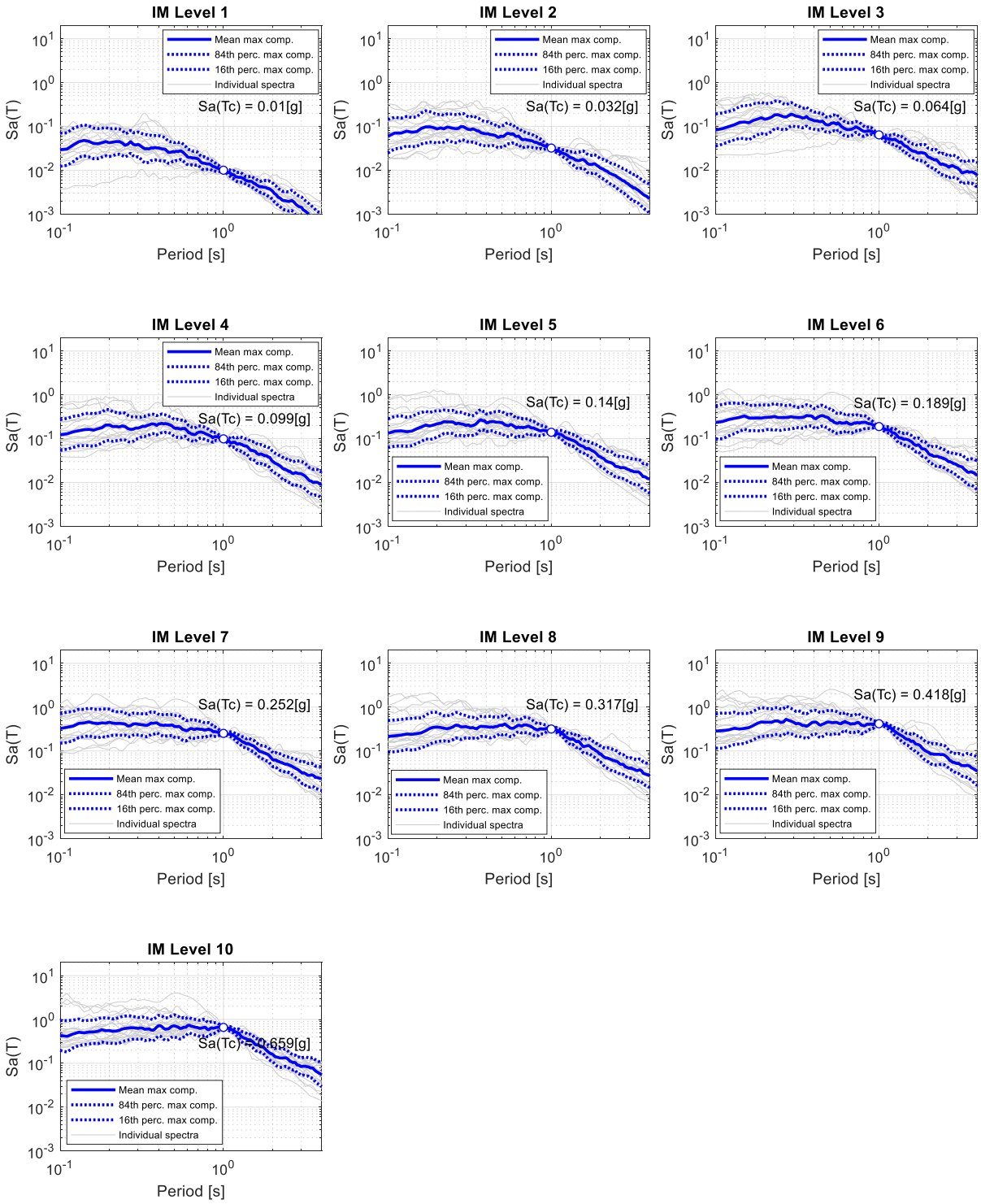

A.2.4 GM record sets for MSA (Naples, soil A), $Sa(2.0s)$

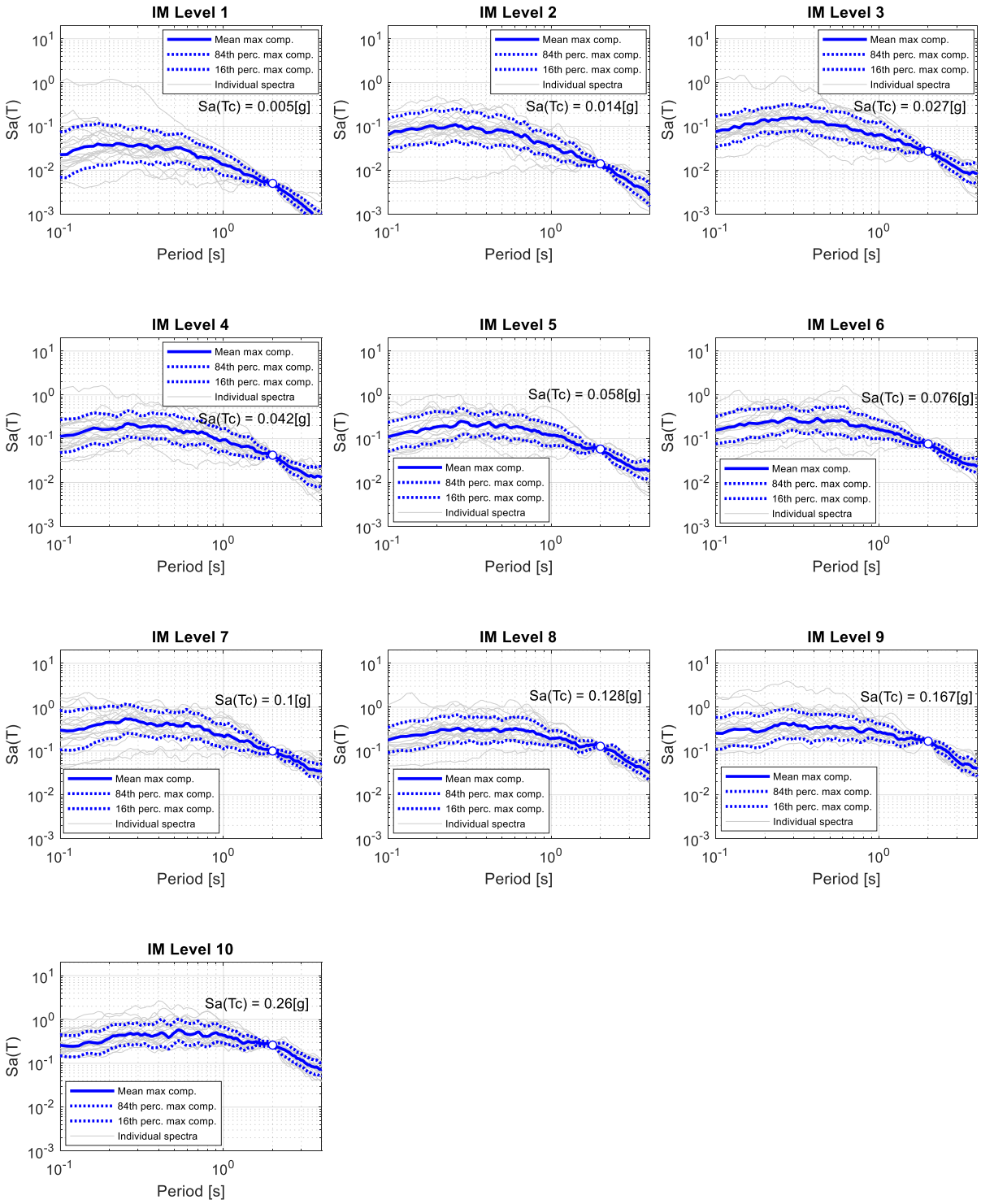

A.3.1 GM record sets for MSA (Milan, soil A), $Sa(0.15s)$

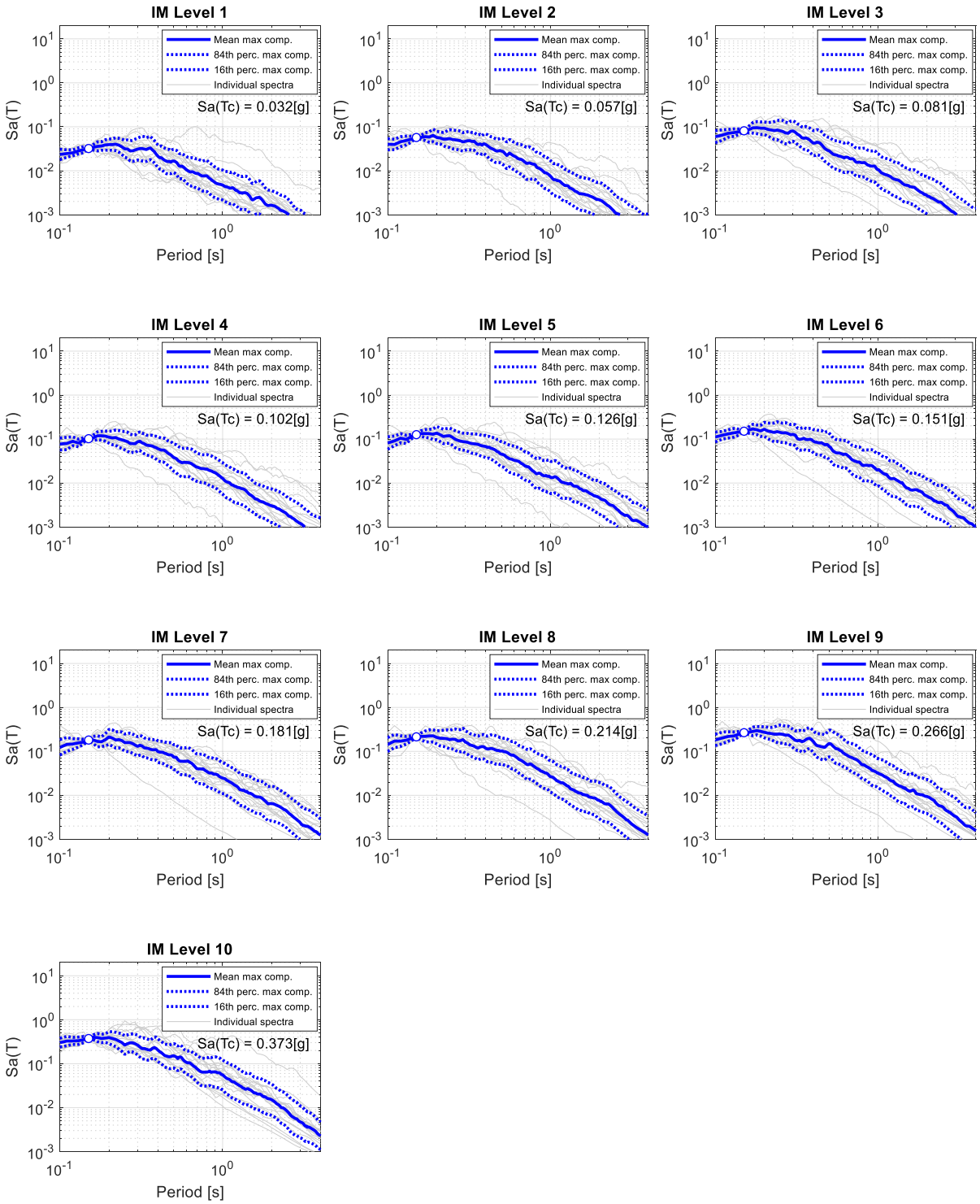

A.3.2 GM record sets for MSA (Milan, soil A), $Sa(0.5s)$

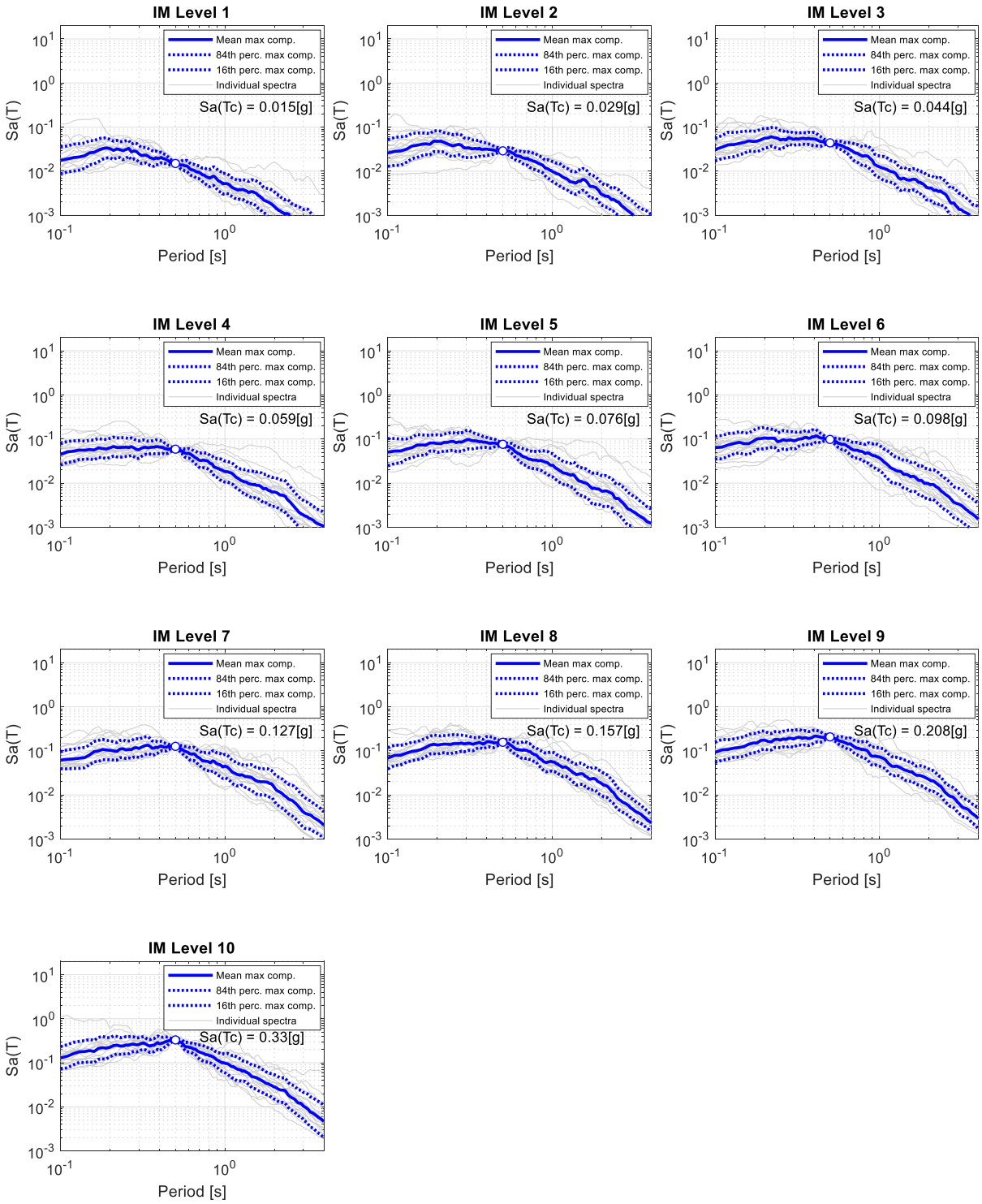

A.3.3 GM record sets for MSA (Milan, soil A), $Sa(1.0s)$

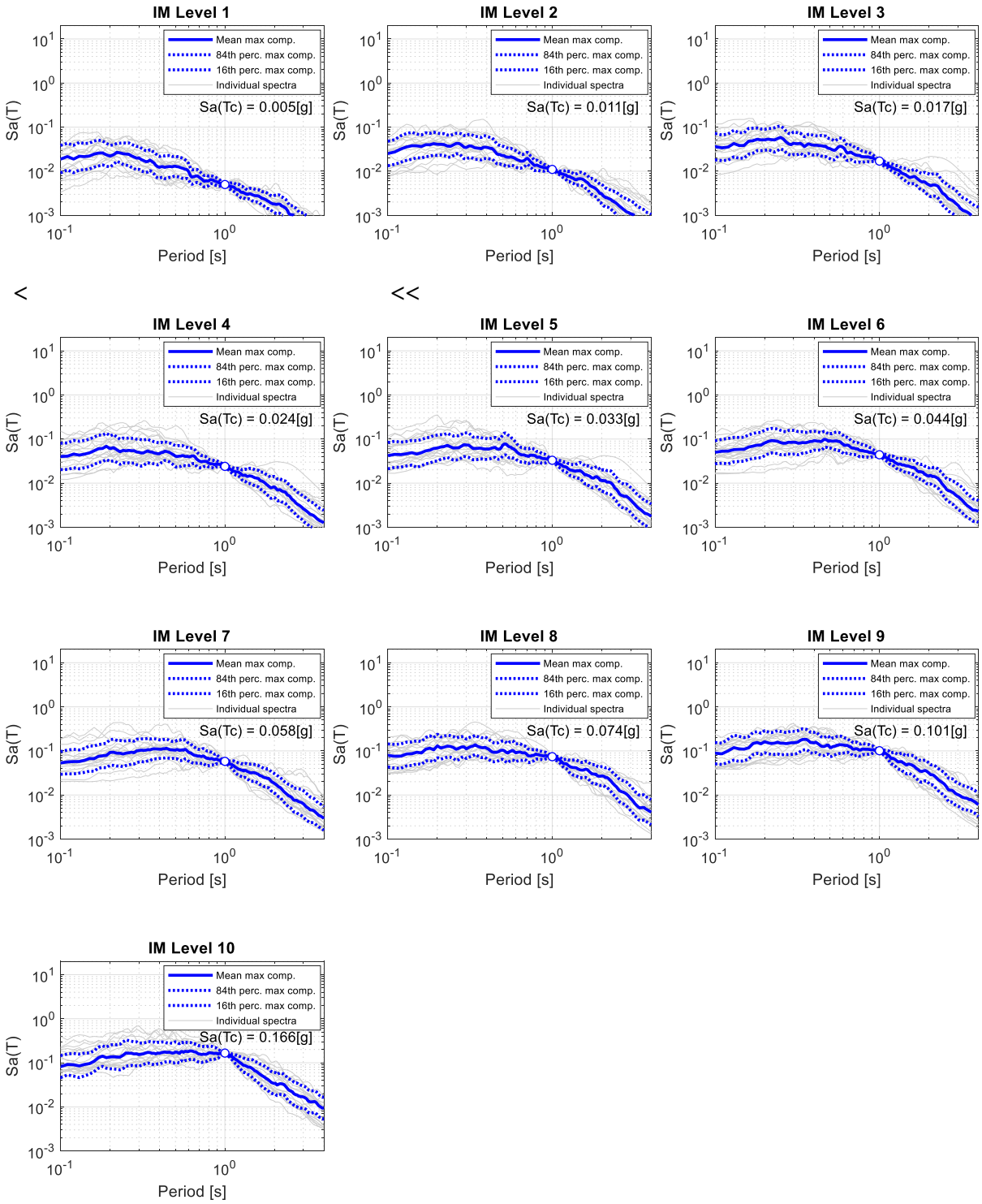

A.3.4 GM record sets for MSA (Milan, soil A), $Sa(2.0s)$

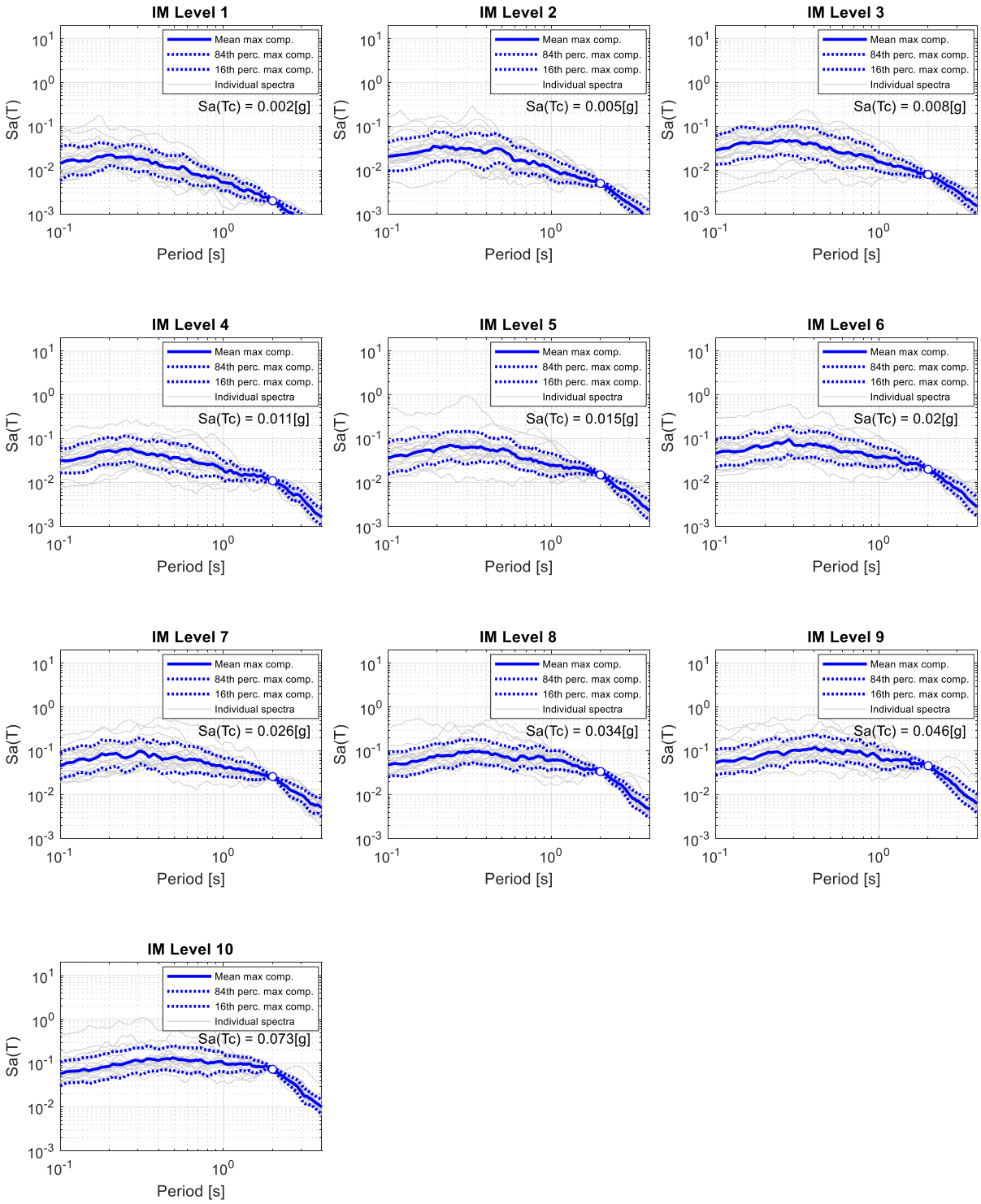

A.4.1 GM record sets for MSA (L'Aquila, soil C), *PGA*

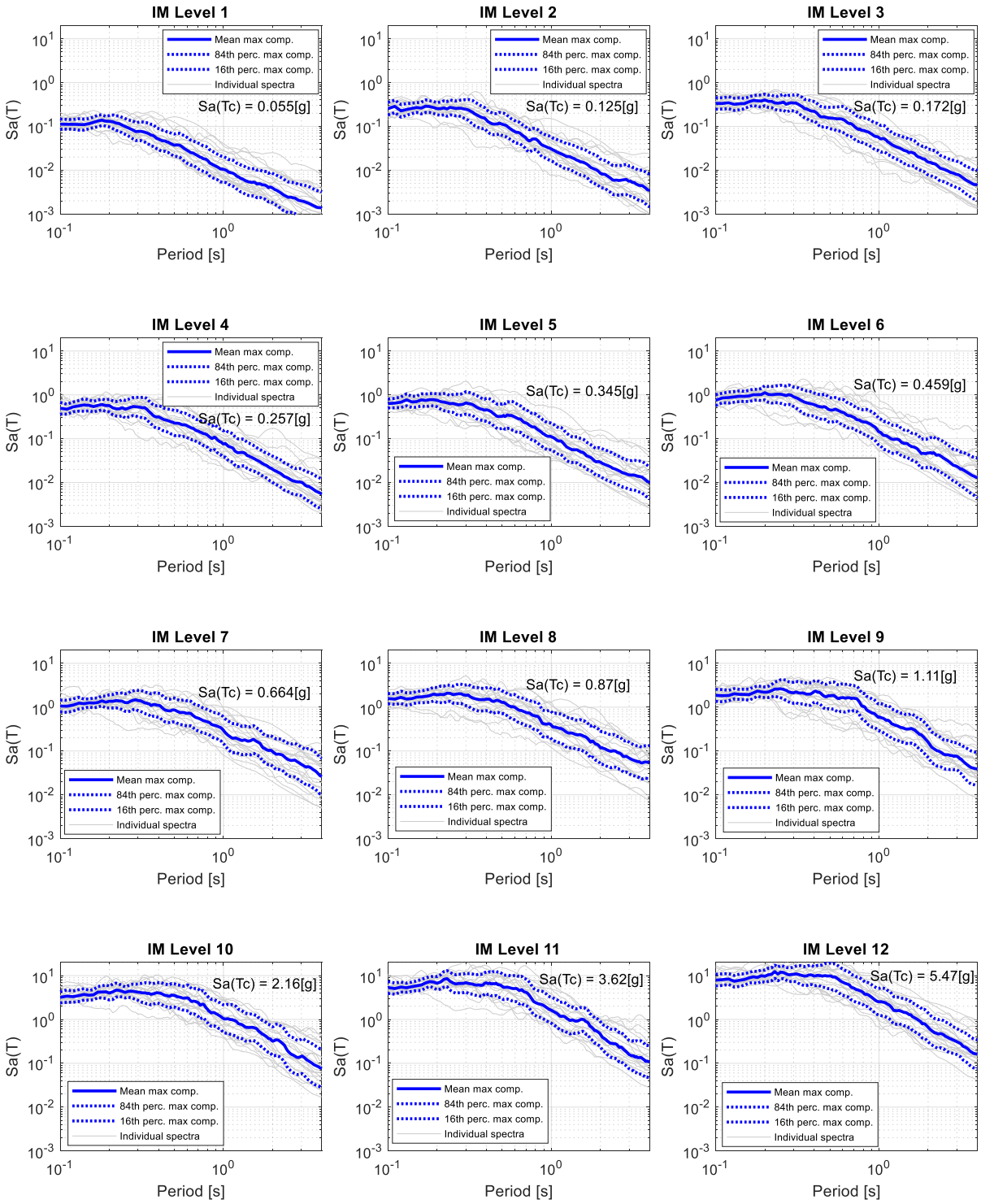

A.4.2 GM record sets for MSA (L'Aquila, soil C), $Sa(0.15s)$

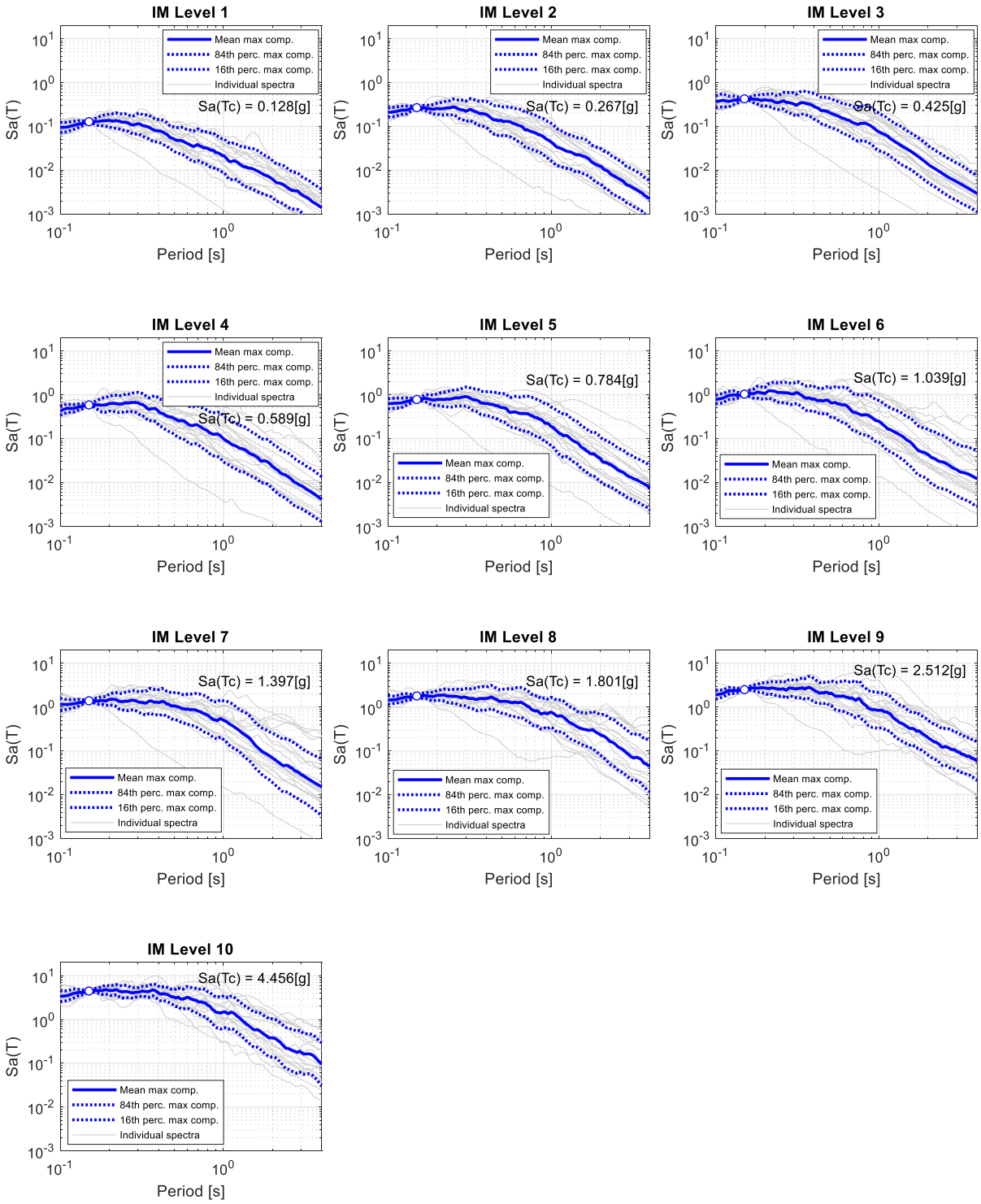

A.4.3 GM record sets for MSA (L'Aquila, soil C), $Sa(0.5s)$

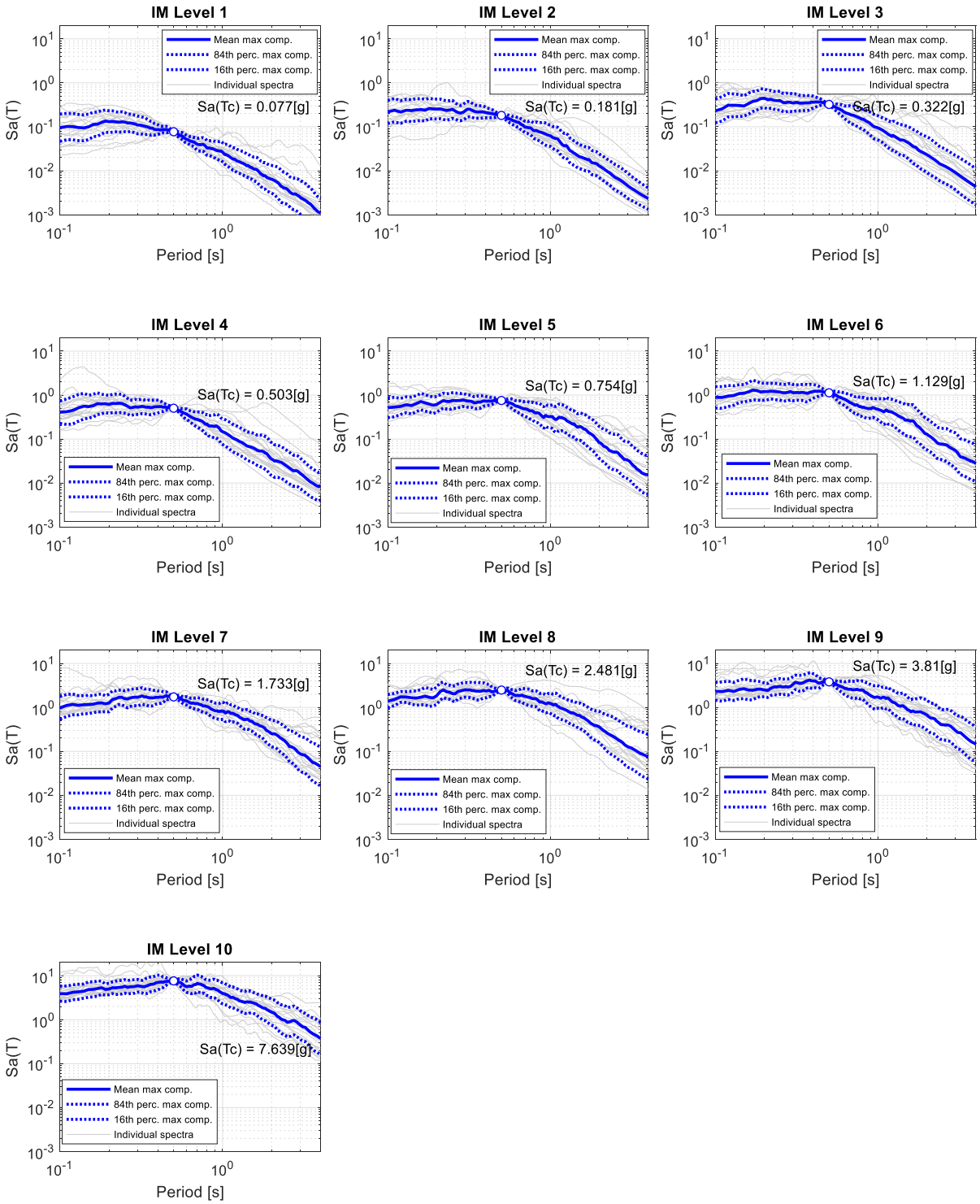

A.4.4 GM record sets for MSA (L'Aquila, soil C), $Sa(1.0s)$

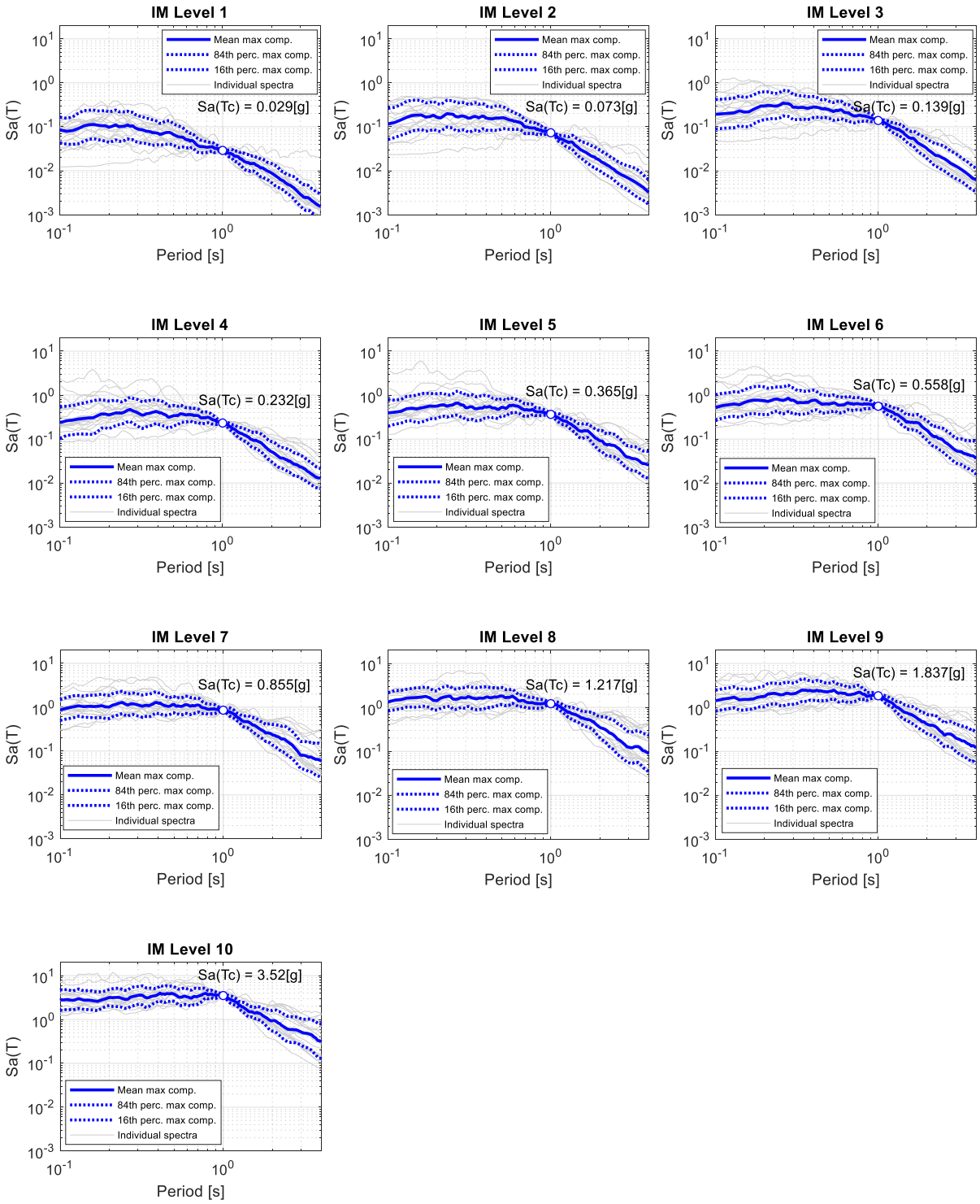

A.4.5 GM record sets for MSA (L'Aquila, soil C), $Sa(1.5s)$

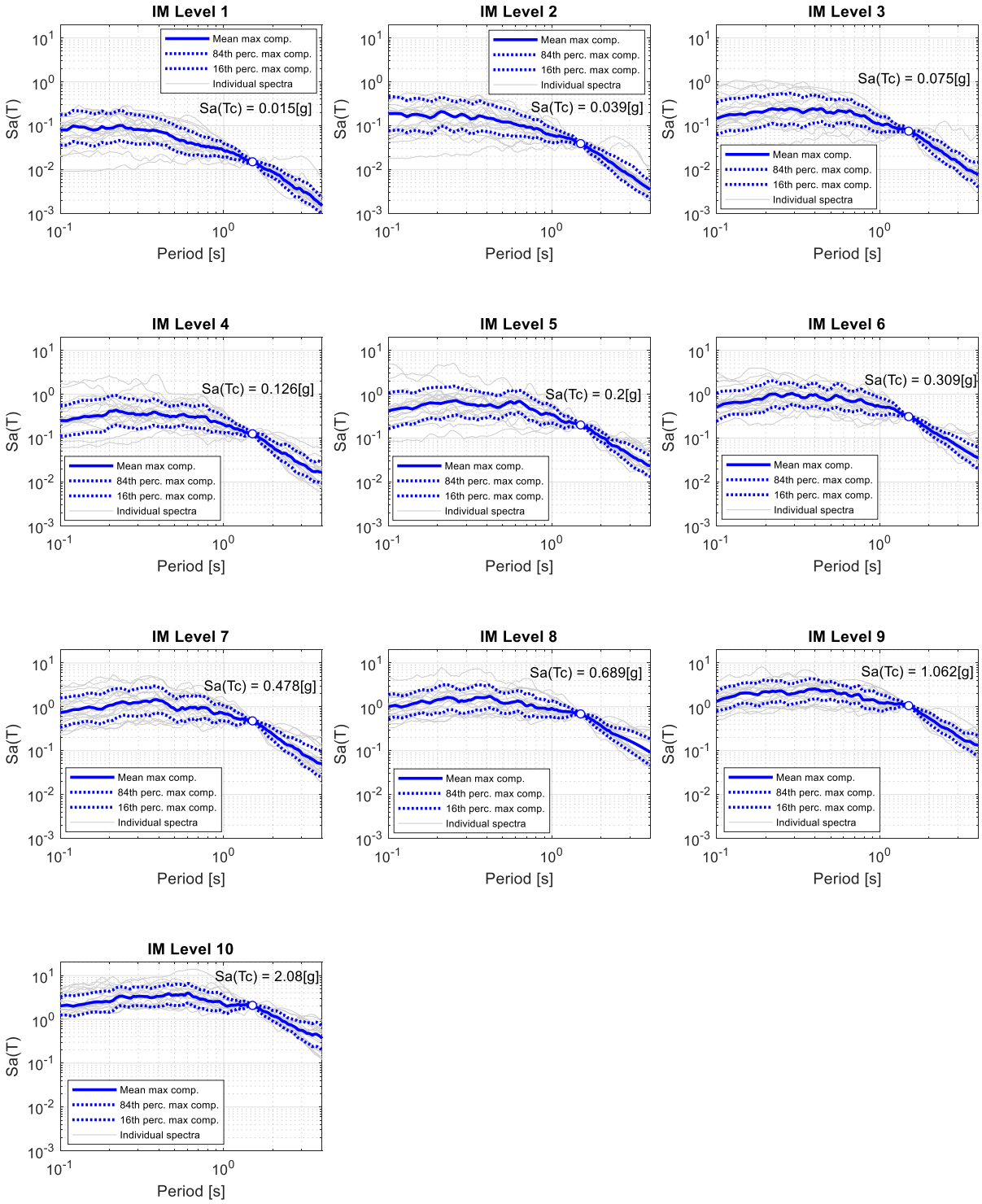

A.4.6 GM record sets for MSA (L'Aquila, soil C), $Sa(2.0s)$

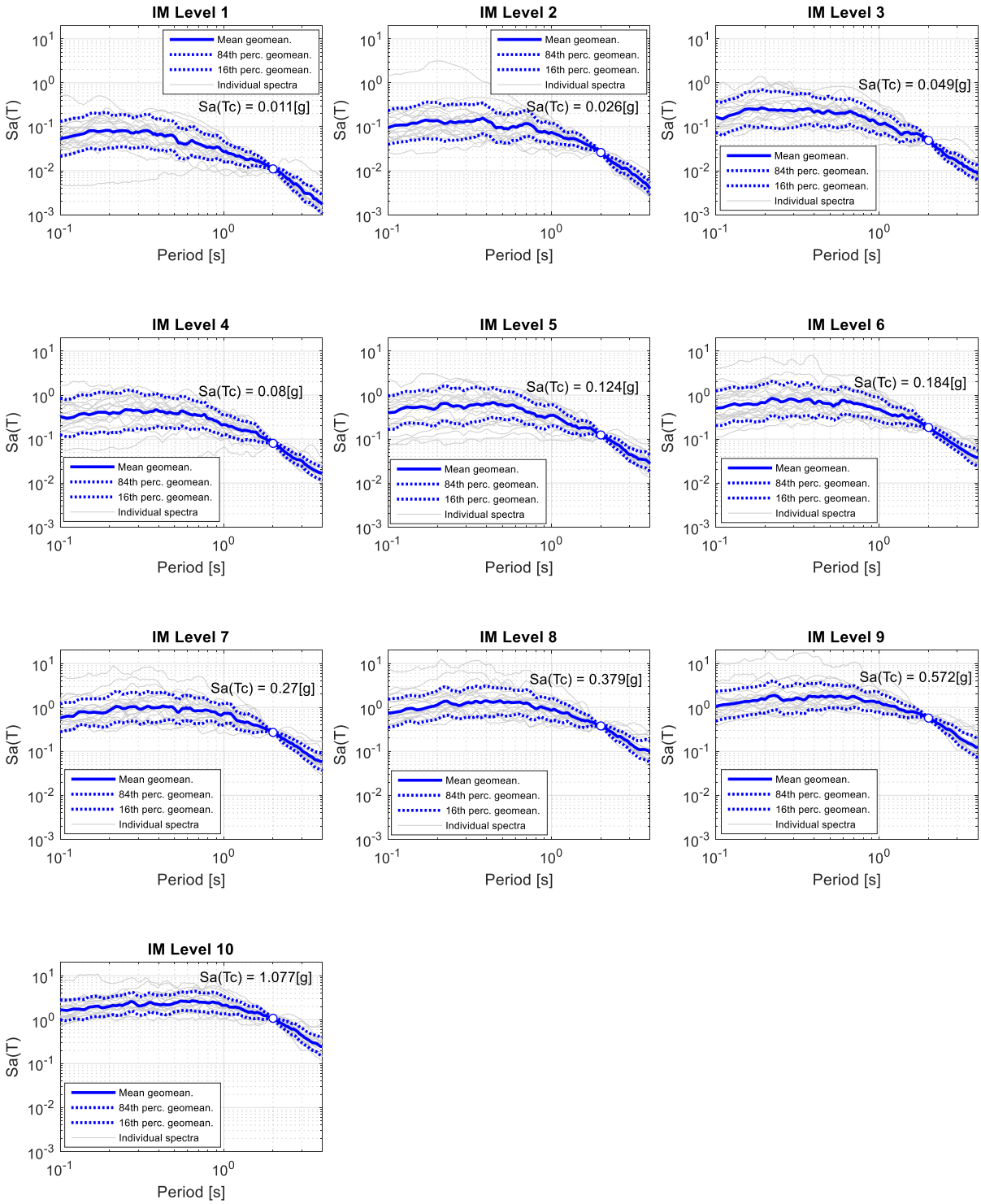

A.5.1 GM record sets for MSA (Naples, soil C), $Sa(0.15s)$

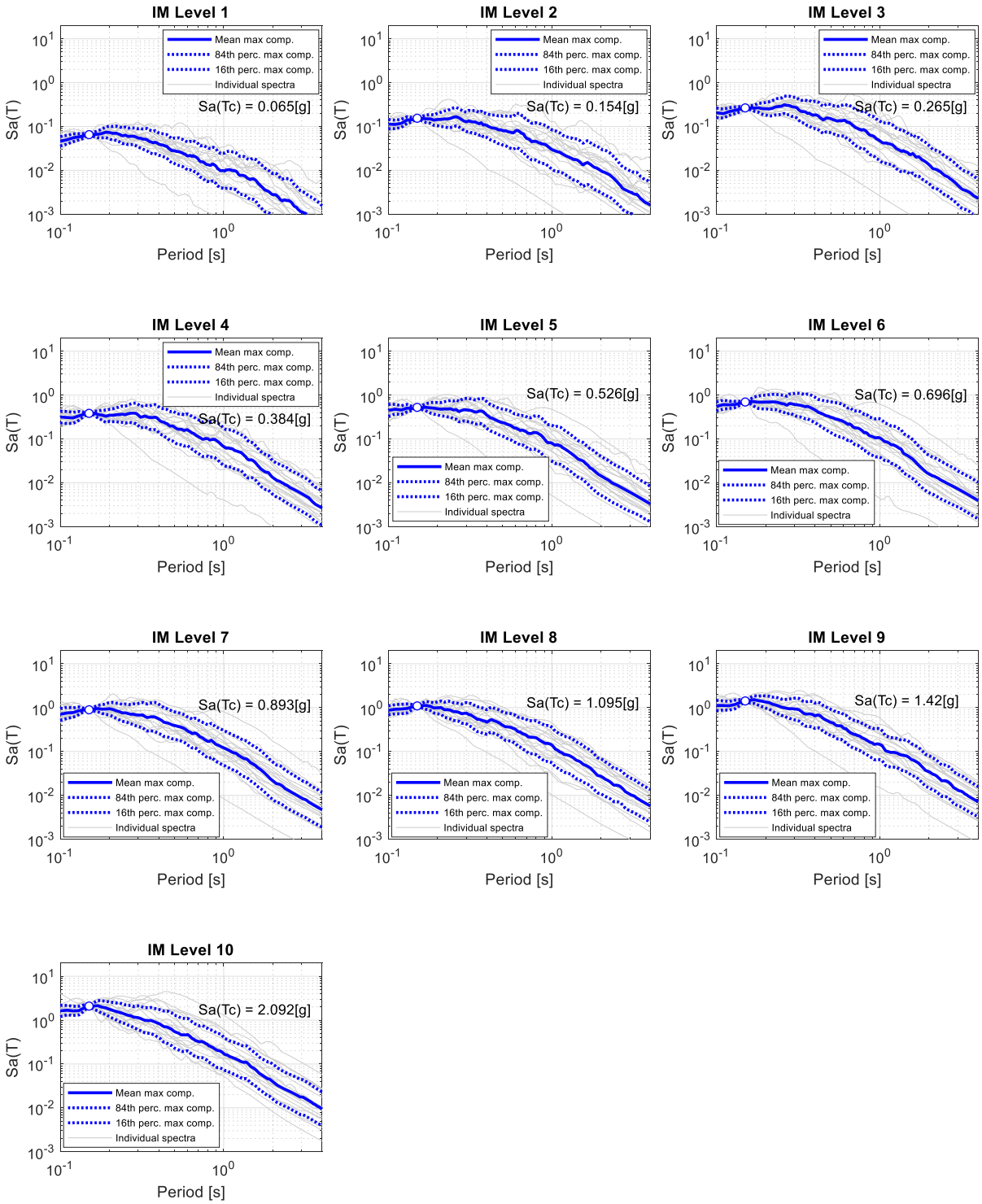

A.5.2 GM record sets for MSA (Naples, soil C), $Sa(0.5s)$

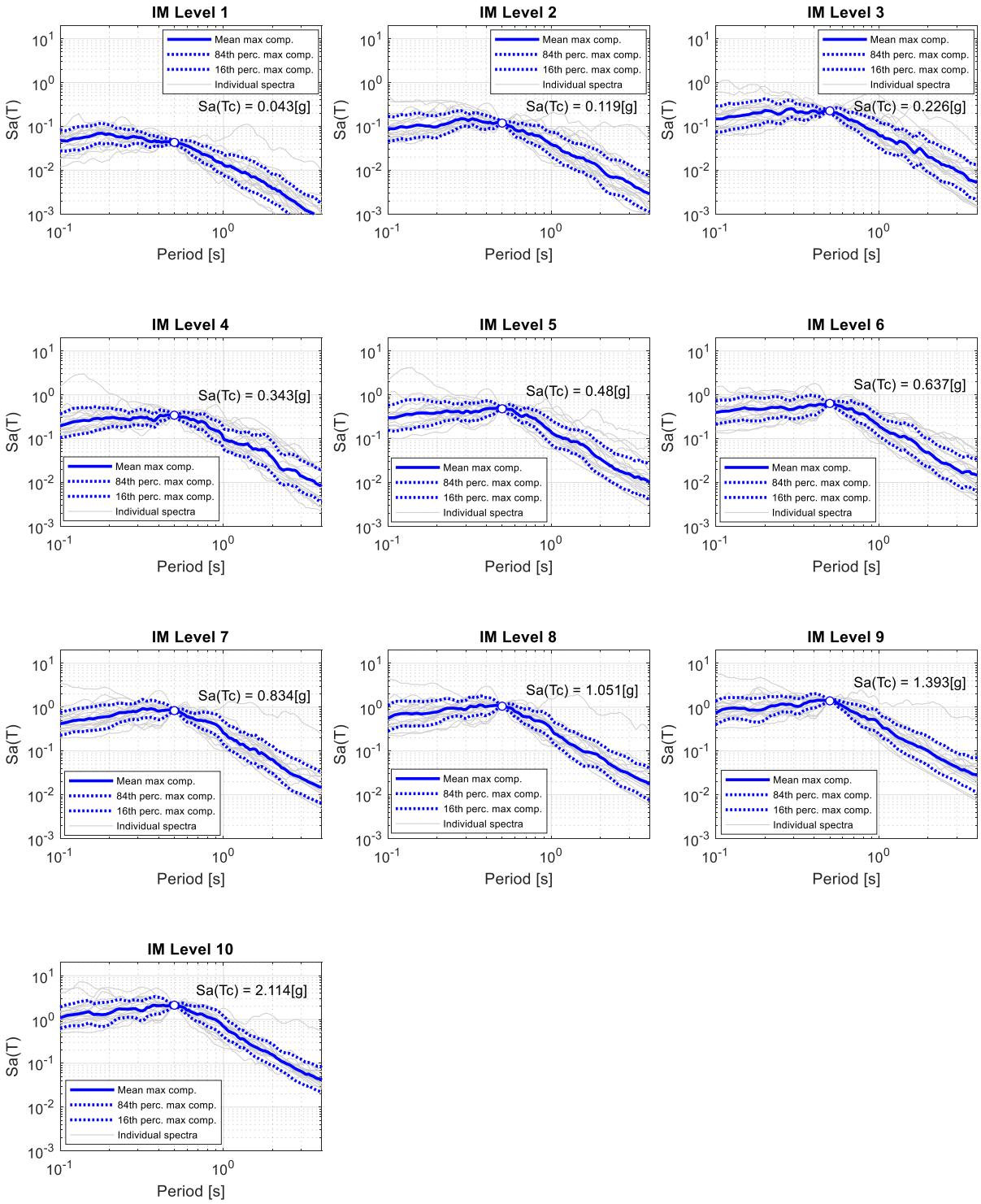

A.5.3 GM record sets for MSA (Naples, soil C), $Sa(1.0s)$

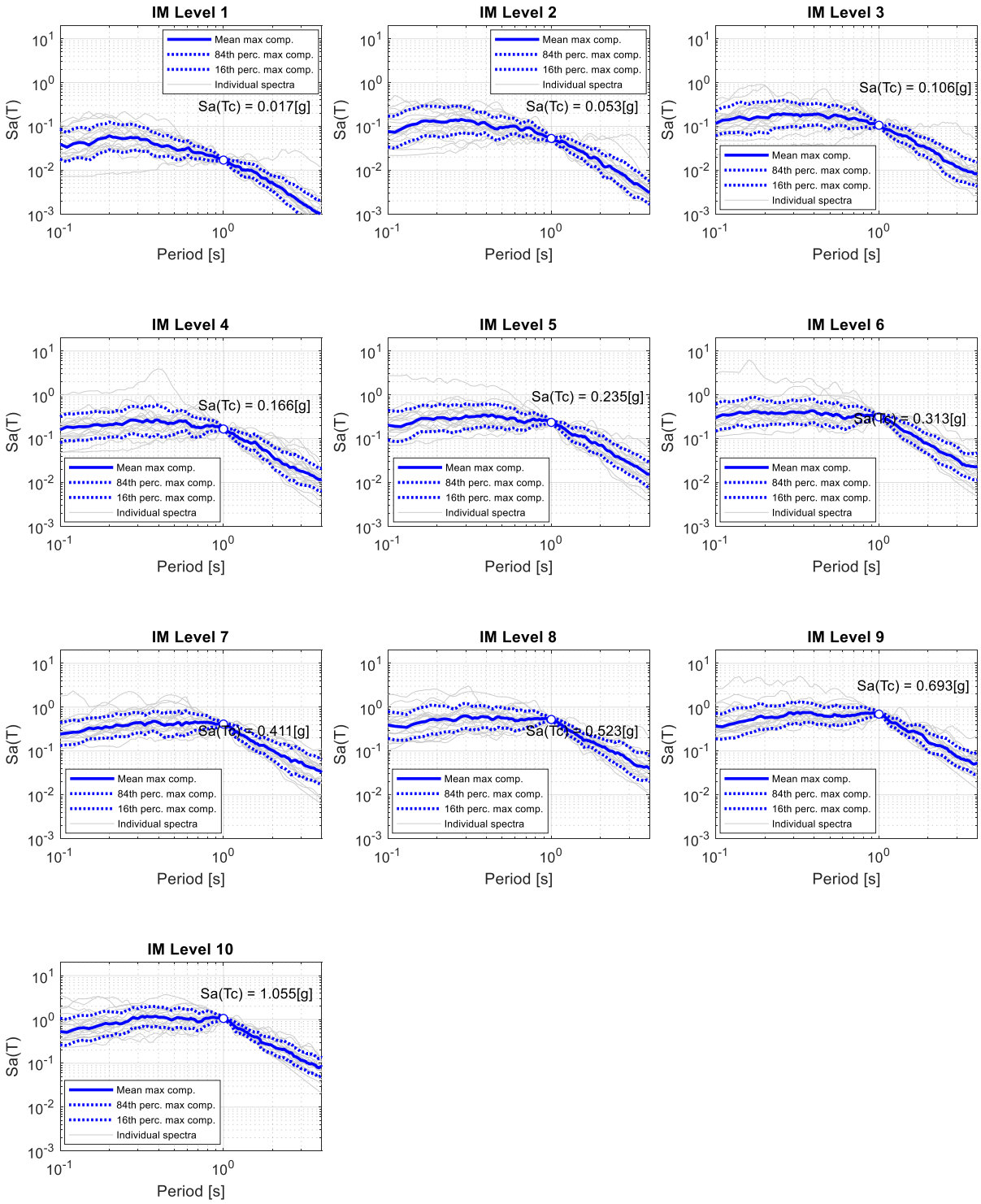

A.5.4 GM record sets for MSA (Naples, soil C), $Sa(1.5s)$

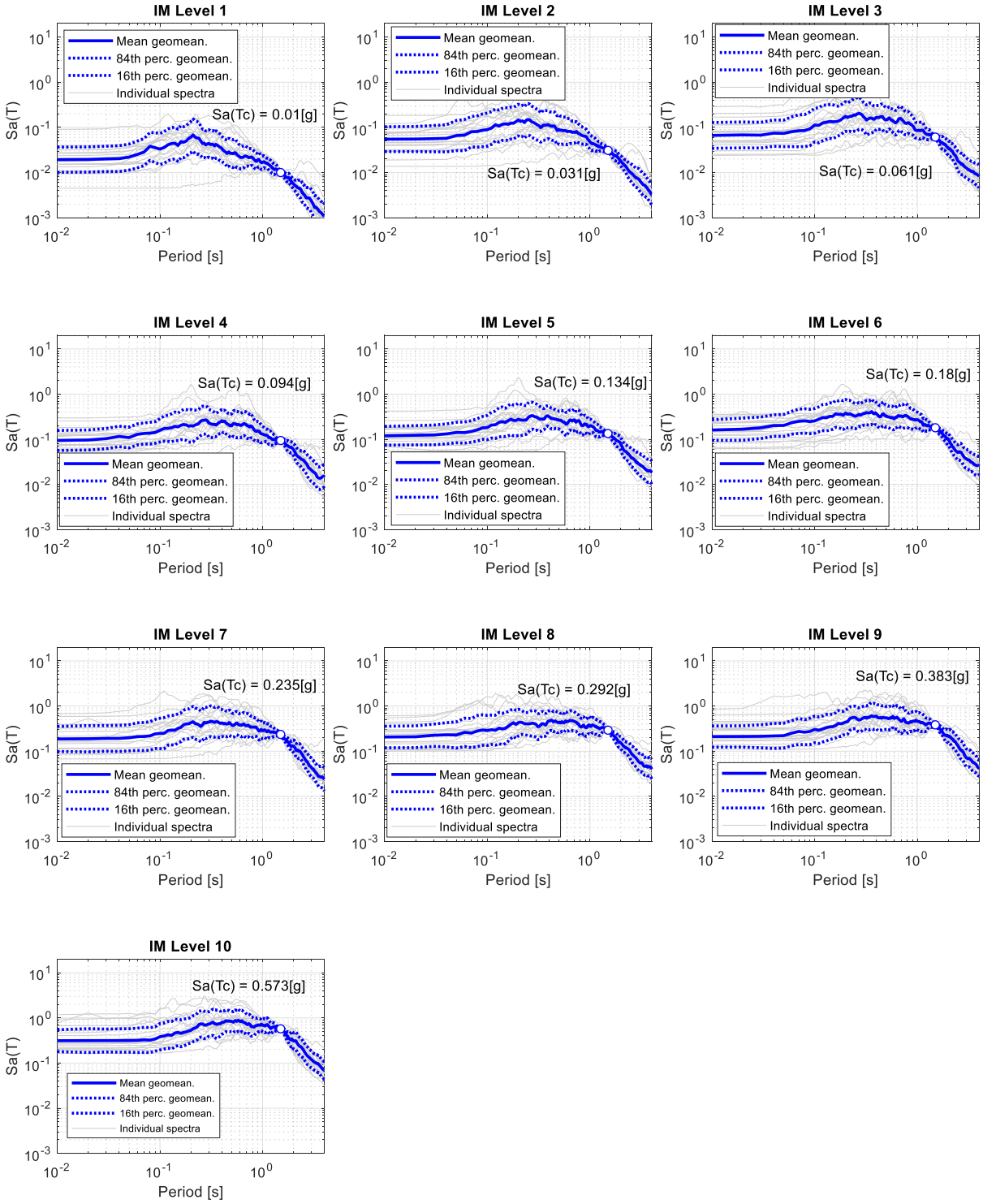

A.5.5 GM record sets for MSA (Naples, soil C), $Sa(2.0s)$

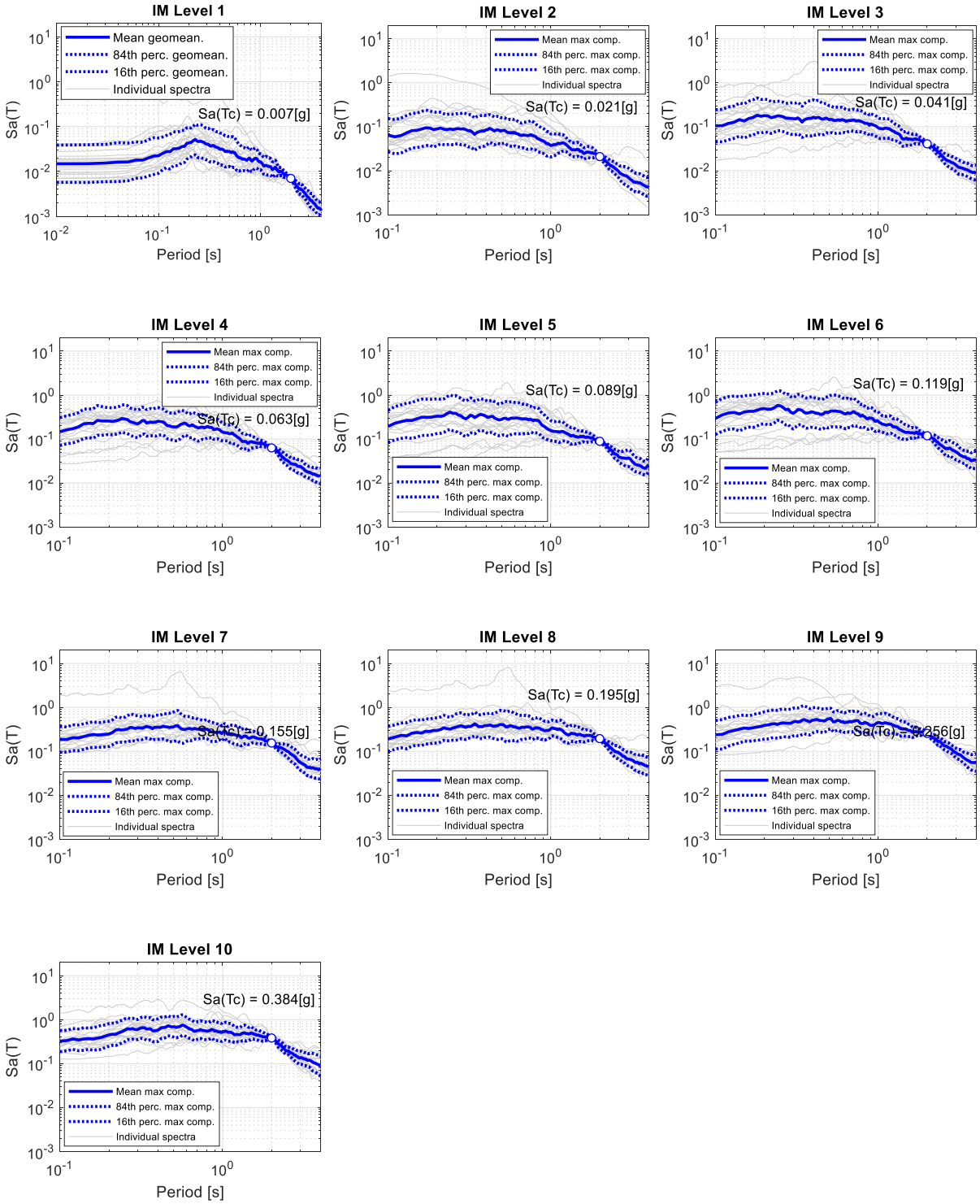

A.6.1 GM record sets for MSA (Milan, soil C), $Sa(0.15s)$

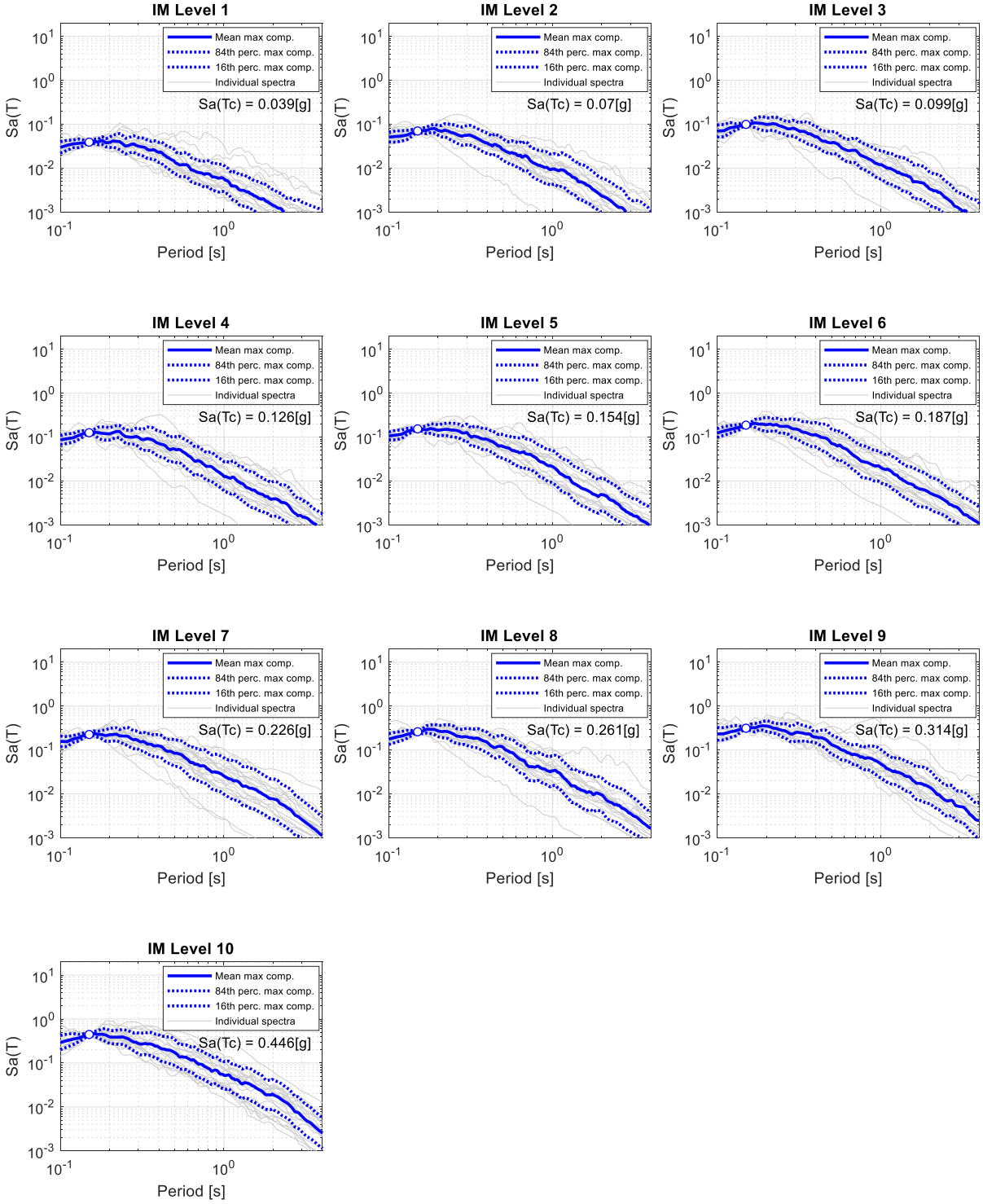

A.6.2 GM record sets for MSA (Milan, soil C), $Sa(0.5s)$

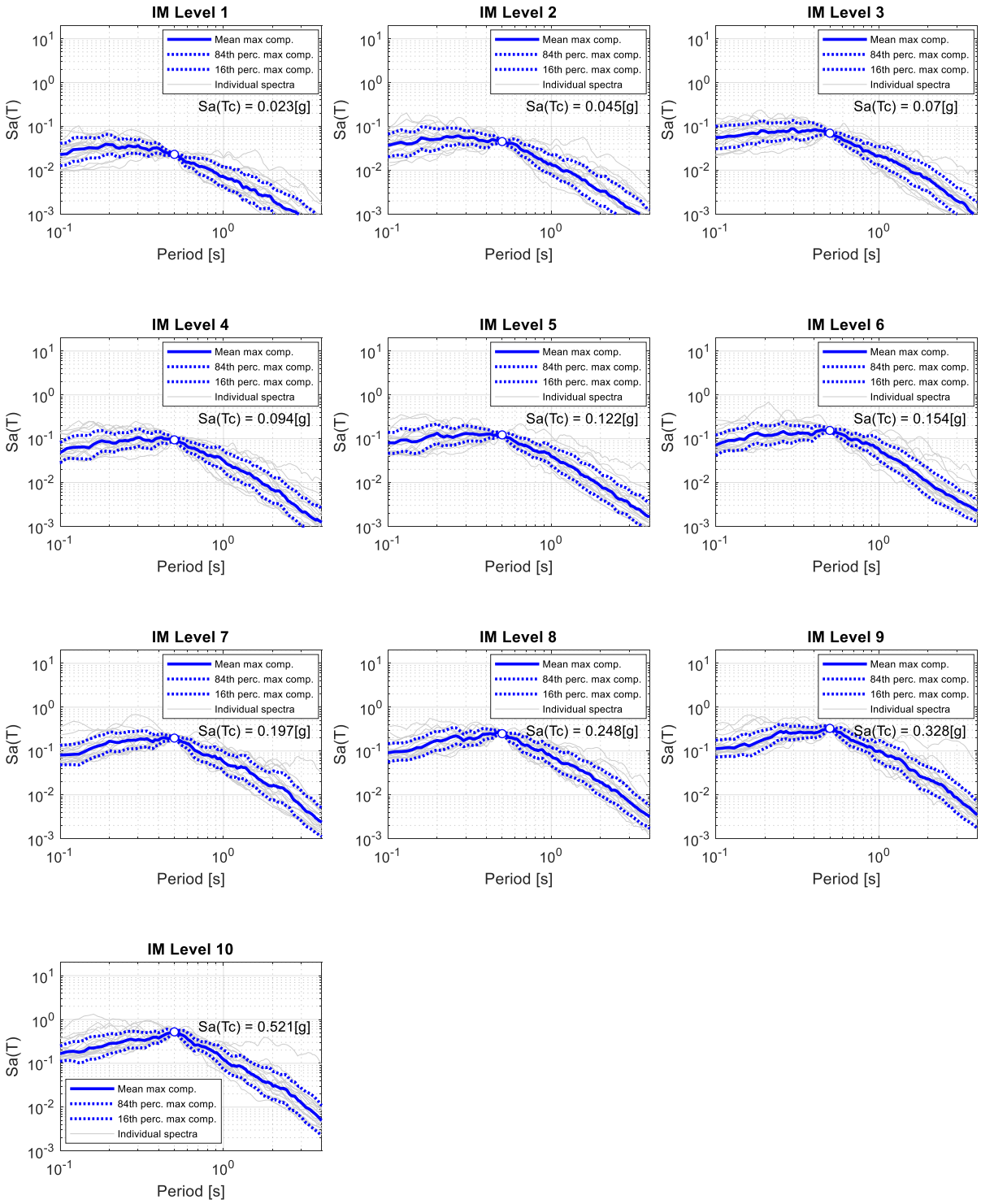

A.6.3 GM record sets for MSA (Milan, soil C), $Sa(1.0s)$

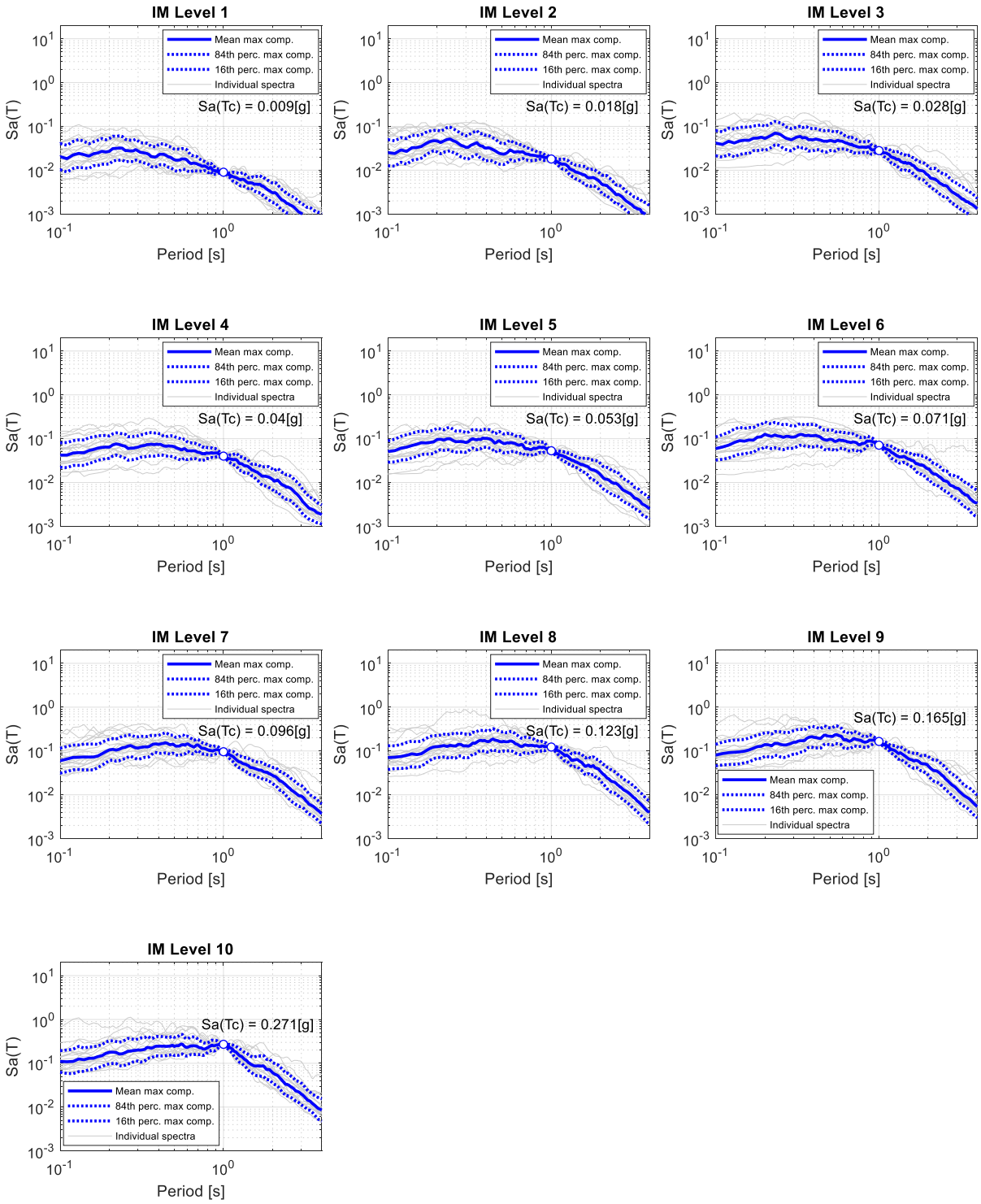

A.6.4 GM record sets for MSA (Milan, soil C), $Sa(1.5s)$

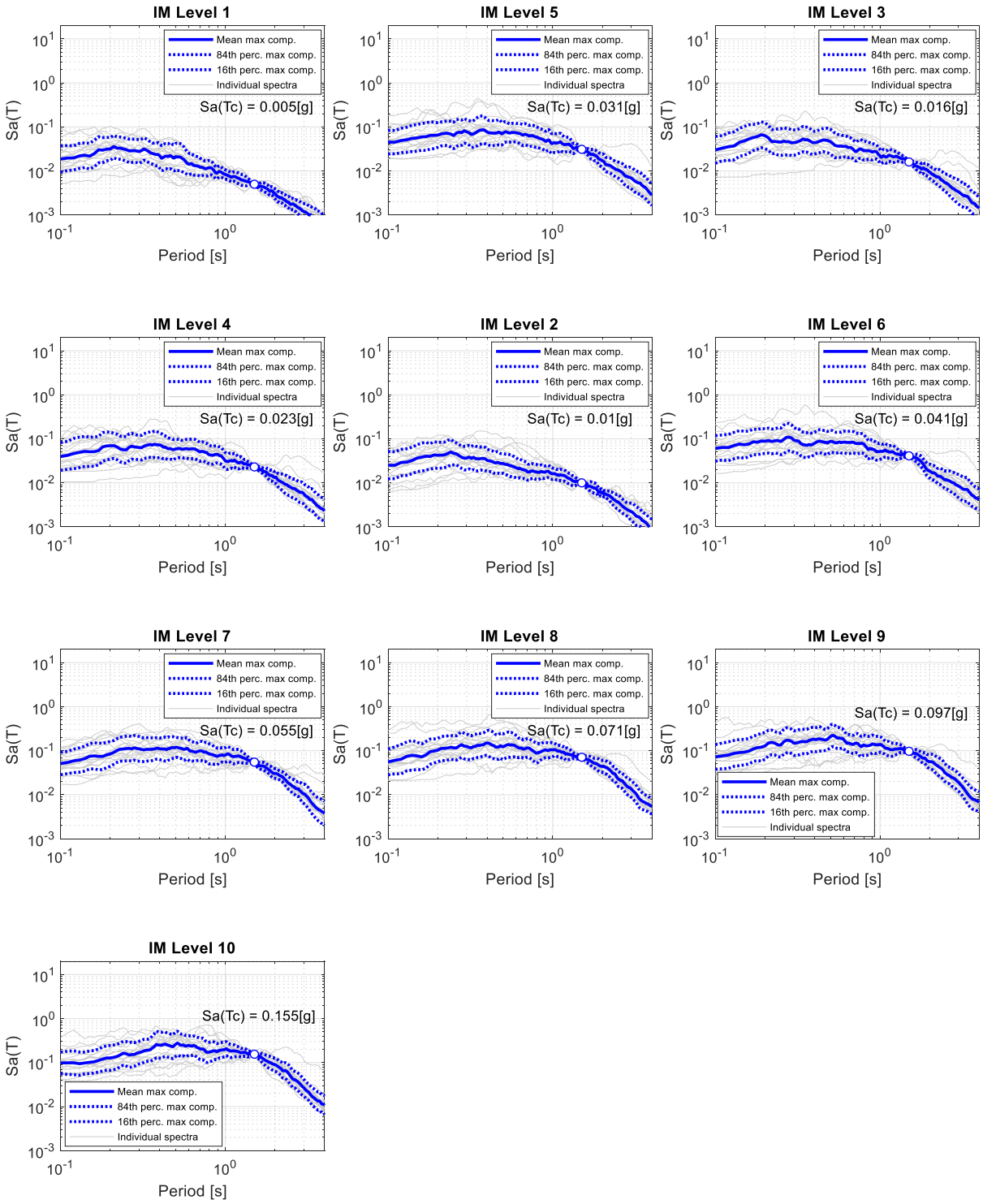

A.6.5 GM record sets for MSA (Milan, soil C), $Sa(2.0s)$

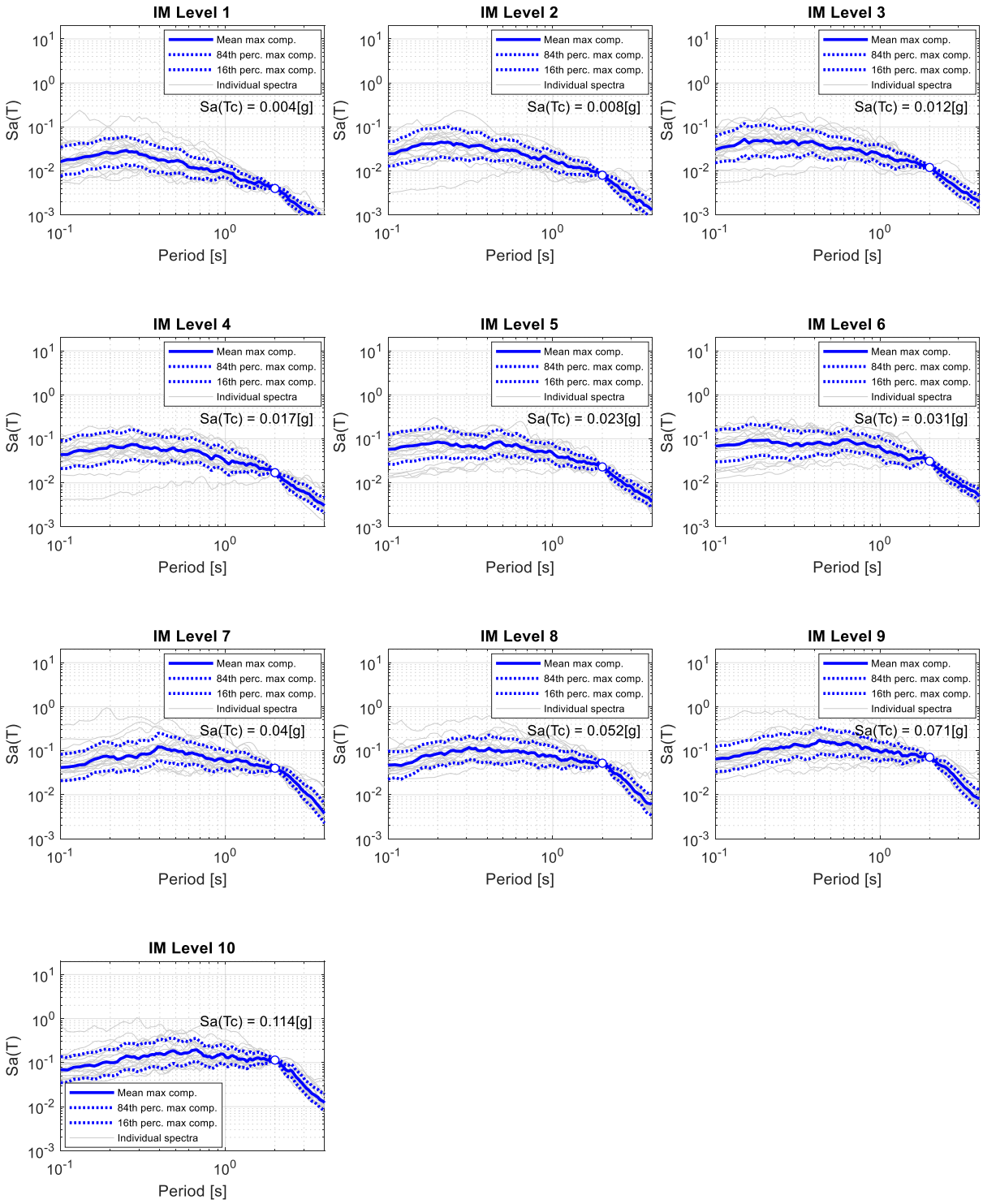

A.7 – PEER ground motion record sets